BIO-INSPIRED METAL AND METAL-OXIDE NANOPARTICLES: SYNTHESIS, CHARACTERIZATION AND APPLICATIONS

SANJAY KUMAR SINGH

UNDER THE GUIDANCE OF

Dr. ASMITA PRABHUNE

BIOCHEMICAL SCIENCES DIVISION

NATIONAL CHEMICAL LABORATORY

PUNE - 411008, INDIA

AND CO-GUIDANCE OF

Dr. B.L.V. PRASAD

JUNE 2008

BIO-INSPIRED METAL AND METAL-OXIDE NANOPARTICLES: SYNTHESIS, CHARACTERIZATION AND APPLICATIONS

THESIS SUBMITTED TO THE UNIVERSITY OF PUNE

FOR THE DEGREE OF

DOCTOR OF PHILOSOPHY

IN

BIOTECHNOLOGY

BY

SANJAY KUMAR SINGH

BIOCHEMICAL SCIENCES DIVISION
NATIONAL CHEMICAL LABORATORY
PUNE-411008
INDIA

JUNE 2008

Dedicated to my parents and teachers

CERTIFICATE

This is to certify that the work discussed in the thesis entitled **"BIO-INSPIRED METAL AND METAL-OXIDE NANOPARTICLES: SYNTHESIS, CHARACTERIZATION AND APPLICATIONS"** by **SANJAY KUMAR SINGH**, submitted for the degree of ***Doctor of Philosophy in Biotechnology*** was carried out under my supervision at the Biochemical Sciences and the Materials Chemistry Divisions of the National Chemical Laboratory, Pune, India. Such materials as have been obtained by other sources have been duly acknowledged in this thesis. To the best of my knowledge, the present work or any part thereof has not been submitted to any other University for the award of any other degree or diploma.

Date: **Dr. (Mrs.) Asmita Prabhune**

Place: Pune (Research Guide)

CERTIFICATE

This is to certify that the work discussed in the thesis entitled **"BIO-INSPIRED METAL AND METAL-OXIDE NANOPARTICLES: SYNTHESIS, CHARACTERIZATION AND APPLICATIONS"** by **SANJAY KUMAR SINGH**, submitted for the degree of ***Doctor of Philosophy in Biotechnology*** was carried out under my joint supervision at the Biochemical Sciences and the Materials Chemistry Divisions of the National Chemical Laboratory, Pune, India. Such materials as have been obtained by other sources have been duly acknowledged in this thesis. To the best of my knowledge, the present work or any part thereof has not been submitted to any other University for the award of any other degree or diploma.

Date: **Dr. B. L.V. Prasad**

Place: Pune (Research Co-Guide)

DECLARATION

I hereby declare that the work described in this thesis entitled **"BIO-INSPIRED METAL AND METAL-OXIDE NANOPARTICLES: SYNTHESIS, CHARACTERIZATION AND APPLICATIONS"** submitted for the degree of ***Doctor of Philosophy in Biotechnology*** has been carried out by me at the Biochemical Sciences and the Materials Chemistry Divisions of the National Chemical Laboratory, Pune, India under the joint supervision of Dr. (Mrs.) Asmita Prabhune and Dr. B.L.V. Prasad. Such materials as have been obtained by other sources have been duly acknowledged in this thesis. The work is original and has not been submitted in part or full by me for award of any other degree or diploma in any other University.

Date: **Sanjay Kumar Singh**

Place: Pune (Research Student)

Acknowledgement

It gives me great pleasure to extend my sincere gratitude and appreciation towards the people who have been involved, directly or indirectly, to make the research work described in this thesis possible.

First and foremost among them is my research co-guide and research advisor Dr. B. L. V. Prasad whose constant support and guidance has been always precious to make this thesis possible. His valuable suggestions and fruitful discussions made significant contribution to make this thesis feasible. I am also thankful to him for providing me an opportunity to learn cell culture work, which has opened a new horizon to my future research.

I would also like to thank my research guide Dr. Asmita Prabhune, without her support this thesis would not have completed. I am thankful for her regular guidance, encouragement, cooperation and appreciation. I would like to thank her for all the help that she has provided throughout, especially at the end of my research work.

I would also like to thank Dr. Murali Sastry for giving me the opportunity to work in this excellent field of nanotechnology. I am also thankful to him for his guidance, critical suggestions, motivations and endless enthusiasm that he has shown in my research work.

My research work has involved significant contribution from a lot of collaborative work both within NCL and outside. Among them, my sincere thanks goes to Dr. Alok Dhawan of IITR, Lucknow for all cytotoxicity and genotoxicity related experiments. His useful suggestions and critical remarks also helped a lot to shape this thesis in present form. I am really thankful to him for all the help that he provided during our stay at Lucknow. I would also like to acknowledge Dr. Mahima Bajpayee, Miss. Poonam Singh, Mr. Ritesh Shukla and, Miss. Vyom Sharma for their friendly nature, help in data anlaysis and in vitro experiments during our stay at Lucknow. I wish to acknowledge once more Miss. Poonam Singh for staying with us even after office hours during our experiments. I wish to thank Dr. C. V. Ramanna and Mr. Pitamber Patel for their help in sophorolipid purification and NMR measurements. I would also like to thank Dr. P. V. Satyam and Mr. Umananda M. Bhatta of IOP, Bhubneshwar for HRTEM measurements. I would like to extend my sincere thanks to Dr. Renu Pasricha for all the TEM measurements.

I would also like to thank Dr. S. Sivram, Director, NCL and Dr. Sourav Pal, HOD, Physical Chemistry Division, for allowing me to carry out research at this institute and providing with the required facilities. I am thankful to CSIR, Govt. of India, for the research fellowship.

I express my deep gratitude to Dr. Satish Ogale for his support, useful discussions and significant inputs. I also thank Dr. Ramesh R. Bhonde from the National Center for Cell Sciences, University of Pune for being the member of the work evaluation committee. I would also like to acknowledge Prof. J. K. Pal for all his help during initial days of my research. I am also thankful to Mrs. Suguna

Adhyanthya for her help during my research at NCL. Dr. Pankaj Poddar is also gratefully acknowledged for his friendly nature and all the help that he provided during my visa application.

My acknowledgement would be incomplete without the special mention of my former and current lab-mates for their help in the experiments and encouragement. I extend my sincere appreciation to Dr. Debabrata, Dr. Sumant, Dr. Anita, Dr. Saikat, Dr. Kannan, Dr. Shankar, Dr. Senthil, Dr. Hrushi, Dr. Ambrish, Dr. Akhilesh, Dr. Amit, Dr. Atul, Dr. Vipul, Dr. Sourabh, Maggie, Deepti, Manasi, Ajay, Sudarshan, Prathap, Priyanka, Sheetal, Dr. Vijay, Vilas, Anal, Ravikumar, Anil, Minakshi, Imran, Umesh, Ramya, Baisakhi, Adhish, Neeraj, and Vivekanand for creating a cordial atmosphere and helping me. I enjoyed the company of some at the cricket ground and badminton court. I would again like to thank Maggie, Manasi and Deepti for helping me in this thesis correction. I am really thankful to Maggie for always being there to help me during my stay at NCL.

I would also like to thank Saif, Haider, Swarna, Gauri, Mugdha, Atul, Sandeep, Deepak, Neha, and Dina who had worked with me for their M. Sc. project. I am also thankful to my NCL friends Balchandra, Nagesh, Shekhar, Sunil, Dharmendra, Pushpesh and, Ravindra for their support and cheerful discussions. I would also like to thank my roommate and collaborator Mr. Rasesh Parikh for all the time that we shared and for his continious help even for small things.

I wish to thank Namita Das, Namita Mathur, Rajendra, Raghvendra, Nidhi and Amit as my graduation friends and Pawan, Om Prakash, Ruchna, Chetna, Neha as my postgraduation friends for all the encouragement and help in some or other ways.

I would like to thanks Mr. Deepak, Mr. Punekar and Mr. Pardesi from the Physical Chemical Division office for helping me extensively with the routine official and administrative work. I would also like to thank NCL Library staff, administrative staff, and technical staff at CMC for their assistance in the administrative issues during this time.

This thesis would not have been possible without the strong faith, continious support and encouragement of my family, because of all their efforts I am here. I wish to express my deep gratitude to my mother for her support, trust, patience and blessing that led me to successfully complete my doctoral research. I am really very thankful to my brother, Alok for all his help.

…Sanjay Singh

Table of Contents

Chapter IV: A Novel Biological Approach for Metal Nanoparticles and their Antibacterial Applications

Chapter I

Introduction

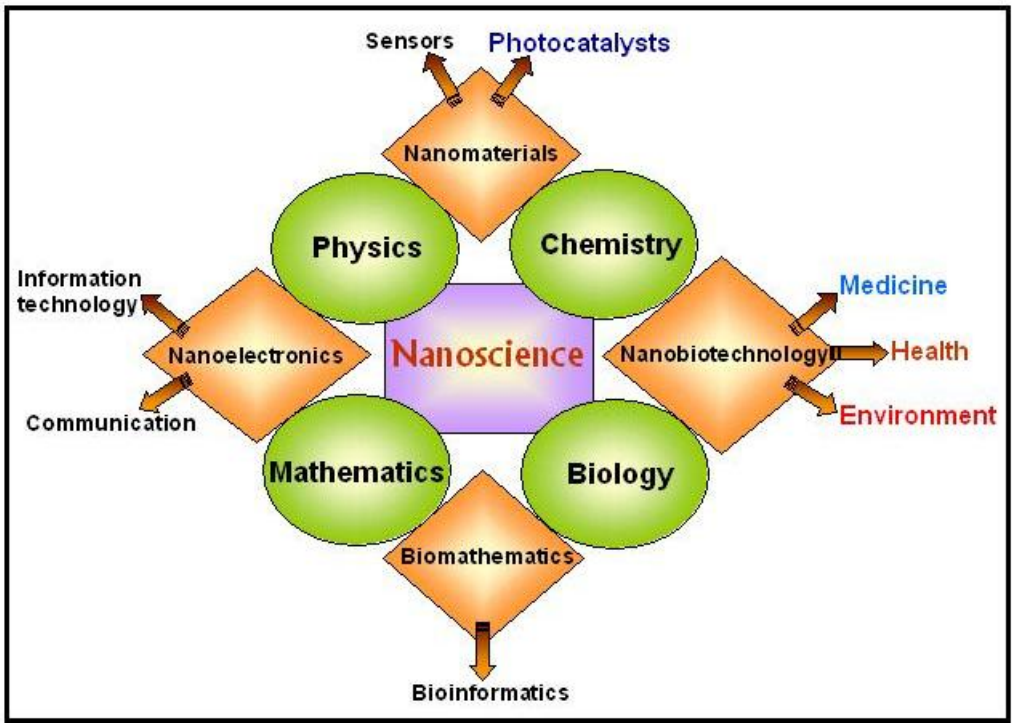

This chapter is an introduction to the thesis and covers various aspects of nanoscience that are pertinent to the thesis. The definition and a brief historical perspective of nanoscience have been presented first. The synthetic procedures, restricted mainly to the classes of nanomaterials considered in our work, are briefly summarized. Further, the toxic effects of nanomaterials on biological systems at cellular level are highlighted and the need for toxicity assessments is brought out. Finally a brief outline of the thesis is laid-out.

1.1 Introduction to Nanotechnology

Nanoscience deals with the study of the objects and systems in which at least one dimension is within 1-100 nm range and can be considered as the science and technology that enable us to prepare and understand the various aspects of materials between the molecular and bulk regimes. It embraces many different fields including biology, chemistry, physics, engineering and medicine etc. A nanometer, a billionth of a meter, is about the size of six carbon atoms in a row. The term "nano" is taken from a Greek word "nanos", which means "little old man" or "dwarf".

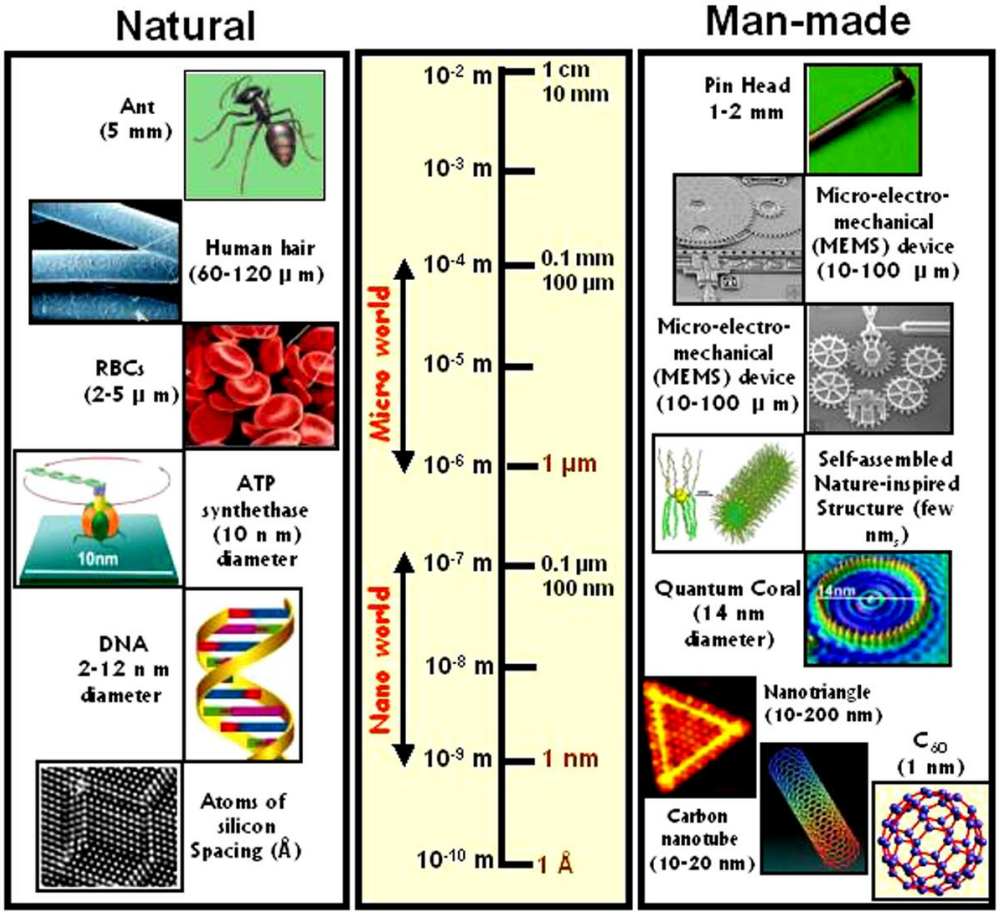

Figure 1.1: *A picture representing the relative sizes of various natural and man-made objects. (Images courtesy: Various sources at http://images.google.com).*

1.2 Historical Background

The utility of small-scale materials has been realized thousands of years ago in making steel, paintings and in vulcanizing rubber etc [1]. Each of these processes is based on the properties of ensembles (majority of them in nanoscale) that impart a

new property to the material very different from atomic/molecular or bulk properties of the same material. A good example is glass containing nanosized metals. An artifact from this period known as Lycurgus cup resides in the British Museum in London. This cup shows different colors (Figure 1.2) in transmitted and reflected and is made from soda lime glass containing gold and silver nanoparticles [2].

Figure 1.2: *The Roman Lycurgus cup showing different colour due to the surface plasmons of gold and silver nanoparticles. Under normal lighting (day-light) it appears green. However, when illuminated from within, it becomes red in colour. The cup illustrates the myth of King Lycurgus. (Images courtesy: www.timkelf.com/Research.html).*

Faraday's pioneer work on systematic synthesis of gold sols in the year 1857 [3], introduced nanoscience as a discipline and it started to swell further. In 1914, the first observations and size measurements of nanoparticles were performed by R. A. Zsigmondy, who carried out a detailed study of gold sols and other nanomaterials having sizes below 10 nm [4]. He used ultramicroscope to see the particles lesser than the wavelength of light. Zsigmondy was also the first who used "nanometer" scale clearly to measure particle size. Further, in 1905, Einstein articulated a theory of the thermal energy based on heat and how it would cause particles to naturally distribute in a certain volume. Robert Brown (in 1827) said that motion of small particles contains an inherent energy that causes them to vibrate constantly, which is now called as "Brownian motion". Moreover, the famous dinner talk entitled "There's Plenty of Room at the Bottom" in 1959 by Richard Feynman of the American Physical Society, discussed the potential possibilities of nanotechnology at

atomic/molecular scale [5] and is now considered as the basis of modern nanoscience research.

In 1969, Leo Esaki pioneered the bottom up approach to synthesize nanosized semiconductors. In 1974, the term "nanotechnology" was first coined by Norio Taniguchi, a professor of Tokyo Science University [6]. In 1981, an imaging device, the scanning tunneling microscopy (STM), was invented by Gerd Binning and Heinrich Rohrer [7], which aided in the better understanding of the nano-world. They won the Nobel Prize for this discovery in physics in 1986. In 1985, Professor Harold Kroto, Richard Smally and Robert Curl, discovered fullerene, a football shaped molecule, made up of sixty carbon atoms [7], that won them Nobel prize in chemistry in 1996. This was followed by the discovery of carbon nanotubes. Those are basically hollow tubes of several nanometers derived from graphite sheets [7].

1.3 Properties of Nanomaterials

At the nanoscale dimensions, the material properties change significantly differing completely from their bulk counterparts. Nanomaterials display new phenomenon associated with the quantized effects and with the preponderance of surfaces and interfaces. The quantization effect arises in nanometer regime because the overall dimensions of objects are comparable to the characteristic wavelength of fundamental excitations in materials.

As the size of material decreases, the percentage of surface atoms increases, thus increasing the reactivity and making them highly reactive catalysts, as surface atoms are the active centers for elementary catalytic processes [8]. For example, iron nanoparticles of sizes 3 nm, 10 nm and 30 nm will have 50 %, 10 % and 5 % of atoms on surface [8]. Among the surface atoms, atoms sitting on the edges and corners are more reactive than those in planes [8]. Also, the percentage of atoms at the edges and corners increases with decrease in the particle size and therefore, smaller metal particles are preferred for catalysis [8]. A schematic representation is shown in Figure 1.3. An interesting feature of metal and semiconductor nanoparticles is their optical property. These nanomaterials exhibit interesting shape and size dependent optical properties due to quantum confinement. However, in a bulk crystal, the properties of

material depend on chemical composition and not on size. Due to the decrease in size of a crystal towards nanometer regime, the electronic structure is altered from continuous electronic bands to discrete or quantized electronic levels. Therefore, the continuous optical transitions between the electronic bands become discrete and the properties of nanomaterial become size dependent [9].

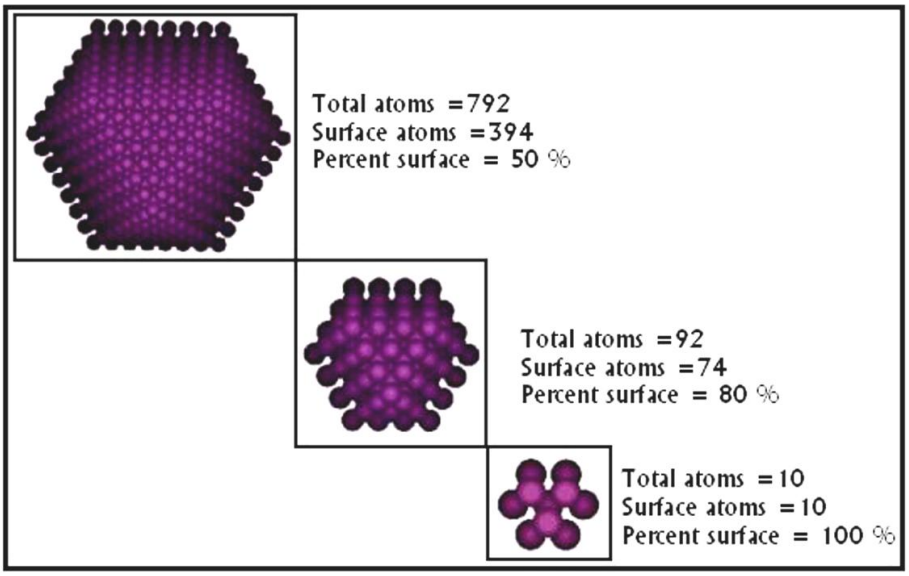

Figure 1.3: *Schematic representation of increasing surface area with decrease in size.* ***(****Image courtesy: www.yu.edu/faculty/afrenkel/page.aspx?id=1325).*

Metal nanoparticle (Au, Ag and Cu) dispersions exhibit colors due to the surface plasmon resonance (SPR) phenomenon, which is caused by the coherent oscillation of conduction band electrons when they interact with electromagnetic field [10]. During SPR, polarization of the electrons with respect to the much heavier ionic core is induced by the electric field of an interacting light wave. This creates a net charge difference at nanoparticle surface, which acts as a restoring force. Thus, a dipolar oscillation of all the electrons with the same phase is created (Figure 1.4). The so observed color originates from the strong absorption by the metal nanoparticles when the frequency of electromagnetic field becomes resonant with the coherent oscillation of electron motion [11]. The frequency and width of SPR depends on the metal nanoparticle size, shape, dielectric constant of the metal itself and the surrounding medium [10]. Similarly, other important properties such as electronic properties [12], magnetic properties [13], melting point [14] and catalytic properties

[15] of the nanomaterials depending on their shape, size, composition and surrounding medium have been studied in great detail.

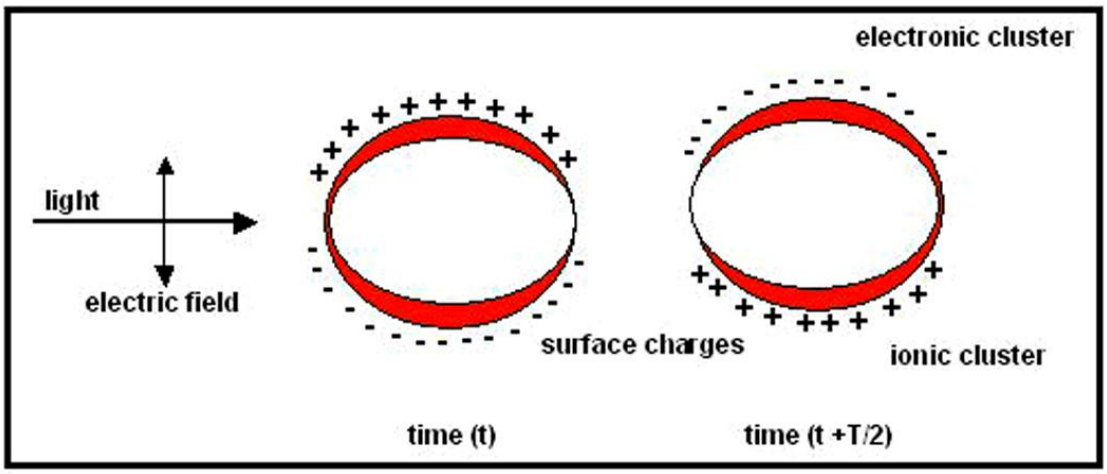

Figure 1.4: *Illustration of the excitation of the dipole surface plasmon oscillation. A dipolar oscillation of the electrons is created with period T. (Figure courtesy: reference 9a).*

Another most important property of nanomaterials, especially semiconductor nanoparticles, is to exhibit photocatalytic behavior. Size dependent properties (quantization) of semiconductors (such as TiO_2 and ZnO etc.) and quantized charging effects in metal nanoparticles provide the basis for developing new and effective systems [16-22]. These nanostructures provide innovative strategies for designing next generation energy conversion devices [23-28]. In a semiconductor, the energy difference between the valence band and the conduction band is known as the 'Band Gap'. When it absorbs radiation from sunlight or illuminated light source (fluorescent lamp), it generates pair of electron and hole. This stage is known as the semiconductor's 'photo-excitation state'. The recombination of electron-hole pair may result in light emission with appropriate further reactions. These semiconductors behave as photocatalysts.

Nanotechnology has created a kind of revolution as this new area encompasses physics, chemistry, materials science and engineering and also biology and medicine. Several applications are envisaged from these interesting materials in the field of sensors [29], catalysis [30], diagnostic tools [31], therapeutic agents [32], drug/gene delivery vehicles [33], solar cells [34], plasmonics devices [35], cosmetics [36], coating materials [37], cell imaging [38], fuel cells [39], photonic band gap materials

[40], single electron transistors [41], non-linear optics devices [42] and surface enhanced raman spectroscopy [43].

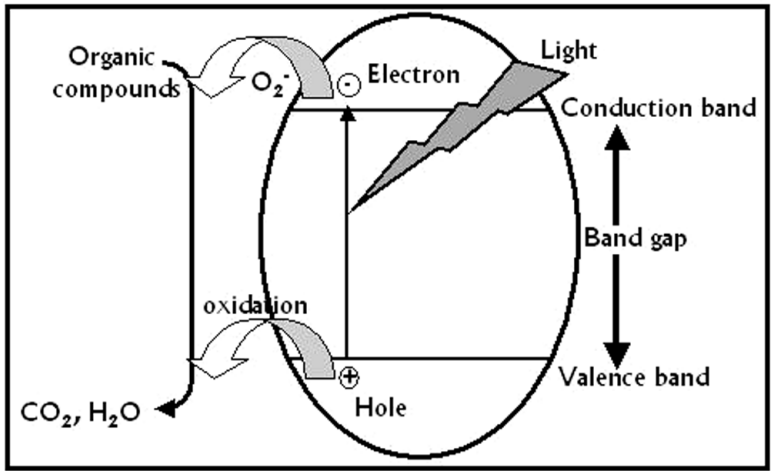

Figure 1.5: *Schematic representation of photocatalytic degradation of an organic compound through light mediated excitation of electron across the band gap.*

1.4 Synthesis of Nanomaterials

The most challenging part of research in the field of nanotechnology is the cost effective and environmentally safe procedures for nanomaterials synthesis. The approach towards nanomaterials synthesis could be broadly divided into two groups following the principle of either "top down approach" or "bottom up approach" (Figure 1.6). The top down approach seeks to fabricate nanodevices on silicon (or other semiconductors) chips directly using electron beam or X-ray lithography. In the bottom-up approach, nanostructures are synthesized from atoms or molecules. In the latter, the synthesis protocols can be further divided into physical methods, chemical methods and biological/bio-inspired methods. A flow chart indicating the different synthetic methods for nanomaterials has been shown in Figure 1.7. Various physical methods have been successfully employed for nanomaterial synthesis such as vapor deposition [44], thermal decomposition [45], spray pyrolysis [46], photoirradiation [47], laser ablation [48], ultrasonication [49], radiolysis [50] and solvated metal atom dispersion [51].

However, chemical methods have had several advantages over physical methods; therefore chemical methods are widely accepted for nanomaterials synthesis. Nanomaterials such as metals, metal oxides and semiconductor

nanoparticles can be synthesized by chemical methods by reduction or oxidation of metal ions or by precipitation of the desired composites (by carrying out appropriate chemical reaction).

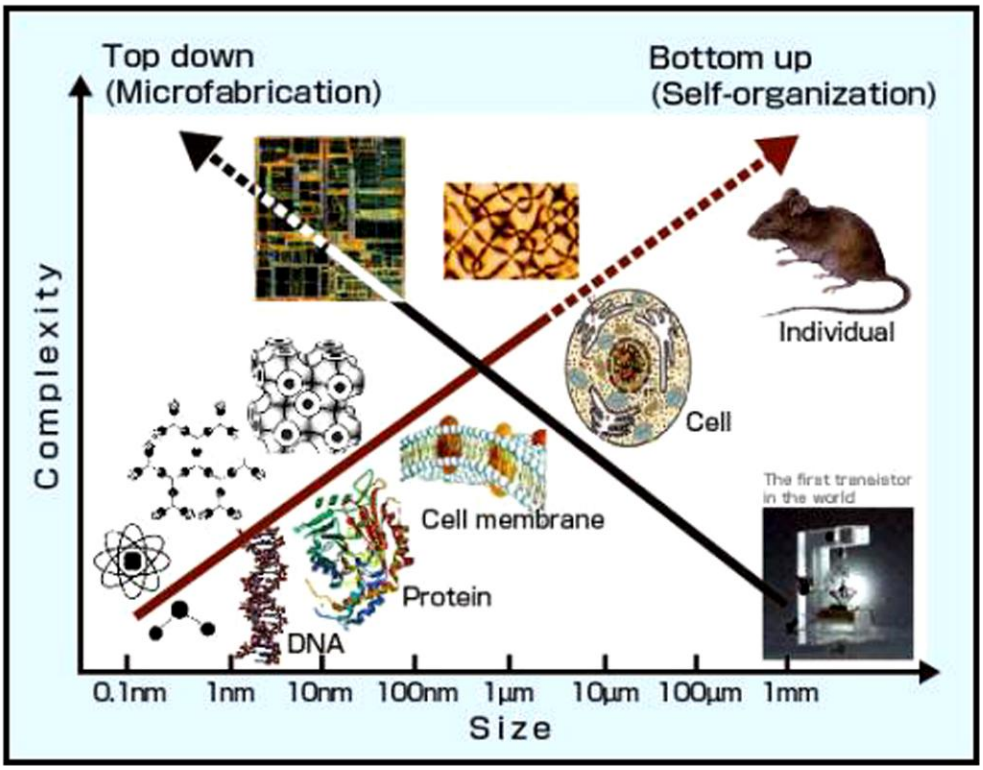

Figure 1.6: *Examples that depict the fabrication (complexicity) of materials at different length scales by 'Top-down' and 'Bottom-up' approaches. (Image courtesy: http://images.google.com).*

Chemical methods may require a capping agent to restrict the growth of particles in the nanometer dimension. The use of capping molecules results in better shape and size control, stability and assembly of nanomaterials. Different capping agents starting from simple ions to various biomolecules have been employed for nanomaterial stability [52]. Following chemical methods nanomaterials can be synthesized in aqueous medium as well as in organic medium too, depending on their intended applications. Aqueous dispersed chemically synthesized metal nanoparticles can be easily phase transferred to organic medium [53]. Although, above-mentioned synthetic procedures result in good control over shape, size and crystallinity, they very often involve the use of hazardous reagents, volatile solvents and intense physico-chemical conditions. Therefore, currently researchers are more interested

towards development of environmentally benign procedures for nanoparticle synthesis that do not use toxic chemicals. This would help in minimizing chemical hazards to health and environment, reducing waste and preventing pollution. As a result, researchers have been focusing their attention towards the bio-inspired/biomimetic processes for nanomaterial synthesis as it operates at environmentally benign conditions. Biological synthesis of nanomaterial has been shown to have several advantages over chemical synthesis including high productivity and low cost.

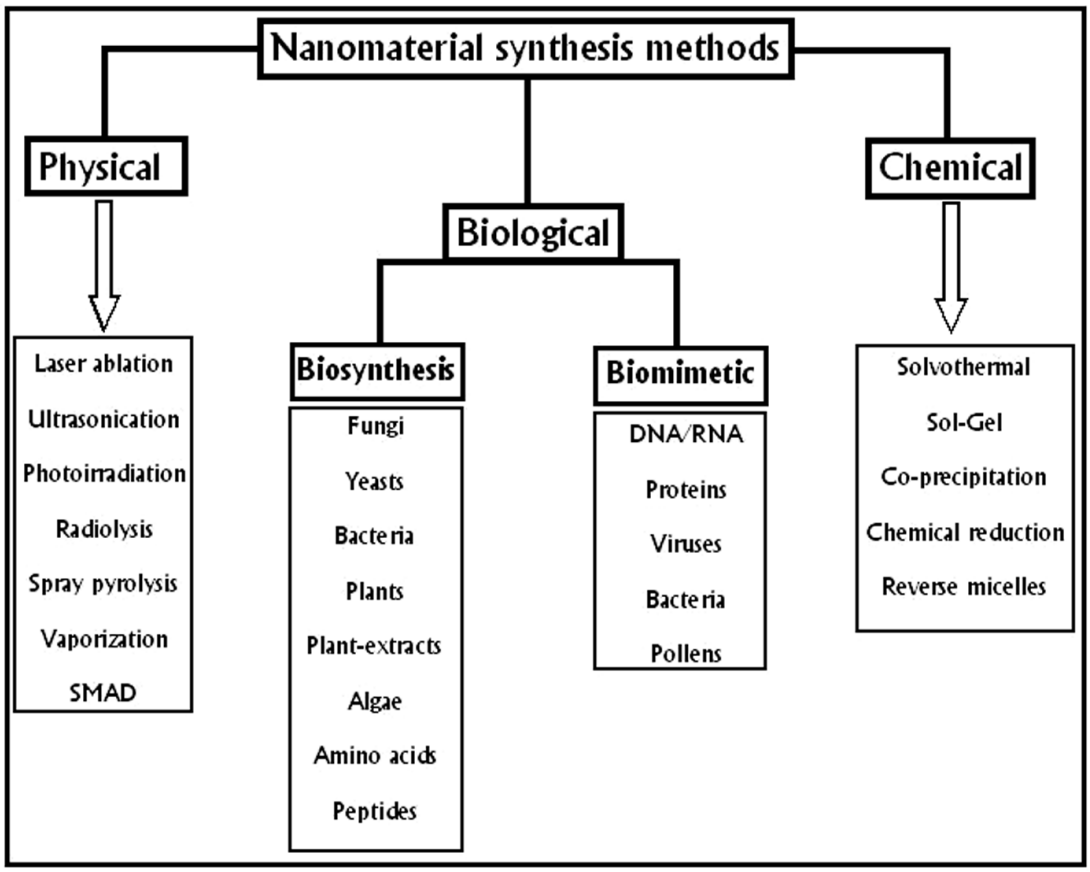

Figure 1.7: *Schematic outlines of the various approaches for the synthesis of nanoparticles.*

Biological methods for nanomaterials synthesis involve either bio-organisms or biomolecules derived from bio-organisms. Among the bio-organisms bacteria [54] and yeasts [55] are well known for detoxification processes that involve reduction of metal ions or the formation of insoluble complexes with the metal ion in the form of nanoparticles. Therefore, the deliberate exposure of metal ions to these microorganisms has evolved as a novel method for nanomaterial synthesis. During the process of nanoparticle synthesis, the biomolecules secreted by microorganisms

restrict the growth of particles over nanometer dimensions and thus act as capping/stabilizing agent. As in this thesis, the biological means have been used for the nanomaterial synthesis; we provide below a succinct synopsis of various biological methods for nanomaterial synthesis.

1.4.1 Biological methods of nanomaterial synthesis

Nature has devised various processes for the synthesis of nano and micro length scaled inorganic materials, which have inspired the development of relatively new and largely unexplored area of research for the biosynthesis of nanomaterials [56]. The synthesis and assembly of nanoparticles by biological routes may lead to the development of clean, nontoxic and environmentally acceptable "green chemistry" procedures, probably involving organisms ranging from bacteria to fungi and even plants [57, 56]. Hence, both unicellular and multicellular organisms are known to produce inorganic materials either intra-or extracellularly [58]. Harnessing these processes and gaining control over them would help us in minimizing chemical hazards to health and environment, reducing waste and preventing pollution.

1.4.1.1 Use of microorganisms for nanomaterial synthesis

Many organisms have been reported to produce inorganic materials either intracellularly or extracellularly. For example, unicellular microorganism such as magnetotactic bacteria synthesizes magnetite nanoparticles [59], and diatoms produce siliceous materials [60]. Multicellular organisms are well known to produce hard inorganic-organic composite complex materials such as bones, shells and spicules [61]. These composite materials consist of an inorganic component and an organic matrix (proteins, lipids or polysaccharides), which mainly control the morphology of the inorganic compound. The surface layer (S-layer) bacteria are reported to synthesize gypsum and calcium carbonate layers [62].

Among the microorganisms, bacteria, being a prokaryote, have received much attention in the area of biosynthesis of nanomaterials. Intracellular synthesis of octahedral gold nanoparticles (5-25 nm) by *Bacillus subtilis* 168 has been shown in earlier reports [63], where the bacterium was reported to reduce Au^{+3} ions from gold chloride to Au^{0} under ambient conditions. Intracellular synthesis of AuNPs (10-20

nm) by Fe(III)-reducing bacteria *Shewanella algae* [64] under anaerobic environment and in the presence of hydrogen gas has been reported by Konishi *et al*. Extracellular synthesis of AuNPs has been reported by Sastry *et al.* [65] (by the actinomycete, *Thermomonospora sp.* (an alkalothermophile) showing optimum growth at pH ~9.0 at 50 ^{0}C). When this actinomycete was exposed to gold ions, it reduced the metal ions extracellularly, yielding polydispersed gold nanoparticles whereas when exposed to pH ~9.0 and at 50 ^{0}C, it showed monodispersed gold nanoparticles having size ~8.0 nm diameter. Monodispersity can be obtained very easily by chemical methods but it is difficult with biological processes especially with microbes. Another interesting report by Ahmad *et al*. [66] which shows that intracellular synthesis of gold nanoparticles occurs in alkalotolerant actinomycete *Rhodococcus* sp., where the nanoparticles are more accumulated on the cytoplasmic membrane than on the cell wall.

Syntheses of silver nanoparticles (AgNPs) have also been reported by various microorganisms. Several bacterial strains are reported to be silver resistant [67] and accumulate silver in their cell wall (25 % of their cell mass) and thus have been used for silver recovery from ore materials. A very interesting report by Klaus-Joerger [68] and co-workers, suggests that the bacterium *Pseudomonas stutzeri* AG259, isolated from a silver mine, resulted in the reduction of the Ag^+ ions and formation of silver nanoparticles of well-defined size and distinct morphology within the periplasmic space of the bacteria when exposed to concentrated aqueous solution of $AgNO_3$. Subsequent results included a report by Nair and Pradeep [69] where nanoparticles of gold, silver, and their alloys have been shown to form upon the reaction of their corresponding metal ions within cells of lactic acid bacteria (*Lactobacillus sp*.) present in buttermilk.

In addition to metal nanoparticles, several reports have been published dealing with the synthesis of semiconductors (quantum dots) such as CdS, ZnS and PbS. Sulfate reducing bacteria bacterium *Clostridium thermoaceticum* and *Klebsiella aerogenes* have been used by Mandal *et al.* [70] for the synthesis of CdS nanoparticles and ZnS nanoparticles from sulfate reducing bacteria under anaerobic conditions. Sweeny *et al.* [71] have reported the intracellular synthesis of CdS

nanoparticles by *E. coli.*, when bacterial cells were incubated with $CdCl_2$ and Na_2S. Further, Labrenz *et al.* [72] have reported synthesis of 2-5 nm diameter sphalerite (ZnS) particles by sulfate reducing bacteria of the family *Desulfobacteriaceae*.

Several sulfate reducing bacterial species have also shown their potentiality towards the synthesis of magnetic nanoparticles such as iron oxide and iron sulfide. Watson *et al.* [73] have reported the synthesis of iron sulfide nanoparticles on the surface of sulfate reducing bacteria and these nanoparticles have been used for adsorption of heavy metal and anions. Magnetotactic bacteria are also well known to synthesize magnetic nanoparticles, for example *Magnetospirillum magneticum* produce two types of particles; some produce magnetic (Fe_3O_4) nanoparticles in chains and some produce greigite (Fe_3S_4) nanoparticles [74], while some others produce both types of nanoparticles. Co, Ni and Cr substituted magnetic nanocrystals were synthesized utilizing thermophilic iron reducing bacteria *Thermoanaerobacter ethanolicus* (TOR-39) by electrochemical process [75]. Further, magnetotactic bacteria *Magnetosprillium magnetotacticum* [74] are known to produce single domain magnetic nanocrystals (Fe_3O_4) that are subsequently arranged into folded chain and close ring morphologies. Bacterial synthesis of extracellular magnetite nanoparticles has been reported by Bharde *et al.* [76]. Exposure of mixture of $K_3Fe(CN)_6$ and $K_4Fe(CN)_6$ to aerobic bacterium *Actinobacter* sp. for 48 h at room temperature resulted in magnetite nanocrystals. We used this bacterium extensively for the nanomaterial synthesis. More details about this bacterium are presented in chapter II.

Eukaryotic organisms such as yeast and fungi have also been explored for nanomaterial synthesis. Intracellular synthesis of CdS nanocrystals resulted, when *Candida glabrata* [77] was exposed to Cd^{2+} ions. Kowshik *et al*. [78] have reported the synthesis of PbS nanocrystals by *Torulopsis* sp. when challenged with Pb^{2+} ions. PbS nanocrystals having 3-5 nm diameter were isolated from cellular biomass by freeze thawing. Synthesis of silver nanoparticles has also been reported by a silver resistant yeast strain, MKY3 [79].

Another eukaryotic organism, which has been used extensively for nanoparticle production starting from simple metal nanoparticles to complex binary and ternary oxides production, is fungi. Gold and silver nanoparticle synthesis has

been reported by two fungal species, *Fusarium oxysporum* and *Verticillium* sp. [80]. Intracellular synthesis of gold and silver nanoparticles by fungus *Verticillium* sp. has been shown by Mukherjee *et al*. The intracellularly synthesized nanoparticles could be easily isolated by ultrasound treatment of fungal biomass-nanoparticle composite after the treatment with surfactant. However, a much easier way would be if nanoparticles could be synthesized extracellularly. Interestingly, extracellular synthesis of gold and silver nanoparticles was reported when *Fusarium oxysporum* was exposed to respective metal ion precursor. Moreover, the extracellular fungal biomass filtrate was also able to reduce Au^{3+} and Ag^{+} ions into their respective metal nanoparticles. Reduction of Au^{3+} and Ag^{+} ions could be ascribed to the reductases secreted by fungus into the solution, whereas the stability of nanoparticles could be attributed to the capping proteins enriched in cystein [81]. Not only individual metal nanoparticles, *Fusarium oxysporum* was also able to reduce Au^{3+} and Ag^{+} ions simultaneously leading to the synthesis of Au-Ag alloy nanoparticles [82]. Shankar *et al*. [83] have reported the synthesis of gold nanoparticles having rod like and prismatic morphology by an endophytic fungus *Colletotrichum* sp.

Apart from metal nanoparticles, extracellular synthesis of CdS nanocrystals with the use of *Fusarium oxysporum* has also been reported by Ahmad *et al.* [84]. Exposure of $CdSO_4$ to the fungal biomass resulted into reasonably monodispersed (5-20 nm) CdS nanocrystals. The conversion of $CdSO_4$ into CdS has been proposed to be the action of sulfate reductases secreted by the fungus, as the exposure of $CdNO_3$ did not result in any CdS nanoparticle. This fungus has also shown its efficacy towards the synthesis of metal-oxide nanoparticles. Bansal *et al.* [85] have shown extracellular synthesis of SiO_2, TiO_2 and ZrO_2 nanoparticles by employing *Fusarium oxysporum*. Also, Bharde *et al.* [86] have reported extracellular synthesis of nanocrystalline magnetite with the exposure of a mixture of $K_3Fe(CN)_6$ and $K_4Fe(CN)_6$ to *Fusarium oxysporum* and *Verticillium* sp. Rautaray *et al.* [87] have reported the extracellular synthesis of $CaCO_3$ and $SrCO_3$ crystals with the exposure of $CaCl_2$ and $SrCl_2$ to fungus *Rhodococcus* sp. and *Fusarium oxysporum.* It is well known that fungi and actinomycetes produce reasonable amount of CO_2 during growth [88]. Therefore, it was hypothesized that the protein-$CaCO_3$ composite structures may arise from

aggregation of the secreted protein mediated by Ca^{+} ions and is followed by reaction with CO_2, yielding templated $CaCO_3$ crystals. *Fusarium oxysporum,* has also been reported to rapidly biotransform the naturally occurring amorphous plant biosilica into crystalline silica and leach out silica extracellularly at room temperature in the form of 2-6 nm crystalline silica nanoparticles capped by proteins secreted by fungus [89]. Selective bioleaching of silica and enrichment of zirconia in zircon sand by the reaction between fungus *Fusarium oxysporum* and zircon sand has been shown [90]. It was hypothesized that fungal enzymes specifically hydrolyze the silicates present in the sand to form silicic acid, which undergo condensation by certain other fungal enzymes resulting in room-temperature synthesis of silica nanoparticles. Further, the same fungus was found able to synthesize, ferroelectric barium titanate nanoparticles extracellularly at room temperature [91].

Diatoms, unicellular alga, are another group of eukaryotic organisms (order *Bacillariophyceae*) found in almost every water habitat on the earth and often-dominated phytoplankton bloom in the oceans [92]. Diatoms exhibit beautiful architecture of their cell wall made up of biosilica [93]. Diatom biosilica is mainly made up of hydrated SiO_2 with a small proportion of organic macromolecules. The cell walls are ordered in a nanometer to micrometer scale [94] and diatoms could precisely reproduce them during each cell division cycle. Diatoms have also reported for the synthesis of silica formation [94].

1.4.1.2 Use of plant extracts for nanomaterial synthesis

In addition to the microbial synthesis of nanomaterial synthesis, extracts from various parts of plants have also been employed for gold and silver nanoparticle synthesis. One of them is *Equisetum* sp. (horsetail) [95, 96]. This provides a possibility to explore plants as a means for synthesizing metal nanoparticles analogous. Indeed, Yacaman and co-workers have shown that gold and silver nanoparticles are formed within different parts of live Alfalfa plant on accumulating the corresponding metal ions from solid media [97, 98]. In an attempt towards deliberate synthesis of metal nanoparticles using plants, Sastry and co-workers showed that various plant extracts like that of *Geranium* sp. [99, 100], neem (*Azadirachta indica*) [83], lemon grass (*Cymbopogan flexuosus*) [102, 103] and amla

(*Emblica officinalis*) [104] can be used for the size and shape-directed biosynthesis of gold [101–105], silver [99, 101, 105] and gold–silver bimetallic core–shell nanoparticles [101].

1.4.2 Biomimetic synthesis of nanoparticle

Biomimetic synthesis has provided a new way of nanomaterials preparation and their further assembly [106]. Biomineralization process, defined as the formation of solids in biological systems, has been an inspiration to researchers for controlled synthesis of inorganic materials [107]. In biomineralization, self-assembly of organic based templates such as ferritin [108] of collagen provides a scaffold for the assembly of inorganic materials. Recently it has been shown that the native protein cage of lumazine synthase mineralizes iron oxides in a biomimetic way analogous to the feritin system [108].

Further, there are a number of physiological functions in organisms that necessitates the biosynthesis of nanoparticles ranging from metal regulation/storage to detoxification to structural assemblies. Consequently, the production of nanoparticles is mediated by various types of protein templates suited to guide nanoparticle formation and function. For instance, they provide a spatially delineated cage which confines nanoparticle synthesis to the physical dimensions of the protein cavity, while encapsulating the newly formed nanoparticles. Iron storage protein, ferritin, have been used for the first time to mineralize metal nanoparticles. By using ferritin as a model template, proteins not typically associated with metals were crafted to mimic ferritin's activity.

Douglas *et al.* [109] have successfully reported that the assembled viral protein cages can be altered in order to provide an organic scaffold for inorganic nanomaterial synthesis constrained within the viral cage structure. They further reported that the selective nanomaterial synthesis depends on a spatial and electrostatic registry between the organic and the inorganic phases to start the nucleation of the mineral. Alteration of charge on the interior of the cage results in a completely different chemical reactivity and thus the chemical plasticity of the viral protein cage. Furthermore, it is likely that altering, by design, the chemical nature of

other protein cages will impart the capacity to direct the synthesis of a broad range of nanomaterials.

Diatom, *Cylindrotheca fusiformis* is known to synthesize nanostructures from silicic acid using species-specific peptides known as silaffins [110]. The R5 peptide, a bioinspired analogue derived from the NatSil protein in *Cylindrotheca fusiformis*, has been used for the synthesis of TiO_2 [111] from the non-natural substrate, titanium bis(ammonium lactato)-dihydroxide.

Biomimetic synthesis of single crystalline silver nanoplates using the extract of unicellular green alga *Chlorella vulgaris* has also been successfully performed by Xie *et al*. [112]. They have reported that the proteins present in the extract were responsible for synthesis of nanoplates and provided a dual role of silver ion reduction and shape control. They further identified that hydroxyl groups present in Tyr residues and carboxyl groups in Asp and/or Glu residues were the most active functional groups for silver ion reduction and for directing the anisotropic growth of silver nanoplates, respectively. Further, based on this, they designed a simple bifunctional tripeptide with one Tyr residue as the reduction source and the two carboxyl groups in the Asp resides as shape directors, which could produce small silver nanoplates with low polydispersity (>55%).

Naik *et al.* [113] have reported the *in vitro* synthesis of silver nanoparticles using silver-binding peptides identified from a combinatorial phage display peptide library. Further, Xu *et al*. [114] have also shown AG3(AYSSGAPPMPPF) mediated synthesis of silver nanoparticles. AG3 (AYSSGAPPMPPF) is an inorganic-binding peptide that specifically and selectively binds to silver, demonstrated by phage display library according to Stone group [113]. They reported that silver-binding peptide AG3 was immobilized on the surface of protonated poly(ethylene terephthalate) (PET) film, which was prepared for biomimetic synthesis of silver particles *in vitro*.

Biological systems exhibit precisely controlled synthesis, biomineralization, of nanomaterials by the use of diverse biomolecular templates. These templates include amino acids, peptides, proteins and viruses, which show precisely defined metal

binding sites, spatial organization, structurally confined cages/cavities/pores and an environment that protects against oxidation/aggregation of nanoparticles.

Mann *et al.* have successfully shown the *in situ* biomineralization of iron sulfide nanoparticles from both native and reconstituted iron oxide cores of ferritin by utilizing the permeability of the protein for a sulfur-containing source such as Na_2S [115]. Other nanoparticles have also been synthesized by the use of ferritin as a template such as Fe_3O_4 [116], α-MnOOH [117], Co(O)OH [118], UO_2 [119] and CdS [120].

Ferritin like protein systems has been identified in the bacterium *Listeria innocua*, which display a cage-like structure [121]. This unusual protein is comprised of only 12 peptide subunits and is substantially smaller in magnitude than native ferritin. Douglas *et al.* [121] have used this protein for the synthesis of ferromagnetic iron oxide particles (~ 4.5 nm) identified as cubic iron oxide phase (γ-Fe_2O_3). Also, the *L. innocua* ferritin like proteins served as template for controlled mineralization of two different oxide phases of cobalt, Co(O)OH and Co_3O_4, at two different reaction temperatures 23 and 65 ºC respectively [122]. Substantial differences in crystallinity of the cobalt mineral core were observed between the two synthetic routes. The mineralization reaction carried out at higher temperatures yielded more crystalline nanomaterials, while the low-temperature synthesis tended toward amorphous material. The high crystallinity obtained at higher temperatures is most likely due to removal of structural waters present in the protein cavity and the surpassed energy barrier of nucleation at 65 ºC [122].

Another class of proteins, which have been used for nanomaterial synthesis, is heat shock proteins (Hsp). Hsp represent an essential class of proteins, which act as molecular chaperones to partially denature proteins [123]. These proteins are rapidly expressed in all organisms at increased levels in response to cellular stresses such as elevated temperatures, chemical or heavy metal exposure, pH extremes, osmotic variations, and infection or disease state [124]. Aida *et al*. have demonstrated the inclusion of already preformed CdS nanoparticles within the chaperonin proteins of GroEL from *Escherichia coli* and *T.th* cpn from *Thermus thermophilus* HB8 [125]. Also, Douglas *et al*. have used a small 24 subunit heat shock protein isolated from the

hyperthermophillic archaeon, *Methanococcus jannaschii*, as a biomimetic template for the oxidative mineralization of iron [126].

Viruses represent another example of viable nanoparticle templates resulting from their structural polymorphism and defined composition. In general, viruses exist in a variety of sizes and morphologies ranging from 30 nm spherical viruses to 300 nm rod-like structures. Additionally, all viruses are comprised of a compact self-sustaining packet of genetic material enveloped within a functional protein capsid ideally suited for their survival and propagation. Thus, the above mentioned characteristics have inspired the programmed synthesis of nanoparticles using these viral templates, resulting into highly ordered nanoparticle arrays of spatially confined particles. Exposure of TMV to $[AuCl_4]^-$, $[PtCl_6]^{2-}$ and Ag^+ ion precursors, followed by reduction with hydrazine and photo reduction resulted in viruses coated with respective nanoparticles. Reduction of $[AuCl_4]^-$ and $[PtCl_6]^{2-}$ by hydrazine at an acidic pH induced nucleation at the positively charged lysine and arginine residues along the outer surface of the viral template. Thus, Au^0 and Pt^0 spheroidal nanoparticles of 8.6 ± 3.0 nm and 2.5–5.0 nm, respectively, were locally externalized at the virus surface with Au^0 TMV surface [127]. Templates of TMV were also employed with different synthetic protocols for the synthesis and assembly of different nanomaterials such as CdS, PbS and iron oxide [128]. Recently, Young *et al*. have designed a Cowpea Chlorotic Mottle Virus (CCMV) virion cage with an anionic interface that favorably binds Fe (II) and Fe (III) ions and then subsequently controls the oxidative hydrolysis to size-constrained iron oxide minerals [129]. Further, Kao *et al*. performed the replacement of the RNA core of brome mosaic virus (BMV) with 2.5 – 4.5 nm Au^0-(citrate) nanoparticles. It was achieved by sequentially disassembling the BMV virions into individual capsomeres, reassembling the BMV virions in the presence of Au^0 nanoparticles, and purifying the resultant BMV encapsulated Au^0 particles [130].

1.4.2.1 Biomimetic synthesis: Carbohydrates/Oligosaccharides as reducing/capping agent for Glyconanoparticles

Carbohydrates, together with nucleic acids and proteins, are important biomolecules for life. Nanoparticles conjugated with carbohydrates,

glyconanoparticles, have also been considered as good biomimetic models of carbohydrate presentation at the cell surface and gained researchers attraction due to their increasing potential applications in the field of glycobiology, biomedicine and material science. Other biomolecules (such as proteins, peptides, DNA and RNA) have been extensively used for the synthesis and functionalization of different nanomaterials [131, 132, 133-138] whereas very few systems are reported involving carbohydrates [139].

On the other hand functionalization with modified saccharide system is receiving great attention these days. Penadés and co-workers first reported the synthesis of glyconanoparticles by the addition of methanolic solution of a neoglycoconjugate functionlized with a thiol group, to an aqueous solution of $HAuCl_4$ and its subsequent reduction by $NaBH_4$ [140]. This method was further used for the synthesis of different glyconanoparticles functionalized with tetrasaccharide [141], trisaccharide [140], diasaccharides lactose and maltose or monosaccharide glucose [142]. Different linkers of hydrophobic (alkanes) and hydrophilic (polyethylene glycol derivatives) nature were used to bind the carbohydrate to the gold core [142]. Lin *et al.* [143] have also used the same synthetic protocol to prepare gold nanoparticles functionalized with glucose, mannose, galactose and mannosides. Further, Gervay-Hague *et al.* [144] have shown the same with glucose and galactose. A three-step procedure has also been used by Lakowicz *et al*. [145] to prepare hybrid silver glyconanoparticles. Recently, Panacek *et al.* [146] have synthesized silver nanoparticles capped with different saccharides, which showed high antibacterial activity against different bacterial species including highly multiresistant strains. Glyco-conjugated semiconductor nanoparticles (quantum dots) have been synthesized by several groups and different approaches have been followed [147]. Most commonly, QDs are first prepared at high temperature in presence of capping agents to avoid aggregation. Further, in second step, the biomolecules were conjugated with so synthesized QDs. Thiol capped QDs have been bio-conjugated with different biomolecules such as peptides and proteins [148, 149, 150, 151-156], antibodies [149, 154-158], DNA [159-162] and other molecules [163-165] too.

1.5 Toxicity effects of nanomaterials over mammalian cells

Thus, in this chapter till now we have discussed the various methods of nanomaterial synthesis via biological routes including microbial, biomimetic and carbohydrate-mediated synthesis. The so obtained nanomaterials offer good water dispersibility and high stability, probably due to dense capping of biomolecules over their surface. However, the toxicity evaluation of nanomaterials is as essential as their synthesis as it would provide an idea to safe use and limit of nanoparticle exposure to human beings. As the field of nanoscience is relatively new and developing field, very less is known about its future consequences. Nanoparticles are increasingly used in a wide range of applications in science, technology and medicine. Unfortunately, a material that has been shown to be safe and biocompatible at bulk level may turnout to be toxic at nano-level. For example, bulk TiO_2 particles have been considered safe and could be use in sunscreen formulations, as it reflects and scatters UVB and UVA from sunlight [166]. However, TiO_2 particles of nanometer dimension were found to cause free radical formation in skin cells and DNA damage [166]. Bulk TiO_2 is generally considered to be inert whereas nano-TiO_2 can be highly photo reactive in presence of UV light [167]. Thus, it becomes extremely important that we treat every nanomaterial as unknown material and evaluate its toxicity thoroughly.

The unique properties, especially high reactivity and small size, of nanomaterials make them to react with the biological systems. Moreover, very little knowledge about the risk of nanomaterials and the scarcity of data gives rise to a host of fear and alarming scenarios [168]. According to the U.S. department of Labor, in U.S. alone 2 million people work with nanometer diameter particles regularly in development, production and use of nanomaterials and products [169]. Therefore, it becomes almost essential to check the toxicity of any kind of new nanomaterial before their use for bio-applications. Very commonly for any material, there are three routes of entry into human body; via “natural” porters such as skin, intestinal tract and respiratory tract, or intentional delivery through injection, intravenous (i.v.), intraperitonial (i.p.) or intramuscular (i.m.).

1.5.1 Factors influencing the effect of nanomaterials over mammalian cells

Several factors influencing the effect of nanomaterials over human system have been reported, which could be broadly divided into two parts.

1.5.1.1 Particle Size

Particle size acts as a limiting factor for accessibility of nanoparticles to cells and cell compartments. Recent studies have revealed that particle size alone can strongly affect the efficiency of cellular uptake [170]. Furthermore, the surface/size ratio increases exponentially with decreasing particle sizes, leading to the increased surface reactivity, which might lead to greater biological activity per given mass compared with larger particles. Therefore, particle internalization into tissues, cells and organelles results in toxicity or the induction of oxidative stress [171].

1.5.1.2 Particle Surface chemistry

The degree of hydrophilicity/hydrophobicity of a surface is an important property to evaluate, since it regulates cell-surface adhesion, protein denaturation at the interface, and the selective adsorption of components from the liquid phase [172]. Variations in the hydrophobicity of the nanoparticle surface can result in different translocation routes in various biological compartments, different coatings of the surface by endogenous materials, and differences in the interfacing of the solid with cells [173]. For example, coating poly (methyl methacrylate) nanoparticles with different types and concentrations of surfactants significantly change their body distribution [174].

Pott *et al.* [187] have shown that TiO_2 nanoparticles coated with a silane compound (to make the surface hydrophobic) becomes toxic and lethal to rats especially at the dose > 2 mg. However, later studies showed that the intratracheal doses of 250 and 500 μg of the same hydrophobic, silanized ultra fine TiO_2 did not show toxicity and induced a much lower pulmonary inflammation in comparison to the hydrophilic, uncoated dusts [188]. Furthermore, the studies from Warheit *et al.* [189] showed that the n-octyltriethylsilane (OTES) coating on the pigment grade TiO_2 particle does not cause significant pulmonary toxicity.

Various other studies dealing with toxicological effects of nanoparticles could be summarized as:

Key studies on toxicological effects of Nanoparticles	**References**
NPs have a higher deposition probability particularly in the small airways and the alveolar region of the lungs.	[175]
NPs have a high specific surface area, which can catalyse reactions and which can adsorb high amounts of toxic substances (like PAH), making them a carrier into the deep lung during inhalation.	[176]
NPs are taken up by other cells of the respiratory epithelia such as epithelial cells and dendritic cells.	[177]
NPs are less well phagocytized by alveolar macrophages than larger particles and inhibit their phagocytic ability, inhibit macrophage motility.	[178]
NPs adversely affect cardiac functions and vascular homeostasis.	[179]
NPs may form complexes with similar sized proteins and bio molecules, which may result in functional changes of the latter.	[180]
NPs have greater access to interstitial spaces than larger particles.	[181]
NPs affect immunity.	[182]
NPs can cause more inflammatory effects than larger particles.	[183]
NPs have access to systemic circulation.	[184]
NPs induce more oxidative stress than fine particles.	[185]
The large surface area of ultra fine particles and its composition and structure play a pivotal role in the above-mentioned interactions with biological target cells, body fluids and tissues.	[186]

Chart 1.1: *Crucial findings on the biological effects of Nanoparticles (NPs) (Modified from Borm and Kreyling, 2004).*

1.5.2 Uptake, possible transport and biodistribution of nanoparticles in living organisms

Oberdorster *et al.* [190] have reported that in rat or mice, after inhalation, 20 nm TiO_2 particles were deposited in the alveoli and accessed the pulmonary interstitium to a significantly larger extent than 250 nm TiO_2 nanoparticles [190, 191]. This resulted in a prolonged retention of smaller particles in the lung. Several other studies have shown that the response to instillation or inhalation of TiO_2 nanoparticles in different species (hamster, rat or mouse) differs. Under similar conditions, rat developed more severe inflammatory responses than mice, while clearance of particles from the lungs of both the species was found impaired [192]. In contrast, the clearance rate of hamster is totally unaffected at all applied particle concentrations. Further, some *in vivo* studies have been performed with different metal oxide nanoparticles against different cell types. Cells can take up metal oxides and carbonaceous nanoparticles by different mechanisms (Figure 1.8). In several human cell lines nanoparticles such as TiO_2, SiO_2 and ZrO_2, were taken up by the cells [193]. The so incorporated particles were detected in autophagic vacuoles, along with amorphous cellular material and membranes [194], and within cytoplasm too.

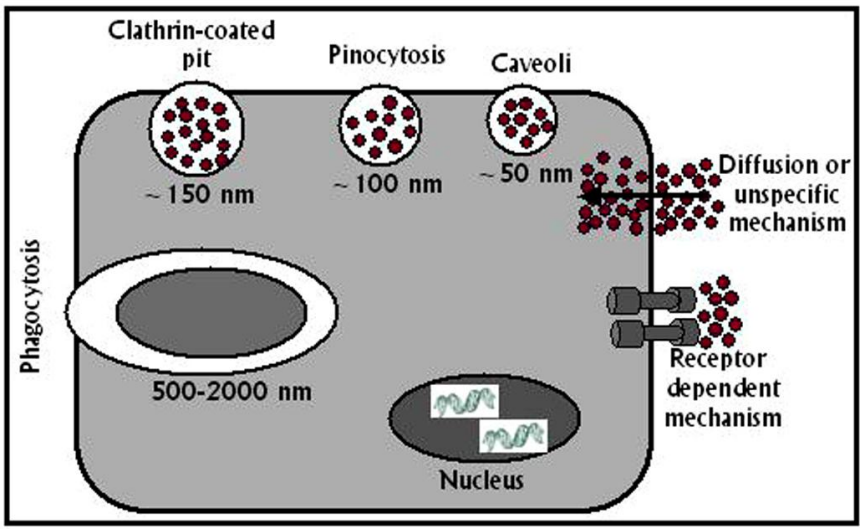

Figure 1.8: *Schematic representations of possible cellular uptake pathways for particles of different sizes. (Courtesy: reference 195b).*

Nanoparticles can be transported into cells through endocytosis, which can be broadly divided into two categories: phagocytosis and pinocytosis. Phagocytosis,

involves the uptake of larger particles (0.25-10 mm), is performed by specialized cells such as macrophages and neutrophils. However, pinocytosis is the uptake of fluids and solute, occurs in all cell types and is mediated by four basic mechanisms: macropinocytosis, clathrin-mediated endocytosis, caveolae-mediated endocytosis and clathrin-caveolae and dynamin-independent endocytosis [195]. Among these, clathrin mediated endocytosis is the most common uptake mechanism in all mammalian cells [195]. The uptake of nanomaterials inside the cells by endocytic pathways has been reported in detail [196, 197-199].

To induce even bio-distribution, it is generally understood that drug delivery nano vehicles should be small enough (less than 100 nm) to avoid non-selective uptake by macrophages of the reticuloendothelial system (RES) in the liver and spleen [200], but larger than 5 nm (molecular weight 30000 to 40000) to escape rapid renal clearance [201]. Most nanoparticles are known to be rapidly taken up by the spleen and liver, mainly by macrophages, and therefore, their half-life in the circulation is generally short. In particular, particles possessing a hydrophobic surface are likely to localize in the spleen and liver. Many airborne nanoparticles (<100 nm) are prone to accumulation in the lungs as well as in the spleen and liver. Accumulation of nanoparticles in other organs such as heart, kidney, brain, testis and uterus has also been reported recently [202]. A clear mechanism for nanoparticle uptake has not been reported yet, but it seems to be dependent on primary particle and agglomerate size.

1.5.3 Toxicological Effects of nanoparticles on Cellular Processes

Large number of reports has been published in the field of nanotoxicology, which can be defined as ‘‘science of engineered nanodevices and nanostructures that deals with their effects in living organisms’’[203]. It has been observed by many groups that cell proliferation or cell adhesion ability was significantly decreased by various nanomaterials such as single walled carbon nanotubes [204-206], multi walled carbon nanotubes [207, 208] or other carbon based materials [207], iron oxides (Fe_2O_3, Fe_3O_4 or its derivatives) [199, 209, 206, 210-212], various types of quantum dots [213, 214], TiO_2 and several metals and metal oxides [210]. Sometimes these materials caused cell death too as measured by MTT (3-(4,5-dimethylthiazol-2-yl)-

2,5-diphenyltetrazolium bromide) assay, quantifying the number of attached cells. It has been postulated by lactate dehydrogenase (LDH) leakage test that the cell membrane damage was significant when iron oxide [210] and various metals and metal oxides [210, 215] were treated with cell lines. It has been reported that incorporated oxide nanomaterials can lead to inflammatory responses, which include the formation of pro-inflammatory cytokines such as IL-1, IL-6, IL-8 and TNF-α. Silica nanoparticles [216] and multi walled carbon nanotubes [217] have been reported to produce inflammation response with activation of signaling cascade like mitogen-activated protein kinase (MAPK) cascades. It has also been reported that carbon based nanoparticles induce oxidative stress, which has been characterized by formation of reactive oxygen species (ROS), accumulation of peroxidation products (such as malondialdehyde) and depletion in concentration of antioxidant molecules such as glutathione (GSH) [204, 218]. The possible events after interaction of nanoparticles with cells have been shown in Figure 1.9.

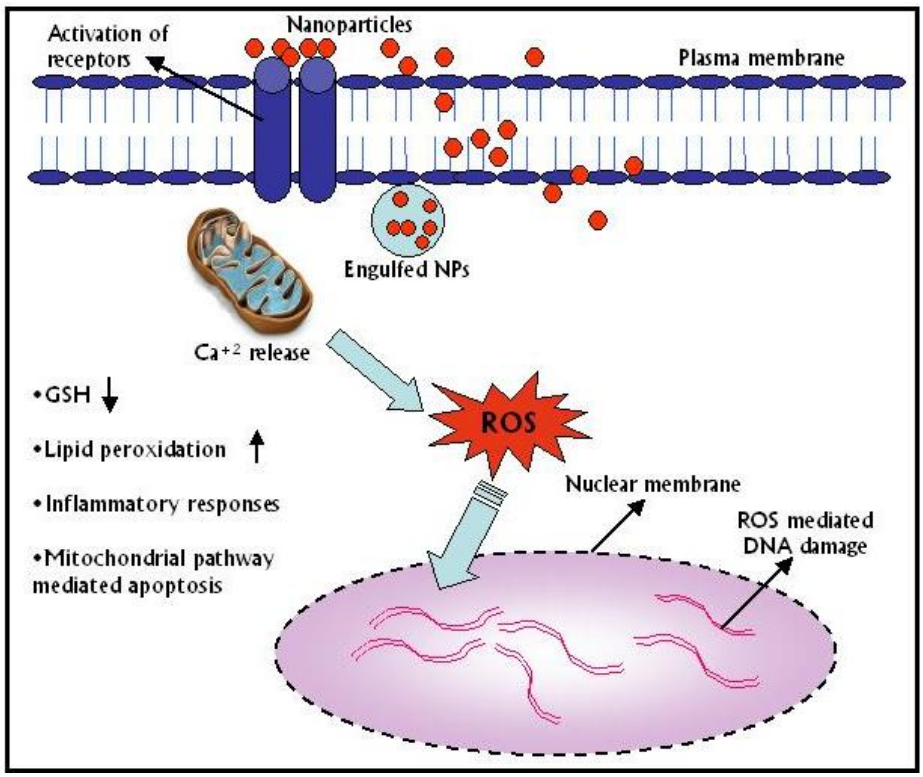

Figure 1.9: *Schematic representation of possible events after interaction of nanoparticles with cells. Particles may interact with receptors or may cause oxidative stress that induces an increase in intracellular calcium concentration, decrease intracellular GSH and/or increase in lipid peroxidation and finally mitochondrial pathway mediated apoptosis.*

A step ahead from cytotoxic effects of nanomaterials study of genotoxic (DNA damage) effects via oxidative stress of the same becomes very important. A detailed study of cellular DNA damage in response to these nanomaterials is an important area of present day nanotechnology research. Cytotoxic effects often result in the suppression and/or overexpression of certain proteins/enzymes, malfunctioning of certain enzymes and even cell death, whereas genotoxicity can lead to even more serious consequences. Genetic insults are mostly repaired by DNA surveillance machinery of the cell and if not repaired they may incorporate the said damage in next generation leading to mutations and other genetic disorders. Oberdorster demonstrated that nanomaterial (Fullerene C_{60}) induced oxidative stress in juvenile fish causes brain damage along with changes in gene function [219]. Therefore, complete toxicity study (including cytotoxicity and genotoxicity) of any newly synthesized nanomaterial or nanomaterials synthesized by novel route, should be performed before its use for any application.

No doubt, nanomaterials are going to be the future technology and would lead in each field of science including physics, chemistry, engineering and biology. For this, precisely controlled or designed nanoparticles should be developed depending on their necessities. Simultaneously, toxicity of synthesized nanomaterials should be studied in detail to provide their biocompatability and thus safety guidelines. There are currently no general guidelines to assess the potential risk of nanoparticles and no regulatory framework for their human-related applications. Therefore, more vigorous investigations on the potential toxicity and safety assessment of nanoparticles are urgently needed to establish minimum safety standards.

1.6 Outline of the Thesis

The thesis consists of six chapters.

The ***Second Chapter*** describes the extracellular synthesis of Si/SiO_2 nanocomposites using *Actinobacter* spp. (Gram positive bacteria). This environmentally benign method was used to synthesize elemental silicon along with silica nanoparticles in the form of nanocomposites. These findings were confirmed with HRTEM, XRD and XPS (showed the signature of silicon as well as silica) etc

techniques. Calculated band gap energy, based on emission spectra, match well with the reported values for Si embedded in SiO_2. Nanocomposites of ca. 10 nm have been seen under TEM. Very primitive information about proteins involved in synthesis (reduction/capping) of nanocomposites has also been described.

The ***Third Chapter*** describes the extracellular synthesis of titania (TiO_2) and zinc oxide (ZnO) nanoparticles using *Actinobacter* spp. These findings were confirmed by various techniques such as FTIR, XRD, XPS and HRTEM etc. A comparison of photocatalytic degradation of dye (methylene blue) between TiO_2 and ZnO nanoparticles in different light conditions has also been discussed. TiO_2 was found to be photocatalytically more active in UV-light than zinc oxide while ZnO was found more active in sunlight than TiO_2.

The ***Fourth Chapter*** describes the biotransformation of oleic acid into sophorolipids using yeast (*Candida bombicola*). These sophorolipids consist of a dimeric glucose (also called as sophorose) linked by a glycosidic bond to the penultimate carbon of the fatty acid. Synthesis, isolation, purification and characterization of these sophorolipids have been explained in detail. Further, these sophorolipids were used as reducing and capping agents for metal (Au and Ag) nanoparticle synthesis. Fairly stable and nearly monodispersed nanoparticles were found. These metal nanoparticles were characterized with different techniques such as UV-vis, TEM and XRD etc. AgNPs were used as potential antibacterial agents and it was found that a concentration of 20 µg/mL of AgNPs is sufficient to reduce the cell viability of *Bacillus subtilis* (a Gram positive bacterium) up to 99.6 % within 1h of exposure. These AgNPs at a concentration of 1 µg/mL show strong antibacterial activity against *Pseudomonas aeruginosa* (Gram negative bacterium). Detailed investigation with the help of AFM imaging shows leaking out of cytoplasmic matter due to the cell membrane rupture.

The ***Fifth Chapter*** describes the comparative cytotoxicity and genotoxicity study of biosynthesized metal oxide nanoparticles (between B-TiO_2 and B-ZnO) and metal nanoparticles (between OA-SL-AuNPs and OA-SL-AgNPs). As the oxides have applications in cosmetic products, A431 (Human epithelial carcinoma) cell lines were chosen for the toxicity studies. MTT assay for cytotoxicity and Comet assay for

genotoxicity assessment has been performed. Comparison between B-TiO_2 and B-ZnO has shown the better biocompatability of TiO_2 over ZnO nanoparticles at mM concentrations. HepG2 (Human hepatic carcinoma) cell lines were used for cytotoxicity as well as genotoxicity studies of sophorolipid reduced gold (OA-SL-AuNPs) and silver nanoparticles (OA-SL-AgNPs). These nanoparticles are biocompatible below their millimolar concentrations. A comparison of % mitochondrial activity and comet parameters of OA-SL-AgNPs and OA-SL-AuNPs respectively show an increased cytotoxicity and genotoxicity of the former. The cytotoxicity and genotoxicity studies of sophorolipid (SL) alone have also been presented.

The ***Sixth chapter*** summarizes the work presented in the thesis and emphasizes on the possible further research in this area.

1.7 References

[1] Indian craftsmen, artisans used nanotech 2000 years ago.

[2] http://cobweb.ecn.purdue.edu/~photspec/Press_files/NewsnViews_Leonhardt.pdf.

[3] Faraday, M. *Philosophy Trans.* **1857**, *147*, 145.

[4] Zsigmondy, R. "Colloids and the Ultramicroscope", 1914, J.Wiley and Sons, NY.

[5] Feynman, R. P. *Engg. Sci.* **1960**, *23*, 22**.**

[6] Taniguchi, N. On the *Basic Concept of 'Nano-Technology'*. In: *Proceedings of the international conference on production engineering.* 1974, Tokyo, Part II, Japan Society of precision Engineering, pp. 18-23: Tokyo: JSPE.

[7] (a) Curl, R. F.; Smalley, R. E. *Science*, **1988**, *242*, 1017. (b) Sumio, I. *Nature*, **1991**, *354*, 56. (c) Binnig, G.; Rohrer, H.; Gerber, Ch.; Weibel, E. *Surface Studies by Scanning Tunneling Microscopy*, **1982**, *49*, 57. (d) Binnig, G.; Quate, C. F.; Geber, Ch. *Phys. Rev. Letters* **1986**, *56*, 930.

[8] Klabunde, K. J. '*Nanoscale Materials in Chemistry*' (Ed.), 2000, John Wiley, New York, pp. 18-22.

[9] (a) Brus, L. E. *Appl. Phys. A* **1991**, *53*, 465. (b) Alivisatos, A. P. *Science* **1996**, *271*, 933. (c) Gaponenko. *Optical Properties of Semiconductor Nanocrystals*; 1998, Cambridge University Press: Cambridge, U.K. (d) Alivisatos, A. P. *J. Phys. Chem.* **1996**, *100*, 13226.

[10] (a) Link, S.; El-Sayed, M. A. *Int. Rev. Phys. Chem.* **2000**, *19*, 409. (b) Link, S.; El-Sayed, M. A. *Annu. Rev. Phys. Chem.* **2003**, *54*, 331. (c) Kreibig, U.; Vollmer, M. *Optical Properties of Metal Clusters*; 1995, Springer: Berlin, Germany. (d) Kerker, M. *The Scattering of Light and Other Electromagnetic Rediation*; 1969, Academic: New York. (e) Bohren, C. F.; Huffman, D. R. *Absorption and Scattering of Light by Small Particles*; 1983, Wiley: New York.

[11] Burda, C.; Chen, X.; Narayanan, R.; El-Sayed, M. A. *Chem. Rev*. **2005,** *105*, 1025.

[12] (a) Andersen, N. A.; Lian, T. *Ann. Rev. Phy. Chem.* **2005**, *56*, 491. (b) Kamat, P. V. *J. Phys. Chem. B* **2002**, *106*, 7729. (c) McConnell, W. P. *et al., J. Phys. Chem. B* **2000**, *104*, 8925.

[13] (a) Kleemann, W *et al. Phy. Rev. B* **2001**, *63*, 1344231. (b) Park, J, I.; Cohen, J. *J. Am. Chem. Soc.* **2001**, *123*, 5743. (c) Liu, S. M. *Chem. Commun*. **2004**, *10*, 2726.

[14]. (a) Qu, J. R.; Hu, M. A.; Chen, J. Z.; Han, W. *J. China Univ. Geosci*. **2005**, *30*, 195. (b) Willert, M.; Rothe, R.; Landfester, K.; Antonietti, M. *Chem. Mater*. **2001**, *13*, 4681.

[15]. (a) Jensen, T.; Kelly, L.; Lazarides, A.; Schatz, G. C. *J. Cluster Sci.***1999**, *10*,

295. (b) Fiorani, D.; Testa, A. M.; Lucari, F.; D'Orazio, F.; Romero, H. *Physica B* **2002**, *320*, 122. (c) Dormann, J. L. *et al. J. Magnet. Magnet. Mater*. **1998**, *187*, L139. (d) Jiang, C.; Markutsya, S.; Tsukruk, V. V. *Langmuir* **2004**, *20*, 882. (e) Saponjic, Z. V. *et al. Adv. Mater*. **2005**, *17*, 965.

[16] Henglein, A. *Chem. Rev.* **1989**, *89*, 1861.

[17] Steigerwald, M. L.; Brus, L. E. *Acc. Chem. Res.* **1990**, 23, 183.

[18] Brus, L. *J. Phys. Chem.* **1986**, *90*, 2555.

[19] Weller, H. *Adv. Mater*. **1993**, *5*, 88.

[20] Banyai, L.; Koch, S. W. *Semiconductor quantum Dots*; 1993, World Scientific Publishing Co.: River Edge, NJ.

[21] Kamat, P. V. *Native and surface modified semiconductor nanoclusters*, in *Molecular leVel artificial photosynthetic materials. Progress in Inorganic Chemistry Series*; 1997, Meyer, J.; Ed.; John Wiley & Sons, Inc.: New York; pp. 273-243.

[22] Alivisatos, P. *J. Phys. Chem.* **1996**, *100*, 13226.

[23] Kamat, P. V. *J. Phys. Chem. B* **2002**, *106*, 7729.

[24] Adams, D.; Brus, L.; Chidsey, C. E. D.; Creager, S.; Cruetz, C.; Kagan, C. R.; Kamat, P. V.; Lieberman, M.; Lindsay, S.; Marcus, R. A.; Metzger, R. M.; Michel-Beyerle, M. E.; Miller, J. R.; Newton, M. D.; Rolison, D. R.; Sankey, O.; Schanze, K. S.; Yardley, J.; Zhu, X. *J. Phys. Chem. B* **2003**, *107*, 6668.

[25] Thomas, G. K.; Kamat, P. V. *Acc. Chem. Res.* **2003**, *36*, 888.

[26] Shipway, A. N.; Katz, E.; Willner, I. *ChemPhysChem.* **2000**, *1*, 18.

[27] Willner, I.; Kaganer, E.; Joselevich, E.; Durr, H.; David, E.; Gunter, M. J.; Johnston, M. R. *Coord. Chem. Rev.* **1998**, *171*, 261.

[28] Ward, M. D. *Chem. Soc. Rev.* **199**7, 5, 365.

[29] (a) Haes, A. J.; Van Duyne, R. P. *Anal. Bioanal. Chem.* **2004**, *379*, 920. (b) Niemeyer, C. M. *Angew. Chem. Int. Ed.* **2001**, *40*, 4128. (c) Niemeyer, C. M. *Angew. Chem. Int. Ed.* **2003**, *42*, 5974. (d) Parak, W. J.; Gerion, D.; Pellegrino, T.; Zanchet, D.; Micheel, C.; Williams, S. C.; Bodreau, R.; Gros, M. A. L.; Larabell, C. A.; Alivisatos, A. P. *Nanotechnology* **2003**, *14*, R15. (e) Caski, A.; Maubach, G.; Born, D.; Reichert, J.; Fritzsche, W. *Single Mol.* **2002**, *3*, 275.

[30] (a) Roucoux, A.; Schulz, J.; Patin, H. *Chem. Rev.* **2002**, *102*, 3757. (b) Lewis, L. N. *Chem. Rev.* **1993**, *93*, 2693.

[31] (a) Rosi, N. L.; Mirkin, C. A. *Chem. Rev.* **2005**, *105*, 1547. (b) Lawrie, G. *et al.*, *Langmuir* **2006**, *22*, 497.

[32] (a) Liu, G. *et al.*, *Biochim. Biophysic. Acta* **2005**, *1741*, 246. (b) Loo, C. *et al.*, *Tech. Cancer Res. Treat*. **2004**, *3*, 33. (c) Liu, C. *et al.*, *Neuroscience Lett*. **2006**, *406*, 189. (d) Chan, W. C. W. *Biol. Blood Marrow. Trans*. **2006**, *12*, 87.

[33] (a) Otsuka, H.; Nagasaki, Y.; Kataoka, K. *Adv. Drug Delivery Rev*. **2003**, *55*, 403. (b) McAllister, D. V. *Proc. Natl. Acad. Sci. USA.* **2003**, *100*, 13775.

[34] (a) Andersen, N. A.; Lian, T. *Ann. Rev. Phys. Chem*. **2005**, *56*, 491. (b) Yae. S. *et al., Solar Energy Mater. Solar Cells* **2007**, *91*, 224.

[35] (a) Zou, S.; Schatz, G. C. *Phy. Rev. B* **2006**, *74*, 125111. (b) Maier, S. A.; Friedman, M. D.; Barclay, P. E.;Painter, O. *Appl. Phys. Lett.* **2005**, *86*, 1. (c) Maier, S. A. *et al.*, *Adv. Mater*. **2001**, *13*, 1501.

[36] (a) Cengiz, E.; Wissing, S. A.; Muoller, R. H.; Yazan, Y. *Intl. J. Cosmetic Sci.* **2006**, *28*, 371. (b) Villalobos-Hernández, J. R.; Muoller-Goymann, C. C. *Int. J. Pharmaceutics.* **2006**, *322*, 161.

[37] (a) Pradell, T.; Molera, J.; Bayés, C.; Roura, P. *Appl. Phys. A* **2006**, *83*, 203. (b) José Yacamán, M.; Rendón, L.; Arenas, J.; Serra Puche, M. C. *Science* **2006**, *273*, 223. (c) Baglioni, P.; Giorgi, R. *Soft Matter* **2006**, *2*, 293.

[38] (a) Yelin, D.; Oron, D.; Thiberge, S.; Moses, E.; Silberberg, Y. *Optics Express*, **2003**, *11*, 1385. (b) Wang, Y. *et al., Nano Lett.* **2005**, *4*, 1689. (c) Sokolov, K. *et al., Cancer Res.* **2003**, *63*, 1999. (d) El-Sayed, I. H.; Huang, X.; El-Sayed, M. A. *Nano Lett.* **2005**, *5*, 829. (e) Grainger, R. G. *Brit. J. Rad.* **1882**, *55*, 1.

[39] Fichtner, M. *Adv. Engg. Mater.* **2005**, *7*, 443.

[40] Moran, C. E.; Steele, J. M.; Halas, N. J. *Nano Lett*. **2004**, *4*, 1497.

[41] (a) Simon, U. In *Nanoparticles: From Theory to Application*, Schmid, G., Ed. Wiley-VCH, Weinheim, 2004. (b) *Nanomaterials: Synthesis, Properties, and Applications*, edited by A. S. Edelstein and R. C. Cammarata (Institute of Physics Publishing, Bristol, U.K., 1996).

[42] (a) Maier, S. A.; Brongersma, M. L.; Kik, P. G.; Meltzer, S.; Requicha, A. A. G.; Atwater, H. A. *Adv. Mater.* **2001**, *13*, 1501. (b) Maier, S. A.; Brongersma, M. L.; Kik, P. G.; Atwater, H. A. *Phys. Rev. B*, **2002**, *65*, 193408. (c) Wang, Y. *Acc. Chem. Res.* **1991**, *24*, 133. (d) Yoffe, A. D. *Adv. Phys.* **1993**, *42*, 173.

[43] Li, X.; Xu, W.; Zhang, J.; Jia, H.; Yang, B.; Zhao, B.; Li, B.; Ozaki, Y. *Langmuir* **2004**, *20*, 1298.

[44] (a) Wegner, K.; Walker, B.; Tsantilis, S.; Pratsinis, S. E. *Chem. Eng. Sci.* **2002**, *57*, 1753. (b) Oha, S.; Choi, C.; Kwon, S.; Jin, S.; Kim, B.; Park, J. *J. Magn. Magn. Mater.* **2004**, *280*, 147. (c) Chevallier, J. *Thin Solid Films* **1977**, *40*, 223. (d) Perekrestov, V. I. *Tech. Phys. Lett.* **2005**, *31*, 830.

[45] (a) Wang, Y.; Zhang, L.; Meng, G.; Liang, C.; Wang, G.; Sun, S. *Chem. Commun.* **2001**, *24*, 2632. (b) Teng, X.; Black, D.; Watkins, N. J.; Gao, Y.; Yang, H. *Nano Lett.* **2003**, *3*, 261. (c) Hou, Y.; Kondoh, H.; Kogure, T.; Ohta, T. *Chem. Mater*. **2004**, *16*, 5149.

[46] (a) Kim, J. H.; Germer, T. A.; Mulholland, G. W.; Ehrman, S. H. *Adv. Mater.* **2002**, *14*. 518. (b) Okuyama, K.; Lenggoro, I. W. *Chem. Eng. Sci.* **2003**, *58*, 537. (c) Suh, W. H.; Suslick, K. S. *J. Am. Chem. Soc.* **2005**, *127*, 12007.

[47] (a) Zhou, Y.; Wang, C. Y.; Zhu, Y. R., Chen, Z.Y. *Chem. Mater.* **1999**, *11*, 2310. (b) Li, H. X.; Lin, M. Z.; Hou, J. G. *J. Crystal Growth* **2000**, *212*, 222. (c) Mallick, K.; Wang, Z. L.; Pal, T. *J. Photochem. Photobiol. A* **2001**, *140*, 75. (d) Chen, W. X.; Lee, J. Y.; Liu, Z. *Chem. Commun.* **2002**, *21*, 2588. (e) Jin, R.; Cao, Y. C.; Hao, E.; Métraux, G. S.; Schatz, G. C.; Mirkin, C. A. *Nature* **2003**, *425*, 487. (f) Sakamoto, M.; Tachikawa, T.; Fujitsuka, M.; Majima, T. *Langmuir* **2006**, *22*, 6361.

[48] (a) Amendola, V.; Polizzi, S.; Meneghetti, M. *J. Phys. Chem. B* **2006**, *110*, 7232. (b) Amendola, V.; Rizzi, G. A.; Polizzi, S.; Meneghetti, M. *J. Phys. Chem. B* **2005**, *109*, 23125. (c) Balchev, I.; Minkovski, N.; Marinova, Ts.; Shipochka, M.; Sabotinov, N. *Mater. Sci. Eng. B* **2006**, *135*, 108. (d) Mafuné, F.; Kohno, J.; Takeda, Y.; Kondow, T. *J. Phys. Chem. B* **2000**, *104*, 8333. (e) Zhu, X. P.; Suzuki, T.; Nakayama, T.; Suematsu, H.; Jiang, W.; Niihara, K. *Chem. Phys. Lett.* **2006**, *427*, 127.

[49] (a) Chen, W.; Cai, W.; Lei, Y.; Zhang, L. *Mater. Lett.* **2001**, *50*, 53. (b) Chen, W.; Cai, W.; Zhang, L.; Wang, G.; Zhang, L. *J. Colloid Interface Sci.* **2001**, *238*, 291. (c) Dhas, N. A.; Raj, C. P.; Gedanken, A. *Chem. Mater.* **1998**, *10*, 1446. (d) Fujimoto, T.; Terauchi, S.; Umehara, H.; Kojima, I.; Henderson, W. *Chem. Mater.* **2001**, *13*, 1057. (e) Nemamcha, A.; Rehspringer, J.; Khatmi, D. *J. Phys. Chem. B* **2006**, *110*, 383. (f) Pol, V. G.; Grisaru, H.; Gedanken, A. *Langmuir* **2005**, *21*, 3635.

[50] (a) Kurihara, K.; Kizing, J.; Stenius, P.; Fender, J. H. *J. Am. Chem.Soc.* **1983**, *105*, 2574. (b) Mulvaney, P.; Henglein, A. *J. Phys. Chem.* **1990**, *94*, 4182. (c) Joshi, S. S.; Patil, S. F.; Iyer, V.; Mahumuni, S. *Nanostruct. Mater.* **1998**, *7*, 1135. (d) Henglein, A.; Giersig, M. *J. Phys. Chem. B* **1999**, *103*, 9533. (e) Dimitrijevic, N. M.; Bartels, D. M.; Jonah, C. D.; Takahashi, K.; Rajh, T. *J. Phys. Chem. B* **2001**, *105*, 954. (f) Doudna, C. M.; Bertino, M. F.; Blum, F. D.; Tokuhiro, A. T.; Lahiri-Dey, D.; Chattopadhyay, S.; Terry, J. *J. Phys. Chem. B* **2003**, *107*, 2966.

[51] (a) Stoeva, S. I.; Prasad, B. L. V.; Uma, S.; Stoimenov, P. K.; Zaikovski, V.; Sorensen, C. M.; Klabunde, K. J. *J. Phys. Chem. B* **2003,** *107*, 7441. (b) Ponce, A. A.; Klabunde, K. J. *J. Mol. Catal.* **2005**, *225*, 1. (c) Smetana, A. B.; Klabunde, K. J.; Sorensen C. M. *J. Colloid Interface Sci.* **2005**, *284*, 521. (d) Klabunde, K. J.; Timms, P. S.; Skell, P. S.; Ittel, S. *Inorg. Synth.* **1979**, *19*, 59. (e) Davis, S. C.; Klabunde, K. J. *Chem. Rev.* **1982**, *82*, 153. (f) Stoeva, S.; Klabunde, K. J.; Sorensen, C. M.; Dragieva, I. *J. Am. Chem. Soc.* **2002**, *124*, 2305.

[52] Katz, E.; Willner, I. *Angew. Chem. Int. Ed*. **2004**, *43*, 6042.

[53] Sastry, M.; Kumar, A.; Mukherjee, P. *Colloids and Surf. A* **2001**,*181*, 255.

[54] Stephen, J. R.; Maenaughton, S. J. *Curr. Opin. Biotechnol.* **1999**, *10*, 230.

[55] Mehra, R. K.; Winge, D. R. *J Cell. Biochem.* **1991**, *45*, 30.

[56] Sastry, M.; Ahmad, A.; Khan, M. I.; Kumar, R. *Microbial nanoparticle production.* In: Niemeyer C. M.; Mirkin, C. A. (eds) Nanobiotechnology. Wiley-VCH, Weinheim, Germany, 2004**,** pp 126–135.

[57] Bhattacharya, D.; Rajinder, G. *Crit Rev Biotechnol.* **2005**, *25*, 199.

[58] Mann. S. *Biomimetic materials chemistry*. VCH Publishers, New York, 1996.

[59] (a) Lovley, D. R.; Stolz, J. F.; Nord, G. L.; Philips, E. J. P. *Nature* **1987,** *330*, 252. (b) Dickson, D. P. E. *J. Magn. Magn. Mater*. **1999**, *203*, 46.

[60] (a) Mann, S. *Nature* **1993**, *365*, 499. (b) Oliver, S.; Kupermann, A.; Coombs, N.; Lough, A.; Ozin, G. A. *Nature* **1995,** *378*, 47. (c) Kroger, N.; Deutzmann, R.; Sumper, M. *Science* **1999,** *286*, 1129.

[61] Lowenstam, H. A. *Science* **1981**, *211*, 1126.

[62] (a) Pum, D.; Sleytr, U. B. *Trends Biotechnol.* **1999,** *17*, 8. (b) Sleytr, U. B.; Messner, P.; Pum, D.; Sara, M. *Angew. Chem. Int. Ed.* **1999,** *38*, 1035.

[63] (a) Beveridge, T. J.; Murray, R. G. E. *J. Bacteriol.* **1980,** *141*, 876. (b) Southam, G.; Beveridge, T. J. *Geochim. Cosmochim. Acta.* **1994,** *58*, 4527. (c) Fortin, D.; Beveridge, T. J. *From biology to biotechnology and medical applications*. In: Baeuerien E (ed) Biomineralization, Wiley-VCH, Weinheim, 2000**,** pp 7–22.

[64] Konishi, Y.; Nomura, T.; Tsukiyama, T.; Saitoh, N. *Trans. Mater. Res. Soc. Jpn.* **2004,** *29*, 2341.

[65] Sastry, M.; Ahmad, A.; Khan, M. I.; Kumar, Rajiv, *Currect science* **2003**, *2*, 162.

[66] Ahmad, A.; Senapati, S.; Khan, M. I.; Ramani, R.; Srinivas, V.; Sastry, M. *Nanotechnology* **2003**, *14*, 824.

[67] Silver, S. *FEMS Microbiol. Rev.* **2003,** *27*, 341.

[68] (a) Klaus, T.; Joerger, R.; Olsson, E.; Granqvist, C. G. *Proc. Natl. Acad. Sci. U.S.A.* **1999**, *96*, 13611. (b) Klaus, T. J.; Joerger, R.; Olsson, E.; Granqvist, C. G. *Trends Biotechnol.* **2001**, *19*, 15. (c) R. Joerger, T. Klaus and C. G. Granqvist, *Adv. Mater.* **2000**, *12*, 407.

[69] Nair, B.; Pradeep, T. *Cryst. Growth Des.* **2002**, *2*, 293.

[70] Mandal, D.; Bolander, M. E.; Mukhopadhyay, D.; Sarkar, G.; Mukherjee, P. *Appl. Microbiol. Biotechnol*. **2006**, *69*, 485.

[71] Sweeney, R. Y.; Mao, C.; Gao, X.; Burt, J. L.; Belcher, A. M.; Georgiou, G,; Iverson, B. L. *Chem. Biol.* **2004**, *11*, 1553.

[72] Labrenz, M.; Druschel, G. K.; Thomsen-Ebert, T.; Gilbert, B.; Welch, S. A.; Kemner, K. M.; Logan, G. A.; Summons, R. E.; Stasio, G. D.; Bond, P. L.; Lai, B.; Kelly, S. D.; Banfield, J. F. *Science* **2000**, *290*, 1744.

[73] (a) Watson, J. H. P.; Croudace, I. W.; Warwick, P. E.; James, P. A. B.; Charnock, J. M.; Ellwood, D. C. *Sep. Sci. Technol.* **2001,** *36*, 2571. (b) Watson, J. H. P.; Ellwood, D. C.; Soper, A. K.; Charnock, J. *J. Magn. Magn. Mater.* **1999,** *203*, 69.

[74] Philipse, A. P.; Maas, D. *Langmuir* **2002**, *18*, 9977.

[75] Roh, Y.; Lauf, R. J.; McMillan, A. D.; Zhang, C.; Rawn, C. J.; Bai, J.; Phelps, T. J. *Solid State Commun.* **2001**, *118*, 529.

[76] Bharde, A.; Wani, A.; Shouche, Y.; Joy, P. A.; Prasad, B. L. V.; Sastry, M. *J. Am. Chem. Soc*. **2005**, *127*, 9326. \

[77] (a) Dameron, C. T.; Reese, R. N.; Mehra, R. K.; Kortan, A. R.; Carroll, P. J.; Steigerwald, M. L.; Brus, L. E.; Winge, D. R. *Nature* **1989,** *338*, 596. (b) Reese, R. N.; Winge, D. R. *J. Biol. Chem.* **1988,** *263*, 12832.

[78] (a) Kowshik, M.; Vogel, W.; Urban, J.; Kulkarni, S. K.; Paknikar, K. M. *Adv. Mater.* **2002**, *14*, 815. (b) Kowshik, M.; Deshmukh, N.; Vogel, W.; Urban, J.; Kulkarni, S. K.; Paknikar, K. M. *Biotechnol. Bioeng.* **2002**, *78*, 583.

[79] Kowshik, M.; Ashtaputre, S.; Kharrazi, S.; Vogel, W.; Urban, J.; Kulkarni, S. K.; Paknikar, K. M. *Nanotechnology* **2003,** *14*, 95.

[80] (a) Mukherjee, P.; Senapati, S.; Mandal, D.; Ahmad, A.; Khan, M. I.; Kumar, R.; Sastry, M. *Chembiochem* **2002**, *3*, 461. (b) Ahmad, A.; Mukherjee, P.; Senapati, S.; Mandal, D.; Khan, M. I.; Kumar, R.; Sastry, M. *Coll. Surf. B* **2003**, *28*, 313.

[81] Gole, A.; Dash, C.; Ramakrishnan, V.; Sainkar, S. R.; Mandale, A. B.; Rao, M.; Sastry, M. *Langmuir* **2001**, *17*, 1674.

[82] Senapati, S.; Ahmad, A.; Khan, M. I.; Sastry, M.; Kumar, R. *Small* **2005**, *1*, 517.

[83] Shankar, S. S.; Ahmad, A.; Parischa, R.; Sastry, M.; *J. Mater. Chem.* **2003**, *13*, 1822.

[84] Ahmad, A.; Mukherjee, P.; Mandal, D.; Senapati, S.; Khan, M. I.; Kumar, R.; Sastry, M. *J. Am. Chem. Soc.* **2002,** *124*, 12108.

[85] (a) Bansal, V.; Rautaray, D.; Bharde, A.; Ahire, K.; Sanyal, A.; Ahmad, A.; Sastry, M. *J. Mater. Chem*. **2005**, *15*, 2583. (b) Bansal, V.; Sanyal, A.; Rautaray, D.; Ahmad, A.; Sastry, M. *Advanced Materials*, **2005**, *17*, 889. (c) Bansal, V.; Rautaray, D.; Ahmad, A.; Sastry, S. *J. Mater. Chem*. **2004**, *14*, 3303.

[86] Bharde, A.; Rautaray, D.; Bansal, V.; Ahmad, A.; Indranil, S.; Mohammaf, Y.; Sanyal, M.; Sastry, M. *Small*, **2006**, *2*, 135.

[87] (a) Rautaray, D.; Ahmad, A.; Sastry, M. *J. Am. Chem. Soc*. **2003**, *125*, 14656.(b) Rautaray, D.; Sanyal, A.; Bharde, A.; Ahmad, A.; Sastry, S. *Cryst. Growth Des.* **2005,** *5*, 399.

[88] Couriol, C.; Amrane, A.; Prigent, Y. *J. Biosci. Bioeng.* **2001**, *91*, 570.

[89] Bansal, V.; Ahmad, A.; Sastry, M. *J. Am. Chem. Soc*. **2006**, *128*, 14059.

[90] Bansal, V.; Syed, A.; Bhargava, S. K.; Ahmad, A.; Sastry, M. *Langmuir* **2007,** *23*, 4993.

[91] Bansal, V.; Poddar, P.; Ahmad, A.; Sastry, M. *J. Am. Chem. Soc*. **2006**, *128*, 11958.

[92] Smetacek, V. *Nature* **1999**, *397*, 475.

[93] Werner, D. In *Biology of Diatoms, Botanical Monographs, Vol. 13* (Ed. D. Werner), Blackwell Scientific Publications, Oxford, 1977, pp. 1-17.

[94] (a) Pickett-Heaps, J.; Schmid, A. M. M.; Edgar, L. A. In *Progress in Phycological Researc*h; Round, F. E., Chapman, D. J., Eds. Biopress: Bristol, 1990; pp 1-169. (b) Gordon, R.; Drum, R. W. *Int. Rev. Cytol.* **1994**, *150*, 243. (c) Mann, S. *Nature* **1993**, *365*, 499. (d) Oliver, S.; Kupermann, A.; Coombs, N.; Lough, A.; Ozin, G. A. *Nature* **1995**, *378*, 47.

[95] Cannon, H. L.; Shacklette, H. T.; Bastron, H. *Metal Absorption by Equisetum (horsetail),* United States Geological Survey Bulletin 1278–A, 1968, A1–A21.

[96] Shacklette, H. T.; Lakin, H. W.; Hubert, A. E.; Curtin, G. C. *Absorption of Gold by Plants,* United States Geological Survey Bulletin 1314–B, **1970**, 1–23.

[97] Lakin, H. W.; Curtin, G. C.; Hubert, A. E.; Shacklette, H. T.; Doxtader, K. G. *Geochemistry of Gold in the Weathering Cycle*, United States Geological Survey Bulletin **1974,** *1330*, 1–80.

[98] Torresdey, J. L. G. *et al. Nano Lett.* **2002**, *2*, 397.

[99] Torresdey, J. L. G. *Langmuir* **2003**, *19*, 1357.

[100] Shankar, S. S.; Ahmad, A.; Sastry, M. *Biotech. Progress* **2003**, *19*, 1627.

[101] Shankar, S. S.; Rai, A.; Ahmad, A.; Sastry, M. *J. Colloid Interface Sci.* **2004**, *275*, 496.

[102] Shankar, S. S.; Rai, A.; Ankamwar, B.; Singh, A.; Ahmad, A.; Sastry, M. *Nat. Mater.* **2004**, *3*, 482.

[103] Shankar, S. S.; Rai, A.; Ahmad, A.; Sastry, M. *Chem. Mater.* **2005**, *17*, 566.

[104] Ankamwar, B.; Damle, C.; Ahmad, A.; Sastry, M. *J. Nanosci. Nanotechnol.* **2005**, *5*, 1665.

[105] (a) Mann, S.; Meldrum, F. C. *Adv. Mater.* **1991**, *3*, 316. (b) Mann, S.; Archibald, D. D.; Didymus, J. M.; Douglas, T.; Heywood, B. R.; Meldrum, F. C.; Reeves, N. J. *Science* **1993**, *261*, 1286. (c) Shenton, W.; Pum, D.; Sleytr, U. B.; Mann, S. *Nature* **1997**, *389*, 585. (d) Braun, E. Eichen, Y.; Sivan, U.; Ben-Yoseph, G. *Nature* **1998**, *391*, 775. (e) Whaley, S. R.; English, D. S.; Hu, E. L.; Barbara, P. F.; Belcher, A. M. *Nature* **2000**, *405*, 665. (f) Xu, G.; Aksay, I. A.; Groves, J. T. *J. Am. Chem. Soc.* **2001**, *123*, 2196.

[106] *Biomimetic Materials Chemistry* (Ed: S. Mann), VCH, Weinheim 1996.

[107] Chasteen, N. D.; Harrison, P. M. *J. Struct. Biol.* **1999**, *126*, 182.

[108] Shenton, W.; Mann, S.; Colfen, H.; Bacher, A.; Fischer, M. *Angew. Chem. Int. Ed.* **2001**, *40*, 442.

[109] Douglas, T.; Strable, E.; Willits, D.; Aitouchen, A.; Libera, M.; Young, M. *Adv. Mater.* **2002**, *14*, 415.

[110] Kroger, N.; Deutzmann, R.; Sumper, M. *J. Biol. Chem.* **2001**, *276*, 26066.

[111] Sewell, S. L.; Wright, D. W. *Chem. Mater.* **2006,** *18*, 3108.

[112] Xie, J.; Lee, J. Y.; Wang, D. I. C.; Ting, Y. P. *ACSnano* **2007**, *1*, 429.

[113] Naik, R. R.; Stringer, S. J.; Agarawal, G.; Jones, S. E.; Stone, M. O. *Nat. Mat.* **2002**, *1*, 169.

[114] Xu, Z.; Jinchun, C.; Peng, Y.; Wantai, Y. *J. Inorg. Biochem.* **2005**, *99*, 1692.

[115] Douglas, T.; Dickson, D. P. E.; Betteridge, S.; Charnock, J.; Garner, C. D.; Mann, S. *Science* **1995**, *269*, 54.

[116] Meldrum, F. C.; Heywood, B. R.; Mann, S. *Science* **1992**, *257*, 522.

[117] Meldrum, F. C.; Douglas, T.; Levi, S.; Arosio, P.; Mann, S. *J. Inorg. Biochem.* **1995**, *58*, 59.

[118] Douglas, T.; Stark, V. T. *Inorg. Chem.* **2000**, *39*, 1828.

[119] Meldrum, F. C.; Wade, V. J.; Nimmo, D. L.; Heywood, B. R.; Mann, S. *Nature* **1991**, *349*, 684.

[120] Wong, K. K. W.; Mann, S. *Adv. Mater.* **1996**, *8*, 928.

[121] Allen, M.; Willits, D.; Mosolf, J.; Young, M.; Douglas, T. *Adv. Mater.* **2002**, *14*, 1562.

[122] Allen, M.; Willits,D.; Young, M.; Douglas, T. *Inorg. Chem.* **2003**, *42*, 6300.

[123] Ehrnsperger, M.; Lilies, H.; Gaestel, M.; Buchner, J. *J. Biol. Chem.* **1999**, *274*, 14867.

[124] Treweek, T. M.; Morris, A. M.; Carver, J. A. *Aust. J. Chem.* **2003**, *56*, 357.

[125] Ishii, D.; Kinbara, K.; Ishida, Y.; Ishii, N.; Okochi, M.; Yohda, M.; Aida, T. *Nature* **2003**, *423*, 628.

[126] Flenniken, M. L.; Willits, D. A.; Brumfield, S.; Young, M. J.; Douglas, T. *Nano Lett.* **2003**, *3*, 1573**.**

[127] Dujardin, E.; Peet, C.; Stubbs, G.; Culver, J. N.; Mann, S. *Nano Lett.* **2003**, *3*, 413.

[128] Shenton, W.; Douglas, T.; Young, M.; Stubbs, G.; Mann, S. *Adv. Mater.* **1999**, *11*, 253.

[129] Douglas, T.; Strable, E;. Willits, D.; Aitouchen, A.; Libera, M.; Young, M. *Adv. Mater.* **2002**, *14*, 415.

[130**]** Dragnea, B.; Chen, C.; Kwak, E.; Stein, B.; Kao, C. C. *J. Am. Chem. Soc.* **2003**, *125*, 6374.

[131] Niemeyer, C. M.; Angew. *Chem. Int. Ed.* **2001**, *40*, 4128.

[132] Katz, E.; Willner, I. *Angew. Chem. Int. Ed.* **2004**, *33*, 6042.

[133] Murray, C. B.; Kagan, C. R.; Bawendi, M. G. *Annu. Rev. Mater. Sci.* **2000**, 30, 545.

[134] Daniel, M.-C.; Astruc, D. *Chem. Rev.* **2004,** *104***,** 293.

[135] Drechesler, U.; Erdogan, B.; Rotello, V. M. *Chem. Eur. J.* **2004**, *10*, 5570.

[136] Verma, A.; Rotello, V. M. *Chem. Comm.* **2005,** *3*, 303.

[137] Wang, J. *Small* **2005**, *1*, 1036.

[138] Huber, D. L. *Small* **2005**, *1*, 482.

[139] de la Fuente, J. M.; Penadés, S. *Glycoconj. J.* **2004**, *21*, 149.

[140] de la Fuente, J. M.; Barrientos, A.G.; Rojas, T. C.; Rojo, J.; Cañada, J.; Fernández, A.; Penadés, S. *Angew. Chem. Int. Ed.* **2001**, *40*, 2257.

[141] de Paz, J. L.; Ojeda, R.; Barrientos, A. G.; Penadés, S.; Martín-Lomas, M.; *Tetrahedron: Asymmetry* **2005**, *16*, 149.

[142] Barrientos, A. G.; de la Fuente, J. M.; Rojas, T. C.; Fernández, A.; Penadés, S. *Chem.- Eur. J.* **2003**, *9*, 1909.

[143] Lin, C.-C.; Yeh, Y.-C.; Yang, C.-Y.; Chen, G.-F.; Chen, Y.-C.; Wu, Y.-C.; Chen, C.-C. *Chem. Commun.* **2003**, *23*, 2920.

[144] Nolting, B.; Yu, J.-J.; Liu, G.-Y.; Cho, S.-J.; Kauzlarich, S.; Gervay-Hague, J. *Langmuir* **2003,** *19*, 6465.

[145] Zhang, J.; Geddes, C. D.; Lakowicz, J. R. *Anal. Biochem.* **2004**, *332*, 253.

[146] A. Panacek, L. Kvıtek, R. Prucek, M. Kolar, R. Vecerova, N. Pizurova, Virender K. Sharma,Tatjana Nevecna, R Zboril *J. Phys. Chem. B* 2006, *110*, 16248-16253.

[147] Sutherland, A. J. *Curr. Opin. Solid State Mater. Sci.* **2002**, *6*, 365.

[148] Chan, W.C.W.; Nie, S. *Science* **1998**, *281*, 2016.

[149]Mattousi, H.; Mauro, J. M.; Goldmann, E. R.; Anderson, G. P.; Sundar, V. C.; Mikulec, F. V.; Bawendi, M.G. *J. Am. Chem. Soc.* **2000**, 122, 12142. (b) Alivisatos, A. P. *Pure Appl. Chem.* **2000**, *72*, 3.

[150] de la Fuente,J. M.; Fandel, M.; Berry, C.C.; Riehle, M.; Cronin, L.; Aitchison, G.; Curtis, A.S.G. *ChemBioChem* **2005**, *6*, 989.

[151] Winter, J. O.; Liu, T. Y.; Korgel, B. A.; Schmidt, C. E. *Adv. Mater.* **2001**, *13* 1673.

[152] Akerman, M. E.; Chan, W. C. W.; Laakkonen, P.; Bhatia, S. N. Ruoslahti, E. *Proc. Natl. Acad. Sci. U. S. A.* **2002**, *99*, 12617.

[153] Hanaki, K.; Momo, A.; Oku, T.; Komoto, A.; Maensono, S.; Yamaguchi, Y.; Yamamoto, K. *Biochem. Biophys. Res. Commun.* **2003**, *302*, 496.

[154] Spreitzer, G.; Whitling, J. M.; Madura, J. D.; Wright, D.W. *Chem. Commun.* **2000,** *3***,** 209.

[155] Sapra, S.; Nanda, J.; Sarma, D. D.; Abed El-Al, F.; Hodes, G. *Chem. Commun.* **2001**, *21*, 2188.

[156] Goldman, E. R.; Balghian, E. O.; Mattousi, H.; Kuno, M. K.; Mauro, J. M.; Tron, P. T.; Anderson, G. P. *J. Am. Chem. Soc.* **2002**, *124*, 6378.

[157] Wu, X.; Liu, H.; Liu, J.; Haley, K. N.; Treadway, J. A.; Larson, J .P.; Ge, N.; Peale, F.; Bruchez, M. P. *Nat. Biotechnol.* **2003**, *21*, 41.

[158] Jaiswal, J. K.; Mattousi, H.; Mauro, J. M.; Simon, S. M. *Nat. Biotechnol.* **2003**, *21*, 47.

[159]Dubertret, B.; Skourides, P.; Norris, D. J.; Noireaux, V.; Brivanlou, A. H.; Libchaber, A. *Science* **2002**, *298*, 1759.

[160] Mahtab, R.; Rogers, J. P.; Murphy, C. J. *J. Am. Chem. Soc.* **1995**, *117*, 9099.

[161] Gerion, D.; Parak, W. J.; Williams, S. C.; Zanchet, D.; Micheel, C. M.; Alivisatos, A. P. *J. Am. Chem. Soc.* **2002**, *124*, 7070.

[162] Maxwell, D. J.; Taylor, J. R.; Nie, S. J. *J. Am. Chem. Soc.* **2002**, *12*4, 9609.

[163] Rosenthal, S. J.; Tomlinson, I.; Adkins, E. M.; Schroeter, S.; Adams, S.; Swafford, L.; McBride, J.; Wang, Y.; DeFelice, L. J.; Blakely, R. D. *J. Am. Chem. Soc.* **2002**, *124*, 4586.

[164] Westenhoff, S.; Kotou, N. A. *J. Am. Chem. Soc.* **2002**, *124*, 2448.

[165] Potapova, I.; Mruk, R.; Preht, S.; Zentel, R.; Basché, T.; Mews, A. *J. Am. Chem. Soc.* **2003**, *125*, 320.

[166]Dunford, R.; Salinaro, A.; Cai, L.; Serpone, N.; Horikoshi, S.; Hidaka, H.; Knowland, J. *FEBS Lett.* **1997**, *418*, 87.

[167] Serpone, N.; Salinaro, A.; Emeline, A. (SPIE - C. J. Murphy, Ed.), **2001**, *2*, 86.

[168] Colvin, V. L. *Nat. Biotechnol.* **2003**, *10*, 1166.

[169**]** U.S. department of Labor, Bureau of Labor Statistics (www.bls.gov).

[170] Rejmen, J.; Oberle, V.; Zuhorn, I. S.; Hoekstra, D. *Biochem. J.* **2004**, *377*, 159.

[171] (a) Oberdorster, G.; Oberdorster, E.; Oberdorster, J. *Health Perspect*. **2005**, *113*, 823. (b) Duffin, R.; Clouter, A.; Brown, D. M.; Tran, C. L.; Macnee, W.; Stone, V.; Donaldson, K. *Ann. Occup. Hyg*. **2002**, *46*, 242.

[172] Van Oss, C. J. 1994. Pages 7–45, 75, 80 In *Interfacial Forces in Aqueous Media.* Marcel Dekker, Inc., New York, NY.

[173] Fubini, B. *Environ. Health Perspect.* **1997**, *105*, 1013.

[174] Araujo, L.; Lobenberg, R.; Kreuter, J. J. *Drug Target.* **1999**, *6*, 373.

[175] Bair, W. J.; Willard, D. H. *Health Physics* **1963,** *9*, 253.

[176] Seaton, A.; MacNee, W.; Donaldson, K.; Godden, D. *Lancet.* **1995**, *345*, 176.

[177] (a) Ferin, J.; Oberdörster, G.; Penney, D. P. *Am. J. Respir. Cell Mol. Biol.* **1992**, *5*, 535.

[178] Lundborg, M.; Johard, U.; Lastbom, L.; Gerde, P.; Camner, P. *Environ. Res.* **2001**, *86*, 244.

[179] Stone, P. H.; Godleski, J. J. *Am. Heart J.* **1999**, *138*, 804.

[180] Borm, P. J. A.; Kreyling, W. A. *J. Nanosci. Nanotechnol.* **2004**, *4*, 1.

[181] Stearns, R. C.; Murthy, G. G. K.; Skornik, W. *et al. ICEM* 1994, 13, 763.

[182] Behrendt, H.; Becker, W. M. *Curr. Opin. Immunol.* **2001,** *13*, 709.

[183] Donaldson, K.; Stone, V.; Clouter, A.; Renwick, L.; MacNee, W. *Occup. Environ. Med.* **2001**, *58*, 211.

[184] (a) Nemmar, A.; Hoet, P. H. M.; Vanquickenborne, B.; Dinsdale, D.; Thomeer, M.; Hoylaerts, M. F.; Vanbilloen, H.; Mortelmans, L.; Nemery, B. *Circulation.* **2002**, *105*, 411. (b) Oberdörster, G.; Sharp, Z.; Atudorei, V.; Elder, A.; Gelein, R.; Lunts, A.; Kreyling, W.; Cox, C. *J. Toxicol. Environ. Health. Part A* **2002**, *65*, 1531. (c) Kreyling, W. G.; Semmler, M.; Erbe, F.; Mayer, P.; Takenaka, S.; Schulz, H.; Oberdörster, G.; Ziesenis, *J. Toxicol. Environ. Health Part A* **2002**, *65*, 1513.

[185] (a) Stone, V.; Shaw, J.; Brown, D. M.; MacNee, W.; Faux, S. P.; Donaldson, K. *Toxicol. In Vitro.* **1998**, *12*, 649. (b) Stone, V.; Tuinman, M.; Vamvakopoulos, J. E.; Shaw, J.; Brown, D. M.; Pettersson, S.; Faux, S. P.; Borm, P.; MacNee, W.; Michaelangeli, F.; Donaldson, K.; Tieze, F. *European Respiratory Journal* 2000, *15*, 297.

[186] Donaldson, K.; Brown, D.; Clouter, A.; Duffin, R.; MacNee, W.; Renwick, L.; Tran, L.; Stone, V. J. *Aerosol. Med.* **2002**, *15*, 213.

[187] (a) Pott, F.; Althoff, G. H.; Roller, M.; Hohr, D.; Friemann, J. *High acute toxicity of hydrophobic ultrafine titanium dioxide in an intratracheal study with several dusts in rats.* In: Mohr, U.; Dungworth, D. L.; Brain, J. D.; Driscoll, K. E.; Grafstrom, R. C.; Harris, C. C. editor. *Relationships Between Respiratory Disease and Exposure to Air Pollution.* ILSI Press, Washington, D.C; 1998. pp.

270–272. (b) Pott, F.; Roller, M.; Althoff, G. H.; Hohr, D.; Friemann, J. *Acute lung toxicity of hydrophobic titanium dioxide in an intratracheal carcinogenicity study with nineteen dusts in rats.* In: Vostal J. editor. Health Effects of Particulate Matter in Ambient Air Proceedings of an International Conference sponsored by the Air and Waste Management Association and the Czech Medical Association. 1998. pp. 301–307.

[188] Oberdörster, G. *Int. Arch. Occup. Environ. Health.* **2001**, *74*, 1.

[189] Warheit, D. B.; Reed, K. L.; Webb, T. R. *Ann. Occup. Hyg.* **2002**, *46*, 207.

[190] Baggs, R. B.; Ferin, J.; Oberdorster, G. *Vet. Pathol.* **1997**, *34*, 592.

[191] Ferin, J.; Oberdorster, G.; Penney, D. P. *Am. J. Respir. Cell Mol. Biol.* **1992**, *6*, 535.

[192] Hext, P. M.; Tomenson, J. A.; Thompson, P. *Ann. Occup. Hyg.* **2005**, *49*, 461.

[193] Kern, K.; Worle-Knirsch, J. M.; Krug, H. F. *Signal Transduct.* **2004**, *3-4*, 149.

[194] Peters, K.; Unger, R. E.; Kirkpatrick, C. J.; Gatti, A. M.; Monari, E. *J. Mater. Sci. Mater. Med.* **2004**, *15*, 321.

[195] (a) Conner, S. D.; Schmid, S. L. *Nature* **2003**, *422*, 37. (b) Krug, H. F.; Kern, K.; Worle-Knirsch, J. M.; Diabate, S. Page 162 In *Nanomaterials-Toxicity, Health and Enviornmental Issues,* Kumar, S. S. R.; Ed. Wiley-VCH, Weinheim, 2006.

[196] Oh, J. M.; Choi, S. J.; Kim, S. T.; Choy, J. H. *Bioconjugate Chem.* **2006**, *17*, 1411.

[197] Kam, N. W.; Liu, Z.; Dai, H. *Angew. Chem. Int. Ed.* **2006**, *45*, 577.

[198] Xing, X.; He, X.; Peng, J.; Wang, K.; Tan, W. *J. Nanosci. Nanotechnol.* **2005**, *5*, 1688.

[199] Berry, C. C.; Wells, S.; Charles, S.; Aitchison, G.; Curtis, A. S. *Biomaterials* **2004**, *25*, 5405.

[200] Moghimi, S. M.; Hunter, A. C.; Murray, J. C. *Pharmacol. Rev.* **2001**, *53*, 283.

[201] Fang, J.; Sawa, T.; Akaike, T.; Akuta, T.; Sahoo, S. K.; Khaled, G.; Hamada, A. Maeda, H. *Cancer Res.* **2003**, *63*, 3567.

[202] Chen, Z. N.; Yoshimura, T.; Abe, M.; Tsuge, K.; Sasaki, Y.; Ishizaka, S.; Kim, H. B.; Kitamura, N. *Chemistry* **2001**, *7*, 4447.

[203] Oberdorster, G.; Oberdorster, E.; Oberdorster, J. *Environ. Health Perspect.* **2005**, *113*, 823.

[204] Manna, S. K.; Sarkar, S.; Barr, J.; Wise, K.; Barrera, E. V.; Jejelowo, O.; Rice-Ficht, A. C.; Ramesh, G. T. *Nano Lett.* **2005**, *5*, 1676.

[205] Cui, D.; Tian, F.; Ozkan, C. S.; Wang, M.; Gao, H. *Toxicol. Lett.* **2005**, *155*, 73.

[206] Shvedova, A. A.; Castranova, V.; Kisin, E. R.; Schwegler-Berry, D.; Murray, A. R.; Gandelsman, V. Z.; Maynard, A.; Baron, P. *J. Toxicol. Environ. Health A* **2003**, *66*, 1909.

[207] Magrez, A.; Kasas, S.; Salicio, V.; Pasquier, N.; Seo, J. W.; Celio, M.; Catsicas, S.; Schwaller, B.; Forro, L. *Nano Lett.* **2006**, *6*, 1121.

[208] Bottini, M.; Bruckner, S.; Nika, K.; Bottini, N.; Bellucci, S.; Magrini, A.; Bergamaschi, A.; Mustelin, T. *Toxicol. Lett.* **2006**, *160*, 121.

[209] Gupta, A. K.; Gupta, M. *Biomaterials* **2005**, *26*, 1565.

[210] Hussain, S. M.; Hess, K. L.; Gearhart, J. M.; Geiss, K. T.; Schlager, J. J. *Toxicol. In Vitro* **2005**, *19*, 975.

[211] Pisanic, T. R. *Biomaterials* **2007**, *28*, 2572.

[212] Berry, C. C.; Wells, S.; Charles, S.; Curtis, A. S. *Biomaterials* **2003**, *24*, 4551.

[213] Shiohara, A.; Hoshino, A.; Hanaki, K.; Suzuki, K.; Yamamoto, K. *Microbiol. Immunol.* **2004**, *48*, 669.

[214] Lovric, J.; Bazzi, H. S.; Cuie, Y.; Fortin, G. R.; Winnik, F. M.; Maysinger, D. *J. Mol. Med.* **2005**, *83*, 377.

[215] Jeng, H. A.; Swanson, J.; J. *Environ. Sci. Health, Part A*, **2006**, *41*, 2699.

[216] Ovrevik, J.; Lag, M.; Schwarze, P.; Refsnes, M. *Toxicol. Sci.* **2004**, *81*, 480.

[217] Monteiro-Riviere, N. A.; Nemanich, R. J.; Inman, A. O.; Wang, Y. Y.; Riviere, J. E. *Toxicol. Lett.* **2005**, *155*, 377.

[218] Pulskamp, K.; Diabate, S.; Krug, H. F. *Toxicol. Lett.* **2007**, *168*, 58.

[219] Oberdorster, E. *Environ. Health Perspect.* **2004**, *112*, 1058.

Chapter II

Bacterial Synthesis of Si/SiO_2 Nanocomposites

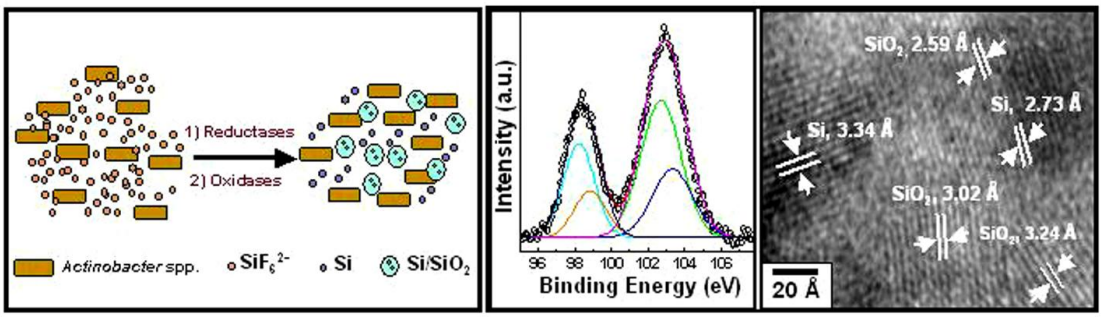

Silicon nanomaterials as well as those embedded in SiO_2 matrix have been the foci of numerous investigations due to their potential material applications in photonic devices. The known methods for preparing Si/SiO_2 nanocomposites involve either physical or chemical vapor deposition or ion implantation methods, which are then treated at or above 1000 °C. At present, there is growing need to develop environmentally benign nanomaterial synthesis processes which do not use harsh experimental conditions and toxic chemicals. An attractive alternative is to use microorganism for nanomaterial synthesis. This chapter describes a new method for the synthesis of Si/SiO_2 nanocomposites under ambient conditions with the use of bacteria (Actinobacter spp.). The reduction and hydrolysis of the precursor, which results in Si nanocrystals passivated by SiO_2 matrix is hypothesized to be mediated by the reductases and hydrolases/oxidases enzymes. Biocompatability study of the resultant nanocomposites has also been performed against human skin carcinoma cell line. Different experimental techniques have been used to characterize this material and details are discussed in this chapter.

The work described in this chapter has been published as: **Singh, S.**; Bhatta, U. M.; Satyam, P. V.; Dhawan, A.; Sastry, M.; Prasad, B. L. V. *J. Mater. Chem*. **2008,** *18***,** 2601-2606.

2.1 Introduction

In order to meet the needs of new generation, high-performance composites are required for the fabrication of micro-electronic, optoelectronic and catalytic devices, chemical and biological sensors [1], energy transducers, "smart" medical implants [2] and faster “biochips” with higher capacity [3]. Silicon (Si), Silica (SiO_2) and Silicon/Silica (Si/SiO_2) nanocomposites have always been a center of attraction for material scientists due to their innumerable technological applications and biological importance. Silicon is the second most abundant element in the earth’s crust [4] and is essential for the functioning of various metabolic reactions in variety of plants, animals and microbes [5]. It is required for the production of structural materials [6] (e.g. the frustules of diatoms, cell wall of certain higher plants and bone and cartilage of higher animals). It is widely used in the manufacturing of semiconductors, glasses, ceramics, plastics, elastomers, resins, mesosporous molecular sieves and catalysts, optical fibers and coatings, insulators, moisture shields, photoluminescent polymers, and cosmetics [7]. Recently Hochbaum *et al*. [8] have reported that silicon nanowires can generate electricity when a temperature differential is applied across them. Silicon nanostructures have been the choice for photovoltaic cells, and nanocrystalline silicon is expected to enhance many of the required performance parameters. On the other hand silica, occupies a prominent position in scientific research, because of its wide use in various industrial applications, such as catalysis, pigments, pharmacy, electronic and thin film substrates, electronic and thermal insulators, and humidity sensors [9]. Nano silica also plays an important role in silica-based materials such as resins, catalysts and molecular sieves [10].

Si is the basic material of the modern microelectronics, but unfortunately, it does not show efficient light emission due to its indirect band gap and exciton binding energy of few meV. For all these reasons, the photoluminescence (PL) from Si is observed at low temperature, which makes its use unpractical in optoelectronic circuits and devices [11]. In order to achieve high emission yields from Si, several systems have been proposed [12]. One of these systems is based on nanostructured Si, where quantum confinement and exciton localization play a major role in the light

emission process [12d-e]. As a light source, Si nanocrystals show additional advantage over bulk Si because the electrical carriers are confined in a region where no defects are present, which is mainly due to the fact that the host material (normally SiO_2) ensures an efficient passivation of defects and recombination centers. For this reason, different systems based on Si and SiO_2 have been recently investigated, like SiO_2 layers doped with Si nanocrystals[12e], Si/SiO_2 superlattices [12f], oxidized porous Si [13] or single nanometer-thick Quantum Wells of crystalline silicon [14]. The unique electronic structure of silicon nanocrystals embedded in silica (SiO_2) is enabling new light emitting [15, 16] and flash memory devices [17] that can be fabricated with standard methods of microelectronics technology. Interface between Si and SiO_2 in nano regime show interesting electronic states, which play important role in the physics of such devices. Therefore, there is growing need of $Si\text{-}SiO_2$ based materials.

There are large numbers of methods for Si/SiO_2 nanocomposite synthesis and have been successfully reported including laser ablation, chemical vapor deposition, thermal evaporation etc [18]. Among the biological synthesis, silica biomineralization (formation of inorganic materials under the control of an organism) on earth is dominated by simple aquatic life forms including unicellular organisms like radiolarians, diatoms and synurophytes and also multicellular sponges [19].

The biomimmetic synthesis of nanomaterials mainly involves three systems namely, magnetotactic bacteria (synthesize magnetic nanoparticles), diatoms (synthesize silica nanoparticles) and calcareous algae (synthesize calcium carbonate crystals), all of which are amongst the simplest form of life [20]. These microorganisms form crystals and composites of proteins with amorphous inorganic materials as a complex structure within their body. Among these, silica production is not only important commercially, the intricate patterns and thus ensuing beautiful structure of silica in aquatic organisms has also caught the attention. Thus, morphologically controlled synthesis of silica structures with the involvement of a number of proteins, peptides and synthetic additives under various physical reaction environments has been reported [21]. Three families of cell wall proteins (frustulins, pleuralins and silaffins) from the diatom *Cylindrotheca fusiformis* have been isolated

and characterized [22]. Also, extremely long chain polyamines have been discovered as an important constituent of silica [23]. It has been revealed that frustulins and pleuralins are not involved in silica formation because they become associated with the silica only after its deposition on cell wall [24]. In contrast, silaffins and polyamines exert a drastic influence on *in vitro* silica formation and thus show direct involvement in silica nanoparticle synthesis [25].

Further, Foo *et al*. [26] have reported the use of chimeric (fusion) proteins to synthesize silica nanocomposites. This protein consists of mainly silk (spidroin protein) and silica forming domains (R5 peptide) for the synthesis of silk and silica nanocomposites. R5 peptide is well known for silica precipitation, while spidroin protein 1 (MaSp 1), a protein found in *Nephila clavipes* spider dragline silk is known to form highly stable (β-sheet) secondary structures with impressive mechanical properties. Under *in vivo* experimental conditions, this chimeric protein result in the formation of silica nanoparticles having narrow size distribution than the silica nanoparticles produced with R5 peptide alone.

Nanocomposites of other metal oxides (Germanium-oxide) with Si have also been reported from photosynthetic marine diatom *Nitzschia frustulum* by Rorrer *et al.* [27]. The Si-Ge-oxide composite materials exhibit novel semiconducting and optoelectronic properties with microelectronic device applications [28]. Other reports on biosynthesis of silica nanoparticles include fungus *Fusarium oxysporium* mediated extracellular synthesis by Sastry *et al*. [29], natural and synthetic analogues of silaffins, silicatein as well as lysozyme [30], block co-polypeptides [31], poly-L-lysine/lysine/poly (allylamine hydrochloride) [32], small molecules [33] and chitosan [34] etc.

In this chapter, we describe the extracellular bacterial synthesis of silicon/silica nanocomposites. The most important and remarkable finding is the synthesis of elemental silicon totally at ambient conditions. These nanocomposites show room temperature photoluminescence due to the interface between Si crystals in a SiO_2 matrix at nanoscale size regime. The possible proteins/enzymes involved in the process of Si/SiO_2 nanocomposite synthesis have been analyzed by SDS-PAGE and the over expression of few new proteins was observed. The molecular weights of

these proteins resembled well with the molecular weights of hydrolases and reductases, which was in accordance with the earlier reports [35]. The presence of protein coating on the resultant nanocomposites has been confirmed by FTIR spectroscopy. The formation of silicon is comprehensively and conclusively proven by XPS, XRD and HRTEM studies. Further, a concentration dependent biocompatability study of Si/SiO_2 nanocomposites has also been discussed. Another interesting feature of this study is the formation of crystalline SiO_2 (a mixed phase of tridymite and crystoballite polymorphs) as compared to amorphous silica formation, which is generally seen, in chemical synthetic procedure [36].

2.2 Biosynthesis of Si/SiO_2 nanocomposites using *Actinobacter* spp.

This part describes the extracellular synthesis and characterizations of Si/SiO_2 nanocomposites using *Actinobacter* spp. (a Gram-positive bacterium). This bacterium was discovered from an aqueous mixture of potassium ferri/ferrocyanide salts (in 2:1 ratio). This mixture was left open for a period of a week. Bacterial growth was observed as turbidity, which was further isolated and preserved in solution of 30 % (v/v) glycerol and LB (1:1 ratio). The bacterial culture was further maintained on Luria-Bertini-Agar slant at 4 °C. The bacteria have been identified by molecular taxonomy method of 16S r-RNA sequencing using bioinformatics tools [35].

2.2.1 Experimental Details

A pre-inoculum was made by seed cultures of *Actinobacter* spp. in 10 mL of Luria-Bertini-broth (LB) culture medium and incubated for 24 h at 37 ^oC. This pre-inoculum was then added to 90 mL of LB culture medium in 500 mL Erlenmeyer flask and incubated for 24 h under shaking conditions (200 rpm) at 37 ^oC. In its log phase of growth-cycle, the bacterial cells were harvested and washed with autoclaved water thoroughly under sterile conditions. The harvested bacterial biomass (~1 gm of wet weight) was then resuspended in 100 mL aqueous solution of sterile 10^{-3} M K_2SiF_6 in 500 mL Erlenmeyer flask and kept on a shaker (200 rpm) at 37 ^oC. The reaction between the bacterial biomass and SiF_6^{2-} was carried out for a period of 48 h. The reaction products were collected after separating the bacterial biomass from the reaction medium through centrifugation at 5000 rpm for 10 min. The so obtained bio-

transformed products were analyzed and characterized with UV-vis spectrophotometer, FTIR, TEM, XRD, XPS, HRTEM and Fluorescence (PL) spectrophotometer etc. In a control experiment, the harvested bacterial biomass was resuspended in autoclaved deionized water in the absence of K_2SiF_6 and the filtrate obtained thereafter was characterized for the presence of Si/SiO_2 nanocomposite. As expected this reaction did not result in the formation of Si/SiO_2 nanocomposite. In another experiment, the hydrolysis of SiF_6^{2-} in autoclaved deionized water in the absence of bacterial biomass was studied by TEM and FTIR. This control experiment was also negative as no Si/SiO_2 nanocomposite could be detected.

To identify the bacterial protein(s) responsible for hydrolysis of the aqueous anionic complex of SiF_6^{2-} in to Si/SiO_2 nanocomposites and it's capping, the extracellular protein profile of the bacterial culture supernatant was checked for the induction of new protein/s upon K_2SiF_6 addition. Proteins were analyzed by 10 % SDS-PAGE (Sodium Dodecyl Sulphate Polyacrylamide Gel Electrophoresis). First, the cultured bacterial biomass was suspended in 100 mL of sterile distilled water and aqueous 10^{-3} M K_2SiF_6 solution for a period of 48 h at 30 ^oC under shaking (200 rpm) conditions. The filtrate containing the extracellular proteins secreted by the bacteria in presence of salt precursor (K_2SiF_6) was separated from the bacterial biomass by centrifugation at 5000 rpm for 10 min. This extracellular filtrate was then lyophilized and the dried protein was dissolved in minimum volume of 10 % phosphate buffer and dialyzed (using a 12 kDa cutoff dialysis membrane) against distilled water at 4 ^oC. In a separate set of experiments, all the conditions were kept same except the addition of salt precursor. The obtained proteins were purified as stated above. The dialysis products obtained were analyzed by 10 % SDS-PAGE, carried out at pH 8.5 and run along with the protein standard molecular weight marker according to the procedure published by Laemmli [37]. The polyacrylamide gels were stained using silver staining protocol.

2.2.1.1 Cytotoxicity Studies

The A431 (human epithelial carcinoma) cell line was used for the cytotoxicity study of Si/SiO_2 nanocomposites. The A431 cell line (ATCC No. CRL-1555) was initially procured from National Center for Cell Sciences, Pune, India and has been

maintained at Indian Institute of Toxicological Research, Lucknow, India. The cells were maintained in Dulbecco's Modified Eagle Medium (DMEM) medium supplemented with 10 % Fetal Bovine Serum (FBS), 1 mM sodium pyruvate, 2 mM glutamine, 50 U/mL penicillin, 50 mg/mL streptomycin and 100 mM non-essential amino acids. Cells were cultured for 3-4 days (80 % confluency) before the assay. For MTT assay, the cells were seeded in 96 well plates at a density of 10,000-15,000 cells/well in 100 µL of complete medium. The cells were incubated for 24 h in a humidified incubator at 37 ^{o}C and in the atmosphere of 5 %-CO_2-95 % air. After incubation, the complete medium was discarded and 100 µL of freshly prepared Si/SiO_2 nanocomposites (a range of concentration) in DMEM were added to each well.

MTT Assay

A stock solution of 10 mM was prepared by mixing 6 mg of Si/SiO_2 nanocomposites in 10 mL of DMEM. This mixture was sonicated thrice for one minute each with an interval of 10 seconds at 15 watts. MTT [3-(4,5-dimethylthiazoyl-2-yl)-2,5-diphenyltetrazolium bromide], a pale yellow dye is converted into formazan, a violet compound by the activity of succinate dehydrogenase of mitochondria. Since the conversion takes place in living cells, the amount of formazan produced is directly correlated with the number of viable cells present. The MTT assay was done following the method of Mosmann [38] with slight modification. In brief, cells (10,000-15,000 cells/well in 100 µL of medium) were seeded in a 96 well plate and allowed to adhere for 24 h at 37 °C in 5 %-CO_2-95 % air atmosphere. Medium was replaced with serum free medium containing Si/SiO_2 nanocomposites ranging from 10 mM to 50 µM and incubated for 3 h at 37 °C. The treatments were discarded and 100 µL serum free medium and 10 µL MTT (5 mg/mL) in PBS was added to each well and re-incubated for another 1 h at 37 °C. The reaction mixture was carefully taken out and 200 µL of DMSO was added to each well and mixed thoroughly. After 10 min, the absorbance was read at 530 nm, using Multiwell Microplate Reader (Biotek, USA). The untreated sets were also run parallel under the identical conditions and served as control. The relative cell viability in

percentage was calculated as (*A*530 of treated samples/*A*530 of untreated samples) x 100. The data presented are the mean ± SD from three independent experiments.

Morphological analysis

Morphology of cells before and after the Si/SiO_2 nanocomposites treatment was examined under the phase-contrast inverted microscope (Leica Germany). The changes in the cells were quantified using automatic image analysis software Leica Q Win 500, hooked up with the inverted phase-contrast microscope.

2.2.2 Sample Characterizations

The purified and dried silica powder was crushed with KBr, pelleted and the FTIR spectra were recorded on a Perkin-Elmer Spectrum One instrument at a resolution of 4 cm^{-1}. Samples for the Transmission Electron Microscopy (TEM) were prepared by drop coating the isolated and resuspended solution on carbon-coated copper grids. Selected area electron diffraction (SAED) as well as High Resolution Transmission Electron Microscopy (HRTEM) measurements were also carried out from the same TEM grid. TEM measurements were performed on a JEOL model 1200EX instrument operated at an accelerating voltage of 120 kV. HRTEM measurements were carried out on a JEOL–JEM-2010 UHR instrument operated at a lattice image resolution of 0.14 nm. X-Ray Diffraction (XRD) measurements of drop coated films of reaction products on glass substrate were carried out on a Philips PW 1830 instrument operated at a voltage of 40 KV and a current of 30 mA with Cu Kα radiation. X-ray photoemission spectroscopy (XPS) measurements of films of the nanocomposites cast on to Cu substrates were carried out on a VG MicroTech ESCA 3000 instrument at a pressure better than $1X10^{-9}$ Torr. The general scan and C 1s, Si 2p, N 1s, O 1s and F 1s core level spectra were recorded with un-monochromatized Mg Kα radiation (photon energy = 1253.6 eV) at pass energy of 50 eV and electron takeoff angle (angle between electron emission direction and surface plane) of 60°. The overall resolution was ~1 eV for the XPS measurements. The core level spectra were background corrected using the Shirley algorithm [39] and the chemically distinct species were resolved using a nonlinear least squares fitting procedure. The core level binding energies (BEs) were aligned with the adventitious carbon binding

energy of 285 eV. UV-vis spectra of Si/SiO_2 nanocomposites were monitored on Jasco-V-570 UV\Vis\NIR spectrophotometer operated at a resolution of 2 nm.

These characterization techniques are common and have been used for the different samples in subsequent chapters and any additional technique used otherwise is mentioned in the chapter itself.

2.3 Results and Discussions

2.3.1 Transmission electron microscopic analysis

The objects having nanometer size dimensions can be easily seen under TEM. Figure 2.1 shows TEM images of nanocomposites synthesized by *Actinobacter* spp. after 48 h of reaction with salt precursor (K_2SiF_6). TEM images from extracellular bacterial supernatant (Figure 2.1 A and B) show the presence of quasi-spherical particles having average size ~7.0 nm (Figure 2.1 B, inset). The particles are well separated from each other, as they are capped/stabilized by biomolecules, mainly proteins, present on their surface. Selected Area Electron Diffraction (SAED) pattern (Figure 2.1 C) of the as-prepared nanocomposites clearly shows the presence of crystalline nature of these particles. The obtained diffraction rings could be indexed on the basis of crystalline silica wherein the obtained d values (3.12 Å, 2.85 Å, and 1.91 Å) match reasonably well with the reported d values (3.11 Å, 2.84 Å and 1.90 Å) for the [2 1 4], [3 0 2] and [3 1 13] planes of tridymite phase of SiO_2 [40]. The extracellular supernatant apart from the protein-coated nanocomposites, also contain large amount of extra proteins, which may not participate in nanoparticle capping/stabilization. In order to get rid of extra proteins, the extracellular supernatant was calcined at 400 °C for 4 h. This calcined product was further analyzed under TEM (Figure 2.1 D and E) and aggregates of nanomaterials could be seen. The formation of aggregates could be attributed to the loss of capping proteins. Also, the SAED pattern from calcined sample showed the presence of diffraction spots indicating the improvement in crystallinity of the nanoparticles. The SAED pattern recorded from the calcined sample could be again indexed on the basis of tridymite and crystoballite polymorph of silica [40]. It could be hypothesized that addition of K_2SiF_6 causes stressful environment (ionic stress) to bacterial cells and in order to

nullify this, bacterial cells secrete large amount of proteins including certain enzymes (probably hydrolases and reductases). These enzymes reduce the stress by converting the toxic ionic form (SiF_6^{2-}) into Si/SiO_2 nanocomposite, thus precipitating these Si/SiO_2 from solution.

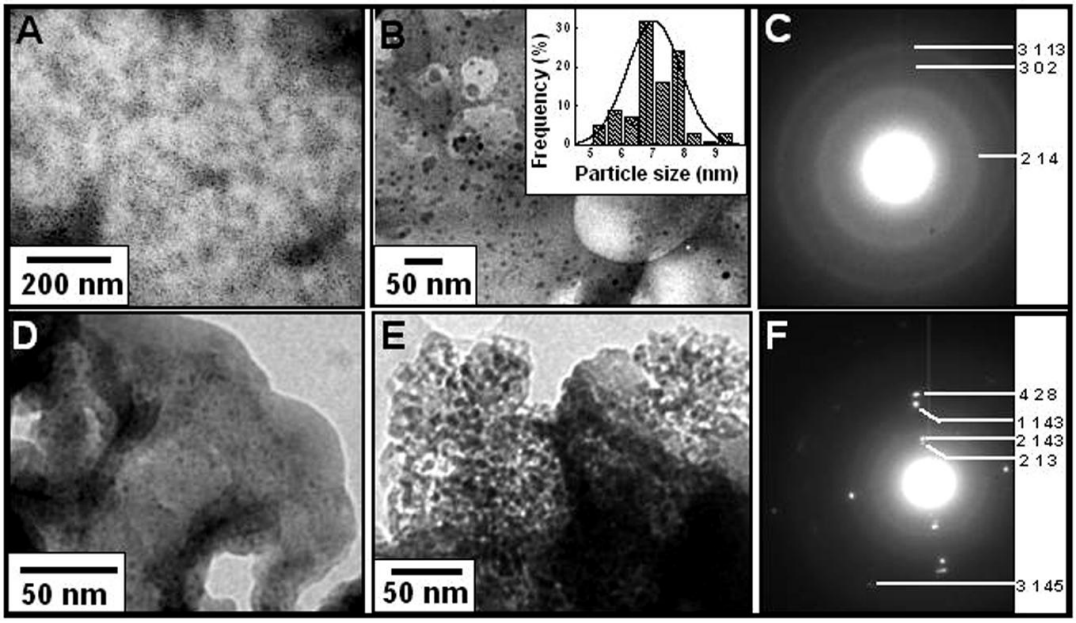

Figure 2.1: *TEM images of as synthesized (A and B) nanocomposites obtained after 48 h of reaction between Actinobacter spp. and K_2SiF_6. SAED pattern (C) shows the crystalline nature of particles and the diffraction rings could be indexed on the basis of tridymite polymorph of silica. Calcination of as synthesized nanoparticles leads to aggregation of particles (D and E) and SAED pattern (F) shows the presence of diffraction spots, which could again be indexed on the basis of tridymite and crystoballite polymorph of silica.*

2.3.2 X-ray diffraction and photoluminescent spectra analysis

Figure 2.2 A represents the XRD patterns of the drop cast film of reaction products on a glass substrate. The XRD patterns show the characteristic Bragg reflections of Si and SiO_2. The XRD pattern from as synthesized (curve-1) sample was indexed on the basis of crystoballite (⑩ and 'C') and tridymite ('T') polymorph of silica. The interesting feature is the peak that could not be indexed to any SiO_2 polymorph but matches well with pure Si (★).The broadened XRD peaks indicate the small size of Si/SiO_2 composites. After calcination (curve-2) of as synthesized particles, XRD pattern was again indexed for the mixed phase (crystoballite and tridymite) of silica and the XRD peaks corresponding to Si [(111) and (311)] become

more distinct and intense [40]. Thus, it could be concluded from XRD patterns that elemental silicon is present in SiO_2 matrix in the form of Si/SiO_2.

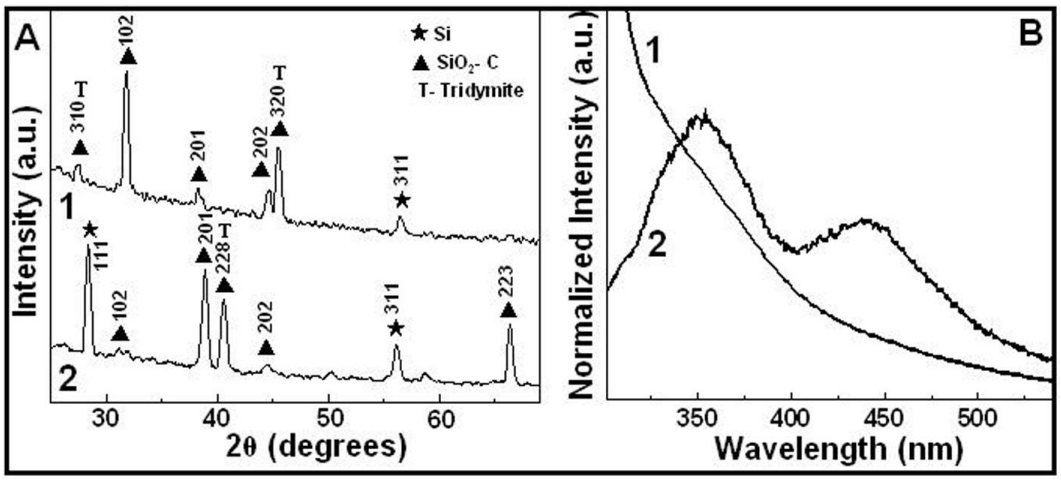

Figure 2.2: *(A) XRD pattern recorded from dried films of Si/SiO_2 nanocomposites synthesized by the reaction between K_2SiF_6 and bacterium Actinobacter spp. Characteristic diffraction patterns consisting of mixed phase of crystoballite (C) and tridymite (T) polymorph of silica and elemental silicon (Si) have been indexed in as synthesized (curve-1) and calcined sample (curve-2). (B) Absorbance (curve-1) and emission (curve-2) spectra recorded from as synthesized Si/SiO_2 nanocomposites.*

Figure 2.3 B shows the UV-vis spectra of as synthesized Si/SiO_2 nanocomposites synthesized using *Actinobacter* spp. The absorbance monotonously increases with decrease in wavelength and is generally featureless except for a small change in the slope at 425 nm. Interestingly, there are two emission bands one at λ = 352 nm and the other at λ = 442 nm. As the excitation is at 280 nm, the emission at ~352 nm can be attributed to the tryptophan and tyrosine residues of the protein capping present on the nanoparticles. However, the longer wavelength (~ 442 nm) emission is very interesting. This could be ascribed to the elemental silicon present the sample. Credence to this hypothesis comes from well-established reports that polycrystalline silicon shows an emission peak at λ = 450 nm corresponding to 2.80 eV [41]. Based on the emission spectra (Figure 2 B, curve-2), centering at ~ 442 nm, we have calculated the corresponding band gap energy to be 2.79 eV for longer wavelength emission. Thus, emission spectra also confirmed the presence of Si. This phenomenon of photoluminescence occurs when there is interface between Si nanocrystals in SiO_2 matrix at nanoscale size regime [15]. It is well predicted by theory [42] and inferred from experiment that an "interface state" is formed at the

interface between the Si nanocrystals and the SiO_2 matrix. The microscopic nature of these interface states is still under debate [42].

2.3.3 X-ray Photo-electron Spectroscopy (XPS)

Further, the synthesis of Si/SiO_2 nanocomposites by *Actinobacter* spp. was established by XPS. Figure 2.3 represents the XPS spectra recorded from the as synthesized Si/SiO_2. The C 1s, Si 2p, N 1s, O 1s and F 2p core level spectra were recorded with an overall resolution of ~1 eV. The core level binding energies (BEs) were aligned with the adventitious carbon binding energy of 285 eV. Figure 2.3 A shows the C 1s core level spectrum that could be decomposed into three chemically distinct components centered at 281.9 eV, 285.0 eV and 287.19 eV. The low binding energy peak at 281.9 eV is attributed to the presence of aromatic carbon present in amino acids from proteins bound to the surface of silica nanoparticles [43]. The high binding energy peak at 287.19 eV is attributed to electron emission from carbons in carbonyl groups (aldehydic or ketonic carbon) present in proteins bound to the nanoparticles surface [44, 45]. The C 1s component centered at 285.0 eV is due to electron emission from adventitious carbon present in the sample. In Figure 2.3 B, the Si 2p spectrum could be resolved in to two spin-orbit pairs (spin-orbit splitting ~0.6 eV) [46] with $2p_{3/2}$ binding energies (BEs) of 98.8 eV [47] and 103.3 eV [48, 49].

The high BE components at 103.3 eV (Si $2p_{3/2}$) and 102.7 eV (Si $2p_{1/2}$) agree excellently with the reported values for SiO_2, while low BE components present at 98.84 eV (Si $2p_{3/2}$) and 98.20 eV (Si $2p_{1/2}$) match with the reported values for silicon [47]. The absence of any peak from F 2p levels (inset Figure 2.3 C) unambiguously supports the almost complete hydrolysis of SiF_6^{2-} ions in to Si/SiO_2 nanocomposites. Figure 2.3 C shows the N 1s core level spectra that could be decomposed into two chemically distinct components centered at 399.6 eV and 402.2 eV. The high binding energy and lower binding energy components can be attributed to the presence of protonated amines and free amines present in the capping proteins respectively [49]. Higher binding energy component can also be attributed to N atoms present in amide bonds.

In addition to C 1s, N 1s and Si 2p, the sample was also scanned for O 1s signal (Figure 2.3 D) that shows two components having BEs of 532.2 eV and 529.8 eV. Oxygen in the Si-O-Si environment is known to show an O 1s BE component at 532.5 eV [46] while the low binding energy component at 529.8 eV could be attributed due to the oxygen present in capping proteins. Thus, XPS data further supports our assertion that as synthesized sample contains Si/SiO_2 nanocomposites.

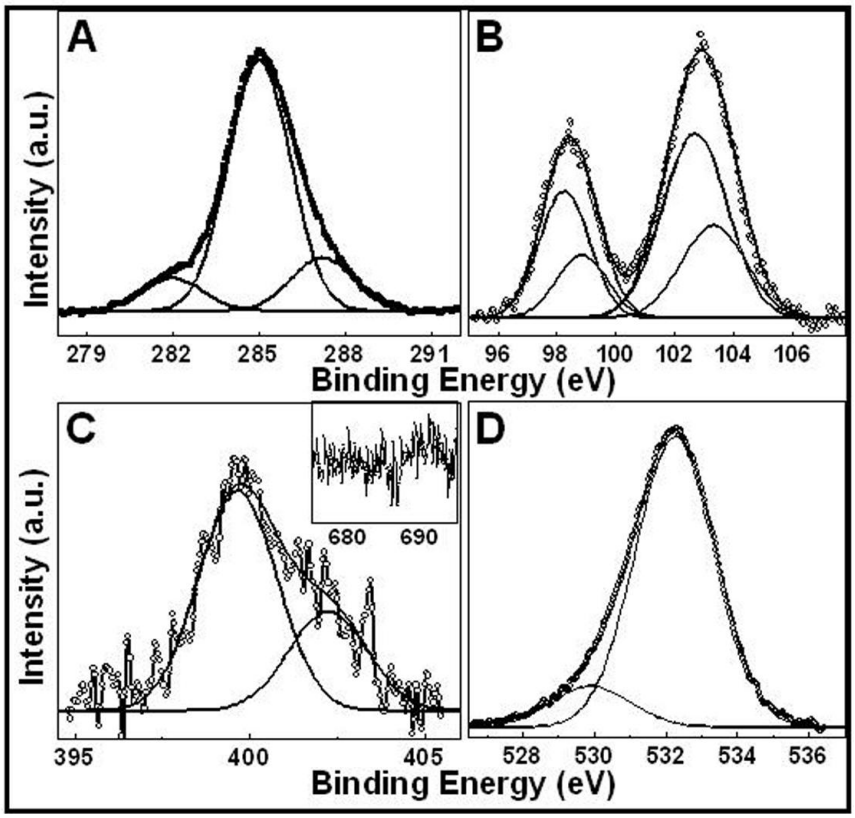

Figure 2.3: *XPS data recorded from dried films of as synthesized Si/SiO_2 nanocomposites synthesized by the reaction between K_2SiF_6 and bacterium Actinobacter spp. The core level spectra recorded from C 1s (A), Si 2p (B), N 1s (C), O 1s (D) and F 1s (inset C). The raw data is shown in the form of symbols, while the chemically resolved components are shown as solid lines and details have been discussed in text.*

2.3.4 HRTEM analysis

As a final confirmation for the presence of elemental silicon along with silica in the as synthesized sample, HRTEM investigation was undertaken which reveal the atomic arrangement in crystal lattice. Figure 2.4 shows the clear lattice planes (indicated by ★) having separations of 3.34 Å (Figure 2.4 A), 2.73 Å (Figure 2.4 A) and 3.10 Å (Figure 2.4 C), that match reasonably well with reported values (3.29 Å,

2.69 Å and 3.13 Å) for (200), (211) and (111) planes respectively of Si [40]. Further, along with the presence of lattice planes for silicon, HRTEM images reveal lattice planes (indicated by ▲) at 3.24 Å (Figure 2.4 A and B), 3.02 Å (Figure 2.4 A) and 2.59 Å (Figure 2.4 A) matching reasonably well with reported values of silica [40]. By close observation of Figure 2.4 A, it can be seen that Si (2.73 Å) is surrounded by the SiO_2 (2.59 Å, 3.02 Å and 3.24 Å). Thus it may be concluded that Si core-SiO_2 shell morphology is present in the sample.

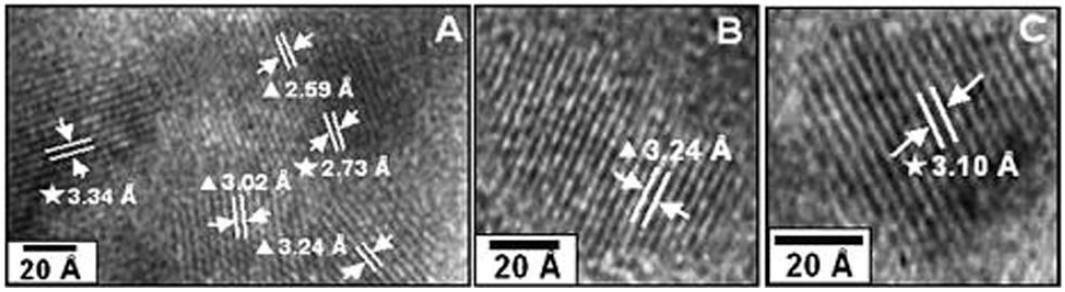

Figure 2.4: *HRTEM images taken from as synthesized Si/SiO_2 nanocomposites formed by the reaction between K_2SiF_6 and bacterium Actinobacter spp. Images from different regions were taken which show the presence of lattice spacings matching with Si (★) and SiO_2 (▲).*

2.3.5 FTIR spectral characterization and SDS-PAGE analysis

Figure 2.5 A shows the FTIR spectrum recorded from the extracellular supernatant after 48 h of reaction between *Actinobacter* spp. and salt precursor (K_2SiF_6). In Figure 2.5 A, curve-b and c show the FTIR spectra recorded from the as synthesized and calcined sample of Si/SiO_2 nanocomposites respectively while curve-a is FTIR spectra recorded from K_2SiF_6 alone. As expected, curve-a does not show any Si-O vibration band specific to SiO_2. The FTIR spectra recorded from as synthesized sample (curve-b) shows a prominent resonance band at 1100 cm^{-1}. This band is attributed to the excitation of antisymmetric Si-O-Si streching vibration [48]. This band (curve-c) becomes more intense and distinct after calcination of as synthesized sample at 400 °C for 4 h, which could be ascribed to the improved crystallinity as observed by SAED and XRD. Presence of proteins on nanoparticle surface was also confirmed by FTIR. As synthesized sample shows a broad band centering at 1640 cm^{-1} (curve-b) that can be attributed to the combined signals of amide-I and amide-II bands, characteristic to the proteins. These bands become very low in intensity (curve-c) after calcination of as synthesized sample. The weak

intensity after calcination of amide-I and II suggests the partial removal of proteins from the nanocomposites and retention of only those actually attached to the nanoparticle surfaces for capping. Amide-I and II bands are completely absent in FTIR spectrum of K_2SiF_6 (curve-a).

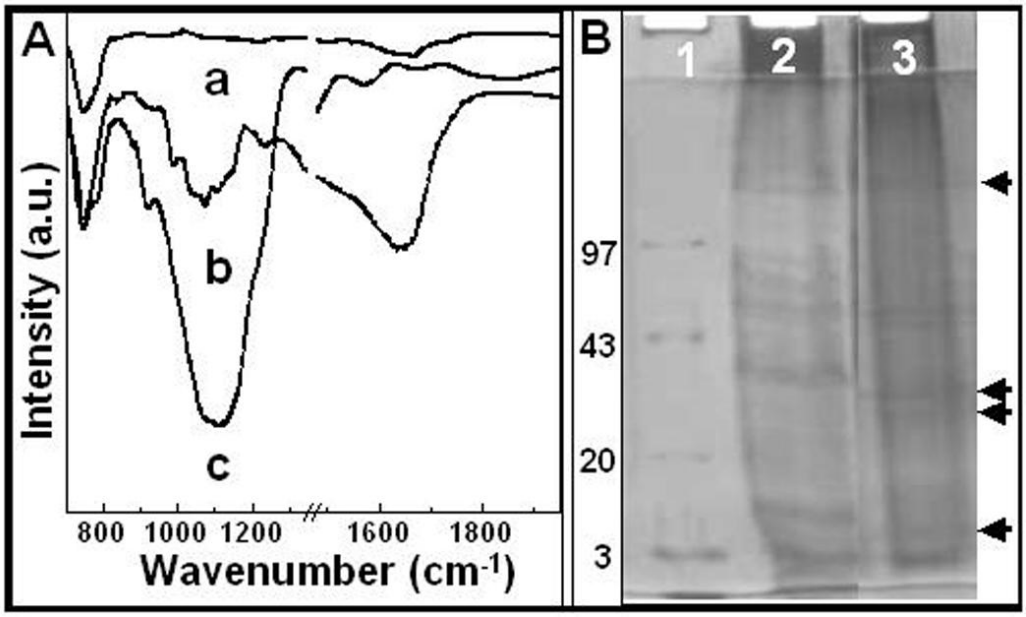

Figure 2.5: *(A) FTIR spectra recorded from powdered Si/SiO_2 nanocomposites synthesized by the reaction between K_2SiF_6 and bacterium Actinobacter spp. Curve-a, b and c respectively corresponds to the FTIR spectra recorded from K_2SiF_6, as synthesized Si/SiO_2 and calcined Si/SiO_2 sample. (B) Silver stained SDS-PAGE pattern showing the extracellular protein profile of Actinobacter spp. on 12 % resolving gel. Lane-1 corresponds to standard protein molecular weight marker with respective molecular weight. Lane-2 and 3 respectively correspond to the extracellular protein profile of Actinobacter spp. in absence and presence of K_2SiF_6 salt and the extra proteins overexpressed in lane-3 are shown by arrows.*

Figure 2.5 B shows the SDS-PAGE pattern from the extracellular protein profile of *Actinobacter* spp. culture supernatant in absence (lane-2) and presence (lane-3) of K_2SiF_6. In comparison with the control (lane-2), it can be clearly observed that there are four new proteins, indicated by arrows (lane-3) that could have resulted due to the stress created by the addition of K_2SiF_6 to the bacterial biomass. When compared with standard protein molecular weight markers (lane-1) the molecular weight of these newly expressed proteins were found to be 5, 30, 35 and 105 kDa. It has been reported that this bacterium (*Actinobacter* spp.) secretes the enzymes having molecular weights 30 and 35 kDa which could reduce Au^{3+} or Ag^{+} ions to their respective metallic nanoparticles, thus exhibiting their reductase activity [35]. Thus it

can be conjectured that these proteins could be involved in the formation of elemental silicon. The other new protein having higher molecular weight (105 kDa) has been observed to be involved in iron-oxide nanoparticle synthesis [35], and can be considered as probable causative for silica (SiO_2) synthesis. Another low molecular weight protein (5 kDa) could be ascribed for nanoparticle capping. Thus, on the basis of overexpressions of these four new proteins the mechanism for the formation of Si along with SiO_2 can be partially explained.

2.3.6 MTT Assay

Since, Si/SiO_2 nanocomposites are being used in several applications, especially related to diagnosis, their contact with human skin is strong possibility. Therefore**,** a preliminary biocompatability study of Si/SiO_2 nanocomposites have been performed by MTT assay against human epithelial carcinoma cell lines (A431). Figure 2.6 shows the % cell survival (% mitochondrial activity) of A431 cells against different concentrations of Si/SiO_2 nanocomposites exposed for 3 h.

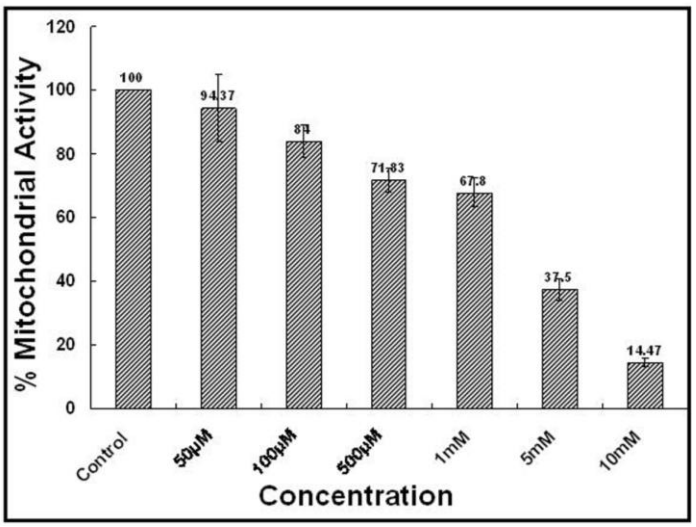

Figure 2.6: *MTT results of different concentrations of Si/SiO_2 nanocomposites exposed to human skin carcinoma cells (A431) for 3 h.*

It is clear from the graph that at very high concentrations of Si/SiO_2 nanocomposites (10 mM and 5 mM) induce significant cytotoxicity, as only 14.5 % and 37.5 % cell survival was recorded. The other lower concentrations such as 1 mM, 500 µM, 100 µM and 50 µM respectively show 67.5 %, 71.8 %, 84 % and 94.3 % cell survival. The cell morphology (Figure 2.7) study also reveals that the exposed cells

are well intact, adhered, healthy (Figure 2.7 D, E and F) and similar to control (untreated) cells (Figure 2.7 A) when the Si/SiO_2 nanocomposite concentrations were below 1 mM. Cell morphology drastically changes when the nanocomposite concentrations were taken above 1 mM, as only distorted cells associated with Si/SiO_2 nanocomposites could be seen (Figure 2.7 B and C). Thus, it could be understood that Si/SiO_2 nanocomposites are fairly biocompatible below 1 mM concentration.

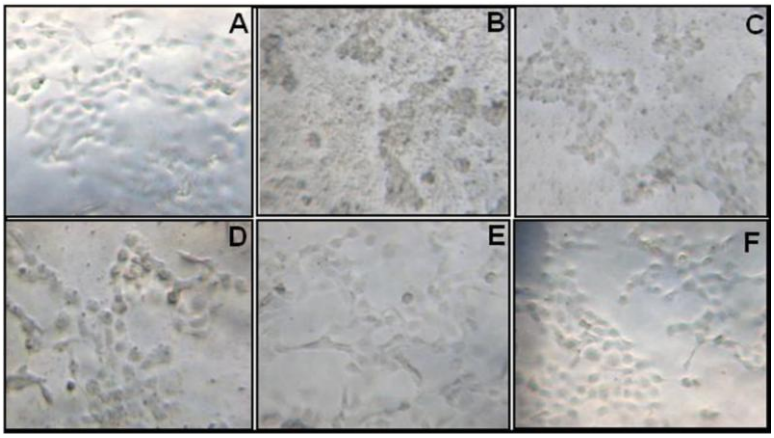

Figure 2.7: *Cell morphology of human skin carcinoma cell line treated with different concentrations of Si/SiO_2 nanocomposites for 3 h. Untreated cells (A) show well intact morphology while cells treated with higher concentrations (10 mM and 5 mM) of Si/SiO_2 nanocomposites (B and C) show distorted cell morphology attached with clusters of Si/SiO_2 nanocomposites. Cells treated with lower concentrations (1 mM, 500 µM, and 50 µM) of Si/SiO_2 nanocomposites show well intact cell morphology (D, E and F).*

2.4 Conclusions

The room temperature synthesis of sub 10 nm Si/SiO_2 nanocomposites by *Actinobacter* spp. has been described in this chapter. These nanocomposites have been characterized by TEM, FTIR, XRD, XPS and HRTEM. Although, there are reports from Sastry's group for fungus mediated, room temperature syntheses of silica nanoparticles, the bacterial synthesis of elemental silicon along with silica is an unique finding in this study. The most remarkable feature of this extracellular synthesis of Si/SiO_2 nanocomposites is the complete aerobic and environmentally benign conditions, used. The XRD patterns and XPS spectra clearly indicates the presence of silicon and silica both in the biosynthesized reaction product. The probable arrangement of silicon and silica was deduced by HRTEM images, which shows that Si/SiO_2 nanocomposites are arranged in sort of core-shell type where Si is passivated by SiO_2. These Si/SiO_2 nanocomposites were again investigated by

photoluminescence spectra, where the longer wavelength component and its corresponding band edge confirmed the presence of nano-size silicon formation as photoluminescence has been observed in such systems earlier [49].

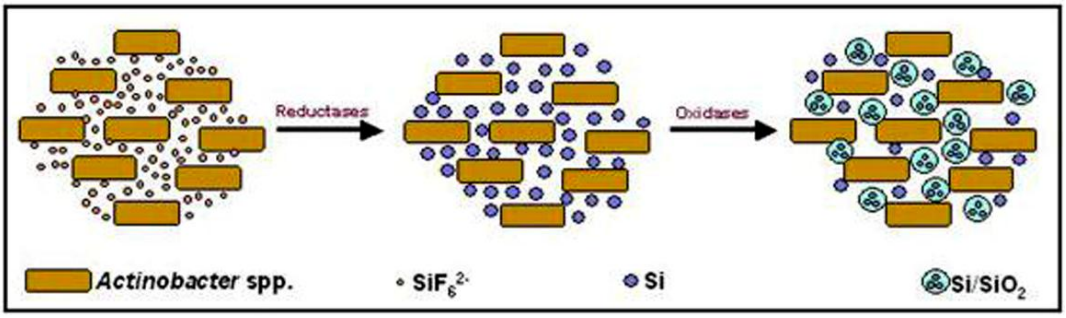

Figure 2.8: *Schematic representation of synthesis mechanism of Si/SiO_2 nanocomposites by Actinobacter spp.*

Further, the biological mechanism involved behind the synthesis of Si/SiO_2 nanocomposites was examined by SDS-PAGE profile of extracellular bacterial cell filtrate, which showed overexpressions of three proteins having molecular weights of 30, 35 and 105 kDa after the addition of K_2SiF_6 to the *Actinobacter* spp. Of these proteins the lower molecular weight proteins could be attributed to reductases in nature, responsible for reduction of Si (IV) ions to elemental Si while higher molecular weight (105 kDa) protein could be hydrolases, involved in hydrolysis of SiF_6^{2-} ions. These events are represented in the Figure 2.8. In order to use these nanocomposites for various applications, it becomes very important to check its biocompatability. Since, these nanocomposites are being used for cosmetics and other products they may come in contact with human skin cells. Thus, a cytotoxicity assay was performed on human epithelial carcinoma cell lines. A concentration dependent study was performed and found that the Si/SiO_2 nanocomposites are fairly biocompatible up to 1 mM concentrations. However, these results are preliminary and require further insight.

2.5 References

[1] Bright, H. *Naval Res. Revs.* **1994**, *46*, 48.

[2] Newnham, R.E. *Mat. Res. Soc. Bull.* **1997**, *22*, 20.

[3] (a) Kozal, M. J.; Shah, N.; Shen, N.; Yang, R.; Fucini, R.; Merigan, T. C.; Richman, D. R.; Morris, D.; Hubbell, E.; Chee, M.; Gingeras, T. R. *Nature Medicine* **1997**, 2, 753. (b) Travis, J. *Science News* **1997**, *151*, 144.

[4] Foth HD: Fundamentals of Soil Science, Edn 6. New York: John Wiley & Sons; **1978**.

[5] (a) Iler, R. K.: *The Chemistry of Silica*: Solubility, Polymerization, Colloid and Surface Properties, and Biochemistry. New York: John Wiley & Sons; 1979. (b) Voronkov, M. G.: *Silicon in Living Systems*. Edited by Corey, J. Y.; Corey, E. R.; Gaspar, P. P.; Chichester: Ellis Horwood Limited 1987.

[6] Perry, C. C.; Tucker, T. K. *J. Inorg. Biochem*. **1998**, *69*, 181.

[7] (a) Auner, N.; Weis, J. Organosilicon Chemistry III: From Molecules to Materials, Wiley–VCH 1998. (b) Auner, N.; Weis, J. Organosilicon Chemistry IV: From *Molecules to Materials*, Wiley–VCH (in press). (c) Ball, P. *Made to Measure: New Materials for the 21st Century*, Princeton University Press, Princeton, NJ, USA 1997.

[8] Hochbaum, A. I.; Chen, R.; Delgado, R. D.; Liang, W.; Garnett, E. C.; Najarian, M.; Majumdar, A.; Yang, P. *Nature* **2008**, *451*, 163.

[9] G. Herbert, *J. Eur. Ceram. Soc*. **1994**, *14*, 205.

[10] Corma, A. *Chem. Rev*. **1997**, *97*, 2373.

[11] Amato, G.; Borini, S.; Rossi, A. M.; Boarino, L.; Rocchia, M. *phys. stat. sol.* **2005**, *202*, 1529.

[12] (a) Altukhov, P. D.; Kuzminov, E. G. *Solid State Commun*. **1999**, *111*, 379. (b) Green, M. A.; Zhao, J.; Wang, A.; Reece, P. J.; Gal, M. *Nature* **2001**, *412*, 805. (c) Sticht, A.; Neufeld, E.; Luigart, A.; Brunner, K.; Abstreiter, G. *J. Lumin.* **1998**, *80*, 321. (d) Simons, A. J.; Cox, T. I.; Loni, A.; Canham, L. T.; Blacker, R. *Thin Solid Films* **1997**, *297*, 281. (e) Pavesi, L.; Negro, L. D.; Mazzoleni, C.; Franzò, G.; Priolo, F. *Nature* **2000**, *408*, 440. (f) Lockwood, D. J.; Lu, Z. H.; Baribeau, J.-M. *Phys. Rev. Lett*. **1996**, *76*, 539.

[13] Amato, G.; Boarino, L.; Midellino, D.; Rossi, A. M. *Philos. Mag. B* **2000**, *80*, 679.

[14] Lu Z. H.; Grozea, D. *Appl. Phys. Lett*. **2002**, *80*, 255.

[15] Pavesi, L.; Negro, L. D.; Nazzoleni, C.; Franzo, G.; Priolo, P. *Nature*, **2000**, *408*, 440.

[16] Ng, W. L. *et al. Nature* **2001**, *410*, 192.

[17] Tiwari, S. *et al. Appl. Phys. Lett*. **1996**, *68*, 1377.

[18] (a) Zhang, Y. F.; Tang, Y. H.; Peng, H. Y.; Wang, N.; Lee, C. S.; Bello, I.; Lee, S.T. *Appl. Phys. Lett*. **1999**, *75*, 1842. (b) Westwater, J.; Gosain, D. P.; Tomiya, S.; Usui, S.; Ruda, H. *J. Vac. Sci. Technol. B* **1997**, *15*, 554. (c) Yu, D. P.; Bai, Z. G.; Ding, Y.; Hang, Q. L.; Zhang, H. Z.; Wang, J. J.; Zou, Y. H.; Qian, W.; Xiong, G. C.; Zhou, H. T.; Feng, S. Q. *Appl. Phys. Lett.* **1998**, *72*, 3458. (d) Yi, L.X.; Heitmann, J.; Scholz, R.; Zacharias, M. *Appl. Phys. Lett*. **2002**, *81*, 4248. (e) Zacharias, M.; Blasing, J.; Veit, P. *Appl. Phys. Lett.* **1999**, *74*, 2614.

[19] Lowenstam, H. A.; Weiner, S. *On Biomineralization*, Oxford University Press, Oxford, 1989.

[20] Pickett-Heaps, J.; Schmid, A. M. M.; Edgar, L. A. in *Progress in Phycological Research*, Round, F. E.; Chapman, D. J. Eds. (Biopress, Bristol, UK) **1990**, *7*, 1.

[21] (a) Patwardhan, S. V., Clarson, S. J.; Perry, C. C. *Chem. Commun.* **2005**, *9*, 1113. (b) Frankel, R. B.; Blakemore, R. P., eds. *Iron Biominerals* (Plenum, New York) **1991**. (c) Kristiansen, J.; Andersen, R. A., eds. *Chrysophytes: Aspects and Problems* (Cambridge Univ. Press, New York **1986**. (d) Margulis, L.; Schwartz, K. V. *Five Kingdoms* (Freeman, New York), **1998**. (e) Schultze-Lam, S.; Harauz, G.; Beveridge, T. H. *J. Bacteriol.* **1992**, *174*, 7971.

[22] (a) Kroger, N.; Bergsdorf C.; Sumper, M. *EMBO J.* **1994**, *13*, 4676. (b) Kroger, N.; Lehmann, G.; Rachel, R.; Sumper, M. *Eur. J. Biochem*. **1997**, *250*, 99. (c) Kroger, N.; Deutzmann, R.; Sumper, M. *Science*, **1999**, *286*, 1129.

[23] Kroger, N.; Deutzmann, R.; Bergsdorf, C.; Sumper, M. *Proc. Natl. Acad. Sci. USA*, **2000**, *97*, 14133.

[24] (a) van de Poll, W. H.; Vrieling, E. G.; Gieskes, W. W. C. *J. Phycol.*, **1999**, *35*, 1044. (b) Kroger, N.; Wetherbee, R. *Protist*, **2000**, *151*, 263.

[25] Sumper, M.; Kroger, N. *J. Mater. Chem.* **2004**, *14*, 2059.

[26] Po Foo, C. W.; Patwardhan, S. V.; Belton, D. J.; Kitchel, B.; Anastasiades, D.; Huang, J.; Naik, R. R.; Perry, C. C.; Kaplan, D. L. *Proc. Natl. Acad Sci. U.S.A.* **2006**, *103*, 9428.

[27] Rorrer, G. L.; Chang, C.; Liu, S.; Jeffryes, C.; Jiao, J.; Hedberg, J. A. *J. Nanosci. Nanotech.* **2005**, *5*, 41.

[28] Rajeshwar, K.; Tacconi, N. R.; Chenthamarakshan, C. R. *Chem. Mater.* **2001**, *13*, 2765.

[29] (a). Bansal, V.; Rautaray, D.; Bharde, A.; Ahire, K.; Sanyal, A.; Ahmad, A.; Sastry, M. *J. Mater. Chem*. **2005**, *15*, 2583. (b). Bansal, V.; Sanyal, A.; Rautaray, D.; Ahmad, A.; Sastry, M. *Advanced Materials*, **2005**, *17*, 889.

[30] Coradin, T.; Coupe, A.; Livage, J. *Colloid Surf. B* **2003**, *29*, 189.

[31] Cha, J. N.; Stucky, G. D.; Morse, D. E.; Deming, T. J. *Nature* **2000**, *403*, 289.

[32] Patwardhan, S. V.; Clarson, S. J. *J. Inorg. Organomet. Polym.* **2002**, *12*, 109.

[33] Coradin, T.; Livage, J. *Colloid Surf. B* **2001**, *21*, 329.

[34] Chang, J. -S.; Kong, Z. -L.; Hwang, D. -F.; Chang, K. L. B. *Chem. Mater.* **2006,** *18*, 702.

[35] (a) Bharde, A.; Wani, A.; Shouche, Y.; Joy, P. A.; Prasad B. L. V.; Sastry, M. *J. Am. Chem. Soc*., **2005,** *127*, 9326. (b) Bharde, A.; Sastry, M. *J. Nanosci. Nanotechnol*. **2007** (in press).

[36] Stober, W.; Fink, A.; Bohn, E., *J. Colloid Interface Sci.* **1968**, *26*, 62.

[37] Laemmli, U. K. *Nature*, **1970**, *227*, 680.

[38] Mosmann, T. *Journal of Immunological Methods*, **1983**, 65, 55.

[39] (a) Shirley, D.A. *Phys. Rev. B* **1972**, *5*, 4709. (b) Kaufmann, E. N. *Characterization of materials*, John Wiley & sons 2003.

[40] The SAED patterns, XRD spectra and HRTEM lattice spacing were indexed with reference to the crystal structures from the ASTM charts: SiO_2 (chart card no. 42-1401, 11-0695 and 16-0152 for tridynite polymorph) and Si (chart card no. 010787 and 17-0901).

[41] Rani, J. R.; Pillai, V. P. M.; Ajimsha, R. S.; Jayaraj, M. K.; Jayasree, R. S. *J. Appl. Phys.* **2006**, *100*, 014302.

[42] (a). Wolkin, M. V.; Jorne, J.; Fauchet, P. M.; Allan, G.; Delerue, C. *Phys. Rev. Lett.* **1999**, *82*, 197. (b). Degoli, E.; Ossicini, *S. Surf. Sci*. (in the press).

Shankar, S. S.; Rai, A.; Ahmad, A.; Sastry, M. *Chem. Mater*. **2005**, *17***,** 566.
Miyama, T.; Yonezawa, Y. *Langmuir*. **2004**, *20***,** 5918.

[43] Kumar, A.; Mandal, S.; Selvakannan, P. R.; Pasricha, R.; Mandale, A. B.; Sastry, M. *Langmuir*, **2003**, *19*, 6277.

[44] Seo, K. I.; McIntyre, P. C.; Kim, H.; Saraswat, K. C. *Appl. Phys. Lett.* **2005**, *86*, 082904.

[45] Wagner, C. D. *J. Vac. Sci. Technol.* **1978**, *15*, 518.

[46] Wagner, C. D.; Riggs, W. M.; Davis, L. E.; Moulder, J. F.; Muilenberg, G. E. *Handbook of X-ray photoelectron spectroscopy*, Perkin Elmer Corp. Publishers, Eden Prairie, MN, 1979, p. 52.

[47] Lorussoy, G. F.; Stasioyz, G. D.; Casalborex, P.; Mercantik, D.; Ciottik, M. T.; Cricentiz, A.; Generosiz, R.; Perfettiz, P.; Margaritondoy, G. *J. Phys. D: Appl. Phy*. **1997**, *30*, 1794.

[48] Innocenzi, P.; Falcaro, P.; Grosso, D.; Babonneau, F. *J. Phys. Chem B* **2003**, *107*, 4711.

[49] (a) Ledoux, G.; Gong, J.; Huisken, F.; Guillois, O.; Reynaud, C. *Appl. Phys. Lett.* **2002**, *80*, 4834. (b) Wolkin, M. V.; Jorne, J.; Fauchet, P. M.; Allan, G.; Delerue, C. *Phys. Re*v. *Lett*. **1999**, *82*, 197.

Chapter III

Bacteria Mediated Synthesis of Nanocrystalline TiO_2 and ZnO and their Photocatalytic Applications

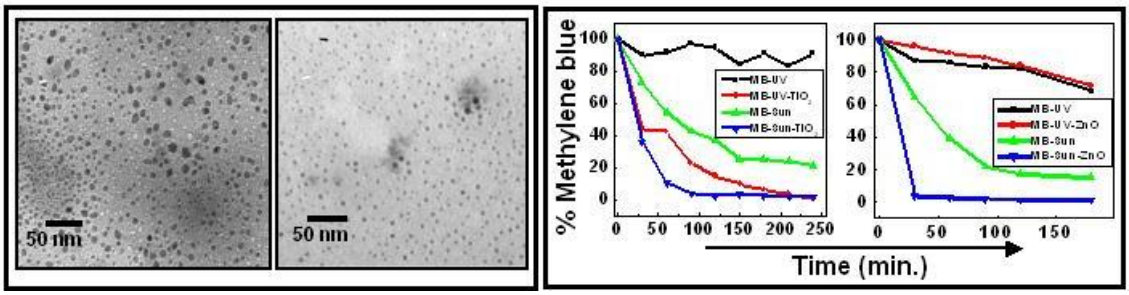

TiO_2 and ZnO nanoparticles are probably the first ones that have gained entrance to the market for their photocatalytic and UV-absorbent properties. As large volumes of these nanoparticles are required by the industry, the search for environmentally gentle processes for the synthesis of the same is also growing strong. Continuing our quest with the microorganism based synthesis of nanomaterials, we present in this chapter that, when challenged with appropriate precursor, the bacterium Actinobacter spp. can lead to the formation of ZnO and TiO_2 nanoparticles. The biological way of synthesizing these materials probably leads to the insitu doping of elements like C, F and N into their crystal lattice that is evidenced by a red shift in the absorption edge. As the doping is expected to affect the photocatalytic activity of these materials under different light conditions, studies to prove this have also been undertaken here. This chapter delineates those in detail.

The work described in this chapter has been communicated: **Singh, S**.; Sastry, M. Prasad, B.L.V**.** (Communicated).

3.1 Introduction

Nanocrystals of transition metal oxides are a fascinating class of inorganic materials, exhibiting a wide variety of structures, properties and phenomenon. These nanomaterials have attracted a great deal of attention from researchers of various fields due to their numerous technological applications [1] such as, pigments, catalysts, ceramics, energy storage, magnetic data storage, ferrofluids and sensors [2]. Among them, titania (TiO_2) and zinc oxide (ZnO) have been most extensively studied owing to their versatile applications in diverse fields. TiO_2 nanoparticles have found applications in solar cells [3], photocatalysis [4], photochromic devices [5], photovoltaic cells [6, 7], gas sensors [8, 9], catalysts [10], and pigments [11] etc. TiO_2 mainly exists in three crystalline phases, namely anatase, rutile and brookite, which differ in their physical properties (refractive index, dielectric constant and photochemical reactivity). Brookite phase (band gap 3.3eV) [12] is not often used for experimental investigations, as it is stable only at very low temperatures. Rutile (band gap 3.2 eV) is thermodynamically the most stable phase and can be obtained after high temperature calcination [12] while anatase phase (band gap 3.2 eV) is stable at comparatively low temperature. Anatase phase has gained tremendous importance as a photocatalyst for dye decomposition and solar energy conversion due to its high photoactivity [13].

ZnO, also a wide band gap (3.4 eV) II-IV compound semiconductor, has attracted intensive research efforts due to its unique properties and tremendous application in photocatalytic degradation of organic pollutants in water [14], chemical sensors, piezoelectric transducers, transparent electrodes [15], electroluminescent devices, ultra-violet laser diodes [16], solar energy conversion [17], optoelectronic devices [18] and catalysis [19]. Invisible thin film transistors (TFTs) using ZnO have achieved much higher field effect mobility than amorphous silicon TFTs [20]. These transistors can be widely used for display applications. It has been reported that ZnO is better UV emitting phosphor than GaN due to its large exciton binding energy (60 meV), leading to reduced UV lasing threshold and yields higher UV emitting efficiency at room temperature [21]. Also, ZnO films have been used as surface acoustic wave filters for video and radio frequency circuits. Piezoelectric ZnO thin

film has been fabricated into ultrasonic transducer arrays operating at 100 MHz. [22]. Successful reported have demonstrated the ability of bulk and thin films of ZnO as toxic gas sensor [23]. Doping of bulk ZnO with Manganese (p-type) has been theoretically predicted to be possible candidates with ferromagnetic ordering [24]. Also, Vanadium doped (n-type) ZnO films have been reported to have a Curie temperature above room temperature [25]. Recently, there have been several reports for TiO_2 and ZnO nanoparticle synthesis. TiO_2 nanoparticles have been synthesized using sol-gel methods by hydrolysis of titanium precursor [26], micelle and reverse micelle methods [27], solvothermal methods [28], chemical vapor deposition [29] and sonochemical methods [30] etc. On the other hand, ZnO nanoparticle synthesis involves low-pressure chemical vapor deposition [31], spray pyrolysis [32], atomic layer deposition [33], thermal decompositions of precursors [34] and laser heating [35] etc. Moreover, several biological methods for the synthesis of TiO_2 and ZnO nanoparticles have also been reported (described in Chapter I).

TiO_2 and ZnO nanoparticles are well-known photocatalysts and can be successfully implicated in dye degradation and preparation of antibacterial formulations. Organic dyes are one of the main environmental contaminants due to their toxic and non-biodegradable nature. Although, these organic dyes are present in very low concentrations in industrial wastewater, they have shown ample potential to cause disruption of endocrine functioning. These dyes are insufficiently removed by conventional sewage plant treatment due to their high biochemical stability, water solubility and high molecular weight [36]. Therefore, new technologies having more efficiency and less energy consuming protocols are attracting intensive research. As an alternative to the conventional methods, oxidation methods have been reported which involve the generation of reactive oxygen species (ROS), which oxidize a broad range of organic pollutants.

While usage of photocatalysts for dye degradation is an attractive choice, the efficiency of TiO_2 based photocatalytic reactions for sunlight-induced applications like degradation of organic pollutants is hampered by its band gap of around 3.1 eV. This extends its photothreshold from the ultraviolet to the solar spectrum to only about 400 nm, which comprises of <10 % of the solar spectrum [37]. Also, certain

reports have been described that antibacterial activity of TiO_2 nanoparticles involves the illumination of UV-light, which could cause serious damage to plants, animals and human cells [38]. Therefore, need for such photocatalysts, active in sunlight becomes almost essential for safe use. Reports show that the substitutional doping of TiO_2 with non-metals such as C, N, S, and F degrade the organic molecules on excitation with visible light [39]. Very recently, N-doped TiO_2 has been shown to exhibit visible light induced bactericidal activity [39].

In this chapter, we illustrate the extracellular bacterial synthesis of TiO_2 and ZnO nanoparticles at room temperature and under benign conditions. These nanomaterials have been characterized with different techniques such as TEM, FTIR, XRD, XPS and HRTEM etc. Calcination seems to result in *Insitu* doping with C, N and F atoms into TiO_2 crystal lattice, leading to a red shift of absorption edge thus making biosynthesized TiO_2 nanoparticles a visible light active photocatalyst. Photocatalytic applications of these biosynthesized oxide nanoparticles have also been discussed specially in regard with dye (methylene blue) degradation under the illumination of different light conditions. This chapter has been divided into three parts; first and second part deals respectively with synthesis and characterizations of TiO_2 and ZnO nanoparticles. The third part illustrates a comparative study of photocatalytic degradation of methylene blue dye with TiO_2 and ZnO nanoparticles in different light conditions.

3.2 Biosynthesis of nanocrystalline TiO_2 using *Actinobacter* spp.

This part of the chapter describes the extracellular synthesis and characterizations of TiO_2 nanoparticles using a Gram-positive bacterium *Actinobacter* spp. under ambient conditions.

3.2.1 Experimental Details

The aerobic, Gram-positive bacterium *Actinobacter* spp. was isolated from a potassium ferrocyanide and potassium ferricyanide contaminated flask (discussed in Chapter II). The seeding of *Actinobacter* spp. its growth and exposure to inorganic materials have been performed under exactly similar condition as explained in Chapter-II. Here, K_2TiF_6 was the salt precursor instead of K_2SiF_6. The so obtained

reaction products were further analyzed for the presence of TiO_2 nanoparticles using different characterization techniques such as TEM, XRD, FTIR, TGA, XPS and HRTEM etc., discussed in their respective sections of this chapter.

To identify the bacterial protein(s) responsible for hydrolysis of the aqueous anionic complex of TiF_6^{2-} into TiO_2 nanoparticles and it's capping, the extracellular protein profile of the bacterial culture supernatant was checked for the induction of new protein/s upon addition of K_2TiF_6. The methods for identification of new proteins were followed as described in Chapter II.

3.2.2 TEM and HRTEM analysis

Transmission electron microscope (TEM) images of TiO_2 nanoparticles synthesized by *Actinobacter* spp. are shown in Figure 3.1. Dense population of TiO_2 nanoparticles was found distributed over a large area of TEM grid. The as synthesized TiO_2 nanoparticles (Figure 3.1 A and B) show nearly uniform shape and size. Particles are nearly spherical in shape and are of 5.0 - 6.0 nm in size. Small clusters containing several individual TiO_2 nanoparticles embedded in protein matrix are also seen at some places. SAED pattern from as synthesized TiO_2 nanoparticles (Figure 3.1 C) shows a diffuse ring pattern, which has been indexed on the basis of brookite phase. Three rings were indexed to [121], [200], [410] planes, which match well with the reported values of brookite phase [40]. Particle size distribution from as synthesized TiO_2 nanoparticles was performed over 100 particles and average particle size was found to be 5.5 nm (inset, Figure B) in diameter. Apart from the capped proteins, the as synthesized nanoparticle suspensions usually contain huge amount of extra proteins, secreted by *Actinobacter* spp. in the extracellular medium. In order to remove the extra proteins and get a more clear idea about the inorganic material that we are interested in, calcination (400 °C for 3 h) was performed and thus extra proteins were burned out. TEM images of calcined TiO_2 nanoparticles (Figure 3.1 D and E) show the aggregates of particles. The loss of part of capping proteins along with the extra proteins results in particle aggregation. SAED pattern from calcined TiO_2 nanoparticles (Figure 3.1 F) show the spot patterns that were indexed on the basis of mixed phase of brookite and anatase.

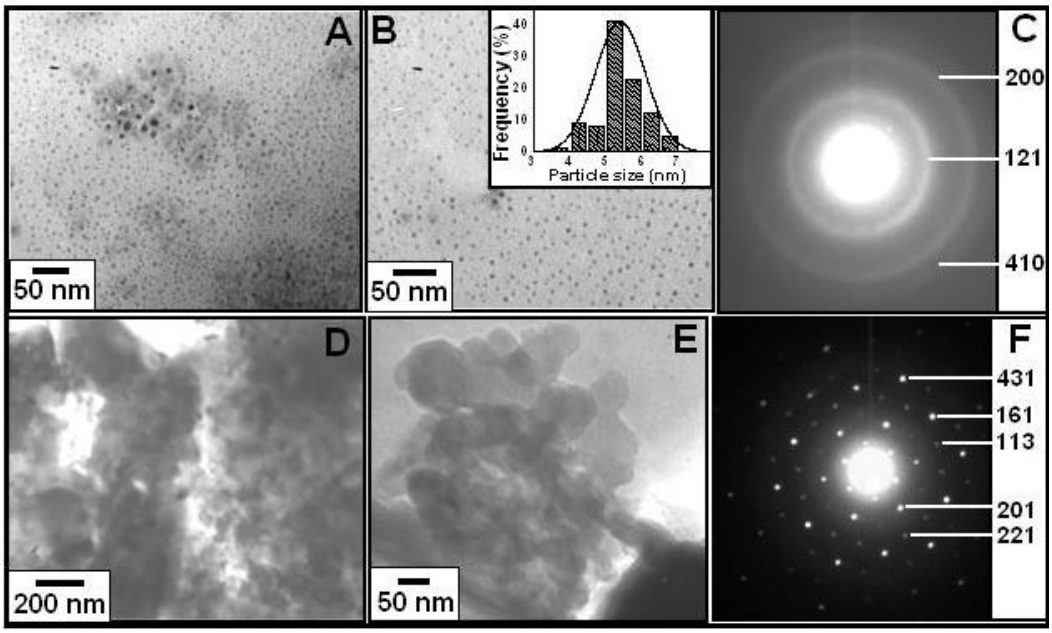

Figure 3.1: *TEM images of as synthesized (A and B) TiO_2 nanoparticles after 48 h of reaction between Actinobacter spp. and K_2TiF_6. SAED pattern (C) shows the crystalline nature of particles and the diffraction rings could be indexed on the basis of brookite polymorph of TiO_2. Particle size distribution (Figure B, inset) from as synthesized TiO_2 nanoparticles shows the average size to be 5.5 nm. Calcination of as synthesized nanoparticles leads to aggregation of particles (D and E) and SAED pattern (F) shows the presence of diffraction spots, which could be indexed on the basis of mixed phase of brookite and anatase.*

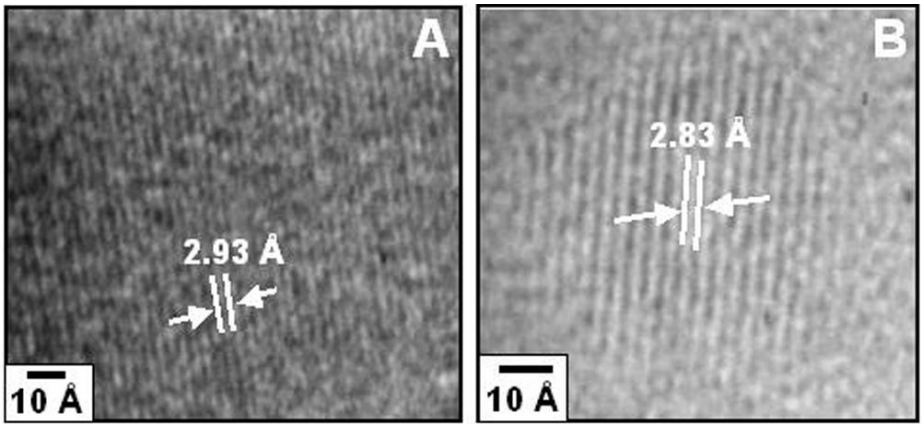

Figure 3.2: *HRTEM images of calcined (A and B) TiO_2 nanoparticles; calcination of as synthesized TiO_2 nanoparticles was performed at 400 ℃ for 4 h. The calculated d-values [2.93 Å] and [2.83 Å] corresponds to [121] and [002] crystal planes of brookite phase of TiO_2.*

Presence of clear diffraction spots after calcination of TiO_2 nanoparticles reveals the improvement of crystallinity. Calcined TiO_2 nanoparticles were further analyzed by high resolution-TEM (Figure 3.2). Clearly resolved lattice fringes of

TiO_2 nanoparticles are observed in the image indicating the crystalline nature of TiO_2 nanoparticles. The interplaner spacing (d-spacing) of [2.93 Å] and [2.83 Å] was assigned to [121] and [002] planes of brookite phase of TiO_2 [40].

3.2.3 TGA analysis

The as synthesized TiO_2 nanoparticle suspension contains huge amount of extra proteins and other impurities. To have an idea about the quantitative amount of pure TiO_2 in the given mass of as synthesized system, thermogravimetric analysis (TGA) was performed. TGA plot (Figure 3.3) from as synthesized TiO_2 nanoparticles show major weight loss at two broad ranges of temperature. The first region was in the range of 300 - 400 ^oC, corresponding to desorption or release of water vapor and some loosely bound organic matter like proteins from the sample. The second region occurred in the range of 500 - 600 ^oC that could be attributed to the combustion and decomposition of organic matters that are strongly bound to the inorganic sample. 15 % weight loss occurs during first stage while during second stage again 15 % of weight loss takes place. Thus, from the given mass of as synthesized TiO_2 a total of 30 % weight loss recorded after heating up to 600 °C. After 650 °C no more weight loss was recorded, indicating the rest 70 % weight to be only of TiO_2.

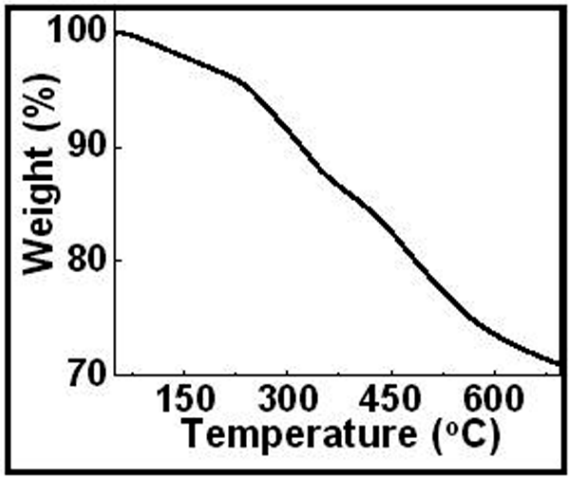

Figure 3.3: *TGA of as synthesized sample of TiO_2 nanoparticles, showing the % weight loss with respect to the steady increase in temperature. Maximum 30 % weight loss recorded after heating up to 700 °C, indicates the presence of 70 % pure TiO_2 in a given mass of as synthesized TiO_2.*

3.2.4 X-Ray Diffraction pattern analysis

Figure 3.5 shows the XRD patterns performed from drop cast films of aqueous TiO_2 nanoparticles on a glass substrate. The XRD pattern from as synthesized TiO_2 nanoparticles (curve-1) shows the characteristic Bragg's reflections of TiO_2 and matches well with the reported values of brookite phase (indicated by "B") and β-phase (indicated by "β") [40]. XRD pattern recorded from the calcined sample of TiO_2 nanoparticles (curve-2) again shows characteristic Bragg's reflections of TiO_2, matching with brookite (indicated by "B"), anatase (indicated by "A") and β-phase (indicated by "β"). Interestingly, calcined sample showed the Bragg's reflection for TiN (2θ = 43.4) [41a] and TiC (2θ = 71.6) [41b] matching with the reported values of (2θ = 43.27) and (2θ = 71.9) respectively. Thus, from XRD patterns it could be concluded that the as synthesized TiO_2 nanoparticles mainly consists of brookite phase but after calcination change in crystal structure occurs which results in the formation of some anatase phase along with brookite phase of TiO_2 with certain extent of doping of "C" "F" and "N" elements and these findings were further confirmed by XPS analysis.

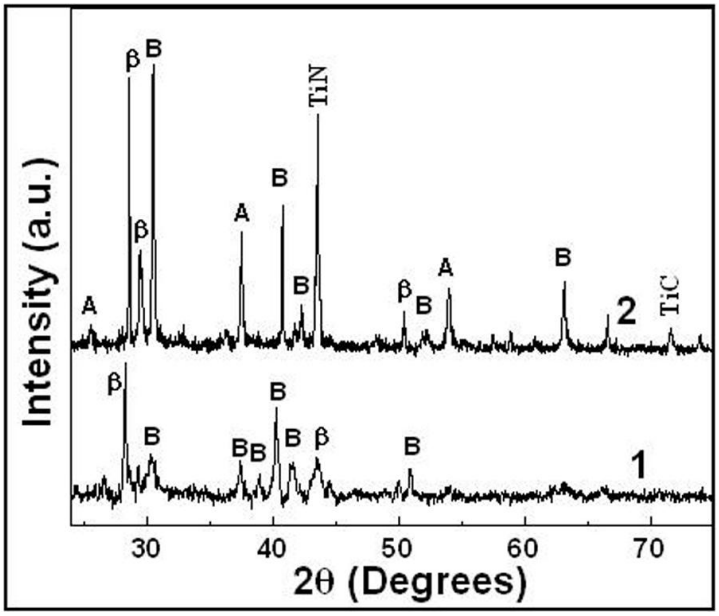

Figure 3.4: *XRD patterns of TiO_2 nanoparticles synthesized after 48 h of reaction between Actinobacter spp. and K_2TiF_6 salt. Curve-1 represents the XRD pattern recorded from as synthesized sample while curve-2 represents the XRD pattern from TiO_2 nanoparticles calcined at 400 ℃ for 3 h. Calcined sample shows the presence of mixed phase (brookite, anatase and β-phase) of TiO_2 nanoparticles.*

3.2.5 X-ray Photo-electron Spectroscopy

The chemical analysis of TiO_2 nanoparticles was carried out by X-ray Photoelectron Spectroscopy (XPS) from the as synthesized TiO_2 nanoparticles after 48 h of the reaction between *Actinobacter* spp. and K_2TiF_6. The sample was prepared on silicon wafer. The C 1s core level spectra (Figure 3.6 A) has three chemically distinct components centered at (282.4 eV), (285.0 eV) and (287.3 eV). The lower binding energy peak at 282.4 eV is attributed to the presence of aromatic carbon present in amino acids from proteins bound to the surface of TiO_2 nanoparticles [42]. The high binding energy peak at 287.3 eV is attributed to electron emission from carbons in carbonyl groups (aldehydic or ketonic carbon) present in proteins bound to the nanoparticles surface [43].

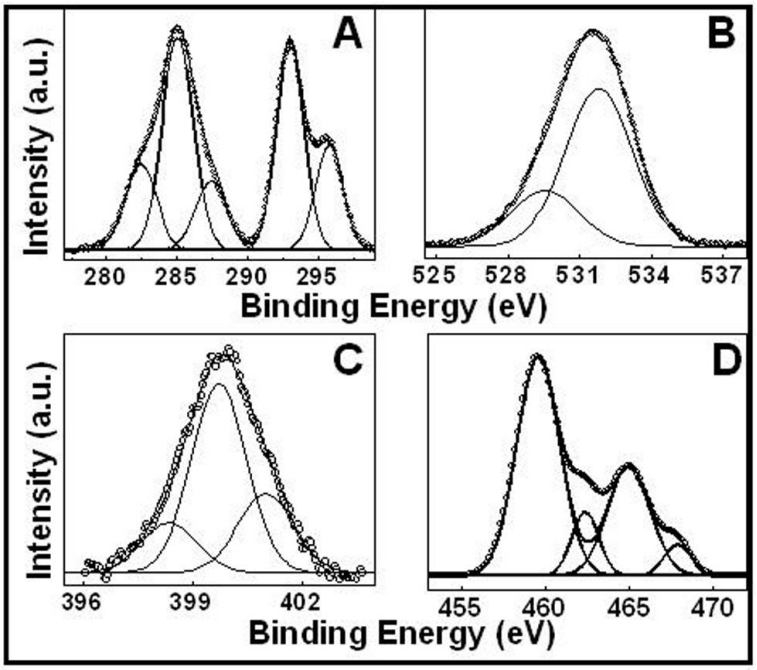

Figure 3.5: *XPS spectra of as synthesized TiO_2 nanoparticles recorded after 48 h of reaction between Actinobacter spp. and K_2TiF_6 salt. The core level spectra was recorded from C 1s (A), O 1s (B), N 1s (C) and Ti 2p (D). The raw data is shown in the form of symbols, while the chemically resolved components are shown as solid lines and details have been discussed in text.*

The C 1s component centered at 285.0 eV is due to electron emission from adventitious carbon present in the sample. The O 1s spectrum (Figure 3.6 B) could be resolved in to two chemically distinct components centering at 529.6 eV and 531.8 eV. The O 1s component present at lower binding energy (529.6 eV) can be assigned

to the lattice oxygen while the O 1s component present at higher binding energy (531.8 eV) is assigned to mixed contributions from surface hydroxide [44] and C=O group present in capping proteins. The XPS spectra for N 1s (Figure 3.6 C) could be resolved in to three chemically distinct components centering at 398.3 eV, 399.7 eV and 401.0 eV. These could be assigned respectively to free N_2, neutral amino group NH_2 and the positively charged ammonium group NH_3^+ present in the capping proteins [45]. Thus, from XPS data of O 1s and N 1s it can be concluded that proteins are definitely associated with TiO_2 nanoparticles. In (Figure 3.6 D), the Ti 2p spectrum could be resolved into two spin-orbit pairs (spin-orbit splitting ~5.7 eV) centered at 459.5 eV & 462.3 eV, and 465.0 eV & 467.8 eV. The chemical components at 459.5 eV and 465.0 eV could be attributed due to Ti $2p_{3/2,}$ and Ti $2p_{1/2}$ respectively present in TiO_2 and match well with the reported values [46]. The chemical components present at higher binding energy (462.2 eV and 467.8 eV) could be attributed to unhydrolysed TiF_6^{2-} ions. The intensity of chemical components of unhydrolysed TiF_6^{2-} ions is much lower than the Ti $2p_{3/2,}$ and Ti $2p_{1/2}$, suggesting that most of the salt precursor has been transformed in to TiO_2.

Further, XPS spectra were also recorded after calcination of biosynthesized TiO_2 nanoparticles at 400 °C for 3 h (Figure 3.7). The C 1s spectrum (Figure 3.7 A) could be fitted in to three chemically distinct components centering at 285.0 eV, 286.7 eV and 288.8 eV. Comparing with XPS spectra of C 1s from as synthesized TiO_2 nanoparticle, the lower binding energy component at 282.4 eV disappears after calcination, suggesting the removal of proteins containing aromatic amino acids. The chemical component present at 285.0 eV could be attributed to the adventitious elemental carbon [47-48] existed in pure TiO_2 sample [49]. The higher binding energy C 1s component (286.7 eV) could be attributed to electron emission from carbons present in proteins, bound to the nanoparticles surface, which mainly consist of carbonyl groups (aldehydic or ketonic carbon) [43]. A close observation of FTIR spectra of calcined TiO_2 nanoparticles (discussed later) shows that even after calcination of biosynthesized TiO_2 nanoparticles at 400 °C, weak intensity of protein (amide-I and II) bands can be seen. Therefore, this successfully explains the origin of C 1s signal at 286.7 eV. The higher binding energy chemical component (288.8 eV)

could be attributed to carbon-doped TiO_2 sample [19, 27] that may be due to the diffusion of the carbon atoms during the thermal treatment. Further, the XPS spectra for N 1s core level (Figure 3.7 B) was fitted into two chemically distinct components centering at 400.0 eV and 403.2 eV, which could be attributed to the N-doped TiO_2 [50, 51] and formation of oxynitride [51b] respectively. Figure 3.7 D shows the XPS spectra from F 1s core level spectra recorded from the calcined sample of biosynthesized TiO_2 nanoparticles. The F 1s core level spectra could be fitted in two chemical components centering at 686.2 eV and 688.0 eV, which can be attributed to the F-containing molecules adsorbed on nanoparticle surface, while higher binding energy component can be attributed to the F atom doped in TiO_2 crystal lattice respectively [52]. Doping of F atoms in TiO_2 lattice (O-Ti-O) leads to the replacement of O-atom by F-atom (O-Ti-F). The doping of "N" "C" and "F" elements in TiO_2 lattice can again be confirmed by Ti 2p spectrum (Figure 3.7 C) recorded from calcined TiO_2, which could be deconvoluted in to one chemically distinct spin-orbit pair ($2p_{3/2}$) centering at 460.8 eV.

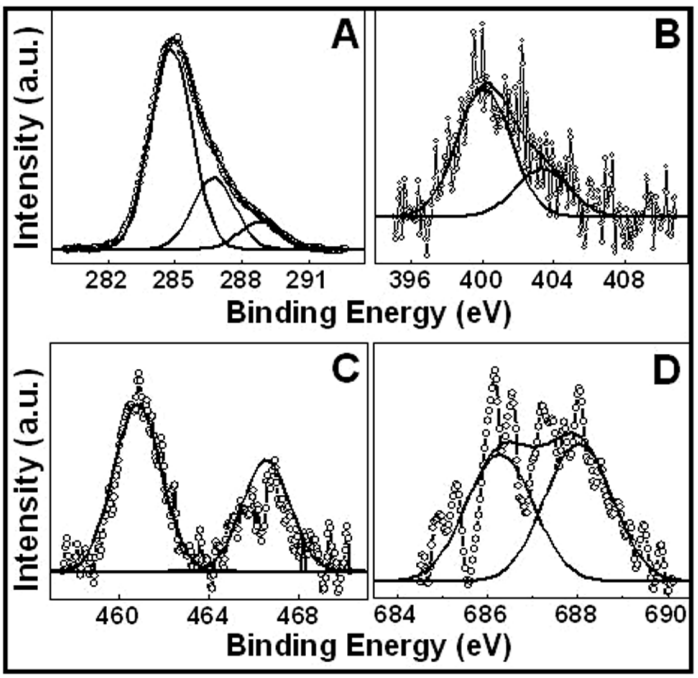

Figure 3.6: *XPS spectra of biosynthesized TiO_2 nanoparticles calcined at 400 ℃ for 3 h. The core level spectra recorded from C 1s (A), N 1s (B), Ti 2p (C) and F 1s (D). The raw data is shown in the form of symbols, while the chemically resolved components are shown as solid lines and details have been discussed in text.*

Thus an increase in binding energy (1.2 eV) as compared to pure TiO_2 was recorded which could be ascribed due to doping of F atoms in TiO_2 lattice. As mentioned earlier, the C 1s and N 1s XPS spectra indicate the possibility of doping in to TiO_2 lattice, while XPS spectra from Ti 2p indicate the possibility of "F" doping. To reconcile these apparently contradictory results, we propose that in the calcined sample all the three elements namely, "C", "N" and "F" are doped and amongst which "F" doping is dominant process. The Ti^{4+} experiences more electron withdrawing effect of "F" than the donating effects due to "C" and "N" doping partially explaining the shift in Ti 2p binding energy towards higher binding energy side. However, further detailed experiments are needed to confirm these results. Well-established reports indicate that N and F co-doped TiO_2 particles display enhanced visible light photocatalytic activity and higher absorption than individually N or F doped TiO_2 particles [52]. Thus, it can be concluded from XRD pattern and XPS spectra of calcined samples of biosynthesized TiO_2 nanoparticles that the calcination results in doping of certain non metallic ("C" "N" and "F") atoms into TiO_2 crystal lattice.

3.2.6 UV-visible spectroscopic analysis

The doping of C and N elements was further supported by UV-visible spectra (Figure 3.8) recorded from as synthesized (curve-1) as well as calcined (curve-2) samples of biosynthesized TiO_2 nanoparticles. UV-vis spectra from as synthesized TiO_2 nanoparticles show absorbance below 380 nm (UV-region), which corresponds to the band gap of 3.3 eV (curve-1), characteristic of brookite phase [12 b] of TiO_2, which is supported by XRD pattern from as synthesized TiO_2 nanoparticles (curve-1). However, calcination at 400 ºC for 3 h results in the enhanced absorbance in UV region and throughout the visible region (curve-2), corresponding to the band gap of 2.64 eV. Therefore a total red shift of 0.7 eV was recorded in the band gap of TiO_2, which could be attributed to the co-doping of C, N and F atoms in TiO_2 lattice. Biomolecules present as nanoparticle capping would probably act as source of C and N atoms while for F atoms unhydrolysed TiF_6^{2-} ions would act as suitable source. These atoms would entrap within the TiO_2 structure and finally get doped within TiO_2 lattice during calcination. Thus, it can be said that co-doping of "C," "N" and "F" atoms results in narrowing of band gap and thereby tuning the absorbance towards

visible region, thus enhancing the photocatalytic activity of TiO_2 nanoparticles in the visible-light region [53].

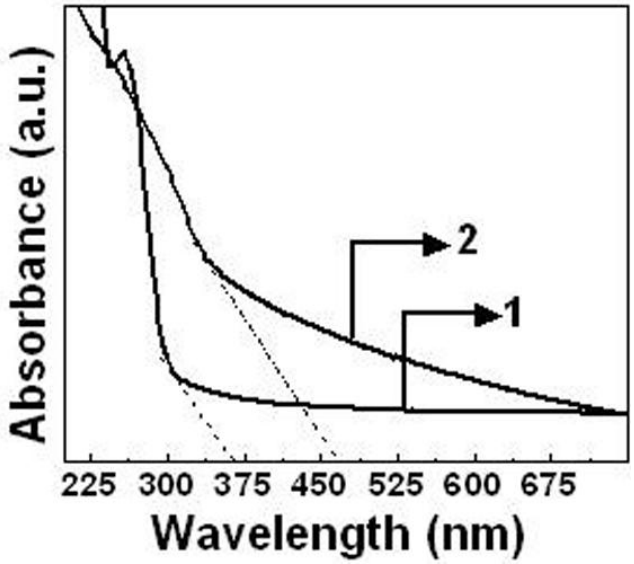

Figure 3.7: *UV-visible spectra recorded from as synthesized TiO_2 nanoparticles (curve-1) and after their calcination at 400 ºC for 3 h (curve-2). The dashed line (curve-1) and dotted line (curve-2) represents the tangents drawn to find out the respective band gap energies.*

3.2.7 FTIR and SDS-PAGE analysis

Figure 3.8 A and B show the FTIR spectrum of TiO_2 nanoparticles synthesized extracellularly by *Actinobacter* spp. In Figure 3.8 A, curve-2 and curve-3 represent the FTIR spectra recorded respectively from as synthesized and calcined (400 °C for 3 h) sample of TiO_2.

The FTIR spectra (Figure 3.8 A and B) were recorded from the bio-transformed reaction products obtained after 48 h of reaction between *Actinobacter* spp. and K_2TiF_6. In the as synthesized TiO_2 nanoparticle sample, clear transmittance peaks at 617 cm^{-1} and 1130 cm^{-1} (Figure 3.8 A, curve-2) were observed which have been referred to the excitation of Ti-O-Ti vibrational modes in the as prepared TiO_2 nanoparticles [54]. These peaks are absent in the spectra (Figure 3.8 A, curve-1) recorded from metal salt precursor (K_2TiF_6). The peak present at 918 cm^{-1} (Figure 3.8 A, curve-2) is due to antisymmetric stretching of Ti-O bonds in Ti-O-Ti [54]. All these three peaks become very intense after calcination (curve-3) suggesting that calcination improves the crystallinity of TiO_2 nanoparticles. This result is in accordance with the changes in SAED pattern of calcined TiO_2 nanoparticles. The

curve-1 in Figure A was recorded from metal salt precursor (K_2TiF_6), which does not show any Ti-O vibration band characteristic to TiO_2. Apart from these, a strong transmittance peak at 1650 cm^{-1} (Figure 3.8 B, curve-2) could be attributed to the combination of amide-I and II bands. The appearance of amide-I and II bands suggest the presence of proteins in as prepared TiO_2 nanoparticles suspension. Dampening in the intensity of these bands (I and II) has been observed in spectra recorded from the calcined sample (Figure 3.8 B, curve-2), which can be attributed to the removal of proteins from the sample except capping proteins. This analysis suggests that proteins are associated with the surface of TiO_2 nanoparticles.

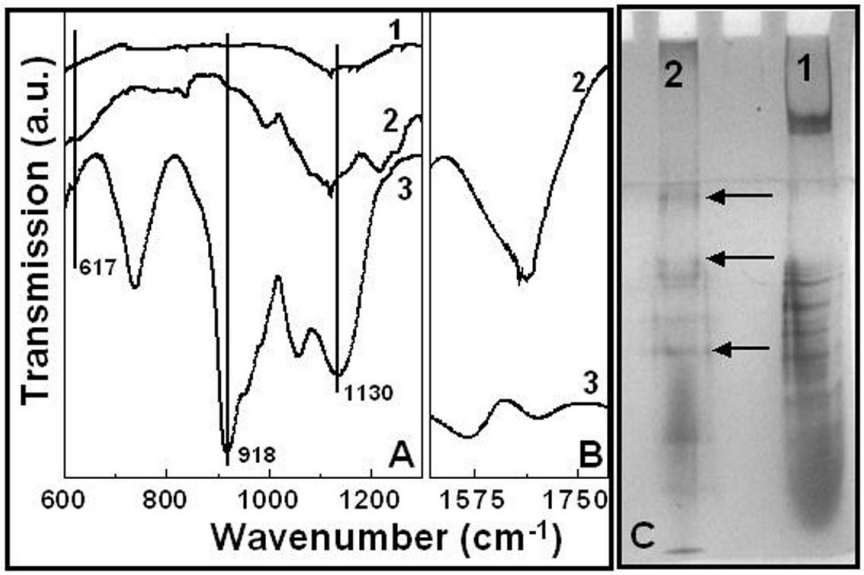

Figure 3.8: *FTIR spectra (A) recorded from as synthesized TiO_2 nanoparticles (curve-2) after 48 h of incubation with Actinobacter spp. and after calcination (curve-3) of as synthesized TiO_2 nanoparticles at 400 ℃ for 3 h. Curve-1 represents the FTIR spectra recorded from metal oxide precursor K_2TiF_6. Solid lines indicate the characteristic vibrations of TiO_2. Signatures of amide-I and amide-II bands in FTIR spectra of as synthesized (Figure B, curve-2) and calcined (Figure B, curve-3) TiO_2 nanoparticles. Silver stained SDS-PAGE pattern (Figure C) showing the extracellular protein profile of Actinobacter spp. on 12 % resolving gel. Lane-1and 3 respectively corresponds to extracellular protein profile of Actinobacter spp. in absence and presence of K_2TiF_6 salt and the extra proteins overexpressed in lane-2 are marked by arrows.*

Figure 3.8 C shows the SDS-PAGE pattern exhibiting the extracellular protein profile obtained from the culture supernatant of *Actinobacter* spp. in absence (lane-1) and presence (lane-2) of K_2TiF_6. Addition of K_2TiF_6 to *Actinobacter* spp. culture was seen to induce the release of new protein/s. On comparing with control (lane-1), it can be clearly observed that there are three newly overexpressed proteins (marked by

arrows). Thus, from SDS-PAGE pattern, it can be concluded that these three overexpressed proteins could have participated in nanoparticle synthesis and capping.

3.3 Biosynthesis of nanocrystalline ZnO using *Actinobacter* spp.

This part of the chapter describes the extracellular bacterial synthesis of ZnO nanoparticles at room temperature. The experimental reaction product was analyzed by different characterization techniques such as TEM, XRD, XPS, and FTIR etc. Preliminary information about the proteins, secreted by *Actinobacter* spp. involved in nanoparticle synthesis and capping has also been presented.

3.3.1 Experimental Details

While keeping all the experimental and culture conditions etc. very similar to those as explained under 3.2.1 section of this chapter, the reaction between bacterial biomass and $Zn(CH_3COO)_2$ was carried out for a period of 48 h. The so obtained culture supernatant was further analyzed for the presence of ZnO nanoparticles using different characterization techniques such as TEM, XRD, FTIR, XPS and HRTEM etc. and this is discussed in their respective sections of this chapter. Two control experiment were also performed; in one case the biomass alone was tested to the presence of ZnO particles, in second, pure zinc acetate (10^{-3} M), kept in solution form without adding bacterial biomass for same period of time and at same conditions was tested for the formation of ZnO nanoparticles. To identify the bacterial protein(s) responsible for hydrolysis of the aqueous $Zn(CH_3COO)_2$ into ZnO nanoparticles and it's capping, the extracellular protein profile of the bacterial culture supernatant was checked for the induction of new protein/s upon $Zn(CH_3COO)_2$ addition. The rest experimental procedure was followed very similar to as described in Part-1 of this chapter.

3.3.2 TEM, HRTEM and EDX analysis

TEM images of ZnO nanoparticles synthesized by *Actinobacter* spp. after 48 h of incubation with $Zn(CH_3COO)_2$ shows a thick population of ZnO nanoparticles (Figure 3.9 A and B) in purified as synthesized sample. The particles ranging from 4 to 10 nm in size were obtained. Particle size distribution was calculated from 100

nanoparticles, showing average particle size ~7.0 nm (Figure 3.10 A). Selected area electron diffraction (SAED) from as synthesized ZnO nanoparticles (Figure 3.9 C) shows clear diffraction spots, suggesting the crystalline nature of particles. The diffraction spots were indexed for [101], [102], [103], [104] and [201] crystal planes of wurtzite polymorph of ZnO [55].

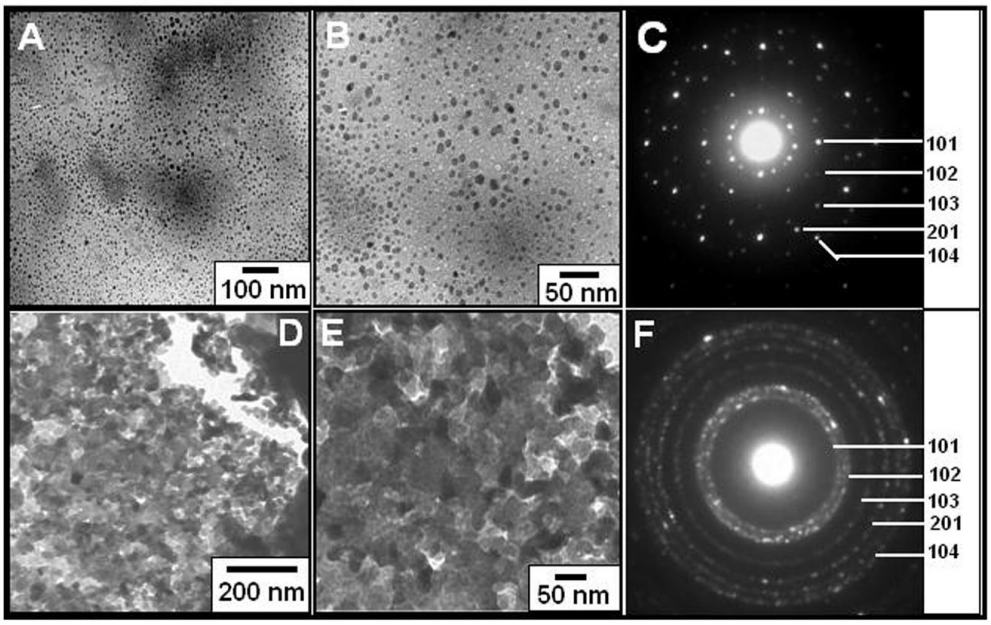

Figure 3.9: *TEM images of as synthesized (A and B) ZnO nanoparticles after 48 h of reaction between Actinobacter spp. and $Zn(CH_3COO)_2$ mixture. SAED pattern (C) shows the crystalline nature of as synthesized particles. Calcination of as synthesized nanoparticles (D and E) leads to the formation of aggregates of particles and SAED pattern (F) could be indexed on the basis of wurtzite phase of ZnO.*

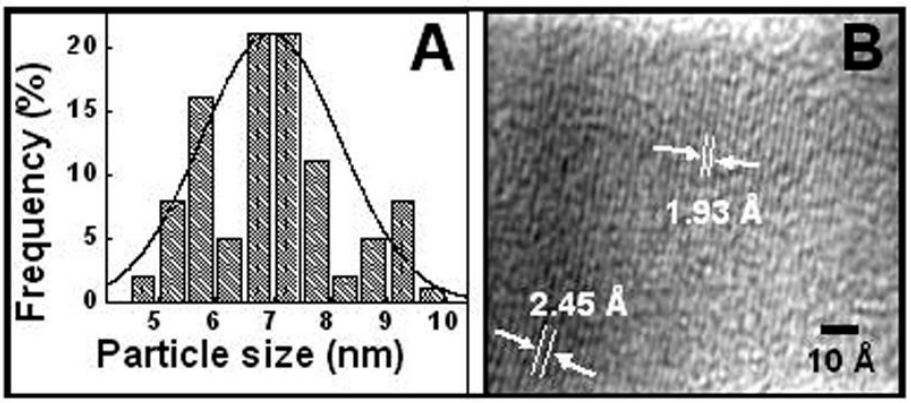

Figure 3.10: *Particle size distribution (A) of as synthesized ZnO nanoparticles after 48 h of reaction between Actinobacter spp. and $Zn(CH_3COO)_2$ mixture, showing average particle size 7.0 nm. HRTEM images (B) of as synthesized ZnO nanoparticles show the lattice spacings matching with wurtzite ZnO.*

As it has been observed many times earlier that proteins cap the as synthesized particles and calcination at 400 °C for 3 h burns the excess proteins present in the form of matrix. TEM images of calcined ZnO nanoparticles (Figure 3.9 D and E) show aggregates of nanoparticles in the form of clusters. Calcination burns the capping proteins and aggregation is observed due to the loss. Therefore, in Figure D and E particles are not very well dispersed and reveal flake like structures of ~50 nm size (Figure 3.9 E). SAED pattern from calcined ZnO nanoparticle (Figure 3.9 F) sample shows clear ring pattern, indexed again based on wurtzite phase of ZnO. These ring patterns were referred for [101], [102], [103], [104] and [201] crystal planes, which matches well with the reported values [55]. HRTEM image (Figure 3.10 B) of as synthesized ZnO nanoparticles show lattice spacings of 1.93 Å and 2.45 Å, matching well with the wurtzite phase of ZnO (1.91 Å and 2.47 Å) for [102] and [101] planes respectively [55].

3.3.3 X-ray diffraction analysis

Figure 3.11 represents the XRD measurements on dried powders of as synthesized (curve-1) and calcined (curve-2) sample of ZnO nanoparticles synthesized by *Actinobacter* spp. after 48 h of exposure with $Zn(CH_3COO)_2$.

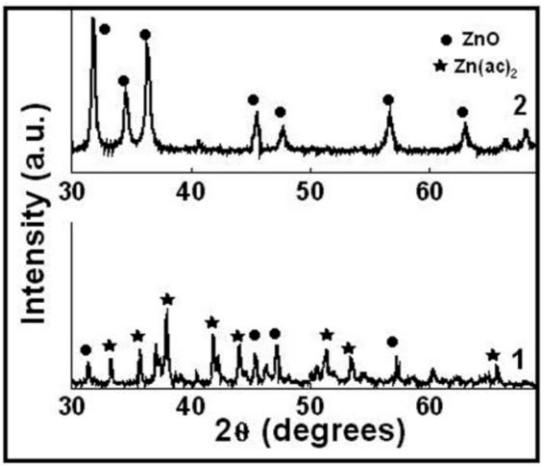

Figure 3.11: *XRD patterns recorded from ZnO nanoparticles after 48 h of incubation of Actinobacter spp. with $Zn(CH_3COO)_2$. The as synthesized sample (curve-1) and calcined (curve-2) samples show the characteristic Bragg's reflection of wurtzite phase of ZnO (indicated by (•). Spectra from as synthesized ZnO nanoparticles show the presence of some unhydrolysed $Zn(CH_3COO)_2$ (indicated by ★) signature as well.*

Characteristic Bragg's diffraction pattern for wurtzite phase of ZnO was recorded and marked by (•). The XRD pattern from as synthesized sample shows several Bragg's reflection identified for zinc acetate (indicated by ★) and ZnO nanoparticles (indicated by •). The zinc acetate impurity was removed from as synthesized sample by dialysis followed by lyophilization and calcination (at 400 °C for 3 h). After purification and calcination as synthesized sample show characteristic crystal planes [100], [002], [102], [110], [103], [112] and [201] for ZnO which match well with the reported values [55].

3.3.4 X-ray Photo-electron Spectroscopy

The synthesis of ZnO nanoparticles by *Actinobacter* spp. was further confirmed by XPS, a sensitive technique, to the oxidation state of elements present in the sample.

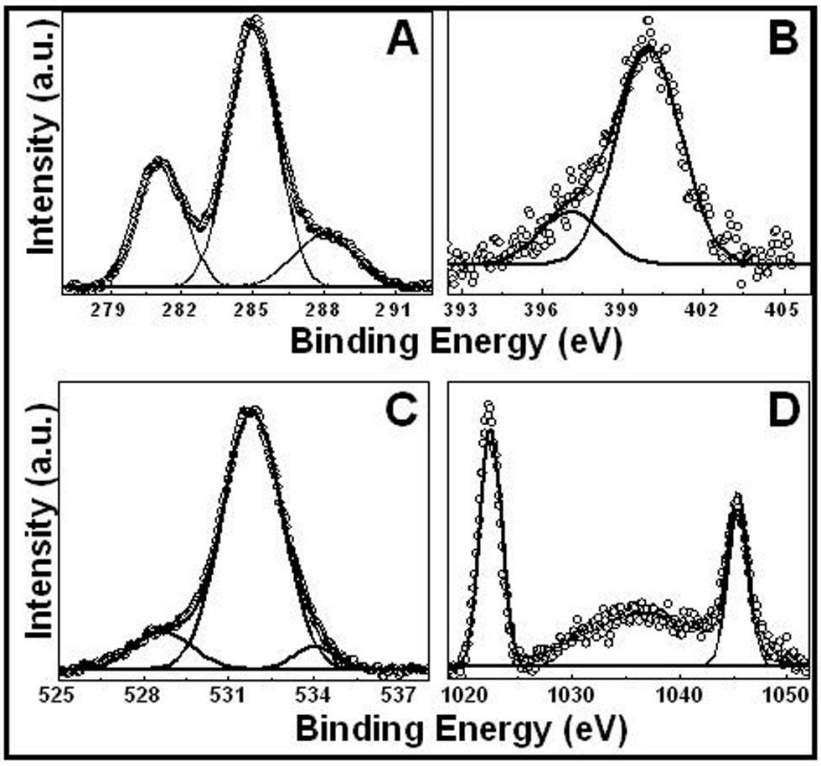

Figure 3.12: *XPS spectra of biosynthesized ZnO nanoparticles synthesized by reaction between Actinobacter spp. and $Zn(CH_3COO)_2$ for 48 h. The core level spectra recorded from C 1s (A), O 1s (B), N 1s (C) and Zn 2p (D). The raw data is shown in the form of symbols, while the chemically resolved components are shown as solid lines and details have been discussed in text.*

Figure 3.12 represents the XPS spectra recorded from as synthesized ZnO nanoparticles. The spectra were recorded for different elements such as C 1s, N 1s, O 1s and Zn 2p. The core level binding energies were aligned with the adventitious carbon binding energy of 285.0 eV. The XPS spectra of C 1s (Figure 3.12 A) could be fitted in to three components centering at 281.0 eV, 285.0 eV and 288.0 eV which could be attributed respectively to the aromatic carbon present in amino acids from proteins bound to the surface of ZnO [42], carbons in carbonyl groups (aldehydic or ketonic carbon) [43] and from adventitious carbon present in the sample. The N 1s core level spectra (Figure 3.12 B) could be fitted into two chemically distinct components centering at 397.0 eV and 400.0 eV. The lower binding energy component could be attributed to nitrogen in iminic (C=N) groups, while higher binding energy component can be attributed to amidic (peptidic) nitrogen in the capping proteins [56]. The O 1s core level spectra (Figure 3.12 C) could be fitted into three distinct components centering at 528.6 eV, 531.7 eV and 533.9 eV. The lower binding energy component could be assigned to the signals coming from surface proteins and free oxygen. The other components at 531.7 eV and 533.9 eV correspond to O^{2-} ions in ZnO and OH groups at ZnO surface [57].

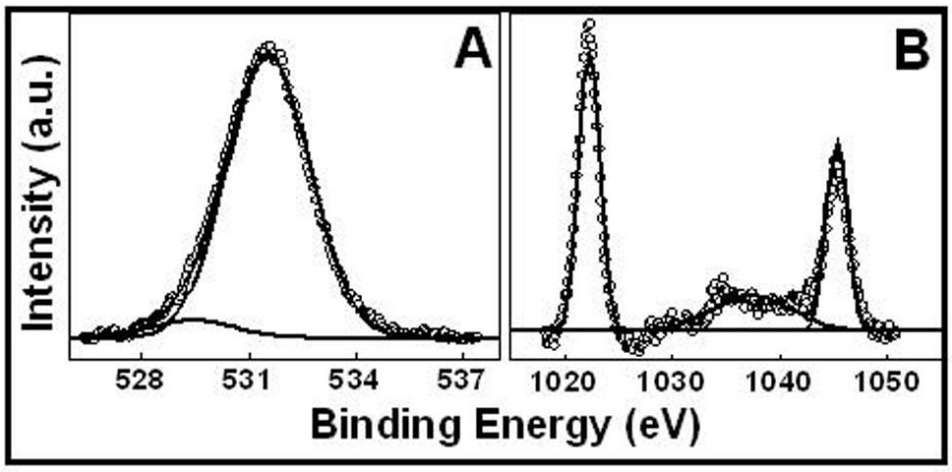

Figure 3.13: *XPS spectra of calcined sample of biosynthesized ZnO nanoparticles synthesized by reaction between Actinobacter spp. and $Zn(CH_3COO)_2$ for 48 h. The core level spectra recorded from O 1s (A) and Zn 2p (B). The raw data is shown in the form of symbols, while the chemically resolved components are shown as solid lines and details have been discussed in text.*

Further, the XPS spectra for Zn 2p core level (Figure 3.12 D) was also fitted in to one spin-orbit pair where Zn $2p_{3/2}$ and Zn $2p_{1/2}$ peak positions were centered at

1022.2 eV and 1045.2 eV (spin-orbit splitting 23.0 eV) respectively, matching well with the reported values for ZnO [58]. Thus, XPS result strengthens our findings for extracellular synthesis of ZnO nanoparticles from *Actinobacter* spp. The binding energy signal of Zn^{+} ions (from zinc acetate) has been reported to be at 1021.4 eV. This is very close to Zn signal from ZnO (1021.7) and due to the low resolution of instrument the presence of unhydrolysed Zn^{2+} ions probably could not be detected.

Further, XPS spectra were recorded from calcined sample of bio synthesized ZnO nanoparticles (Figure 3.13). The O 1s spectra (Figure 3.13 A) could be fitted into two components centering at 529.3 eV and 531.5 eV. The lower and higher binding energy components could be again attributed to the free oxygen and O^{2-} ions in ZnO respectively [57]. The absence of any peak at 533.9 eV suggests probable removal of OH group upon calcination. The Zn 2p core level spectra (Figure 3.13 B) were fitted into one spin-orbit pair centering at 1022.2 eV and 1045.2 eV (spin-orbit splitting 23.0 eV) for Zn $2p_{3/2}$ and Zn $2p_{1/2}$ in ZnO respectively.

3.3.5 UV-visible spectroscopic analysis

The synthesis of ZnO nanoparticles by the use of *Actinobacter* spp. was further confirmed by UV-visible spectra. Figure 3.15 show the UV-visible spectrum (Figure 3.14) recorded from as synthesized (curve-2), calcined sample (curve-3) and zinc acetate (curve-1). The bacterial cell supernatant after 48 h of exposure to $Zn(CH_3COO)_2$ shows the presence of a broad absorbance ranging from 315 nm to 365 nm (curve-2) whereas the calcined sample shows a clear absorbance band centering at 365 nm (curve-3), characteristic for ZnO nanoparticles [52]. This absorbance is absent (curve-1) in the UV-vis spectra recorded from $Zn(CH_3COO)_2$ (precursor), suggesting the formation of ZnO nanoparticles due to the reaction of bacterial proteins/enzymes with precursor. Presence of broad absorbance bands in case of as synthesized ZnO nanoparticle could be assigned to the presence of varying size distribution of nanoparticles, which could be seen in TEM images (Figure 3.9 A and B). Bulk ZnO shows the absorbance at around 383 nm due to its wide band gap (3.34 eV), whereas ZnO in form of nanoparticles show blue shift in absorbance due to the

increase of its band gap. The as synthesized as well as calcined ZnO nanoparticles show clear absorbance in blue region than bulk ZnO.

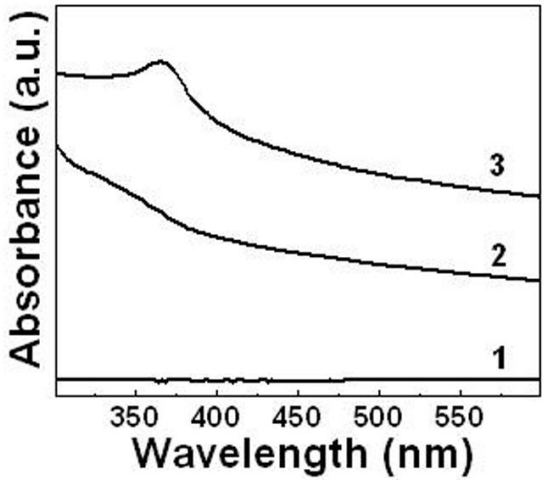

Figure 3.14: *UV-visible spectra recorded from as synthesized ZnO nanoparticles (curve-2) and after their calcination at 400 ºC for 3 h (curve-3) showing characteristic absorbance for ZnO nanoparticles. The spectra from salt precursor (zinc acetate) showing absence of any such absorbance (curve-1).*

3.3.6 FTIR and SDS-PAGE analysis

FTIR spectra recorded from ZnO nanoparticles synthesized by *Actinobacter* spp. after 48h of reaction with $Zn(CH_3COO)_2$ have been shown in Figure 3.15 A and B. Presence of characteristic Zn-O bond streching signal below 600 cm^{-1} in as synthesized (curve-2) and calcined (curve-3) again confirms our assertion of ZnO nanoparticle formation [60]. A broad transmittance peak seen in the spectra of as synthesized sample (curve-2) at 550 cm^{-1} becomes more intense and clear after calcination (curve-3). We believe that the enhancement in crystallinity with calcination involves the loss of amorphous proteins precipitated along with the particles. The FTIR spectra recorded from $Zn(CH_3COO)_2$ salt precursor (curve-1) do not show any signature for Zn-O bond vibrations suggesting that the transmittance signal at 550 cm^{-1} is due to ZnO. Further, the presence of proteins on nanoparticle surface was identified by FTIR (Figure 3.15 B). Presence of a broad transmittance peak centering at 1650 cm^{-1}, could be attributed to the combination of amide-I and II band signals from capping proteins. These bands disappear after calcination (curve-2) suggesting the loss of capping proteins. In order to get more knowledge about the over expressed proteins responsible for metal ion reduction, proteins form bacterial

cell supernatant were isolated, lyophilized and SDS-PAGE was performed (Figure 3.15 C) with standard molecular weight marker (lane-M). The proteins synthesized by *Actinobacter* spp. in absence (lane-C) and presence of $Zn(CH_3COO)_2$ (lane-T) were compared and an overexpression of proteins having molecular weights of ~ 10 and ~ 15 kDa (marked by arrows in lane-T) was observed. These low molecular weight proteins could be considered as responsible cause for nanoparticle synthesis and capping. Therefore, it can be concluded that bacteria under ionic stress conditions, secrete some extra proteins, having molecular weights of around 10 and 15 kDa, which subsequently try to nullify this adverse environment by changing the toxic form of ionic precursors in to insoluble oxide form and precipitate it.

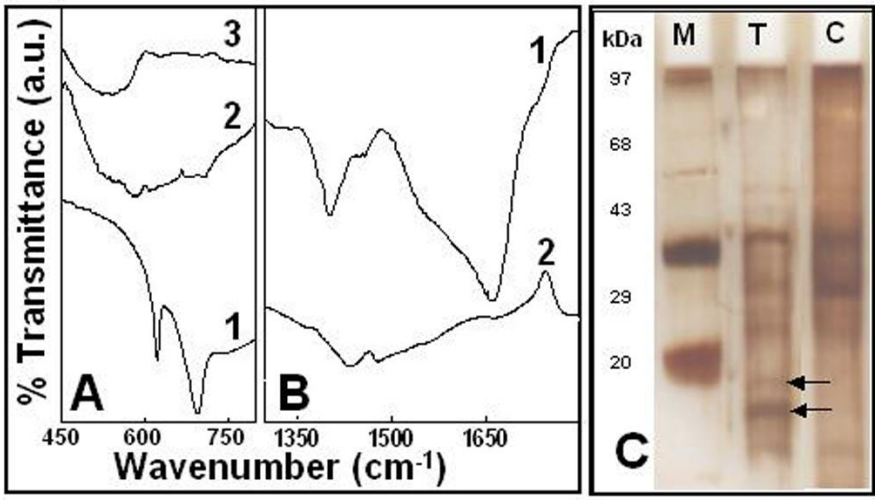

Figure 3.15: *FTIR spectra (A) recorded from as synthesized ZnO nanoparticles (curve-2) after 48 h of incubation with Actinobacter spp. and after calcination (curve-3) at 400 ℃ for 3 h. Curve-1, represents FTIR spectra recorded from metal salt precursor $Zn(CH_3COO)_2$. Figure B, Curve-1 and 2 represents the FTIR spectra recorded from as synthesized and calcined sample of ZnO. Silver stained SDS-PAGE pattern (Figure C) showing the extracellular protein profile of Actinobacter spp. on 12% resolving gel. Lane-C and T respectively corresponds to extracellular protein profile of Actinobacter spp. in absence and presence of $Zn(CH_3COO)_2$ salt and the extra proteins overexpressed in lane-T are marked by arrows.*

3.4 Photocatalytic Application of Biosynthesized TiO_2 and ZnO Nanoparticles

3.4.1 Experimental Details

The synthesis processes of TiO_2 and ZnO nanoparticles by *Actinobacter* spp. have been described in previous sections (part-1 and 2) of this chapter in detail. The

as synthesized nanoparticles contain excess biomolecules in their suspensions. Therefore, in order to enhance the crystallinity of biosynthesized TiO_2 and ZnO, the particles were centrifuged at 15000 rpm for 30 min. followed by calcination of so obtained pellets at 400 ºC for 3 h. The crystalline samples of respective oxides have been well characterized by TEM, FTIR, XRD XPS and UV-vis spectroscopy (described in earlier parts of this chapter). For the study of photocatalytic activity of these biosynthesized TiO_2 and ZnO nanoparticles for degradation of dye (Methylene Blue), different concentrations (0 M, 10^{-3} M and 10^{-4} M) of the sample (TiO_2 and ZnO) were taken with 10^{-5} M concentration of methylene blue (MB). This reaction setup was kept in three different light conditions (dark, sunlight and UV-light). All the reactions were performed in quartz tubes. For UV light exposure, reactions were performed in the home-made photocatalytic reactor and illuminated with a UV lamp source (400 Watts, emission maxima 280 nm, Hanovia, USA) at a distance of 20 cm and for solar light exposure, experiments were performed on a bright sunny day (~ 38 ºC) in an open space between 09:00 to 16:00 hours. The MB degradation during the course of reaction (30 min, 60 min, 90 min, 120 min, 150 min, 180 min and 210 min) was followed by recording its optical absorbance maxima at 664 nm, while establishing a baseline data set with MB solutions exposed directly to various light conditions without addition of any TiO_2 or ZnO. The optical absorbance of dye during the reaction was monitored using Jasco dual beam UV–vis–NIR spectrophotometer. The extent of dye degradation was calculated by the following equation:

$$\% \text{ Discoloration} = \frac{[(\text{Initial Absorbance}) - (\text{Absorbance After Treatment})]}{\text{Initial Absorbance}} \times 100$$

3.4.2 Photodegradation of Methylene blue

Several reports illustrating the mechanism of MB degradation suggest that such a blue-shifted absorption characteristic of N-demethylated derivative(s) of MB (Figure 3.16) is observed. A mixture of N-demethylated analogs of MB broadens the absorption spectra in the visible region. Absorption bands at 654–648nm (irradiation time, 20–30 min), at 620 nm (irradiation time, 60 min), and at 615 nm (irradiation time 90 min) are due to Azure B (AB), Azure A (AA) and Azure C (AC) formation respectively [36].

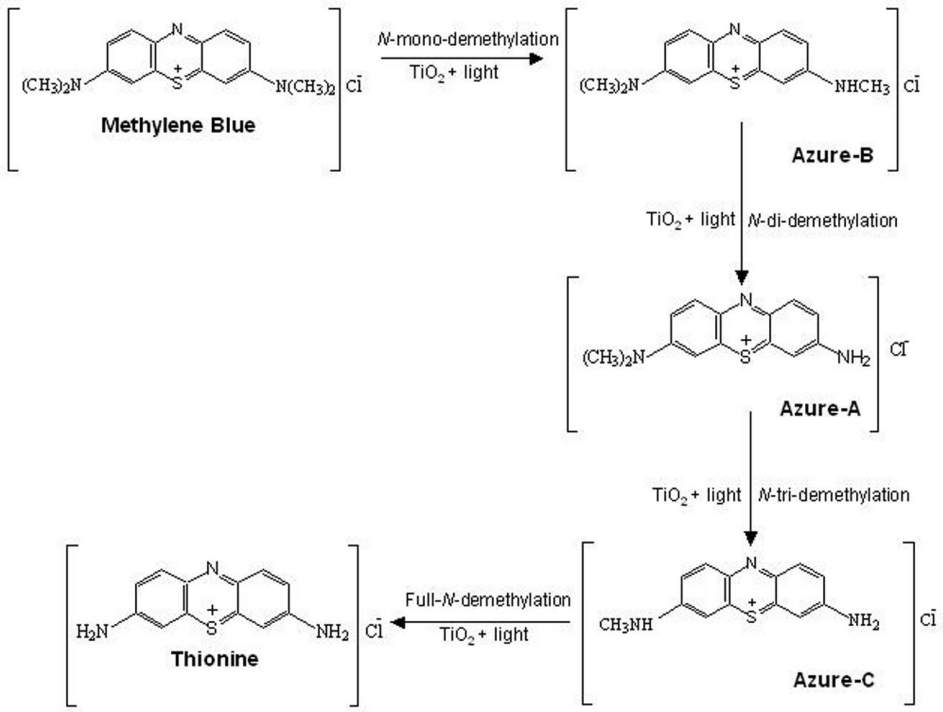

Figure 3.16: *Flowchart showing the mechanism of MB degradation with various levels of N-demethylation and their corresponding structures under the illumination of sunlight and presence of B-TiO2 nanoparticles.*

The photodegradation of MB by biosynthesized TiO_2 (B-TiO_2) nanoparticles under different light conditions has been shown in Figure 3.17. Extent of MB degradation was estimated from absorbance spectra as intact MB shows strong absorbance at 664 nm. Loss of intensity at 664 nm and shift in this peak position was considered as degradation of MB. Under dark conditions, little decrease in intensity of peak at 664 nm was observed and the extent of degradation was found to be same without (Figure 3.17 A) and with (Figure 3.17 B) TiO_2 nanoparticles.

But no shift in absorbance at 664 nm was recorded in either case. When the mixture of TiO_2 nanoparticles and MB was exposed to UV-light, almost complete decomposition of MB was recorded by 240 min of exposure (D). However, little degradation in MB was found when it was exposed to UV-light without TiO_2 nanoparticles (Figure 3.17 C). In this case, the absorbance of MB shows blue shift (from 664 nm to 615 nm) as well as decrease in intensity of MB absorbance. Interesting results were obtained when TiO_2 and MB mixtures were exposed to

sunlight, rapid degradation of MB was recorded which showed complete degradation of MB within 90 min of sunlight exposure (Figure 3.17 F). Although, little decrease in intensity was recorded for MB under the exposure of UV light and sunlight without B-TiO_2 nanoparticles (Figure 3.17 C and E) but no shift in absorbance was recorded, suggesting the importance of TiO_2 as a photocatalyst.

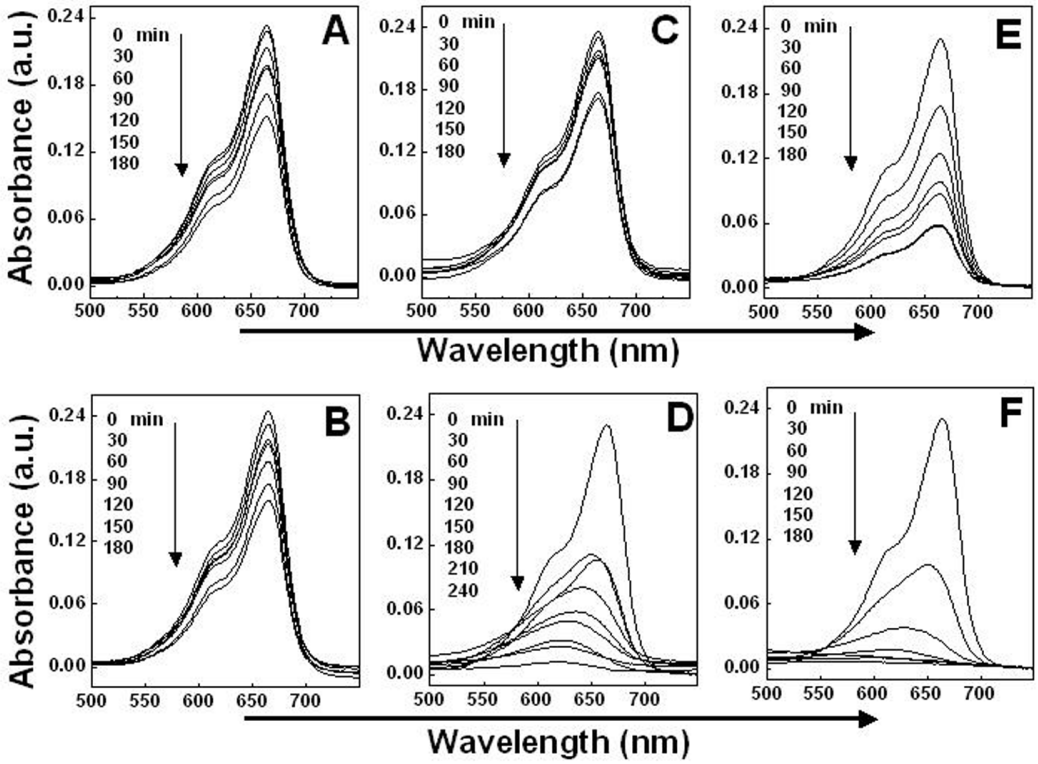

Figure 3.17: *UV-visible spectra of photocatalytically degraded methylene blue dye in different light conditions. A, C and E are MB solutions without TiO_2 nanoparticles, exposed for different time intervals to dark, UV-light and sunlight respectively. B, D and F are MB solutions with TiO_2 nanoparticles, exposed for different time intervals to dark, UV-light and sunlight respectively.*

Thus, it can be concluded that B-TiO_2 is an active photocatalyst for the degradation of MB under the exposure of UV-light as well as sunlight. Moreover, it is more effective under sunlight exposure. Similar to TiO_2, ZnO nanoparticles have also been employed for photcatalytic degradation of various pollutants such as phenol, textile dyes and methyl-orange etc [61]. We have further used biosynthesized ZnO (B-ZnO) nanoparticles for MB degradation under the similar experimental conditions as it was performed for TiO_2. MB treated with B-ZnO nanoparticles under dark conditions, showed negligible degradation (Figure 3.18 A and B) as neither significant change in intensity nor shift in absorbance was recorded.

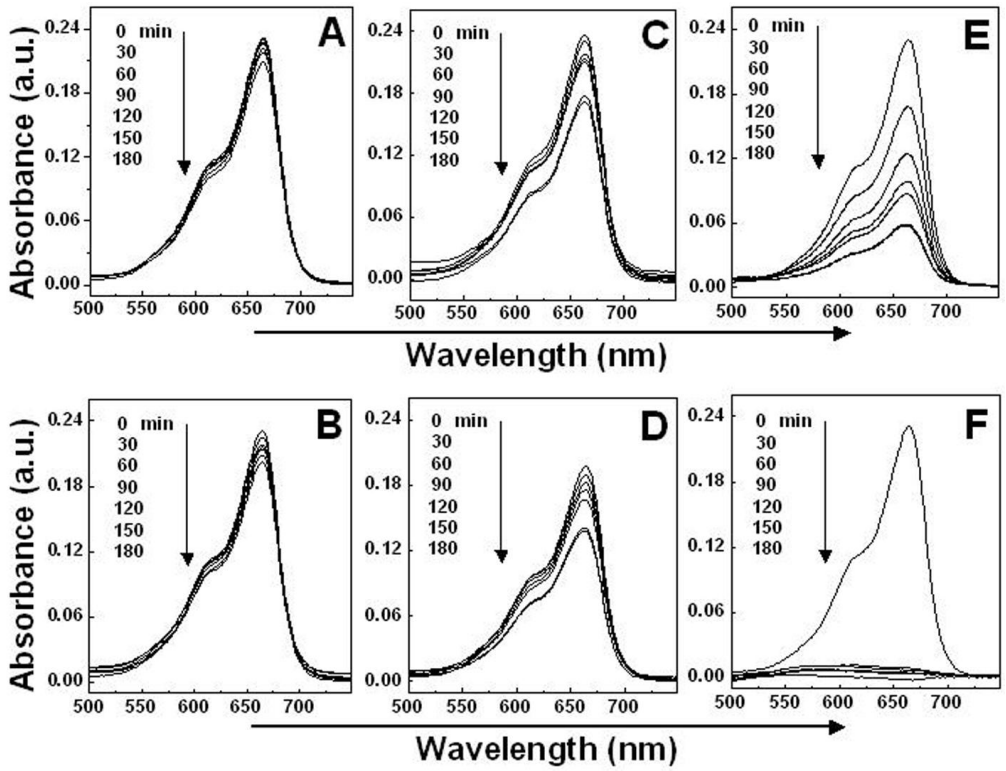

Figure 3.18: *UV-visible spectra of photocatalytically degraded methylene blue dye in different light conditions. A, C and E are MB solutions without ZnO nanoparticles, exposed for different time intervals to dark, UV-light and sunlight respectively. B, D and F are MB solutions with ZnO nanoparticles, exposed for different time intervals to dark, UV-light and sunlight respectively.*

Illumination of UV-light was also found to be ineffective to cause degradation of MB (Figure 3.18 C and D) as even after prolonged (180 min) exposure of UV-light, little degradation was recorded. In this case also, no shift in absorbance of MB was recorded. However, exposure of the mixture of ZnO and MB to sunlight resulted in complete degradation of MB within 30 min (Figure 3.18 E and F) and the solution becomes colorless. In this case the exposure of MB solution to sunlight alone showed decrease in intensity (more than under dark and UV-light exposure) but no shift in absorbance (Figure 3.18 E). The exposure of MB solution under sunlight with B-ZnO showed a rapid decrease in intensity as well as shift in absorbance (Figure 3.18 F). These experiments demonstrated that the presence of both ZnO and sunlight is essential for the degradation of MB.

We have discussed till now about the B-TiO_2 and B-ZnO mediated degradation of MB under different light conditions. A comparative analysis is discussed below, keeping in mind two important parameters:

1. Shift in MB absorbance
2. Decrease in intensity at 664 nm.

Based on these, it was observed that MB alone under dark condition shows no shift in absorbance (Figure 3.19 A, curve-1). Mixture of MB with B-TiO_2 under the exposure of UV-light (Figure 3.19 A, curve-2) shows a significant shift in absorbance from 664 to 615 nm by 240 min exposure. However, in the presence of sunlight the shift was more rapid and recorded from 664 nm to 601 nm within 120 min of exposure. Panel B shows the shift in absorbance of MB with B-ZnO under different light conditions. As the trend follows, MB alone did not show any shift in absorbance (Figure 3.19 B, curve-1). Similarly in the presence of ZnO and UV light the degradation of MB did not result in any significant shift (Figure 3.19 B, curve-2). Interestingly, when the mixture of MB and B-ZnO exposed to sunlight showed a shift from 664 to 565 nm within 180 min. In the following we present a comparison of degradation effects of B-TiO_2 and B-ZnO under different light conditions (Figure 3.20). In sunlight B-ZnO shows a shift in MB absorbance (54 nm) within 30 min of exposure while B-TiO_2 treatment reveals a small shift (15 nm) in this time.

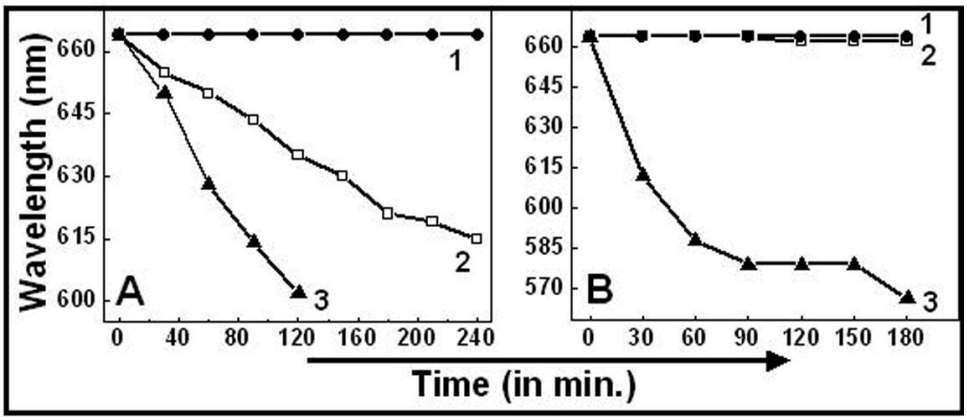

Figure 3.19: *Shift in absorbance of MB (from 664 nm) in different light conditions. Figure A represents the shift in absorbance of MB mixed with B-TiO_2 nanoparticles and exposed to sunlight (curve-3), UV-light (curve-2) and dark (curve-1). Figure B represents the shift in absorbance of MB mixed with B-ZnO nanoparticles and exposed to sunlight (curve-3), UV-light (curve-2) and dark (curve-1).*

As the exposure time is increased (120 min), B-ZnO particles proceed to show a shift of 86 nm in MB absorbance while in B-TiO_2 case a shift of only 64 nm is seen. The B-ZnO exposure ended in a shift of 99 nm whilst the B-TiO_2 treatment left the 64 nm shift constant. In terms of decrease in intensity under UV-light B-TiO_2 leads to a

degradation of 54 %, while in B-ZnO case it is only 20 %. On the other hand, in presence of sunlight, B-ZnO shows a decomposition capacity of >96 %, while in B-TiO_2 it remains at 64 % by the end of 30 min.

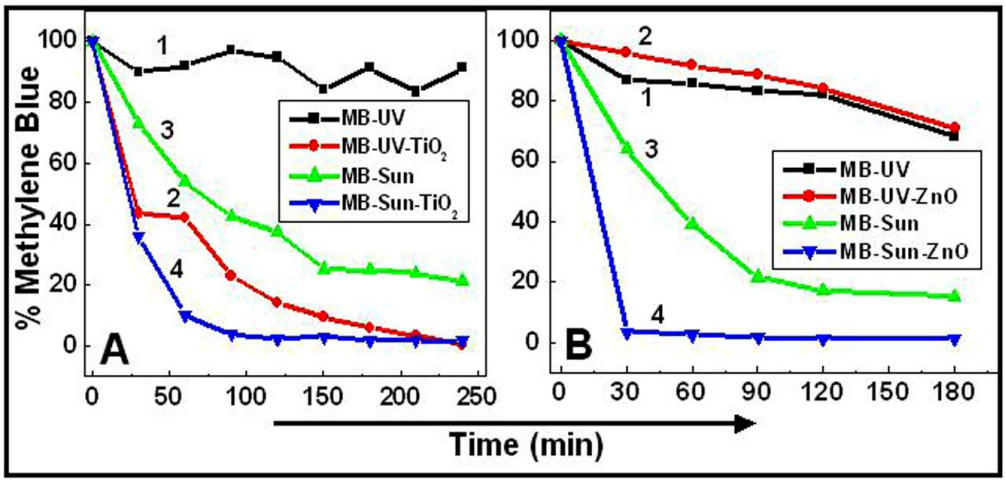

Figure 3.20: *Curves showing % degradation of MB in different light conditions. Figure A (curve-1 and 2) show the MB solutions exposed to UV-light without and with B-TiO_2 nanoparticles, whereas curve-3 and 4 show the MB degradation profile exposed to sunlight, without and with B-TiO_2 nanoparticles respectively. Figure B (curve-1 and 2) show % MB degradation under UV-light, without and with B-ZnO nanoparticles respectively, whereas curve-3 and 4 show the MB degradation profile when exposed to sunlight without and with B-ZnO nanoparticles respectively.*

Thus it can be concluded that in UV-light B-TiO_2 is a better photocatalyst, while B-ZnO does not show any activity in these conditions. In sunlight, though B-TiO_2 shows a better activity as compared to its activity in UV-light, B-ZnO becomes far more active and even out performs B-TiO_2 under these conditions.

3.5. Conclusions

This chapter illustrates a bacterium (Gram-positive) mediated approach for TiO_2 and ZnO nanoparticle synthesis under ambient conditions. The so synthesized particles were below 10 nm in diameter. As a mechanism, it could be hypothesized that the metal ion stressed *Actinobacter* spp. overexpresses certain proteins/enzymes that while trying to minimize the stress convert these ions into their more insoluble oxide counterpart. Proteins are also involved in capping and thereby prevent the particle from further growth. Calcination results in improvement of material crystallinity, which might be due to the loss of amorphous proteins precipititated along with the particles. Calcination of B-TiO_2 nanoparticles seems to suggest the

possible doping of non-metallic elements (C, N and F) that show shift in absorbance from UV region to towards visible region due to their band gap narrowing effect. This property results in sunlight induced photocatalytic degradation of MB dye where B-TiO_2 nanoparticles showed a comparatively enhanced rate of MB degradation under sunlight than UV light. On the other hand B-ZnO nanoparticles were also found to be more photocatalytically active under sunlight even when compared to the above B-TiO_2 system. The enhanced MB degradation activity of B-ZnO nanoparticles under sunlight illumination can be correlated with its strong absorbance (365 nm) close to the visible region of electromagnetic spectrum (Figure 3.14, curve-2). In short, the simple method described here successfully demonstrates the production of TiO_2 and ZnO nanomaterials that may probably be used in multiple applications of nanotechnology.

3.6 References

[1] (a) Schmid, G. *Nanoparticles: From Theory to Application*; Wiley- VCH, Weinheim,

2004. (b) Klabunde, K. J. *Nanoscale Materials in Chemistry*; Wiley-Interscience, New York **2001**. (c) Joo, J.; Yu, T.; Kim, Y. -W.; Park, H. M.; Wu, F.; Zhang, J. Z.; Hyeon, T. *J. Am. Chem. Soc*. **2003**, *125*, 6553. (d) Hyeon, T.; Lee, S. S.; Park, J.; Chung, Y.; Na, H. B. *J. Am. Chem. Soc*. **2001**, *123*, 12798.

[2] Rao, C. N. R.; Raveau, B. *Transition metal oxides*; VCH: New York **1995**.

[3] (a) O'Regan, B.; GrKtzel, M. *Nature* **1991**, *353*, 737. (b) Stergiopoulos, T.; Arabatzis,

I. M.; Katsaros, G.; Falaras, P. *Nano Lett*. **2002**, *2*, 1259.

[4] (a) Tang, J.; Wu, Y.; McFarland, E. W.; Stucky, G. D. *Chem. Commun*. **2004**, *14*, 1670. (b) Cho, Y.; Choi, W.; Lee, C.-H.; Hyeon, T.; Lee, H.-I. *Environ. Sci. Technol*.

2001, *35*, 2988.

[5] Luchi, K., Ohko, Y.; Tatsuma, T.; Fujishima, A. *Chem. Mater*. **2004**, *16*, 1165.

[6] Corma, A. *Chem. Rev*. **1997**, *97*, 2373.

[7] Kroger, N.; Bergsdorf, C.; Sumper, M. *EMBO J*. **1994**, *13*, 4676.

[8] Shimizu, K.; Cha, J.; Stucky, G. D.; Morse, D. E. *Proc. Natl. Acad. Sci. USA*. **1998**, *95*, 6234.

[9] Sumerel, J. L.; Yang, W.; Kisailus, D.; Weaver, J. C.; Choi, J. H.; Morse, D. E. *Chem. Mater*. **2003**, *15*, 4804.

[10] Kroger, N.; Deutzmann, R.; Sumper, M. *Science* **1999**, *286*, 1129.

[11] (a) Kroger, N.; Deutzmann, R.; Bersdorf, C.; Sumper, M. *Proc. Natl. Acad. Sci. USA* **2000**, *97*, 14133. (b) Milligan, A. J.; Morel, F. M. M. *Science* **2002**, *297*, 1848.

[12] (a) Zhang, Q.; Gao, L.; Guo, J. *Appl. Catal. B* **2000**, *26*, 207. (b) Fox, M. A.; Dulay, M. T. *Chem. Rev.* **1993**, *93*, 341. (c) Mo, S. D.; Ching, W. Y. *Phys. Rev. B* **1995**, *51*, 13023.

[13] (a) Fujishima, A.; Honda, K. *Nature* 1972, *238*, 3738. (b) Larson, A.; Falconer, J. L. *Appl*. *Catal*. *B* 1994, *4*, 325. (c) Kamat, P. V.; Dimitrijevic, N. M. *Solar Energy* **1990**, *44*, 83.

[14] (a) Schmid, G. *Nanoparticles*, Wiley–VCH Verlag GmbH & Co. KGaA, **2004**. R.W. Siegel, in: F.F. Fujita (Ed.). (b) *Nanophase Materials: Synthesis, Structure, and Properties*, Springer Series in Material Science, vol. 27, Springer-Verlag, **1994**.

[15] (a) Dura´n, P.; Capel, F.; Tartaj, J.; Moure, C. *Adv. Mater*. **2002**, *14*, 137. (b) Bauer, C.; Boschloo, G.; Mukhtar, E.; Hagfeldt, A. *J. Phys. Chem. B* **2001,** *105*, 5585.

[16] Zhang, X. T.; Liu, L. G.; Zhang, L. G.; Zhang, Y. M.; Lu, M.; Shen, Z. *J. Appl. Phys.* **2002**, *92*, 3293.

[17] Rensmo, H.; Keis, K.; Lindstrom, H.; Solbrand, A.; Hagfeldt, A.; Lindquist, S. E.; Wang, L. N.; Muhammed, M. *J. Phys. Chem. B* **1997**, *101*, 2598.

[18] (a) Zhang, X. T.; Liu, L. G.; Zhang, L. G.; Zhang, Y. M.; Lu, M.; Shen, Z.; Xu, W.; Zhong, G. Z.; Fan, X. W.; Kong, X. G. *J. Appl. Phys.* **2002**, *92*, 3293. (b) Johnson, J. C.; Yan, H.; Schaller, R. D.; Haber, L. H.; Saykally, R. J.; Yang, P. *J. Phys. Chem. B* **2001**, *105*, 11387.

[19] (a) Marci, G.; Augugliaro, V.; Lopez-Munoz, M.; Martin, C.; Palmisano, L.; Rives, V.; Schiavello, M.; Tilley, R. J. D.; Venezia, A. M. *J. Phys. Chem B* **2001**, *105*, 1026. (b) Marci, G.; Augugliaro, V.; Lopez-Munoz, M.; Martin, C.; Palmisano, L.; Rives, V.; Schiavello, M.; Tilley, R. J. D.; Venezia, A. M. *J. Phys. Chem B* **2001**, *105*, 1033.

[20] (a) Nishii, J.; Hossain, F. M.; Takagi, S.; Aita, T.; Saikusa, K.; Ohmaki, Y.; Ohkubo, I..; Kishimoto, S.; Ohtomo, A.; Fukumura, T.; Matsukura, F.; Ohno, Y.; Koinuma, H.; Ohno, H.; Kawasaki, M. *Jpn. J. Appl. Phys.* **2003**, *42*, L347. (b) Hossain, F. M.; Nishii, J.; Takagi, S.; Sugihara, T.; Ohtomo, A.; Fukumura, T.; Koinuma, H.; Ohno, H.; Ka wasaki M. *Physica E* **2004**, *21*, 911. (c) Norris, B. J.; Anderson, J.; Wager, J. F.; Kszler, D. A. *J. Phys. D: Appl. Phys.* **2003**, *36*, L105.

[21] Yang, P.; Yan, H.; Mao, S.; Russo, R.; Johnson, J.; Saykally, R.; Morris, N.; Pham, J.; He, R.; Choi, H. -J. *Adv. Mater.* **2002**, *12*, 323.

[22] Ito, Y.; Kushida, K.; Sugawara, K.; Takeuchi, H. *IEEE Trans. Ultrasonics, Ferroelectrics, and Frequency Control* **1995**, *42*, 316.

[23]. (a) Ryu, H.-W.; Park, B.-S.; Akbar, S. A.; Lee, W.-S.; Hong, K.-J.; Seo, Y.-J.; Shin, D.-C.; Park, J.-S.; Choi, G.-P. *Sens. Actuator B* **2003**, *96*, 717. (b). Sberveglieri, G. *Sens. Actuator B* **1995**, *23*, 103. (c). Rao, G. S. T.; Rao, D. T. *Sens. Actuator B* **1999**, *55*, 166. (d). Cheng, X. L.; Zhao, H.; Huo, L. H.; Gao, S.; Zhao, J. G. *Sens. Actuator B* **2004**, *102*, 248.

[24] (a) Dietl, T. *Semicond. Sci. Technol.* **2002**, *17*, 377. (b) Sharma, P.; Gupta, A.; Rao, K. V.; Owens, F. J.; Sharma, R.; Ahuja, R.; Osorio, J. M.; Johansson, B.; Gehring, G. A. *Nat. Mater.* **2003**, *2*, 673.

[25] Saeki, H.; Tabata, H.; Kawai, T. *Solid State Commun.* **2001**, *120*, 439.

[26] (a) Bessekhouad, Y.; Robert, D.; Weber, J. V. *J. Photochem. Photobiol. A* **2003**, *157*, 47.(b) Oskam, G.; Nellore, A.; Penn, R. L.; Searson, P. C. *J. Phys. Chem. B* **2003**, *107*, 1734.(c) Sugimoto, T. *Adv. Colloid Interface Sci.* **1987**, *28*, 65. (d) Zhang, H.; Finnegan, M.; Banfield, J. F. *Nano Lett.* **2001**, *1*, 81.

[27] (a) Lin, J.; Lin, Y.; Liu, P.; Meziani, M. J.; Allard, L. F.; Sun, Y. P. *J. Am. Chem. Soc.* **2002**, *124*, 11514. (b) Yu, J. C.; Yu, J.; Ho, W.; Zhang, L. *Chem. Commun.* **2001**, 1942. (c) Zhang, D.; Qi, L.; Ma, J.; Cheng, H. *J. Mater. Chem.* **2002**, *12*, 3677. (d) Li, Y.; Lee, N. H.; Hwang, D. S.; Song, J. S.; Lee, E. G.; Kim, S. J. *Langmuir* **2004**, *20*, 10838. (e) Lim, K. T.; Hwang, H. S.; Ryoo, W.; Johnston, K. P. *Langmuir* **2004**, *20*, 2466.

[28] (a) Li, X. L.; Peng, Q.; Yi, J. X.; Wang, X.; Li, Y. D. *Chem. Eur. J.* **2006**, *12*, 2383. (b) Xu, J.; Ge, J. P.; Li, Y. D. *J. Phys. Chem. B* **2006**, *110*, 2497. (c) Wang, X.; Zhuang, J.; Peng, Q.; Li, Y. D. *Nature* **2005**, *437*, 121.

[29] (a) Ayllon, J. A.; Figueras, A.; Garelik, S.; Spirkova, L.; Durand, J.; Cot, L. *J. Mater. Sci. Lett.* **1999**, *18*, 1319. (b) Pradhan, S. K.; Reucroft, P. J.; Yang, F.; Dozier, A. *J. Cryst. Growth* **2003**, *256*, 83.

[30] (a) Zhu, Y.; Li, H.; Koltypin, Y.; Hacohen, Y. R.; Gedanken, A. *Chem. Commun.* **2001**, 2616. (b) Yu, J. C.; Zhang, L.; Li, Q.; Kwong, K. W.; Xu, A. W.; Lin, J. *Langmuir* **2003**, *19*, 7673. (c) Huang, W.; Tang, X.; Wang, Y.; Koltypin, Y.; Gedanken, A. *Chem.Commun.* **2000**, 1415. (d) Xia, H.; Wang, Q. *Chem. Mater.* **2002**, *14*, 2158.

[31] Kobayashi, K.; Matsubara, T.; Matsushima, S.; Shirakata, S.; Isomura, S.; Okada, G. *Thin Solid Films* **1995**, *266*, 106.

[32] Studenikin, S. A.; Golego, N.; Cocivera, M. *J. Appl. Phys.* **1998**, *83*, 2104.

[33] Sang, B.; Konagai, M. *Jpn. J. Appl. Phys.* **1996**, *35*, 602.

[34] Audebrand, N.; Auffre´dic, J.-P.; Loue¨r, D. *Chem. Mater.* **1998**, *10*, 2450.

[35] Wu, R.; Xie, C.; Xia, H.; Hu, J.; Wang, A. *J. Cryst. Growth* **2000**, *217*, 274.

[36] Zhang, T.; Oyama, T.; Horikoshi, S.; Hidaka, H.; Zhao, J.; Serpone, N. *Solar Energy Materials & Solar Cells* **2002**, *73*, 287.

[37] Thompson, T. L.; Yates, J. T. Jr. *Chem. Rev.* **2006**, *106*, 4428.

[38] (a) Seven, O. *et al.*, *J. Photochem. Photobiol. A* **2004**, *165*, 103. (b) Wong, M. S. *et al. Appl. Environ. Microbiol.* **2006**, *72*, 6111.

[39] (a) Sato, S. *Chem. Phys. Lett*. **1986**, *123*, 126. (b) Morikawa, T.; Asahi, R.; Ohwaki, T.; Aoki, A.; Taga, Y. *Jpn. J. Appl. Phys.* **2001**, *40*, 561. (c) Sakthivel, S.; Kisch, H. *ChemPhysChem.* **2003**, *4*, 487. (d) Irie, H.; Watanabe, Y.; Hashimoto, K. *J. Phys. Chem. B* **2003**, *107*, 5483. (e) Lindgren, T. *et al*. *J. Phys. Chem. B* **2003**, *107*, 5709. (f) Gole, J. L.; Stout, J. D.; Burda, C.; Lou, Y.; Chen, X. *J. Phys. Chem. B* **2004**, *108*, 1230. (g) Diwald, O. *et al. J. Phys. Chem. B* **2004**, *108*, 6004. (h) Lettmann, C.; Hildenbrand, K.; Kisch, H.; Macyk, W.; Maier, W. F. *Appl. Catal. B* **2001**, *32*, 215. (i) Sakthivel, S.; Kisch, H. *Angew. Chem., Int. Ed. Engl.* **2003**, *42*, 4908. (j) Umebayashi, T.; Yamaki, T.; Itoh, H.; Asai, K. *Appl. Phys. Lett.* **2002**, *81*, 454. (k) Umebayashi, T.; Yamaki, T.; Tanaka, S.; Asai, K. *Chem. Lett.* **2003**, *32*, 330. (l) Ohno, T.; Mitsui, T.; Matsumura, M. *Chem. Lett.* **2003**, *32*, 364. (m) Wang, C. M.; Mallouk, T. E. *J. Phys. Chem.* **1990,** *94*, 4276. (n) Park, H.; Choi, W. *J. Phys. Chem. B* **2004**, *108*, 4086. (o) Yu, J. C.; Yu, J.; Ho, W.; Jiang, Z.; Zhang, L. *Chem. Mater*. **2002**, *14*, 3808. (p) Chen, X.; Burda, C. *J. Am. Chem. Soc*. **2003**, *125*, 15736.

[40] The XRD and SAED patterns were indexed with reference to the crystal structures from the ASTM charts: titania (ASTM chart card no. 3-0380 for brookite and 04-0477 for anatase).

[41] (a) Y. Wang, C. Feng, Z. Jin , J. Zhang, J. Yang, S. Zhang, *J. Mol. Catal. A: Chem.* **2006**, *260*, 1. (b) The XRD patterns were indexed with reference to the crystal structures from the ASTM charts: TiC (ASTM chart card no. 06-0614).

[42] Shankar, S. S.; Rai, A.; Ahmad, A.; Sastry, M. *Chem. Mater*. **2005**, *17***,** 566.

[43] (a) Miyama T.; Yonezawa, Y. *Langmuir*. **2004**, *20***,** 5918. (b) Kumar, A.; Mandal, S.; Selvakannan, P. R.; Pasricha, R.; Mandale, A. B. Sastry, M. *Langmuir*, **2003**, *19*, 6277.

[44] Moulder, J. F.; Stickle, W. F.; Sobol, P. E.; Bomben, D. *Handbook of X-ray Photoelectron Spectroscopy*; Physics Electronics Int.: Eden Prairie, MN, **1995**.

[45] (a) Wagner, C. D.; Riggs, W. M.; Davis, L. E.; Moulder J. F.; Muilenberg, G. E. *Handbook of X-ray photoelectron spectroscopy*, Perkin Elmer Corp. Publishers, Eden Prairie, MN, **1979**, p. 40. (b) Schiffrin, A. A.; Riemann, W. Auwarter, Y. Pennec, A. Weber-Bargioni, D. Cvetko, A. Cossaro, A. Morgante, J. V. Barth, *Proc. Natl. Acad. Sci. U.S.A. 104*, 5279**.** (c) Gonella, G.; Terreni, S.; Cvetko, D.; Cossaro, A.; Mattera, L.; Cavalleri, O.; Rolandi, R.; Morgante, A.; Floreano, L.; Canepa, M. *J. Phys. Chem. B* **2005**, *109*, 18003.

[46] Wagner, C. D.; Riggs, W. M.; Davis, L. E.; Moulder J. F.; Muilenberg, G. E. *Handbook of X-ray photoelectron spectroscopy*, Perkin Elmer Corp. Publishers, Eden Prairie, MN, **1979**, p. 68.

[47] Gopinath, S.; Hegde, S. G.; Ramaswamy, A.V.; Mahapatra, S. *Mater. Res. Bull*. **2002**, *37*, 1323.

[48] Papirer, E.; Lacroix, R.; Donnet, J. B.; Nanse, G.; Fioux, P. *Carbon* **1995**, *33*, 63.

[49] Li, Y. Z.; Hwang, D.; Lee, N. H.; Kim, S. *Chem. Phys. Lett*. **2005**, *404*, 25.

[50] (a) Sato, S.; Nakamura, R.; Abe, S. *Appl. Catal. A* **2005**, *284*, 131. (b) Sakthivel, S.; Kisch, H. *Chem. Phys. Chem*. **2003**, *4*, 487.

[51] (a) Sakthivel, S.; Kisch, H. *Angew. Chem. Int. Ed*. **2003**, *42*, 4908. (b) Cong, Y.; Chen, F.; Zhang, J.; Anpo, M. *Chemistry Letters*. **2006**, *35*, 800.

[52] D.-G. Huang, S.-J. Liao, J.-M. Liu, Z. Dang, L. Petrik, *J. Photochem. Photobiol. A Chem***. 2006,** *184*, 282**.**

[53] Doping

[54] (a) Shafi, V. P. M.; Ulman, A.; Yan, X.; Yang, N. L.; Himmelhaus M.; Grunze, M. *Langmuir* **2001**, *17*, 1726. (b) Lee, H.; Chen, W. C. *Chem. Mater*. **2001**, *13*, 1137. (c) Nakamura; Imanishi, A.; Murakoshi K.; Nakato, Y. *J. Am. Chem. Soc*. **2003**, *125*, 7443.

[55] The XRD and SAED patterns were indexed with reference to the crystal structures from the ASTM charts: ZnO (ASTM chart card no. 13-0311).

[56] (a) Niwa, Y.; Kobayashi, H.; Tsuchiya, T. *J. Chem. Phys.* **1974**, *60*, 799. (b) Zambonin, G.; Losito, I.; Triffitt, J. T.; Zambonin**,** C. G. *Journal of Biomedical Materials Research***, 2000,** *49***,** 120.

[57] Kunat, M.; Girol, St. G.; Burghaus, U.; ll, Ch. Wo¨ *J. Phys. Chem. B*, **2003**, *107*, 14350.

[58] Wagner, C. D.; Riggs, W. M.; Davis, L. E.; Moulder J. F.; Muilenberg, G. E. Handbook of X-ray photoelectron spectroscopy, Perkin Elmer Corp. Publishers, Eden Prairie, MN, **1979**, p. 84.

[59] (a) Dinda, B.; Icli, S. *Photobiol. A: Chem*. **2001**, 140, 263. (b) Chakrabarti, S.; Dutta, B. K. *J. Hazard. Mater*. *B* **2004**, *112*, 269. (c) Wang, C.; Wang, X.; Xu, B.Q.; Zhao, J. Mai, B.; Pen, P.; Sheng, G.; Fu, J. *J. Photochem. Photobiol. A: Chem*. **2004**, *168*, 47.

[60] Cozzoli, P. D.; Kornowski, A.; Weller, H. *J. Phys. Chem. B* **2005**, *109*, 2638.

[61] (a) Saito, T.; Iwase, T.; Morioka, T. *J. Photochem. Photobiol. B Biol***. 1992**, *14*, 369. (b) Amro, N.; Kotra, L.; Wadu-Mesthrige, K.; Bulychev, A.; Mobashery, S.; Liu, G. *Langmuir* **2000**, *16*, 2789.

Chapter IV

A Novel Biological Approach for Metal Nanoparticle synthesis and their Antibacterial Applications

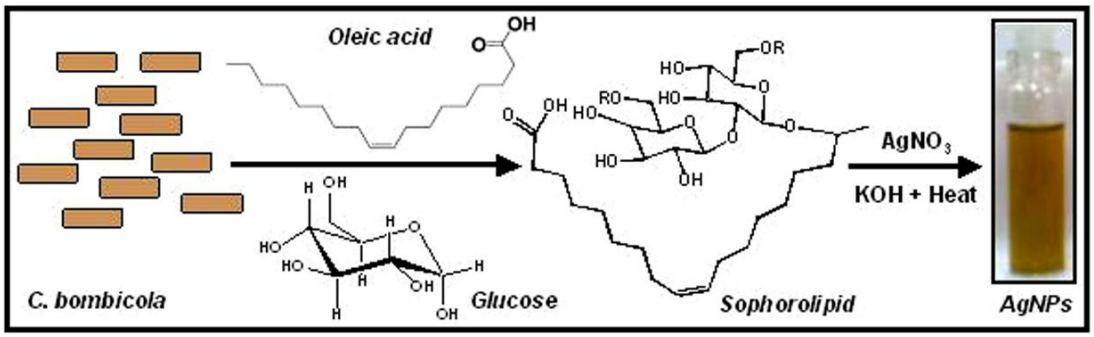

Metal nanoparticles, due to their shape and size dependent optical properties and various biological applications, have become a vital topic of research. Among them, silver nanoparticles have been used extensively, especially for antimicrobial activity as most of the pathogenic microbes are gaining resistance to present day antibiotics. Several products comprising silver nanoparticles starting from toothpastes to refrigerators, washing machines and even surgical accessories etc are becoming accessible to the common man. Looking towards the vast applications, several methods of their synthesis operating at lower cost and biofriendly processes would always be preferred. Therefore, we present in this chapter, a simple bio-surfactant mediated method for metal nanoparticle synthesis. Silver nanoparticles obtained by this process show monodispersity in shape and size can be stored in powder form and exhibit superior antibacterial property. The key step in the whole process is the usage of bio-surfactants, which are obtained by yeast-mediated process, and hence all the advantages highlighted for biosyntheses in the previous chapters.

The work described in this chapter has been communicated as: **Singh, S**.; Patel, P.; Prabhune, A. A.; Ramanna, C. V.; Prasad, B. L.V. **2008.**

4.1 Introduction

Metal and semiconductor nanoparticles have shown important applications in catalysis, biosensing, recording media and optics [1]. In the current scenario, the use of nanoparticles in biomedical applications such as drug delivery [2], cancer-cell diagnostics [3] and therapeutics [4] has given nanotechnology a new dimension. Also, scattering properties of spherical gold nanoparticles have been used in cancer cell imaging by confocal microscopy [3, 5]. Silver has been known to exhibit strong toxicity to a wide range of microorganisms and has been used extensively in many antibacterial applications [6].

An important stipulation for the bio-applicability of nanoparticles is their water dispersibility. Synthesis of water dispersible nanoparticles has been generally achieved by using water soluble polymers [7], oligo and polysaccharides [8] as capping agents, while, reduction has been carried out by citric acid [9], sodium borohydride [10], elemental hydrogen etc [11]. However, it would be advantageous if both the reduction of metal ions and capping of subsequent nanoparticles could be performed by the same molecule. Several protocols have been reported for such synthesis involving the use of amino acids [12], enzymes etc. Willner *et al*. have reported that numerous types of enzymes, such as oxidases, hydroxylases, hydrolytic proteins, or $NAD(P)^+$ dependent enzymes, may be employed as biocatalysts for the synthesis of metal nanoparticles and for the development of optical/electrochemical sensors for the respective substrates [13]. Rangnekar *et al*. have successfully reported the reductive synthesis of AuNPs by enzyme α-amylase and simultaneous surface functionalization of nanoparticles within the same reaction. Further, the functional activity of α-amylase present on the surface of AuNPs was tested and found to be retained in this complex [14].

Biomolecules have been used for nanomaterial synthesis/functionalization and its subsequent applications since decades [15]. These nanomaterial-biomolecules multifunctional systems could be used as useful tool to mimic the behavior of biomolecules in cells and therefore could be helpful to explain the mechanism of complex biological processes with a several potential applications. Glycolipid-

nanoparticles conjugates are recently being developed that are expected to have many applications. Three different types of glyconanoparticles have been reported so far including gold and silver glyconanoparticles [16], glyco-quantum dots [17] and magnetic glyconanoparticles [18]. Glyconanoparticles have unusual physical properties due to its quantum size effect [19], which can be used for the detection and evaluation of interactions. Several biotechnological and biomedicinal such as anti-adhesive property [20] of nanoparticle-carbohydrate systems have already been reported. Other applications such as carbohydrate interactions [21-26], carbohydrate-protein interaction [27, 28, 29], as biolabels [15, 19, 29] and some applications in the field of materials science [30] have also been published recently. The possible applications of glyconanoparticles in various fields of science have been shown in Scheme 4.1.

Three important properties of glyconanoparticles make them suitable model systems for different applications.

1. They are of similar size to many biomolecules and therefore can reproduce or mimic the carbohydrate presentation in glycoproteins etc.
2. They provide a glycocalyx-like surface thus presenting the carbohydrates in a globular and polyvalent configuration on their surfaces.
3. The glyconanoparticles would exhibit unusual physical properties due to their quantum size effect [31, 32], which could be used for the detection and evaluation of interactions.

In continuation of our quest for bio-mediated synthesis of nanomaterials (as described in previous chapters), in this chapter we present the utility of microbially produced sophorolipids (a biosurfactant) for the reduction of metal ions and the simultaneous capping of the so formed nanoparticles. Sophorolipids (SL) are a kind of microbial extracellular biosurfactants produced by yeasts, such as *Candida bombicola*, *Yarrowia lipolytica*, *Candida apicola*, and *Candida bogoriensis* [34]. They are generally present in the form of disaccharide sophoroses linked glycosidically to the hydroxyl group at the penultimate carbon of fatty acids. Sophorolipids mainly occur as mixtures of close ring (macrolactone form) and open

ring (acidic form) structures, which undergo acetylation to various extents at the primary hydroxyl group of the sophorose ring [34, 35].

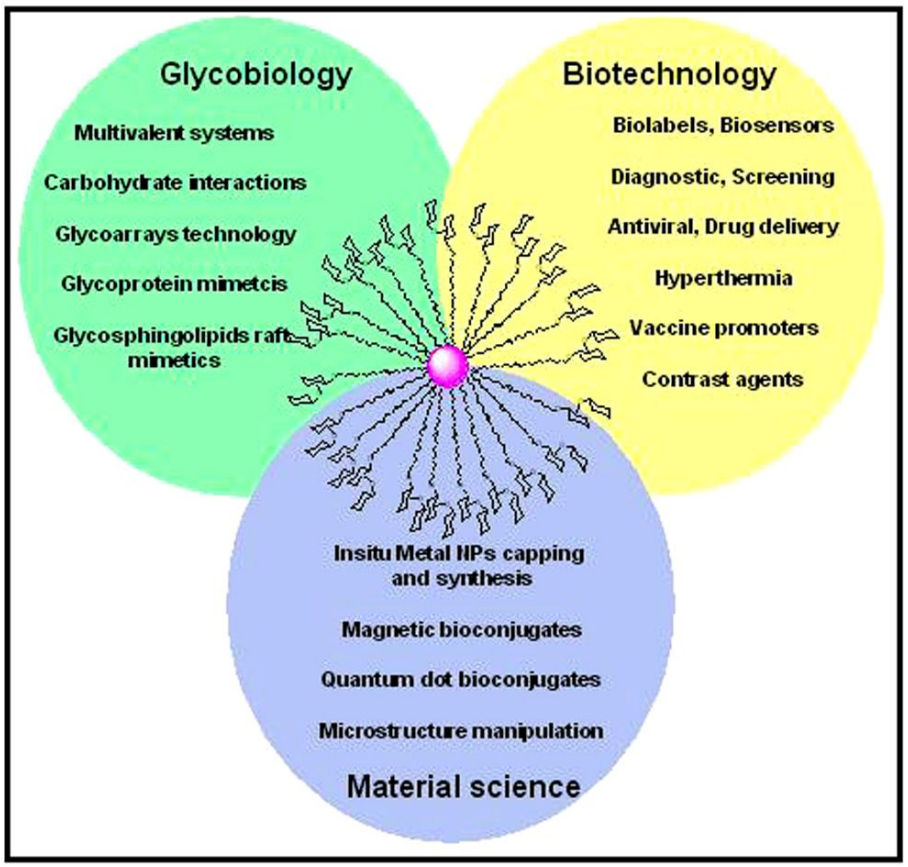

Scheme 4.1: *Schematic representations explaining the potential application of glyconanoparticles in the field of Glycobiology, Biotechnology and Material science. (Scheme courtesy: reference 33).*

It was probably Gorin *et al.* [36] who first described sophorolipids, as extracellular glycolipids synthesized by the yeast *Torulopsis magnoliae*. However, this strain was incorrectly identified and was actually *Torulopsis apicola*, currently known as *Candida apicola*. The structure of the hydroxy fatty acid sophoroside mixture was elucidated as a partially acetylated 2-O-β-D-glucopyranosyl- D-glucopyranose unit attached β-glycosidically to 17-L-hydroxyoctadecanoic or 17-L-hydroxy-Δ9-octadecenoic acid [37]. Within a year, Tulloch *et al*. also reported a new type of sophorolipid from *Candida bogoriensis* (currently known as *Rhodotorula bogoriensis*). The over all structure of sophorolipid is similar to that produced by *Candida apicola*, but differs in its hydroxy fatty acid moiety as the sophorose unit was linked with 13-hydroxydocosaenoic acids. Further, Spencer *et al*. had reported

another sophorolipid secreting yeast species *Candida bombicola* (initially known as *Torulopsis bombicola*), in which the glycolipids structure and production characteristics are nearly same as that of *Candida apicola* [38]. Recently, Chen *et al.* have reported a new strain for sophorolipid synthesis (*Wickerhamiella domericqiae*), which is identical to the major component of the sophorolipids of *C. apicola* and *C. bombicola* [39].

The basic requirement for sophorolipid production is glucose and a fatty acid precursor (oleic acid in this case). The biotransformation is a multistep process, where first step involves the conversion of fatty acids in to a terminal (ω) or penultimate (ω-1) hydroxy fatty acid by the action of a membrane bound nicotinamide adenine dinucleotide phosphate (a reduced form of NADPH) dependent monooxygenase enzyme, cytochrome P450 [40]. In the second step, glucose is glycosidically coupled (at position C-1) to the hydroxyl group of the fatty acid by the action of specific glycosyltransferase-I. Third step involves the addition of a second glucose to C-2 position of the first glucose moiety by glycosyltranferase II [41]. The so obtained crude sophorolipids are obtained as mixture of acidic and non-acetylated molecules. Further, a majority of sophorolipid molecules undergo various extent of esterification. All these can be easily converted to the simple acid form by a mild base hydrolysis.

Silver nanoparticles show excellent toxicity against various microorganisms, which make their use for water purification, wound dressings, inhibitor of HIV viruses etc. very promising [42]. Silver has been known for its bactericidal activity since ancient time [43]. Also, recent research has shown the antibacterial property of silver nanoparticles (AgNPs) [44]. It has been hypothesized that silver has high affinity towards sulfur and phosphorus, which might be the probable reason for antibacterial action. Proteins present on the bacterial cell membrane contain sulfur in abundance and react with silver nanoparticles, which in turn cause malfunction of these proteins [44a, 45]. Also, Ag^+ ions have been reported for their affinity towards phosphorous moieties in DNA, resulting in inactivation of DNA replication. These Ag^+ ions can also react with sulfur-containing proteins/enzymes and lead to inhibition of respective proteins/enzymes [46].

In this chapter, we describe the synthesis of sophorolipid by Yeast (*Candida bombicola*) and its detailed characterizations using FTIR and NMR spectroscopy techniques. Further, the acidic form of the sophorolipid was used for synthesis of stable and nearly monodispersed gold and silver nanoparticles. Most important aspect of this novel method for nanoparticle production involves the usage of sophorolipid in form of reducing as well as capping agent. These nanoparticles were analyzed by different characterization tools such as UV-visible spectroscopy, TEM, FTIR, XRD and TGA etc. Further, the sophorolipid and sophorolipid reduced silver nanoparticles were used for evaluation of their antibacterial property against both Gram-positive and Gram-negative bacterial species. It has been reported that sophorolipid show better bactericidal activity against Gram-positive than Gram-negative bacterial species. However, after formation of silver nanoparticles, where sophorolipids are present on the nanoparticle surface, it showed antibacterial activity against both Gram-positive as well as Gram-negative bacterial species. Interestingly, OA-SL-AgNPs showed bactericidal property even with the concentration of 1 µg/mL against Gram-negative bacteria. Loss of cell membrane (as the reason for antibacterial activity) integrity was proved by lipid peroxidation reaction and AFM imaging of bacterial cell topography.

4.2 Biotransformation of oleic acid into sophorolipid using (*Candida bombicola*)

This part of chapter illustrates about the procedure involved in production of oleic acid derived sophorolipid (OA-SL) molecules by yeast *Candida bombicola* (ATCC No. 22214) and its characterizations. This yeast species was issued from National Center of Industrial Microorganisms (NCIM) at the National Chemical Laboratory Pune on a MGYP-A (maltose, glucose, yeast extract, peptone and agar) slant. This slant was maintained at 4 °C.

4.2.1 Experimental Details

Seeds of *Candida bombicola* were inoculated in 10 mL of freshly prepared MGYP nutrient medium and incubated for 24 h at 30 ºC under shaking condition (200 rpm). This pre-inoculum was added to 90 mL of MGYP nutrient medium in a 500 mL

Erlenmeyer flask and incubated for 48 h at 30 ºC on a shaker (200 rpm). Cells were harvested by centrifugation at 5000 rpm for 10 min. Cell pellets were washed twice with Millipore water under sterile condition. Finally these cell pellets were redispersed in sterile solution of 10 % glucose with 2 mL of oleic acid (dispersed in 2 mL of ethanol) and the flask was kept on a shaker (200 rpm) at 30 ºC for 96 h. As a result of reaction between the yeast biomass with glucose and oleic acid, a brown and viscous liquid (crude-sophorolipid) settled at the bottom of the flask. The crude-sophorolipid was separated by pipette from the biomass and extracted with ethyl acetate. Anhydrous sodium sulfate was added to the ethyl acetate to remove the residual water. Then the sample was filtered and ethyl acetate was removed under vacuum. The unconverted oleic acid was removed by several times washing with n-hexane. This crude sophorolipid (a mixture of lactonic and acidic form) was refluxed for 15 min in 5M-NaOH solutions, which was neutralized with 2N-HCl (up to pH = 6). Further, it was extracted with n-butanol, evaporated till dryness and finally washed with ether and dried under vacuum. The so obtained product contains acidic form of sophorolipid [47] and was characterized by FTIR, NMR and Mass spectroscopy.

4.2.2 Sample characterizations

Mass spectroscopy (EI, 70 eV, direct inlet system) was carried out on a Finnigan MAT-1020 spectrometer. Elemental analysis data were obtained on a Thermo Finnigan Flash EA 1112 Series CHNS Analyser. ^{1}H and ^{13}C NMR spectroscopy measurements were carried out on Bruker AC 200 MHz or Bruker DRX 400 MHz spectrometers, and TMS was used as internal standard.

4.2.3 FTIR spectra analysis

The FTIR spectrum of purified sophorolipid derived from biotransformation of oleic acid by *Candida bombicola* is shown in Figure 4.1 recorded from 400 cm^{-1} to 4000 cm^{-1}. The spectra show a broad band centering at around 3340 cm^{-1}, which could be attributed to the O-H streching mode [48]. Generally, non-hydrogen bonded of free hydroxyl group absorbs strongly in the 3700-3584 cm^{-1} region, while due to intramolecular hydrogen bonding this band shifts towards lower wavenumber (between 3550-3200 cm^{-1}). Therefore, it can be concluded that there is certain amount

of hydrogen bonding involved within the sophorolipid molecules. The asymmetrical stretching (as_{CH2}) and symmetrical stretching (s_{CH2}) of methylene occur at 2922 and 2852 cm^{-1}, respectively confirming the presence of methylene group backbone [48]. The 3006 cm^{-1} band could be assigned to C-H streching vibration of alkene (C=C-H) [49]. A very sharp transmittance band present at 1077 cm^{-1} could be assigned to the C-O stretch of C-O-H groups from the sugar molecules [50]. A weak band present at 1460 cm^{-1} can be attributed to the C-O-H in plane bending of carboxylic acid (-COOH) group present in the acidic form of sophorolipid [48].

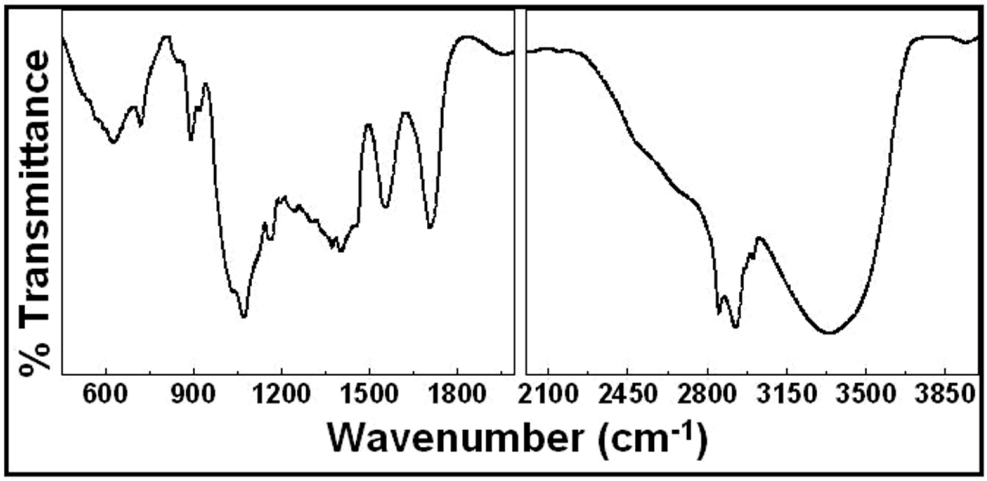

Figure 4.1: *FTIR spectra recorded from powder of purified sophorolipid molecules synthesized by the reaction between oleic acid and Candida bombicola in presence of glucose. Panel A and B are the magnified regions of spectra ranging from 450-2000 cm^{-1} and 2000-4000 cm^{-1} wavenumbers respectively. Spectra showing characteristic transmittance bands for sophorolipid molecules, described in detail in text.*

4.2.4 ^{1}H NMR spectra analysis

^{1}H and ^{13}C NMR spectroscopy measurements were carried out on Bruker AC 200 MHz or Bruker DRX 400 MHz spectrometers, and TMS was used as internal standard. The ^{1}H NMR spectra of purified sophorolipid was taken in $CDCl_3$ and assigned to a typical glycolipids-type pattern. The protons of glucose-H-1' and Glucose-H-1" were identified at 4.46 (d, J = 7.8 Hz, 1H), 4.61 (d, J = 7.8 Hz, 1H) ppm. The signals of protons from –CH=CH– groups were found at 5.31–5.39 (m, 2H) ppm, from -CH_3 group at 2.02-2.03 ppm and multiple signals at 1.25-1.46 (m, 19H) and 1.57–1.64 (m, 4H). The above given resonant values for proton match well with the reported values [51 b, d].

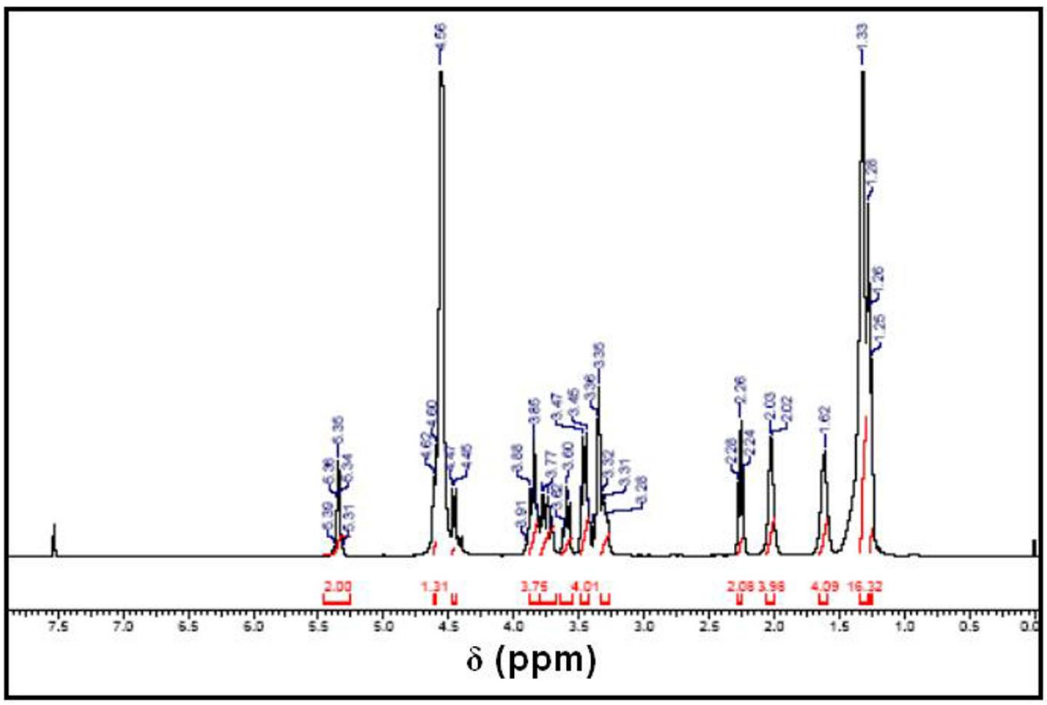

Figure 4.2: *^{1}H NMR spectra recorded from the purified sophorolipid molecules synthesized by the reaction between oleic acid and Candida bombicola in presence of glucose, sample was dissolved in $CDCl_3$.*

4.2.5 Mass spectra analysis

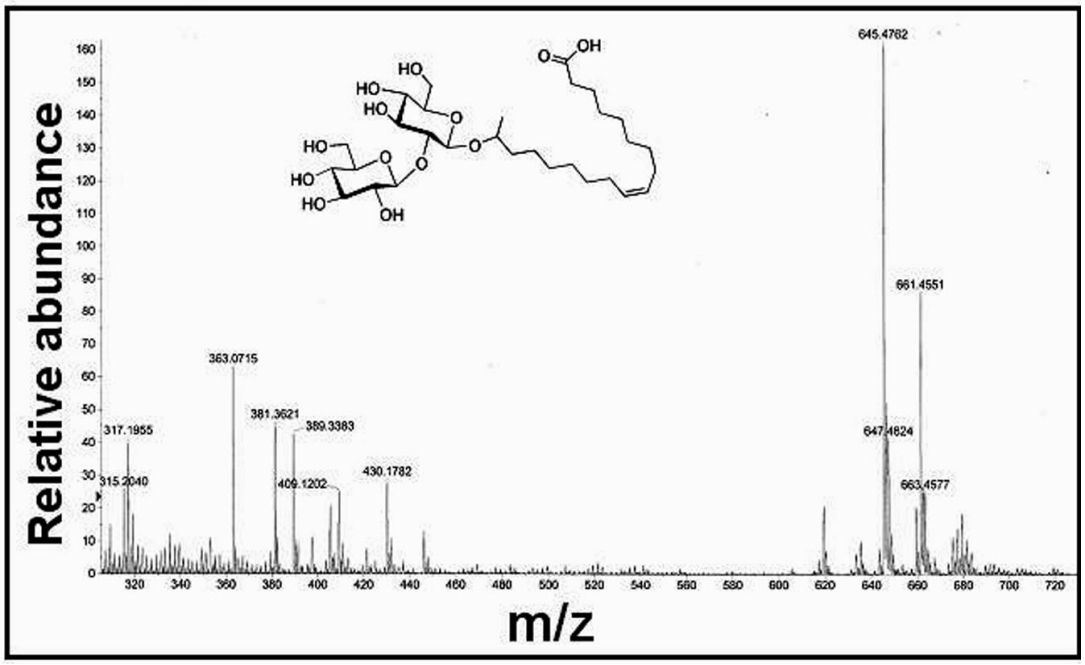

Figure 4.4: *Mass spectra recorded from the purified sophorolipid molecules synthesized by the reaction between oleic acid and Candida bombicola in presence of glucose. The most intense peaks (m/z=645.5 and 661.5) correspond to the sodium and potassium salts of sophorolipid molecules.*

Ions corresponding to the sodium and potassium salt of sophorolipids were obtained at 645.47 and 661.45 respectively. The so calculated molecular weight (~ 621) of sophorolipid corresponds to the unacetylated (6' and 6''=H) product of sophorolipid [52]. These were the most intense peaks in the spectra suggesting the presence of pure sophorolipid molecule. Thus the molecular structure is confirmed as it has shown in Figure 4.4 (inset). MS (ESI): *m/z* = 645.47 (100 %, $[M + Na]^+$); 661.45 (52%, $[M + K]^+$). Anal. Calculated for $C_{30}H_{54}O_{13}$: C, 57.86; H, 8.74. Found: C, 57.60; H, 9.05.

4.2.6 ^{13}C NMR spectra analysis

For further confirmation of molecular structure of sophorolipid ^{13}C NMR spectra measurement was performed, which showed that the resonance signals of $-CH_2-$ groups present in fatty chain moiety were found at 22.1- 37.8 ppm, two carbons from –CH=CH– group in fatty acid chain moiety at 130.9 ppm, glucose-C-1' and glucose-C-1" at 102.5 and 104.7 ppm, glucose-C-6' and glucose-C-6" at 62.8, 63.1 ppm [51d]. The signal at 179.9 ppm proves the presence of acid group present in the sophorolipid. [51d].

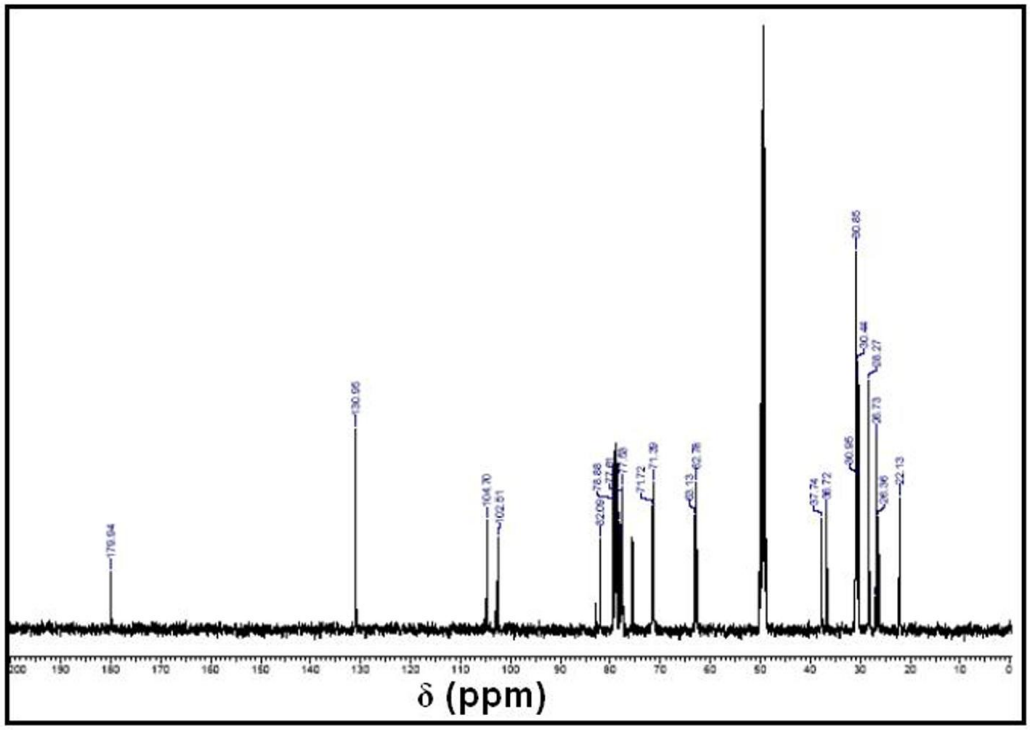

Figure 4.3: *^{13}C NMR spectra recorded from the purified sophorolipid molecules synthesized by the reaction between oleic acid and Candida bombicola in presence of glucose, sample was in $CDCl_3$. The detailed description has been provided in text.*

4.3 Use of sophorolipid for silver nanoparticle synthesis

This part of chapter describes about the reduction of Ag^{+} ions into Ag^{0} by the use of oleic acid derived sophorolipids (OA-SL) by the use of yeast *Candida bombicola*. Here OA-SL acts as both reducing as well as capping/stabilizing agent in AgNPs synthesis. The obtained silver nanoparticles (OA-SL-AgNPs) were characterized with different techniques such as UV-visible spectroscopy, TEM, FTIR spectroscopy, XRD, TGA etc.

4.3.1 Experimental Details

In a typical experiment, 100 mL of 10^{-3} M aqueous $AgNO_3$ solutions was taken with 10^{-3} M OA-SL. To this solution, 1 mL of 1M KOH solution (pH ~11) was added and was allowed to boil for about 5-10 minutes. The colorless solution turned yellow, which indicated the formation of OA-SL-AgNPs. In order to prove that the reduction occurred only at alkaline pH, control experiment was set up in which the above reaction was carried out without the addition of KOH. It was observed that AgNPs formation did not occur under neutral and acidic conditions. In another control experiment the above reaction was performed with $AgNO_3$ and KOH without the addition of SL and it was again observed that even after prolonged boiling there was no formation of AgNPs. This clearly indicates the crucial role of SL as a pH dependent reducing agent for the synthesis of AgNPs. The OA-SL-AgNPs were dialyzed followed by centrifugation at 15000 rpm for 30 min, in order to remove unreduced Ag^{+} ions and free OA-SL molecules. This purified OA-SL-AgNPs were further used for different characterizations.

For oleic acid capped AgNPs (OA-AgNPs) synthesis, 100 mL of 10^{-3} M of $AgNO_3$ was added to the 10^{-3} M of oleic acid (taken in equal volume of water-ethanol mixture). Further, 0.01 grams of $NaBH_4$ was added to this solution. The solution color immediately becomes dark yellow, indicated the formation of OA capped AgNPs. This solution of OA-AgNPs was further, dialyzed to remove unreduced Ag^{+} ions, oleic acid and excess borohydride. Thus, so obtained OA-AgNPs were used for various characterizations and bactericidal experiments.

4.3.2 UV-visible spectra analysis

The UV-visible spectra were recorded from different conditions of OA-SL-AgNPs synthesis (Figure 4.5). Curve-1 is UV-vis spectra recorded from boiled solution of OA-SL with $AgNO_3$ at neutral pH, showing the absence of surface plasmon resonance (SPR) characteristic for AgNPs. Further, $AgNO_3$ solution boiled under alkaline pH without OA-SL also showed absence of any SPR (curve-2). After a substantial optimization of the experimental parameters, reduction of silver ions was concluded successfully by heating equimolar (10^{-3} M) silver nitrate and OA-SL in alkaline solution (1M KOH). The reduction was very rapid (2-5 min) as indicated by the formation of yellow color (Figure 4.5, inset) with a clear and characteristic SPR (at 410 nm) for AgNPs (curve-3) [53]. Therefore, it is clear that alkaline medium is necessary for the reduction of AgNPs by OA-SL. The conditions are very similar to the famous Tollen's reagent. Thus, we hypothesize that OA-SL acts as reducing as well as stabilizing agent for AgNPs synthesis, resulting in to the formation of a layer of OA-SL capping on the surface of AgNPs (inset). These OA-SL-AgNPs were isolated in form of stable powder either by simple centrifuging and air-drying or lyophilization till dryness.

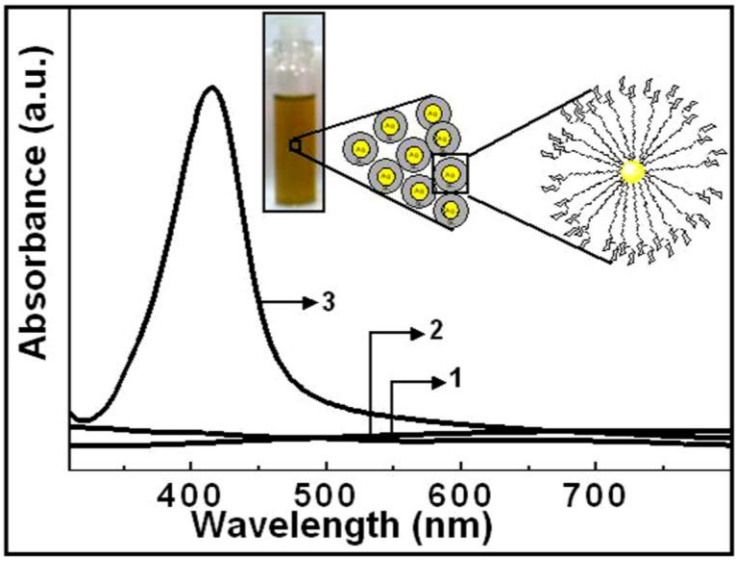

Figure 4.5: *UV-visible spectra recorded from heated solution of OA-SL with $AgNO_3$ in absence (curve-2) and presence (curve-3) of alkaline medium. Curve-1 represents the spectra recorded from the heated solution of $AgNO_3$ in alkaline medium without OA-SL molecules. Curve-3 shows the typical SPR centering at 410 nm, characteristic for silver nanoparticles. Inset shows the colour of solution after heating the OA-SL with $AgNO_3$ in alkaline medium. Also, the cartoon image of probable arrangement of OA-SL on AgNPs surface is shown.*

4.3.3 TEM analysis

Transmission electron microscope images taken from as synthesized and purified solution of OA-SL-AgNPs (Figure 4.6 A and B) shows the nearly uniform distribution of particles varying from ~ 10 - 25 nm in diameter.

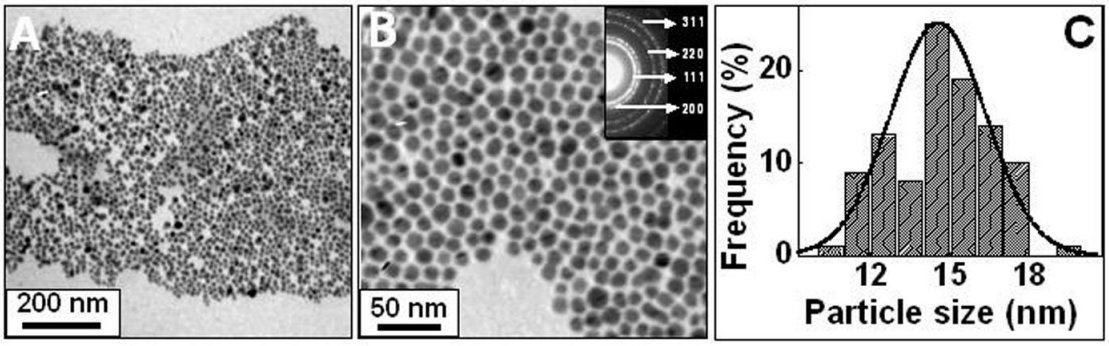

Figure 4.6: *TEM images taken from heated and purified solution of OA-SL with $AgNO_3$ in presence of alkaline medium. Particle size distribution (C) shows the average particle size of ~ 15 nm. SAED pattern shows the ring pattern, which is indexed for [111], [200], [220] and [311] planes of silver (B).*

Particle size distribution was plotted taking 100 nanoparticles into account (Figure 4.6 C), which showed average particle size at ~ 15 nm. Selected area electron diffraction pattern shows the ring pattern suggesting polycrystalline nature of OA-SL-AgNPs. These ring patterns were indexed on the basis of FCC silver (inset B) [54].

4.3.4 X-Ray Diffraction pattern analysis

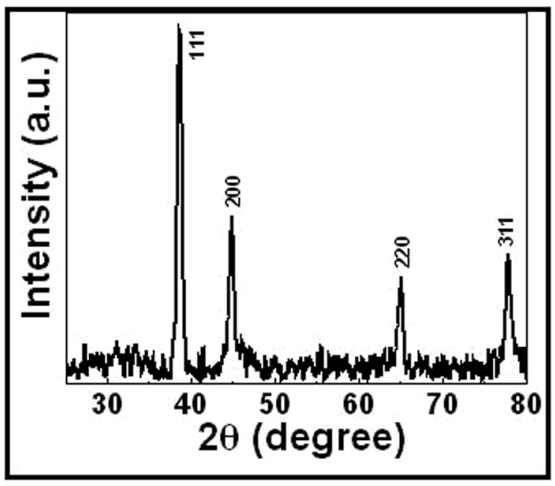

Figure 4.7: *XRD pattern obtained from a solution cast film of aqueous OA-SL-AgNPs on glass surface. The Bragg reflections arising from the film are indexed with respective crystal planes.*

XRD pattern recorded from the drop cast film of aqueous solution of purified OA-SL-AgNPs showed the signature of characteristic Bragg's reflexions for crystalline silver as observed in Figure 4.7. The diffraction peaks were indexed for [111], [200], [220] and [311] crystal planes of silver [54]. The XRD peaks appear to be broadened, suggesting the presence of very small (few nanometers) particles constituting the major population of OA-SL-AgNPs.

4.3.5 FTIR and NMR spectra analysis

The nature and mode of OA-SL capping on nanoparticle, was checked by FTIR and NMR spectra. The FTIR spectra (Figure 4.8) were recorded after the purification of OA-SL-AgNPs (curve-2) as described in experimental section and it was compared with the FTIR spectra of pure OA-SL molecules (curve-1). The regions of interests i.e. carbonyl region (region-I) and olefinic region (region-II) are marked and enlarged in the accompanying panels.

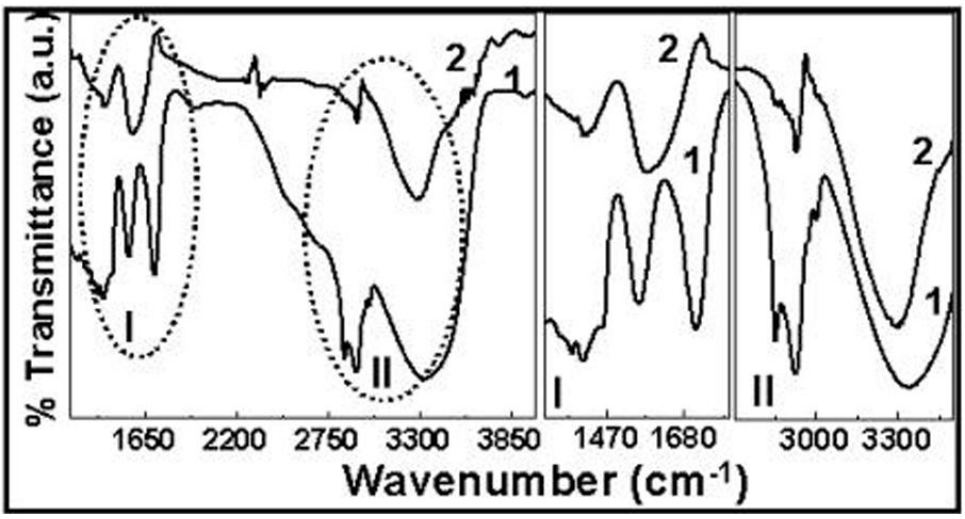

Figure 4.8: *FTIR spectra recorded from purified OA-SL molecules (curve-1) and OA-SL-AgNPs (curve-2). The region of interest (I and II) is enlarged in accompanying panels. Detailed explanations have provided in the text.*

The –C=O stretch at 1709 cm^{-1} (region-I, curve-A) in pure OA-SL is shifted to 1574 cm^{-1} (region-I, curve-2) indicating its binding to the AgNPs surface. The association of –C=C– with the AgNPs surface is evident from the region-II (curve-2) where olefinic–H stretching frequency at 3004 cm^{-1} is absent [49]. Therefore, it can be hypothesized that both the carbonyl and olefinic-H functional groups are significantly involved in AgNPs capping/stabilization, whereas the sophorose unit present in OA-

SL molecules remains free and thus render OA-SL-AgNPs dispersible in aqueous medium.

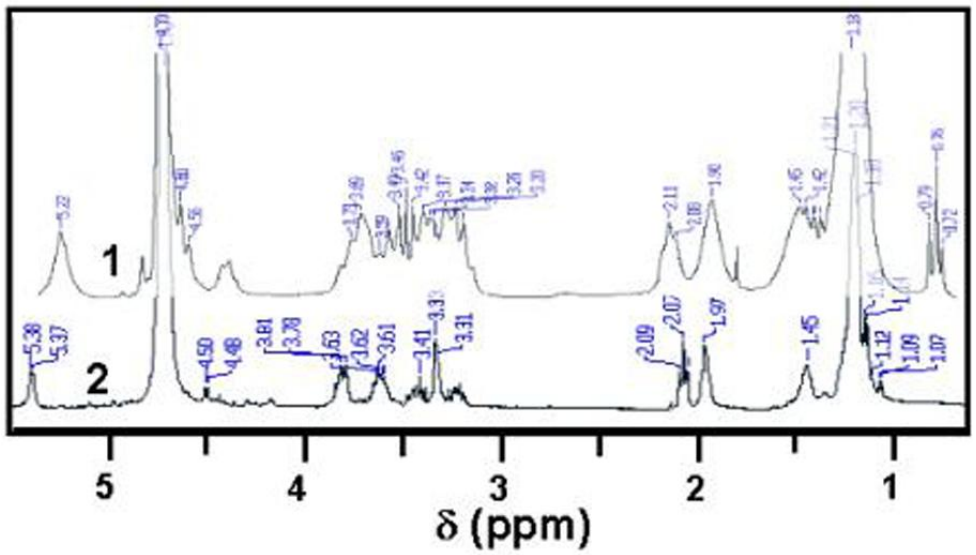

Figure 4.9: *^{1}H NMR spectra taken pure OA-SL molecules (curve-2) and AgNPs capped with OA-SL molecules (curve-1). Spectra shows the downfield shift of δ = 0.16 ppm of the olefinic protons of OA-SL molecule after AgNPs synthesis.*

Also, probably –CH_2OH functional group present in glucose act as reducing agent for Ag^+ ions in to Ag^0. Further, the binding of OA-SL molecules to AgNPs surface through –C=C– is also supported by ^{1}H NMR spectroscopy (Figure 4.9). The spectra (curve-1) clearly show a downfield shift of δ = 0.16 ppm of the olefinic proton (δ = 5.22 ppm) as compared to that in pure OA-SL molecule (δ = 5.38 ppm) (curve-2) [55]. Also, the possibility of binding of some OA-SL molecules to AgNPs surface through –COOH functional group cannot be ruled out. However, it could be concluded that in either case (–COOH or –C=C– group binding to nanoparticle surface), the hydrophilic disaccharide units form the exterior of AgNPs making them water dispersible.

4.3.6 Thermogravimetric Analysis (TGA)

Thermo gravimetric analysis (TGA) was performed on dried powders of OA-SL-AgNPs to calculate the amount of OA-SL molecules present with AgNPs. TGA spectra carried out on OA-SL-AgNPs shows a weight loss in two major regions (Figure 4.10).

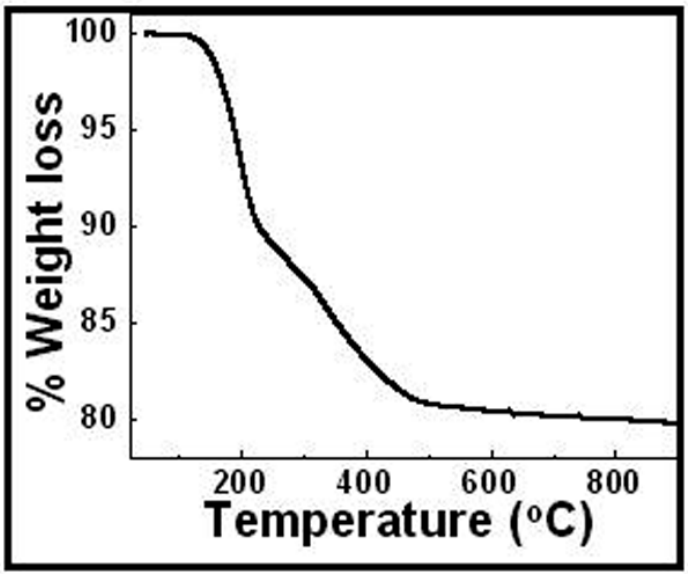

Figure 4.10: *TGA analysis performed on dried powders of OA-SL-AgNPs showing two major regions of weight loss.*

The first region is around 200 ^{o}C (~10 % weight loss) and the second region around 330 ^{o}C (~ 10 % weight loss), which could be ascribed to the evaporation of residual water vapor and sophorolipid (capping) molecules present in the sample respectively. Thus, a total of 20 % weight loss in form of sophorolipid was recorded and rest 80 % of weight could be assigned to AgNPs. Based on simple estimation a population constituting the particles of ~ 15 nm diameter may require ~16 % of capping molecule for stabilization [57]. Whereas in our case the weight loss in form of capping (OA-SL) molecule is slightly higher (20 %), which could be attributed to the dense packing of OA-SL molecules on AgNPs surface or formation of multilayers.

4.3.7 Advantages of OA-SL-AgNPs over OA-AgNPs

Oleic acid (OA), a precursor for sophorolipid, has been used as a capping agent for AgNPs synthesis (OA-AgNPs) [55c]. Therefore, it becomes necessary to compare the two systems for AgNPs synthesis. Oleic acid capping on AgNPs surface depends on the solvent environment, which has been described in detail by Efrima's group [49]. They concluded that in aqueous environment the binding of oleic acid to AgNPs surface takes place through the double bond while in organic environment the –COOH group participates in the binding. The disadvantage of OA capped AgNPs

(OA-AgNPs) is the formation of irreversible aggregates. Also, an exogenous reducing agent needs to be added to accomplish the reduction. However, OA-SL-AgNPs can be easily obtained in form of powder by simple centrifugation/lyophilization. Figure 4.11 shows the UV-visible spectra recorded from as synthesized OA-SL-AgNPs (curve-a), redispersed powders of OA-SL-AgNPs (curve-b), as synthesized OA-AgNPs (curve-c) and redispersed powders of OA- AgNPs (curve-d). It is very clear from UV-visible spectra that after redispersion of powders of OA-SL-AgNPs little aggregation is noticed with no change in position of SPR (at 410 nm) than as synthesized OA-SL-AgNPs. However, redispersed powders of OA-AgNPs (curve-d) showed a broad absorbance (at 400 nm) with diminished intensity, suggesting irreversible aggregation. Also, the redispersed OA-AgNPs powder showed a greenish color (inset, vial-d) than the bright yellow color (inset, vial-b), displayed by the redispersion of OA-SL-AgNPs indicating that OA-AgNPs undergo irreversible aggregation after powder formation. Oleic acid, being a fatty acid, is not very much soluble in water, while after its modification in form of sophorolipid (OA-SL), it becomes readily soluble in aqueous environment. This makes it further advantageous for bio-applications.

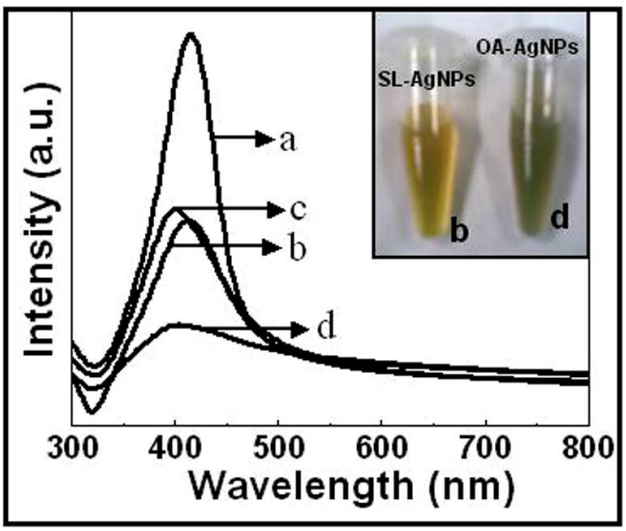

Figure 4.11: *UV-visible spectra recorded from as synthesized OA-SL-AgNPs (curve-a) and as synthesized OA-AgNPs (curve-c) show a clear SPR peak, characteristic to AgNPs. UV-visible spectra recorded from redispersed powders of OA-SL-AgNPs (curve-b) show no change in SPR position, while redispersed powders of OA-AgNPs (curve-d) resulted in to irreversible aggregation with a broad and diminished absorbance. Respective pictures of redispersed powder dispersions of OA-SL-AgNPs (inset-b) and OA-AgNPs (inset-d) is shown in inset.*

4.4 Antibacterial activity of OA-SL-AgNPs and OA-SL

On the basis of above discussion, it is clear that AgNPs synthesized capped with OA-SL is superior to only OA capping. Therefore, it becomes important to further evaluate the advantage of OA-SL-AgNPs over OA-AgNPs and for the same we have chosen the antibacterial activity comparison between the same. Therefore, this part of the chapter gives a brief description about the antibacterial activity of OA-SL-AgNPs against Gram-negative as well as Gram-positive bacterial spp. A concentration dependent antibacterial activity of OA-SL-AgNPs and OA-SL has been described. The probable bactericidal mechanism has been elucidated by lipid peroxidation experiment.

4.4.1 Experimental Details

4.4.1.1 Test of Antibacterial properties

Before performing the antibacterial experiment, the as synthesized OA-SL-AgNPs were dialyzed with 12.5-kDa dialysis membrane for 24 h against copious amount of deionized water in order to remove excess SL and unreduced Ag^+ ions present in nanoparticle solution. The OA-SL-AgNPs, OA-SL etc were autoclaved for 20 min. *Bacillus subtilis* (ATCC 6633, Gram positive bacterium), *Staphylococcus aureus* (ATCC 2079, Gram-positive bacterium) and *Pseudomonas aeruginosa* (ATCC 2207, Gram-negative bacterium) were used for preliminary antibacterial tests of OA-SL alone, following agar-well diffusion method (AWDM) as well as standard dilution micromethod. Pre-inoculums of the above-mentioned bacterial strains were inoculated separately in 100 mL of Luria Bertini medium and incubated (30 °C, 200 rpm) for 24 h in order to perform further experiments. For AWDM, 75 µL of the above said three bacterial strains were separately mixed gently in three different warm (~ 45 °C) and molten Luria-Bertini-Agar solutions (20 mL). These solutions were then poured in three different sterile plates. Wells (~ 7 mm in diameter) were punched in each agar plate using a sterile stainless steel borer. Each well was filled with 100 µL of different concentrations (0.5 %, 1 % and 10 %) of OA-SL. The plates were incubated at 30 °C for 24 h and photograph was taken with a digital camera with a resolution of 2-mega-pixel.

Antibacterial tests of purified OA-SL and OA-SL-AgNPs were performed using standard dilution micromethod. The concentration of as synthesized and purified OA-SL-AgNPs were considered as 100 µg/mL, assuming almost complete reduction of 10^{-3} M (108 µg/mL) of Ag^{+} ions into AgNPs. Based on this the OA-SL-AgNPs were diluted to 5 µg/mL, 10 µg/mL, 20 µg/mL, 40 µg/mL, 60 µg/mL, 80 µg/mL and 100 µg/mL with sterile Millipore water. *Bacillus subtilis* was added to each of these dilutions of SL-AgNPs, at a concentration of 10^{6} CFU/mL and incubated for 12 h under shaking conditions (200 rpm). Aliquots of 100 µL were taken at different time intervals from the above mixture (*Bacillus subtilis* and OA-SL-AgNPs) and plated on Luria-Bertini-Agar plate. The plates were kept for 24 h at 30 °C and bacterial colonies were counted manually. Simultaneously, 100 µL samples was withdrawn from each of the above solutions and drop casted on a freshly peeled off mica chips, dried under dust free environment at room temperature, for AFM analysis. For antibacterial activity assessment against Gram-negative bacterial species, OA-SL-AgNPs were diluted to 5 µg/mL, 10 µg/mL, and 20 µg/mL, rest all the experimental conditions were kept same except the bacterial species, as *Pseudomonas aeruginosa* was taken instead of *Bacillus subtilis*.

Percentage of bacterial cell survival was calculated according to the following formula…

$$\textbf{\% Cell survival} = 100\ X(N_e/N_c) \quad \text{.....(1)}$$

Where, N_e = Number of living bacterial colony on the examination plate

N_c = Number of living bacterial colony on the control plate

While performing antibacterial tests for purified OA-SL against *Bacillus subtilis* and *Pseudomonas aeruginosa*, a range of sophorolipid concentrations (0.25 µg/mL, 0.50 µg/mL, 0.75 µg/mL and 1.0 µg/mL) was taken with bacterial species with a concentration of 10^{5} CFU/mL. Aliquots of 100 µL were taken at different time intervals from the above solutions (bacteria and OA-SL) and plated on Luria-Bertini-Agar plate. The plates were kept for 24 h and incubated at 30 °C. The bacterial colonies were then counted manually. Simultaneously, 100 µL samples was

withdrawn from each of the above solutions and drop casted on freshly peeled off mica chips, dried under dust free environment at room temperature, for AFM analysis.

4.4.1.2 Lipid Peroxidation (LPO) Reaction

Formation of malondialdehyde (MDA) was used as an index to measure lipid peroxidation. MDA was quantified based on its reaction with thiobarbituric acid (TBA) to form a pink MDA-TBA adduct [57], which shows absorbance at 532 nm. 1 mL of bacterial cells treated with OA-SL-AgNPs was mixed with 2 mL of 10 % (wt/vol) trichloroacetic acid, and the solids were removed by centrifugation at 11,000 rpm for 35 min and then for an additional 20 min to ensure that the SL-AgNPs, cells, and precipitated proteins were completely removed. Three milliliters of a freshly prepared 0.67 % (wt/vol) TBA (Sigma Chemical Co.) solution was then added to the supernatant. The samples were incubated in a boiling water bath for 10 min and cooled, and finally the absorbance at 532 nm was measured on Jasco V-570 UV\Vis\NIR spectrophotometer operated at a resolution of 2 nm.

4.4.2 Preliminary antibacterial test of OA-SL

The preliminary and comparative antibacterial activity of pure OA-SL was assessed against *Bacillus subtilis*, *Staphylococcus aureus* and *Pseudomonas aeruginosa* by agar well diffusion method (Figure 4.12).

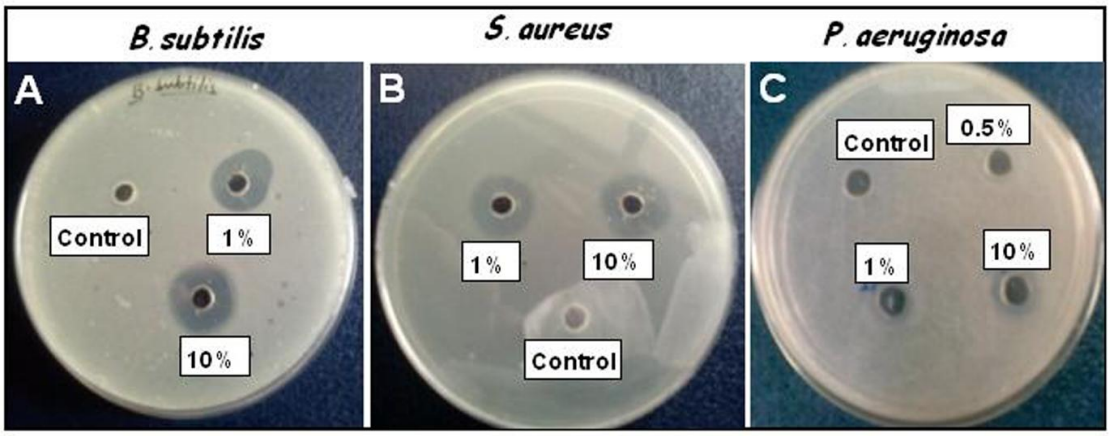

Figure 4.12: *Luria-Bertini-Agar plates showing zone of inhibition of different bacterial colonies (B. subtilis, S. aureus and P. aeruginosa) against different concentrations of pure OA-SL molecules. Pure OA-SL molecules show a clear zone of inhibition against gram-positive bacterial species (A and B) and feeble zone of inhibition against gram-negative bacterium (C).*

A well-defined zone of inhibition was observed at all the concentrations of OA-SL tested against Gram-positive bacteria: *Bacillus subtilis* (Figure 4.12; Plate A) and *Staphylococcus aureus* (Figure 4.12; Plate B), while there was faint zone of inhibition seen only at 10 wt % OA-SL in case of Gram-negative bacteria: *Pseudomonas aeruginosa* (Figure 4.12; Plate C). The difference in bactericidal activity could be related with the cell membrane differences amongst Gram-positive and Gram-negative bacterial strains. Gram-negative bacterium is characterized by extra coating of lipopolysaccharides (LPS) and a thin layer of peptidoglycan, while in Gram-positive bacterium only a thick peptidoglycan layer constitutes the major part of their cell membrane. It seems peptidoglycan layer is more susceptible to OA-SL destruction, which is the outermost and abundant layer in case of Gram-positive bacterial species. However, cell membrane of Gram-negative bacterial species have an extra coating of LPS over a thin peptidoglycan layer, thus probably making their cell membrane more resistant to OA-SL molecules. It has already been reported that pure OA-SL is not very effective against Gram-negative bacteria [51 b] and our results are in accordance with this. In contrast, silver is known to be a broad-spectrum anti-bactericidal agent [58]. Thus it remains to be seen whether OA-SL capping on AgNPs (OA-SL-AgNPs) would impart any effect on the latter's anti-bacterial activity. To address this, antibacterial activity of SL-AgNPs was carried out with *Bacillus subtilis* (Gram-positive) and *Pseudomonas aeruginosa* (Gram-negative).

4.4.3 Antibacterial test of OA-SL-AgNPs against Gram-positive and Gram-negative bacteria

The Gram-positive (*B. subtilis*) and Gram-negative (*Pseudomonas aeruginosa*) bacterium were exposed to different concentrations of OA-SL-AgNPs for 12 h. Samples were taken at different time intervals and plated on luria-bertini-agar plates. Number of bacterial colonies was counted manually after 24 h of incubation at 30 ºC. Figure 4.13 A and B shows the percentage cell survival of *B. subtilis* and it is very clear that at lower concentrations (1 µg/mL, 5 µg/mL and 10 µg/mL) OA-SL-AgNPs showed 28 %, 30 % and 20 % of bacterial cell survival within 3 h of exposure. Also, exposure of OA-SL-AgNPs to *B. subtilis* up to 12 h showed almost similar cell

survival with little decrease. However, OA-SL-AgNPs concentration at 20 µg/mL and above showed almost complete inhibition of bacterial cell survival, as less than 0.6 % cell survival was recorded with in 1 h of exposure (Figure 4.12 B).

Other higher concentrations showed further decrease in cell survival finally leading to as less as 0.16 % survival after 12 h of exposure with 100 µg/mL of OA-SL-AgNPs. The same results are presented in Figure 4.15 and 4.16 in the form of photos of Luria-Bertini-agar plates with grown *B. subtilis* after the treatment with different concentrations of OA-SL-AgNPs. Similarly, different concentrations of OA-SL-AgNPs (1 µg/mL, 5 µg/mL, 10 µg/mL and 20 µg/mL) were incubated with *P. aeruginosa* for 12 h.

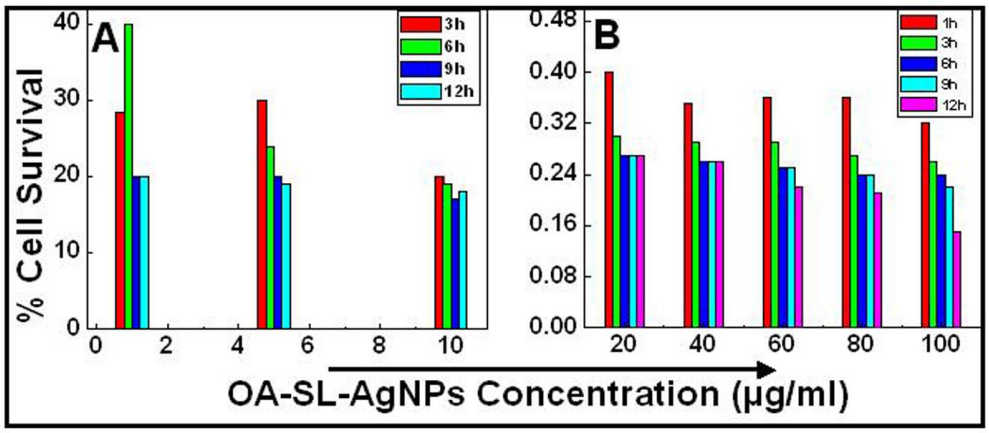

Figure 4.13: *Percentage of viable B. subtilis colonies after the treatment with different concentrations (1 µg/mL, 5 µg/mL and 10 µg/mL in Figure 4.12 A and 20 µg/mL, 40 µg/mL, 60 µg/mL, 80 µg/mL and 100 µg/mL in Figure 4.12 B) of OA-SL-AgNPs for different time intervals. Plates were incubated at 30 ºC for 24 h before colony counting.*

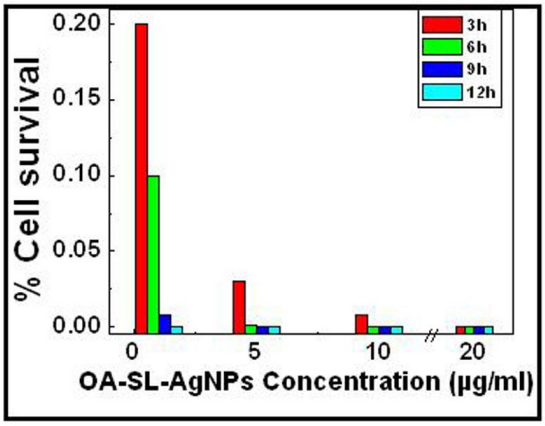

Figure 4.14: *Percentage of viable P. aeruginosa colonies after the treatment with different concentrations (1 µg/mL, 5 µg/mL and 10 µg/mL and 20 µg/mL) of OA-SL-AgNPs for different time intervals. Plates were incubated at 30 ºC for 24 h before colony counting.*

At different time intervals aliquots of 100 µL were plated on luria-bertini-agar plates. These plates were incubated at 30 ºC for 24 h and finally bacterial colonies were counted manually (Figure 4.17). The percentage survival was calculated according to the formula described above (equation No. 1). It is clear from Figure 4.14 that OA-SL-AgNPs showed enhanced bactericidal activity against *P. aeruginosa.* Bacterial cell survival was reduced by 99.8 % with in 3 h of exposure with 1 µg/mL concentrations of OA-SL-AgNPs.

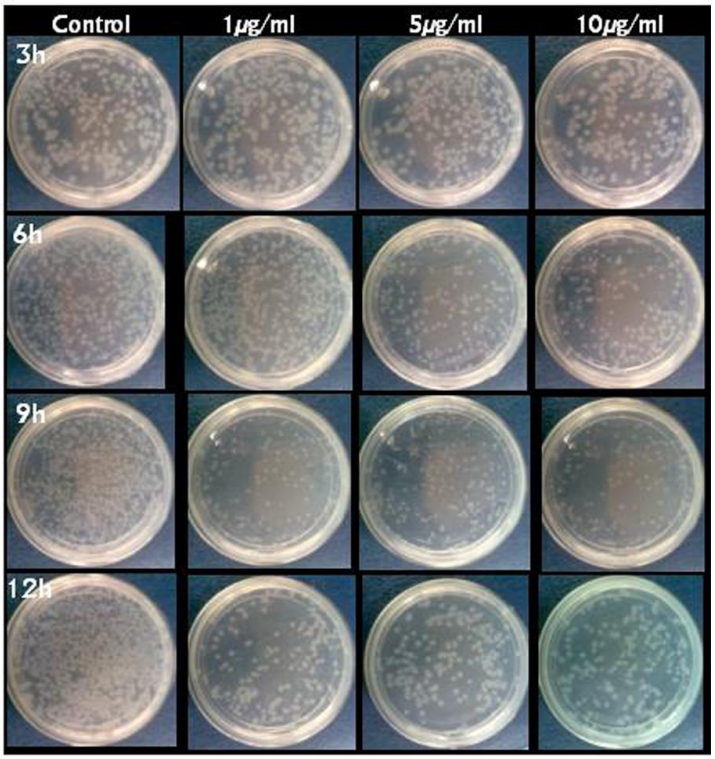

Figure 4.15: *Photos of viable B. subtilis colonies after the treatment with different concentrations (1 µg/mL, 5 µg/mL and 10 µg/mL) of OA-SL-AgNPs for different time intervals. Plates were incubated at 30 ºC for 24 h before taking the photo.*

This concentration showed further more reduction in bacterial cell survival (0.10 %, 0.01 % and 0.0 %) after 6 h, 9 h and 12 h respectively. Further, with 5 µg/mL concentrations of OA-SL-AgNPs exposed to *P. aeruginosa* for 3 h showed 0.03 % cell survival. Other concentration of OA-SL-AgNPs (10 µg/mL and 20 µg/mL) showed almost 100 % killing of *P. aeruginosa* with in 3 h of exposure. The Luria-Bertini-agar plates showing the viable colonies of *B. subtilis* and *P. aeruginosa* exposed to different concentrations of OA-SL-AgNPs are displayed in Figure 4.15, 4.16 and 4.17.

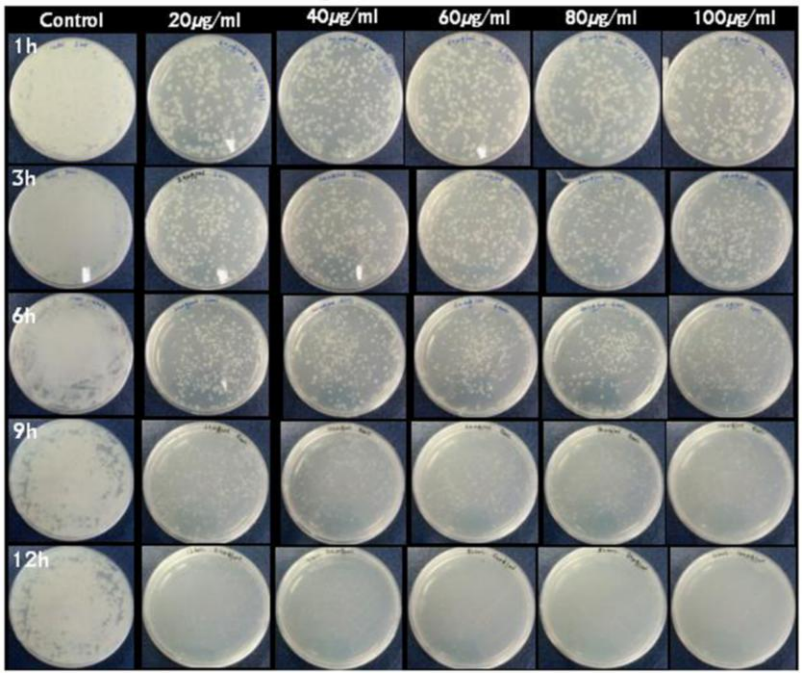

Figure 4.16: *Photos of viable B. subtilis colonies after the treatment with different concentrations (20 µg/mL, 40 µg/mL, 60 µg/mL, 80µg/mL and 100µg/mL) of OA-SL-AgNPs for different time intervals. Plates were incubated at 30 ºC for 24 h before colony count.*

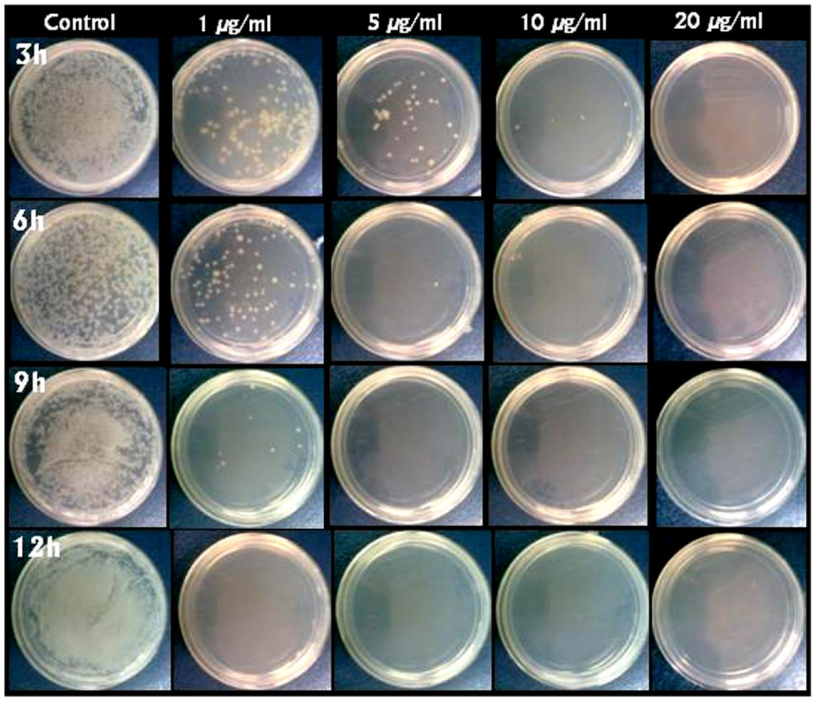

Figure 4.17: *Photos of viable P. aeruginosa colonies after the treatment with different concentrations (1 µg/mL, 5 µg/mL, 10 µg/mL and 20 µg/mL) of OA-SL-AgNPs for different time intervals. Plates were incubated at 30 ºC for 24 h before colony count.*

Thus, from this experiment, it is clear that OA-SL-AgNPs even at lower concentrations show enhanced antibacterial activity against *B. subtilis* as well as *P. aeruginosa.*

4.4.4 AFM image analysis

In order to get information about the bacterial cell morphology we performed contact mode AFM imaging of *B. subtilis* after the treatment with OA-SL-AgNPs.

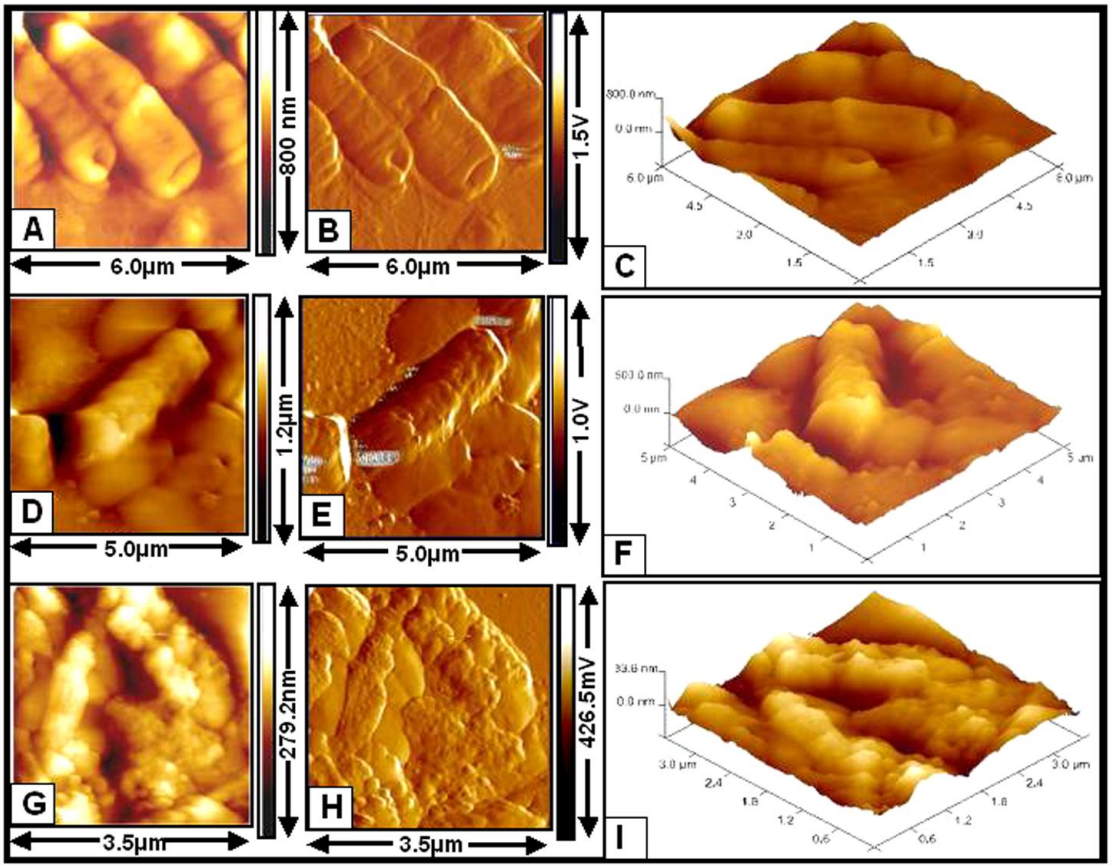

Figure 4.18: *AFM images of B. subtilis cells where A, B and C are height mode, deflection mode and 3D image taken from untreated bacterial cells. D, E and F are height mode, deflection mode and 3D image taken from OA-SL-AgNPs treated bacterial cells incubated for 3 h. G, H and I are AFM image taken from OA-SL-AgNPs treated bacterial cells incubated for 12 h.*

Figure 4.18 A, B and C respectively represents the height mode, deflection mode and 3- dimensional (3D) image of height mode of untreated *B. subtilis* cells (control). Figure D, E and F represents the height, deflection and 3-dimensional image of height mode of 3 h OA-SL-AgNPs treated *B. subtilis* cells. Figure G, H and I represents the height, deflection and 3-dimensional image of height mode of 12 h

treated *B. subtilis* cells with OA-SL-AgNPs. A clear difference can be seen in the morphology of *B. subtilis* cells after the treatment of OA-SL-AgNPs than untreated cells. A smooth cell surface morphology and well intact *B. subtilis* cells can be observed when cells are not treated with OA-SL-AgNPs (Figure 4.18 A, B and C). After the incubation of 3 h, cells started showing the formation of pits and grooves on their cell membrane leading to a roughening of cell morphology (Figure 4.18 D, E and F). Interestingly, after the incubation of *B. subtilis* cells with OA-SL-AgNPs for 12 h, complete disintegration of cell membrane can be seen, as most of the cytoplasmic materials has come out which can be attributed to the high contrast materials present over bacterial cells (Figure 4.18 G, H and I). Shedding of bacterial flagella could also be seen after OA-SL-AgNPs treatment, as compared to healthy cell (Figure A).

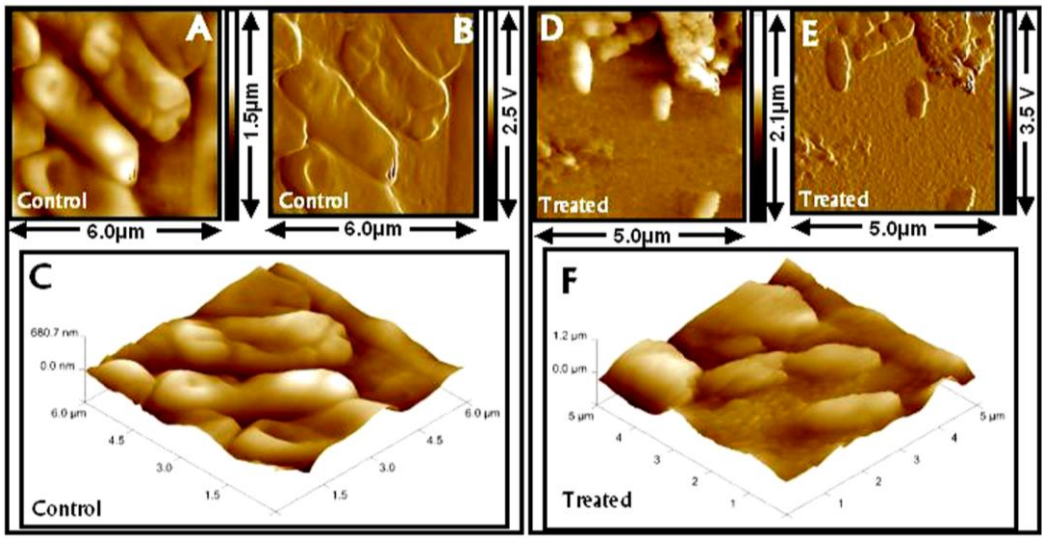

Figure 4.19: *AFM images of P. aeruginosa before (A, B and C) and after (D, E and F) the treatment with OA-SL-AgNPs. Figure A and D are height mode image, B and E are deflection mode image, while C and F are 3-D image.*

Further, the AFM images of *P. aeruginosa* were also taken, which can clearly resolve the differences between live and dead bacteria (Figure 4.19). All the experimental conditions were same as described for *B. subtilis*. Figure 4.19 A, B and C taken from untreated *P. aeruginosa*, showing healthy cells with smooth and intact cell membrane. Figure 4.19 D, E and F are from OA-SL-AgNPs treated *P. aeruginosa* cells. Compared to untreated cells treated bacterial cells showed reduced cell dimensions with rough and ruptured cell membrane. The images from treated *P. aeruginosa* cells also show rough background than untreated cells, which could be

attributed to the oozed out cytoplasmic material and OA-SL-AgNPs. Due to the release of cytoplasm, bacterial cell shrinks and thus smaller cell dimensions could be seen after OA-SL-AgNPs treatment.

4.4.5 Analysis of Lipid peroxidation assay

It has been reported that AgNPs leads to the formation of free radicals, which finally interact with bacterial cell membrane followed by peroxidation of lipids and thus produce malondialdehyde (MDA). Therefore, we have performed lipid peroxidation experiment to confirm the bactericidal mechanism. The bacterial cell supernatant (*B. subtilis,* treated with OA-SL-AgNPs) after boiling with TBA showed a distinct peak (Figure 4.20 A, curve-2) centering at ~ 532 nm, suggesting the presence of MDA. Thus, formation of this pink color MDA-TBA adduct gratified our hypothesis of bacterial cell killing due to the generation of AgNPs mediated free radical generation. However, a weak absorbance could also be seen in case of untreated *B. subtilis* call supernatant (Figure 4.20 A, curve-1), which can be attributed to the formation of some MDA due to their normal biochemical processes and environmental change.

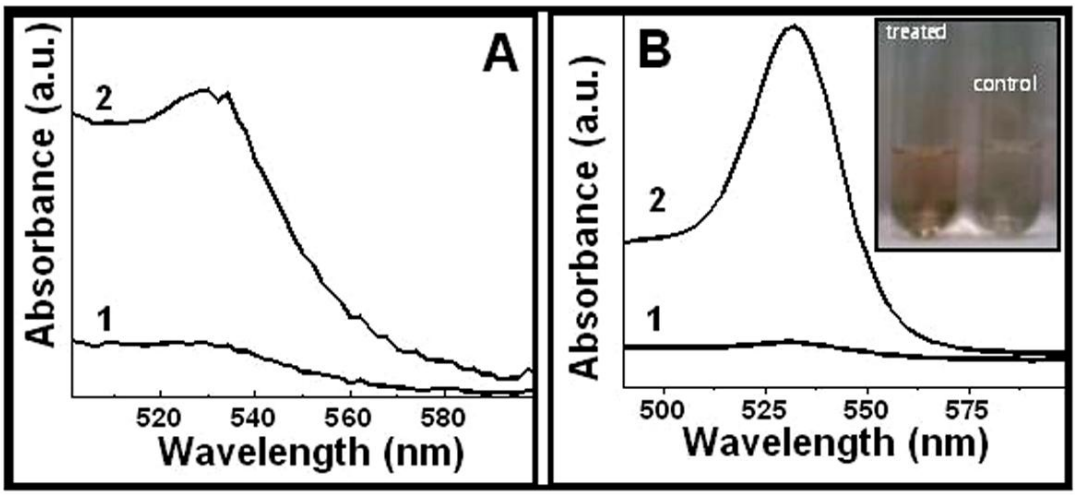

Figure 4.20: *(A) Lipid peroxidation experiment is shown by UV-visible spectra recorded from adduct formed by TBA and MDA released from OA-SL-AgNPs treated (treated, curve-2) and untreated (curve-1) Bacillus subtilis cells. (B) UV-visible spectra recorded from adduct formed by TBA and MDA released from OA-SL-AgNPs treated (treated, curve-2) and untreated (control, curve-1) P. aeruginosa cells. The inset shows the color of respective solution (Figure B).*

Similarly, for Gram-negative bacterial cell (*P. aeruginosa*) (ATCC-2207) membrane damage was also confirmed by lipid peroxidation reaction and shown in figure 4.20 B. Curve-1 (Figure 4.20 B) shows the UV-visible spectra recorded from untreated bacterial cell supernatant while curve-2 was recorded from OA-SL-AgNPs treated bacterial cell supernatant, which is showing a strong absorbance at 532 nm, characteristic for MDA-TBA adduct (formation of pink colour solution). The respective solution color has shown in inset.

Further, experiments were performed where only OA-SL was checked for its bactericidal activity taking the amount of OA-SL present on nanoparticle surface (based on TGA calculations), which did not result into any decrease in bacterial colony count (results have not shown for brevity). Thus, it can be suggested that main causative for bactericidal activity of OA-SL-AgNPs is the AgNPs.

For the mechanism behind the antibacterial activity of AgNPs, two main hypotheses have been put forward. One is the ability of silver to cause pore formation in bacterial cell membrane through the formation of reactive oxygen species (ROS) in the vicinity of bacterial cell membrane and thus increase cell permeability and cell death [59, 60]. The second one is related to the thin layer of Ag^{+} ions, present on the nanoparticle surface or their slow release from the AgNPs itself, that interact with DNA and various cellular enzymes by coordinating to electron donating groups such as thiols, corboxylates, amides, hydroxyls, imidazoles, indoles etc [61, 62]. While the damage of cell membrane leads to the disruption of respiratory chain reactions the interaction of silver ions with DNA inhibits cell division, [61, 62], which ultimately leads to cell death.

The ROS have been postulated to attack polyunsaturated phospholipids present in bacterial cell membrane through lipid peroxidation (LPO) reaction process. This would then pave the way for interaction of silver ions released from OA-SL-AgNPs or the OA-SL-AgNPs themselves with the essential molecules of cells like DNA and enzymes inhibiting the cell division etc. and finally to their death.

The increased activity of OA-SL-AgNPs against Gram-negative bacteria may be attributed to the constitutional differences in the cell membrane of Gram-positive and Gram-negative. The Gram-negative bacteria are characterized with a thin

peptidoglycan layer supported externally by an outer membrane made up of lipopolysaccharides and phospholipids. The OA-SL capping may support a favorable interaction between these lipopolysaccharides/phospholipids and OA-SL capped AgNPs. The presence of porin proteins in this outer layer probably allows a better passage of silver ions inside the bacterial cell once the AgNPs are close to the outer layer. The thin peptidoglycan layer is then accessible to OA-SL-AgNPs making it more susceptible to ROS attack and thus more vulnerable. Conversely, the peptidoglycan layer of Gram-positive bacteria is thicker and hence less vulnerable to the ROS thus requiring more amounts of OA-SL-AgNPs for their killing.

4.4.6 Antibacterial test of OA-AgNPs

As we have discussed the advantages of OA-SL-AgNPs over OA-AgNPs in previous section of this chapter, we also performed bactericidal activity of oleic acid capped AgNPs in similar experimental set up as described above. Bactericidal kinetics was followed up to 12 h. As it is clear from Figure 4.23 that almost 99.7 % bactericidal activity was recorded after incubating the *B. subtilis* cells with 20 µg/mL concentration of OA-AgNPs.

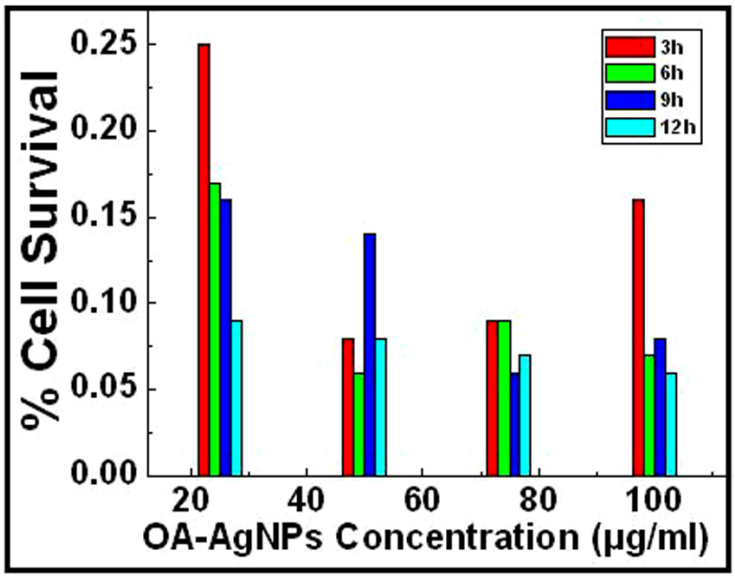

Figure 4.23: *Percentage of viable B. subtilis colonies after the treatment with different concentrations (20 µg/mL, 40 µg/mL, 60 µg/mL, 80 µg/mL and 100 µg/mL) of OA-AgNPs for different time intervals. Plates were incubated at 30 ºC for 24 h before colony counting.*

With further increased concentrations of OA-AgNPs (from 40-100 µg/mL) showed decrease in bacterial cell survival (< 0.15). Corresponding photographs of Luria-Bertini-agar plates are shown in Figure 4.24. Although, almost similar bactericidal activity was shown by as synthesized solutions of OA-AgNPs and OA-SL-AgNPs the stability and storage of OA-SL-AgNPs in form of powder makes it better than OA-AgNPs. Also, OA-SL acts as reducing and capping agent both while for OA-AgNPs synthesis, an external reducing agent ($NaBH_4$) is required.

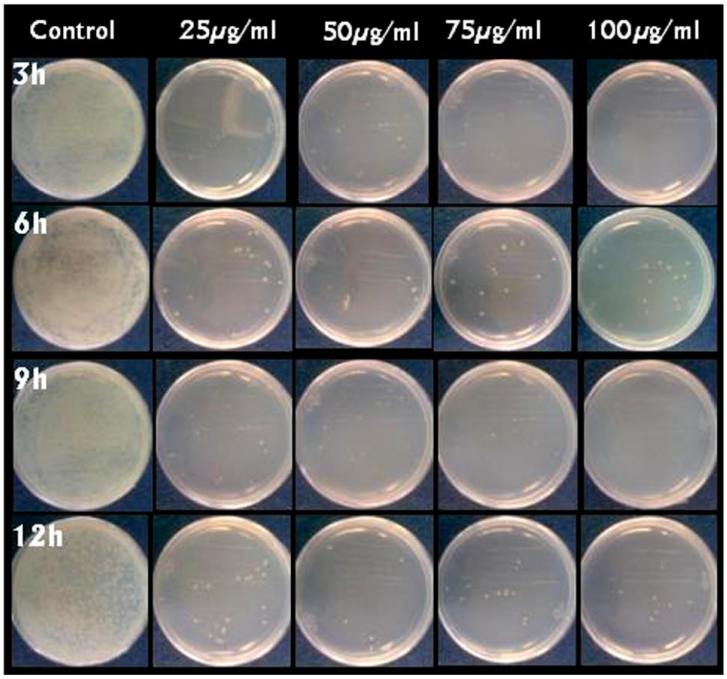

Figure 4.24: *Photos of viable P. aeruginosa colonies after the treatment with different concentrations (25 µg/mL, 50 µg/mL, 75 µg/mL and 1 µg/mL) of OA-AgNPs exposed for 12 h. Plates were incubated at 30 ºC for 24 h before colony count and photograph.*

4.5 Use of OA-SL for synthesis of gold nanoparticles

This part of chapter describes the room temperature synthesis of AuNPs with the use of OA-SL molecules that act as reducing as well as stabilizing/capping agent. These AuNPs were characterized with UV-visible spectroscopy, FTIR spectroscopy and TEM.

4.5.1 Experimental Details

The OA-SL molecules (1 X 10^{-4} M) were added to a solution of $HAuCl_4$ (1 X 10^{-4} M) and incubated for 12 h. The development of purple color indicated the formation of AuNPs. Dialyzing with 12-kDa molecular weight cut-off dialysis

membrane for 24 h, further purified this AuNP solution and characterizations were performed on this purified AuNPs solutions.

4.5.2 UV-visible spectra analysis

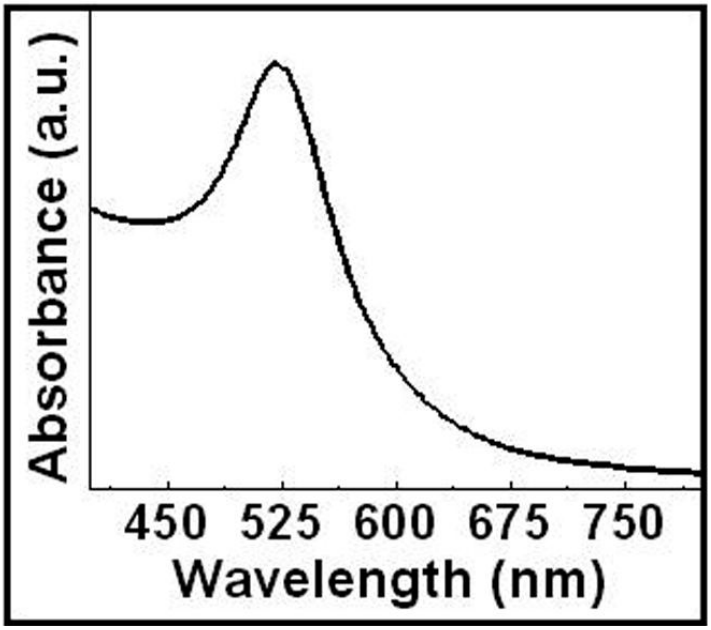

Figure 4.25: *UV-visible spectra recorded from purified solution of OA-SL reduced AuNPs. UV-visible spectra shows characteristic SPR band for AuNPs at 520 nm.*

The UV-visible spectra (Figure 4.25) recorded from OA-SL mediated reduction of Au^{3+} ions to Au^{0} leading to the formation of OA-SL capped AuNPs (OA-SL-AuNPs). The solution colour changes from colorless to purple color. The surface plasmon resonance band at ~ 521 nm, characteristic to AuNPs [54], can be seen. This type of SPR pattern indicates the presence of spherical nanoparticles in the solution.

4.5.3 FTIR spectra analysis

The FTIR spectra (Figure 4.26) recorded from purified OA-SL molecules (curve-1) and OA-SL-AuNPs (curve-2) displays a clear difference between the two spectra, which is marked and enlarged in the accompanying panels. Panel-I represents the carbonyl region (1400 cm^{-1} to 1800 cm^{-1}) and panel-II shows the olefinic and methylene region (2700 cm^{-1} to 4000 cm^{-1}). Panel-I, curve-1 shows the presence of two distinct transmission peaks centering at 1710 cm^{-1}, which could be attributed to the –C=O stretch [48]. This peak gets shifted after AuNPs synthesis to 1636 cm^{-1} suggesting the involvement of carbonyl group in nanoparticle capping. Also, on

magnifying panel-II, clear transmittance peak centering at 2926 cm^{-1} and 2848 cm^{-1} (curve-1) is seen which corresponds respectively to asymmetrical streching and symmetrical streching of methylene groups [48].

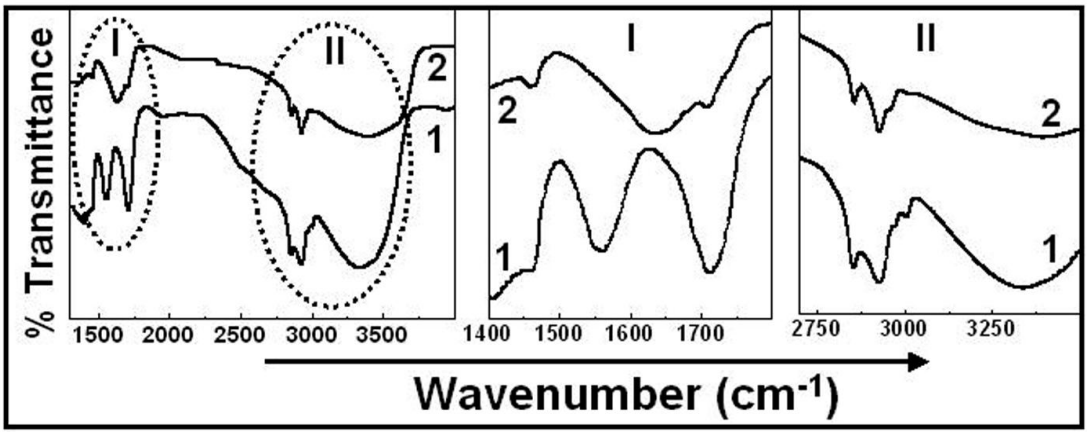

Figure 4.26: *FTIR spectra recorded from purified OA-SL samples (curve-1) and OA-SL-AuNPs sample (curve-2). Carbonyl region (panel-I) and olefinic region (panel-II), marked by circle, is enlarged in the accompanying panels. Details have provided in text.*

FTIR spectra recorded after AuNPs synthesis (curve-2) showed almost no appreciable shift in transmittance peak positions for asymmetrical streching (2929 cm^{-1}) and symmetrical streching (2852 cm^{-1}) of methylene groups, suggesting that these functional groups are not involved in nanoparticle synthesis/capping. Also, in panel-II, curve-1 shows a typical transmittance band at 3004 cm^{-1}, which corresponds to the =C-H streching vibrations [48]. However, the complete disappearance of this band in panel-II, curve-2, suggests its active participation in nanoparticle synthesis/capping.

4.5.4 TEM and XRD pattern analysis

TEM images of OA-SL-AuNPs reveal the formation of spherical shaped nanoparticles. Particles having size of ~ 10 nm could be seen on TEM grid (Figure 4.27). TEM image showed the presence of AuNPs clusters and this could be assigned to the interactions between OA-SL molecules, which bring OA-SL-AuNPs close to each other and thus it looks like aggregate. Based on UV-vis spectra it can be suggested that this aggregation occurs on the TEM grids due to solvent evaporation. The SAED pattern (Figure 4.27 C) obtained from OA-SL-AuNPs were indexed on the basis of FCC structure of crystalline gold [63]. XRD pattern (Figure 4.26 D) also

showed the characteristic Bragg's reflexion, indexed for the [111], [200], [220] and [311] planes of crystalline gold [63].

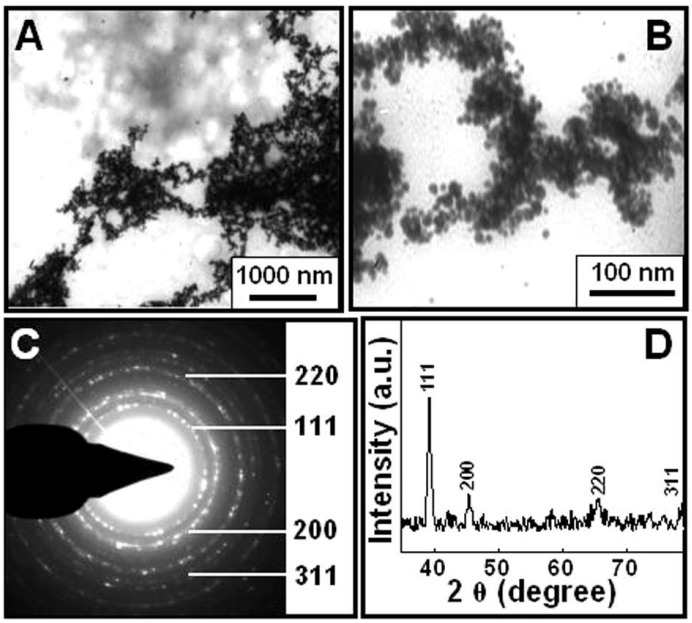

Figure 4.27: *TEM images (A and B), SAED (C) and XRD pattern (D) taken from purified sample of OA-SL-AuNPs. SAED pattern shows clear ring patterns, indexed for different planes of crystalline gold. XRD pattern also shows Bragg's reflexions, characteristic to gold.*

4.6 Conclusions

Successful biotransformation of OA in to corresponding SL by the use of *C. bombicola* and their potentiality for the synthesis of water soluble metal nanoparticles (AgNPs and AuNPs) have been described in this chapter. The so synthesized sophorolipid molecules were completely characterized by FTIR, NMR and Mass spectroscopy. This molecule has shown its ability to act as capping agent for magnetic (Co) nanoparticles too [47]. However, here it has been used as capping/stabilizing agent as well as reducing agent for the production of AuNPs and AgNPs, thus expanding its utility. Conversion of water insoluble oleic acid molecules in to water-soluble sophorolipid molecules is the crucial point, which thereby renders the nanoparticles capped by them, fairly water-soluble. While doing so, the sophorolipid molecules adjust themselves in a manner where they attach to the nanoparticle surface very often through their olefinic functional group and by –COOH functional groups. However, among all these cases their sophorose moiety is exposed towards exterior aqueous medium thereby making the whole nanoparticle system hydrophilic. Another

advantage of this molecule, which makes it even more interesting, is its ability to derive the AgNPs in the form of powder and further its redispersiblity with diminutive aggregation, which is not the case with oleic acid capped AgNPs.

As OA-SL and AgNPs both are well known bactericidal agent, another advantage of OA-SL capped AgNPs is their synergistic antibacterial activity against Gram-negative (*P. aeruginosa*) and Gram-positive (*B. subtilis and S. aureus*) bacterial species. It has been well established in reports that OA-SL alone is not very effective against Gram-negative bacterial species, but after incorporation with AgNPs, it showed improved bactericidal potential (~ 99.5 % bacterial killing within 3 h) against a pathogenic bacterium (*P. aeruginosa*). Almost similar bactericidal activity was observed against gram-positive bacterial species. AFM image and LPO experiments suggest free radicals mediated cell membrane damage, which thereby causes cell death. As from AFM images, cell membrane damage followed by leakage of cytoplasmic material could be seen very obviously.

Glycolipid-nanoparticle conjugates are receiving great attention these days for their potential applications in various fields. The method presented here are probably the easiest to obtain such lipid-nanoparticle conjugates. Further experiments need to be performed to evaluate their possible applications in other fields also.

4.7 References

[1] (a) Moreno-Manas, M.; Pleixats, R. *Acc. Chem. Res.* **2003**, *36***,** 638. (b) Mirkin, C. A.; Letsinger, R. L.; Mucic, R. C.; Storhoff, J. J. *Nature* 1996, *382***,** 607. (c). Han, M.; Gao, X.; Su, J. Z.; Nie, S. *Nature Biotechnol*. 2001, *19***,** 631. (d) Sun, S.; Murray, C. B.; Weller, D.; Folks, L.; Moser, A. *Science* 2000, *287***,** 1989. (e) Kamat, P. V. *J. Phys. Chem. B* **2002**, *106***,** 7729.

[2] (a) West, J. L.; Halas, N. J. *Annu. Rev. Biomed. Eng.* **2003**, *5*, 285. (b) Paciotti, G. F.; Myer, L.; Weinreich, D.; Goia, D.; Pavel, N.; McLaughlin, R. E.; Tamarkin, L. *Drug Deli*V*ery* **2004**, *11*, 169. (c) Jain, K. K. *Technol. Cancer Res. Treat*. **2005**, *4*, 407.

[3] (a) Wu, X.; Liu, H.; Liu, J.; Haley, K. N.; Treadway, J. A.; Larson, J. P.; Ge, N.; Peale, F.; Bruchez, M. P. *Nat. Biotechnol.* **2003**, *21*, 41. (b) Chan, W. C. W.; Maxwell, D. J.; Gao, X.; Bailey, R. E.; Han, M.; Nie, S. *Curr. Opin. Biotechnol*. **2002**, *13*, 40. (c) Alivisatos, A. P. *Nat. Biotechnol*. **2004**, *22*, 47. (d) Sokolov, K.; Aaron, J.; Hsu, B.; Nida, D.; Gillanwater, A.; Follen, M.; Macaulay, C.; Adler-Storthz, K.; Korgel, B.; Discour, M.; Pasqualini, R.; Arap, W.; Lam, W.; Richartz-Kortum, R. *Technol. Cancer Res. Treat.* **2003**, *2*, 491.

[4] Hirsch, L. R.; Stafford, R. J.; Bankson, J. A.; Sershen, S. R.; Rivera, B.; Rrice, R. E.; Hazle, J. D.; Halas, N. J.; West, J. L. *Proc. Natl. Acad. Sci. U.S.A.* **2003**, *100*, 13549.

[5] Sokolov, K.; Follen, M.; Aaron, J.; Pavlova, I.; Malpica, A.; Lotan, R.; Richartz-Kortum, R. *Cancer Res*. **2003**, *63*, 1999.

[6] Morones, J. R.; Elechiguerra, J. L.; Camacho, A.; Holt, K.; Kouri, J. B.; Ramirez, J. T.; Yacaman, M. J. *Nanotechnology* **2005**, *16*, 2346.

[7] Hasell, T.; Yang, J.; Wang, W.; Brown, P. D.; Howdle, S. M. *Mater. Lett*. **2007**, *61*, 4906.

[8] (a) Vigneshwaran, N.; Nachane, R. P.; Balasubramanya, R. H.; Varadarajan, P. V. *Carbohydr. Res*. **2006**, *341*, 2012. (b) Wang, Y.; Wong, J. F.; Teng, X.; Lin, X. Z.; Yang, H. *Nano Lett*. **2003**, *3*, 1555. (c) Pande, S.; Ghosh, S. K.; Praharaj, S.; Panigrahi, S.; Basu, S.; Jana, S.; Pal, A.; Tsukuda, T.; Pal, T. *J. Phy. Chem. C*

2007, *111*, 10806. (d) He, B.; Tan, J. J.; Liew, K. Y.; Liu, H. *J. Mol. Cata. A* **2004**, *221*, 121.

[9] Lee, P. C.; Meisel, D. *J. Phy. Chem*. **1982**, *86*, 3391.

[10] Creighton, J. A.; Blatchford, C. G.; Albrecht, M. G. *J. Chem. Soc., Faraday Trans*. **1979**, *75*, 790.

[11] Evanoff Jr. D. D.; Chumanov, G. *J. Phy. Chem. B* **2004**, *108*, 13948 and references cited there in.

[12] (a) Selvakannan, P. R.; Mandal, S.; Phadtare, S.; Gole, A.; Pasricha, R.; Adyanthaya, S. D.; Sastry, M. *J. Colloid Interface Sci*. **2004**, *269*, 97. (b) Selvakannan, P. R.; Swami, A.; Srisathiyanarayanan, D.; Shirude, P. S.; Pasricha, R.; Mandale, A. B.; Sastry, M. *Langmuir* **2004**, *20*, 7825.

[13] (a) Willner, I.; Heleg-Shabtai, V.; Blonder, R.; Katz, E.; Tao, G. *J. Am. Chem. Soc*. **1996**, *118*, 10321. (b) Willner, I.; Katz, E.; Willner, B. *Electroanalysis* **1997**, *9*, 965.

[14] Rangnekar, A.; Sarma, T. K.; Singh, A. K.; Deka, J.; Ramesh, A.; Chattopadhyay, A. *Langmuir* **2007,** *23*, 5700.

[15] Niemeyer, C. M. *Angew. Chem. Int. Ed.* **2001**, *40*, 4128.

[16] (a) de la Fuente, J. M.; Barrientos, A. G.; Rojas, T. C.; Rojo, J.; Cañada, J.; Fernández, A.; Penadés, S. *Angew. Chem. Int. Ed.* **2001**, *40*, 2257. (b) Huang, H.; Yuan, Q.; Yang, X. *Colloids Surf. B* **2004**, *39*, 31.

[17] (a) Chen, Y.; Ji, T.; Rosenzweig, Z. *Nano Lett.* **2003**, *3*, 581. (b) Sun, X.-L.; Cui, W.; Haller, C.; Chaikof, E. L. *ChemBioChem* **2004**, *5*, 1593. (c) de la Fuente, J. M.; Penadés, S. *Tetrahedron: Asymmetry* **2005**, *16*, 387.

[18] Penades, S.; Martin-Lomas, M.; de la Fuente, J. M.; Rademacher, T. W. Magnetic Nanoparticles, WO 2004/108165 A2

[19] (a) Murray, C. B.; Kagan, C. R.; Bawendi, M.G. *Annu. Rev. Mater. Sci*. **2000**, *30*, 545. (b) Lopez-Cartes, C.; Rojas, T. C.; Litran, R.; Martinez-Martinez, D.; de la Fuente, J. M.; Penades, S.; Fernandez, A. *J. Phys. Chem. B* **2005**, *109*, 8761. (c) Katz, E.; Willner, I. *Angew. Chem. Int. Ed.* **2004**, *33*, 6042.

[20] Rojo, J.; Diaz, V.; de la Fuente, J. M.; Segura, I.; Barrientos, A. G.; Riese,H. H.; Bernad, A.; Penades, S. *ChemBioChem* **2004**, *5*, 291.

[21] Eggens, I.; Fenderson, B. A.; Toyokuni, T.; Dean, B.; Stroud, M. R.; Hakomori, S.; *J. Biol. Chem.* **1989**, *264*, 9476.

[22] Hakomori, S.-I. *Pure Appl. Chem.* **1991**, *63*, 473.

[23] Kojima, N.; Hakomori, S.-I. *J. Biol. Chem.* **1989**, *264*, 20159.

[24] Song, Y.; Withers, D. A.; Hakomori, S.-I.; *J. Biol. Chem.* **1998**, *273*, 2517.

[25] Otsuji, E.; Park, Y. S.; Tashiro, K.; Kojima, N.; Toyokuni, T.; Hakomori, S.-I. *Int. J. Oncol.* **1995**, *6*, 319.

[26] Yu, S.; Kojima, N.; Hakomori, S.-I.; Kudo, S.; Inoue, S.; Inoue, Y. *Proc. Natl. Acad. Sci. U. S. A.* **2002**, *99*, 2854.

[27] Nolting, B.; Yu, J.-J.; Liu, G.-Y.; Cho, S.-J.; Kauzlarich, S.; Gervay-Hague, J. *Langmuir* **2003**, *19*, 6465.

[28] Halkes, K. M.; de Souza, A. C.; Maljaars, C. E. P.; Gerwig, G. J.; Kamerling, J. P. *Eur. J. Org. Chem.* **2005**, *17*, 3650.

[29] Robinson, A.; Fang, J.-M.; Chou, P. T.; Liao, K. W.; Chu, R. M.; Lee, S.-J.; *ChemBioChem* **2005**, *6*, 1899.

[30] Barrientos, A. G.; de la Fuente, J. M.; Rojas, T. C.; Fernández, A.; Penadés, S. *Chem.- Eur. J.* **2003**, *9*, 1909.

[31] Murray, C. B.; Kagan, C. R.; Bawendi, M. G. *Annu. Rev. Mater. Sci.* **2000**, 30, 545.

[32] Lopez-Cartes, C.; Rojas, T. C.; Litran, R.; Martinez-Martinez, D.; de la Fuente, J. M.; Penades, S.; Fernandez, A. *J. Phys. Chem. B* **2005**, *109*, 8761.

[33] de la Fuente, J. M.; Penadés, S. *Biochimica et Biophysica Acta.* **2006**, *1760*, 636.

[34] Bisht, K. S.; Gross, R. A.; Kaplan, D. L. *J Org Chem* **1999**, *64*, 780.

[35] Gorin, A. P. J.; Spencer, J. F. T.; Tulloch, A. P. *Can. J. Chem.* **1961**, *39*, 846.

[36] Cameotra, S. S.; Makkar, R. S. *Curr. Opin. Microbiol.* **2004**, *7*, 262.

[37] (a) Tulloch, A. P.; Spencer, J. F. T. *Can J Chem* **1968,** *46*, 1523. (b) Tulloch, A. P.; Spencer, J. F. T.; Gorin, P. A. J. *Can J Chem* **1962,** *40*, 1326.

[38] Spencer, J. F. T.; Gorin, P. A. J.; Tulloch, A. P. *Antonie Van Leeuwenhoek* **1970**, *36*, 129.

[39] Chen, J.; Song, X.; Zhang, H.; Qu, Y. B.; Miao, J. Y. *Enzyme Microb Technol* **2006,** *39*, 501.

[40] Jones, D. F. *J. Chem. Soc. (C)* **1968**, 2827.

[41] Van Bogaert, I. N. A.; Saerens K.; Muynck, C. D.; Develter,D.; Soetaert, W.; Vandamme, E. *J. Appl Microbiol Biotechnol* **2007**, *76*, 23.

[42] (a) Jain, P.; Pradeep, T. *Biotech. Bioengg*. **2005**, *90*, 59. (b) Tarimala, S.; Kothari, N.; Abidi, N.; Hequet, E.; Fralick, J.; Dai, L. L. *J. Appl. Polymer Sci*. **2006**, *101*, 2938. (c) Melaiye, A.; Sun, Z.; Hindi, K.; Milsted, A.; Ely, D.; Reneker, D. H.; Tessier, C. A.; Youngs, W. J. *J. Am. Chem. Soc*. **2005**, *127*, 2285. (d) Elechiguerra, J. L.; Burt, J. L.; Morones, J. R.; Camacho-Bragado, A.; Gao, X.; Lara, H. H.; Yacaman, M. J. *J. Nanobiotech*. **2005**, 3. This paper can be accessed at http://www.jnanobiotechnology.com/content/3/1/6.

[43] Silver, S.; Phung, L. T. *Annu. Rev. Microbiol*. **1996**, *50*, 753.

[44] (a) Morones, J. R.; Elechiguerra,J. L.; Camacho, A.; Holt, K.; Kouri, J. B.; Ramirez, J. T.; Yacaman, M. J. *Nanotechnology*, **2005**, *16*, 2346. (b) Melaiye, A.; Sun, Z.; Hindi, K.; Milsted, A.; Ely, D.; Reneker, D. H.; Tessier C. A.; Youngs, W. J. *J. Am. Chem. Soc.* **2005**, *127*, 2285. (c) Sondi, I.; Salopek-Sondi, B. *J. Colloid Interface Sci*. **2004**, *275*, 177. (d) Gogoi, S. K.; Gopinath, P.; Paul, A.; Ramesh, A.; Ghosh, S. S.; Chattopadhyay, A. *Langmuir*, **2006**, *22*, 9322. (e) Sambhy, V.; MacBride, M. M.; Peterson, B. R.; Sen, A. *J. Am. Chem. Soc.* **2006**, *128*, 9798. (f) Kim, J. S.; Kuk, E.; Yu, K. N.; Kim, J.-H.; Park, S. J.; Lee, H. J.; Kim, S. H.; Park, Y. K.; Park, Y. H.; Hwang, C.-Y.; Kim, Y.-K.; Lee, Y.-S.; Jeong, D. H.; Cho, M.-H. *Nanomedicine* **2007**, *3*, 95.

[45] Feng, Q. L.; Wu, J.; Chen, G. Q.; Cui, F. Z.; Kim, T. N.; Kim, J. O. *J. Biomed. Mater. Res*. **2000**, *52*, 662.

[46] (a) Gupta, A.; Maynes, M.; Silver, S. *Appl. Environ.Microbiol*. **1998**, *64*, 5042. (b) Matsumura, Y.; Yoshikata, K.; Kunisaki, S.-I.; Tsuchido, T. *Appl. Environ. Microbiol.* **2003**, *69*, 4278.

[47] Kasture, M.; Singh, S.; Patel, P.; Joy, P. A.; Prabhune, A. A.; Ramana, C. V.; Prasad, B. L. V. *Langmuir* **2007**, *23*, 11409.

[48] Silverstaein, R. M.; Webster, F. X. *Spectrometric Identification of Organic Compounds*, Sixth ed. Wiley, New York **1998**.

[49] (a) Wang, W.; Efrima, S.; Regev, O. *Langmuir* **1998**, *14*, 602. (b) Wang, W.; Chen, X.; Efrima, S. *J. Phys. Chem. B* **1999**, *103*, 7238. (c) Bala, T.; Swami, A.; Prasad, B. L. V.; Sastry, M. *J. Colloid Interface. Sci*. **2005**, *283*, 422.

[50**]** Mantsch, H. H.; Chapman, D. *Infrared Spectroscopy of Biomolecules*. Wiley, New York, NY, **1996**.

[51] (a) Zhou, S.; Xu, C.; Wang, J.; Gao, W.; Akhverdiyeva, R.; Shah, V.; Gross, R. *Langmuir*, **2004**, *20*, 7926. b) Rau, U.; Heckmann, R.; Wray, V.; Lang, S. *Biotechnol. Lett*. **1999**, *21*, 973. c) Azim, A.; Shah, V.; Doncel, G. F.; Peterson, N.; Gao, W.; Gross, R. *Bioconj. Chem.* **2006**, *17*, 1523. (d) Chen, J.; Song, X.; Zhang, H.; Qu, Y. B.; Miao, J. Y. *Enzyme Microb Technol* **2006**, *39*, 501.

[52] De Koster, C. G.; Heerma, W.; Pepermans, H. A. M.; Groenewegen, A.; Peters, H.; Haverkamp, J. *Anal. Biochem*, **1995**, *230*, 135.

[53] (a) Link, S.; El-Sayed, M.A.; *J. Phys. Chem. B* **1999**, *103*, 8410. (b) Mulvaney, P.; *Langmuir* **1996**, *12***,** 788.

[54] The SAED patterns, XRD spectra were indexed with reference to the crystal structures from the ASTM charts: silver (chart card no.04-0783).

[55] Such down shielded proton signals have earlier been observed in thiol bound metal nanoparticle cases and are attributed to the proximity of these protons to the metal surface. (a) Terril, R. H.; Postlethwaite, T. A.; Chen, C.-H.; Poon, C.-D.; Terzis, A.; Chen, A.; Hutchison, J. E.; Clark, M. R.; Wignall, G.; Londono, J. D.; Superfine, R.; Flavo, M.; Johnson, C. S., Jr.; Samulski, E. T.; Murray, R. W. *J. Am. Chem. Soc*. **1995**, *117*, 12537. (b) Badia, A.; Singh, S.; Demers, L.; Cuccia, L.; Brown, G. R.; Lennox, R. B. *Chem. Eur. J*. **1996**, *2*, 359. (c) Hasan, M.; Bethell, D.; Brust, M. *J. Am. Chem. Soc*. **2002**, *124*, 1132. (d) Badia, A.; Gao, W.; Singh, S.; Demers, L.; Cuccia, L.; Reven, L. *Langmuir* **1996**, *12*, 1262. (e) Kumar, A.; Mandal, S.; Selvakannan, P. R.; Pasricha, R.; Mandale, A. B.; Sastry, M. *Langmuir* **2003**, *19*, 6277. (f) Leff, D. V.; Brandt, L.; Heath, J. R. *Langmuir* **1996**, *12*, 4723.

[56] Luedtke, W. D.; Landman, U. *J. Phys. Chem*. **1996**, *100*, 13323. (b) Luedtke, W. D. Landman, U. *J. Phys. Chem. B* **1998**, *102*, 6566.

[57] Esterbauer, H.; Cheeseman. K. H. *Methods Enzymol*. **1990**, *186B*, 407.

[58] Panacek, A.; Kvıtek, L.; Prucek, R.; Kolar, M.; Vecerova, R.; Pizurova, N.; Sharma, V. K.; Nevecna, T.; Zboril R. *J. Phys. Chem. B* **2006**, *110*, 16248.

[59] (a) Gupta, A.; Maynes, M.; Silver, S. *Appl. Environ.Microbiol.* **1998**, *64*, 5042. (b) Matsumura, Y.; Yoshikata, K.; Kunisaki, S.-I.; Tsuchido, T. *Appl. Environ. Microbiol.* **2003**, *69*, 4278.

[60] Sondi, I.; Salopek-Sondi, B. *J. Colloid Interface Sci*. **2004**, *275*, 177. (b) Maness, P.-C.; Smolinski, S.; Blake, D. M.; Huang, Z.; Wolfrum, E. J.; Jacoby, W. A. *Appl. Environ. Microbiol*., **1999**, *65*, 4094.

[61] Feng, G. L.; Wu, J.; Chen, G. Q.; Cui, F. Z.; Kim, T. M.; Kim, O. J. *J. Biomed. Mater. Res.* **2000**, *52*, 662. (b) Holt, K. B.; Bard, A. J. *Biochemistry* **2005**, *44*, 13214. (c) Hatchett, D. W.; Henry, S. *J. Phys. Chem.* **1996**, *100***,** 9854. (d) Vitanov, T.; Popov, A. *J. Electroanal. Chem.* **1983**, *159*, 437. (e) Ahrland, S.; Chatt, J.; Davies, N. R. *Q. Rev. Chem. Soc.* **1958,** *12* 265. (f). Alcamo, I. E.; *Fundamentals of Microbiology* 5th edn. Addison Wesley Longman Inc. Reading, MA **1997**. (g) Feng, Q. L. *et al J. Biomed. Mater. Res*. **2000**, *52*, 662. (h) Morones, J. R.; Elechiguerra, J. L.; Camacho, A.; Holt, K.; Kouri, J.; Ramirez, J. T.; Yacaman, M. J. *Nanotechnology* **2005**, *16*, 2346.

[62] Panacek, A.; Kvıtek, L.; Prucek, R.; Kolar, M.; Vecerova, R.; Pizurova, N.; Sharma, V. K.; Nevecna, T.; Zboril R. *J. Phys. Chem. B* **2006**, *110*, 16248.

[63] The SAED patterns, XRD spectra were indexed with reference to the FCC crystal structures from *JCPDS-International Center for Diffraction Data PCPDFWIN* version 1.30, 04-0784.

Chapter V

In vitro Cytotoxicity and Genotoxicity Assessments of Bio-inspired Nanomaterials

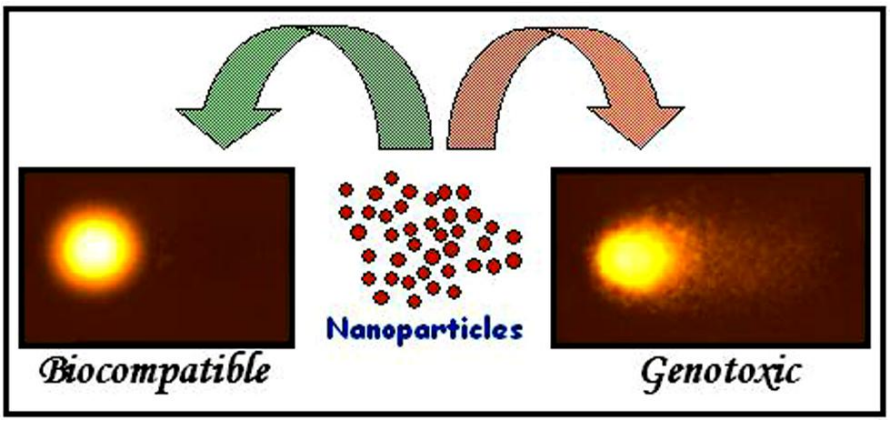

Nanoparticles are being extensively used in medical field especially as diagnostic and therapeutic tools to better understand, detect and treat human diseases. Therefore, understanding toxicity effects of nanoparticles is imperative before their clinical uses. We have discussed several new procedures for the synthesis of AuNPs, AgNPs, TiO_2 NPs and ZnO NPs. These nanomaterials could have some important applications that may make them to come in contact with mammalian cells. Therefore, cytotoxicity (MTT assay) and genotoxicity (COMET assay) experiments have been performed on the nanomaterials prepared by us and the results are described in this chapter. MTT results have proved the biocompatability of OA-SL-AuNPs, OA-SL-AgNPs, B-TiO_2 NPs and B-ZnO NPs up to the concentration of 10^{-4} M, 10^{-4} M, 10^{-3} M and 10^{-6} M respectively. COMET assay, being a very sensitive technique to detect DNA damage, showed that at higher dose (10^{-3} M or above) of nanoparticles DNA damage occurs. We found all the nanomaterials (except B-ZnO) to be not genotoxic up to a much higher concentration (up to 10^{-4} M), whereas, B-ZnO resulted with DNA damage even at 10^{-5} M.

The work described in this chapter has been communicated as: **Singh, S**.; Britto, V. D.; Dhawan, A.; Prasad, B. L. V. **2008**.

5.1 Introduction

The biological responses that the nanoparticles may evince when they come in contact with cells have been briefly described in chapter I. As mentioned there, it looks imperative that any new nanoparticle system that has been obtained by a method different from those existing, needs to be treated with caution and has to be thoroughly evaluated from toxicological perspectives.

Here in this chapter, we present our result of cytotoxicity and genotoxicity effects of the nanoparticles generated by us. The cell lines used for such evaluation have been considered based on the possible application and hence the potential increase in contact of the nanoparticles with the respective cells.

Among the frequently used nanomaterials, gold nanoparticles display several features, which make them best for different biomedical applications starting from ease of synthesis [5], higher stability [6], well known surface chemistry, which helps in surface modification with secondary tags such as peptides and antibodies etc. [7]. A cytotoxicity study by Connor *et al*. [8] shows that gold nanoparticles are taken up by human leukemia cells but are not necessarily toxic to cellular functions. Further, Pan *et al*. [9] reported size dependent cytotoxicity of gold nanoparticles, where 15 nm AuNPs were found to be nontoxic whereas 1.4 nm and 1.2 nm AuNPs resulted in rapid cell death by necrosis and apoptosis respectively. Shukla *et al*. [10] have also reported that AuNPs are non cytotoxic. They reduce the production of reactive oxygen and nitrite species and thus are non-immunogenic and biocompatible. Some reports suggest that AuNPs functionlized with cationic side chains are likely to be toxic to mammalian and bacterial cells due to their strong electrostatic attraction to the negatively charged bilayer [11]. Shape and size dependent uptake of AuNPs into cells followed by their localization in vesicles [12] or nucleus, in case of very small AuNPs [13] has been reported but cytotoxicity has not been observed.

Cytotoxicity studies and effect of AgNPs on L929 fibroblasts proliferation have been reported by Yu *et al.* [14] stating that AgNPs are biocompatible at lower concentrations but not at higher concentrations due to the oxidation of Ag^0 into Ag^+ ions. Further, Hussain *et al.* [15] have shown that AgNPs (10-50 µg/mL) are highly

cytotoxic to BRL3A rat liver cells, which induces increase in LDH (lactate dehydrogenase) release from the cells and subsequently decrease in mitochondrial function. Cytotoxicity of AgNPs was mediated through oxidative stress as significant decrease in GSH (glutathione) level and increase in ROS (reactive oxygen species) level was recorded. Recently Lee *et al.* [16] have studied the biocompatability of single AgNPs in zebra fish. They found that individual AgNPs could passively diffuse into developing embryos *via* chorion pore canals, create specific effects on embryonic development, and selectively generate particular phenotypes in a dose dependent manner.

Another group of nanomaterials that have found their way into majority of applications include oxides such as TiO_2, ZnO, Fe_2O_3 (in cosmetics and sunscreens) SiO_2, (as dental fillings) etc. Oxides are the thermodynamically most stable forms of most of the metals. Some of the metal-oxides (TiO_2, ZnO and SiO_2) have been approved by the Food and Drug Administration (FDA). Sayes *et al*. [17] have successfully reported that cytotoxicity of TiO_2 nanoparticles does not depend on surface area but on phase composition as anatase polymorph showed 100 times more toxicity than equivalent amount of rutile TiO_2. Further, Long *et al.* [18] have studied the neurotoxicity of TiO_2 nanoparticles (P25) on nerve cells (microglea and neurons) and reported that P25 was non-toxic to isolated N27 neurons but stimulates BV2 microglea to produce ROS and damages OS-sensitive neurons in culture of brain striatum. Jeng *et al*. [19] have reported a comparative cytotoxicity study of different oxide nanoparticles (TiO_2, ZnO, Al_2O_3, Fe_3O_4 and CrO_3) and found ZnO extremely toxic to Neuro 2A cells at lower concentrations (50-100 µg/mL). However, other oxides showed no significant toxicity even at higher doses (~ 200 µg/mL).

On the basis of above discussion and details presented in chapter I, it is sufficient to say that being minute enough to be internalized by a wide variety of mammalian cell types the nanoparticles are able to cross the cell membrane [20]. The uptake of nanoparticles has been reported to be size dependent [12] and occurs through specialized cells by endocytosis or phagocytosis. Inside the cells, nanoparticles are stored in certain locations (such as inside vesicles, mitochondria) and are able to exert toxic response. Particles with smaller size carry larger surface

area and thus would involve in generation of a substantial amount of ROS, which play a major role in nanoparticle toxicity [22]. Generation of ROS mediated oxidative stress and decline in antioxidant levels finally leads to inflammation and fibrosis [23]. Numerous reports have been published dealing with cytotoxicity/biocompatability of different nanomaterials but seldom research has been done in the field of genotoxicity of nanomaterials. The assessment of DNA damage is essential since it is the blue print of life and many chemicals/xenobiotics manifest their toxicity in form of genetic insults, leading to serious consequences. In this regard, Dunford *et al*. [24] studied genotoxicity of human fibroblast cells and reported that TiO_2/ZnO nanoparticles from sunscreen were found to induce generation of free radicals and catalyzed DNA damage both in cell free system and *in vitro*.

In this chapter we describe the cytotoxicity and genotoxicity effects of sophorolipid reduced gold nanoparticles (OA-SL-AuNPs), sophorolipid reduced silver nanoparticles (OA-SL-AgNPs), biosynthesized TiO_2 (B-TiO_2) and biosynthesized ZnO (B-ZnO) nanoparticles. MTT assay was performed to study the cytotoxicity, whereas COMET assay was undertaken for genotoxicity evaluation. Before going to the details, the basic information and principles of MTT assay and COMET assay are briefly described here. The synthesis protocol and detailed characterization of B-TiO_2 and B-ZnO nanoparticles have been discussed in previous chapters. Calcined samples (400 ºC for 4 h) of B-TiO_2 and B-ZnO nanoparticles were used for toxicity studies. A comparative discussion about cytotoxicity and genotoxicity effects of SL-AuNPs and SL-AgNPs on A431 cells (human epithelial carcinoma cell line) has been provided. The cytotoxicity and genotoxicity of pure OA-SL have also discussed in detail. Further, a comparative analysis of B-TiO_2 and B-ZnO nanoparticles for their cytotoxicity and genotoxicity on HepG2 (human liver carcinoma) cells have been discussed in detail.

5.1.1 MTT Assay

MTT [3-(4,5-dimethylthiazoyl-2-yl)-2,5-diphenyltetrazolium bromide], a pale yellow dye is converted into formazan, a violet colored compound by the activity of succinate dehydrogenase of mitochondria (Figure 5.1). Since the conversion takes

place in living cells, the amount of formazan produced is directly correlated with the number of viable cells present. The MTT assay was done following the method of Mosmann [27] with slight modification. The molecular structure structure of MTT dye and formazan crystals has been provided in Figure 5.1.

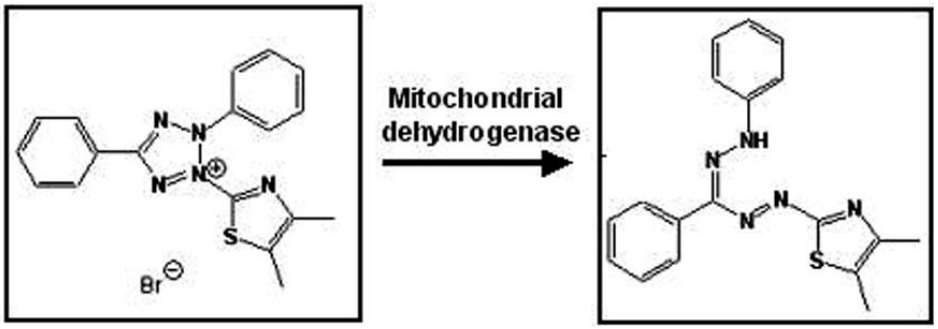

Figure 5.1: *Reduction of MTT dye with functional mitochondrial dehydrogenase enzyme in to water insoluble formazan crystals.*

5.1.2 COMET Assay

COMET assay, also known as Single Cell Gel Electrophoresis (SCGE) assay, is a powerful and sensitive technique for the detection of DNA at the level of individual eukaryotic cell. It can be applied to prokaryotic cells too with the same sensitivity and precision. It was first investigated by Singh *et al.* in 1988.

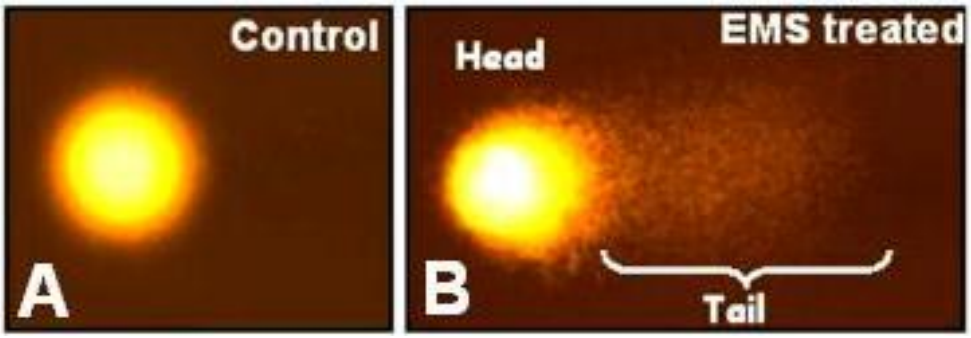

Figure 5.2: *Comet pattern from a healthy cell nucleus (A) and EMS treated cell nucleus (B). EMS (ethyl methyl sulphonate) is a well-known genotoxic material. EMS treated cell exhibit broken pieces of DNA has migrated from the head in form of tail (known as tail DNA). Untreated cell exhibit well intact DNA in form of head.*

This technique has gained popularity as a standard technique for evaluation of DNA damage/repair, biomonitoring and genotoxicity testing. In brief, it involves the encapsulation of cells in a low-melting-point agarose suspension, lysis of the cells in neutral or alkaline (pH >13) conditions and electrophoresis of the lysed cells. Finally,

visual analysis was performed after staining of DNA and fluorescence was monitored to determine the extent of DNA damage. This can be performed by manual scoring or automatically by software. Three different parameters were used as indicators of DNA damage – Olive Tail Moment (OTM; arbitrary units), Tail DNA (%) and Tail Length (mm). These parameters have been described in detail [28, 29]. The OTM is defined as the distance between the center of mass of the tail and the center of mass of the head, in micrometers, multiplied by the percentage of DNA in the tail and is considered to be most sensitive as both the quality and quantity of DNA damage are taken into account.

5.2 Toxicity responses of HepG2 cell towards OA-SL-AuNPs and OA-SL-AgNPs

This part of the chapter describes the MTT assay and COMET assay for cytotoxicity and genotoxicity assessment of OA-SL-AuNPs and OA-SL-AgNPs respectively.

5.2.1 Experimental Details

5.2.1.1 Materials

EMS (ethyl methyl sulphonate) (CAS No. 62-50-0), normal melting point agarose, low melting point agarose and ethidium bromide (EtBr) were purchased from Sigma chemicals (St. Louis, MO). Ca^{+} and Mg^{+} ion free phosphate buffer saline (PBS) were purchased from Hi-Media (Mumbai, India). All other chemicals were obtained locally and were of analytical reagent grade. EMS, a well-known mutagen [29c] was taken as positive control in this study.

5.2.1.2 Synthesis of OA-SL-AuNPs and OA-SL-AgNPs

The method for synthesis of OA-SL-AuNPs and OA-SL-AgNPs has been provided in chapter IV along with detailed characterizations. These nanoparticles were dialyzed for 24 h against millipore water using a dialysis bag of 12.5-kDa cutoff in order to remove excess sophorolipid, unreduced metal ions and other impurities. Further, this nanoparticle solution was concentrated up to 10^{-2} M by centrifugation. This solution was considered as stock solution. Further lower dilutions of SL-AuNPs

and SL-AgNPs for treatment of HepG2 cells were prepared by diluting the stock solution.

5.2.1.3 Cell lines

HepG2 (human hepatic carcinoma) cell line was used for cytotoxicity and genotoxicity study of OA-SL-AuNPs and OA-SL-AgNPs. The HepG2 (ATCC No. HB-8065) cell line was initially procured from National Center for Cell Sciences, Pune, India and has been maintained further in Industrial Institute of Toxicology Research, Lucknow, India. The cells were maintained in Complete Modified Eagle Medium (CMEM) supplemented with 10 % Fetal Bovine Serum (FBS), 1 mM sodium pyruvate, 2 mM glutamine, 50 U/mL penicillin, 50 mg/mL streptomycin and 100 mM non-essential amino acids. Cells were cultured for 3-4 days (80 % confluency) before the assay.

5.2.1.4 Sample Preparation for MTT assay

The above-mentioned stock solution (10^{-2} M) of OA-SL-AuNPs and OA-SL-AgNPs were used to make the working nanoparticle suspension by serial dilution method. 100 µL of stock solution of OA-SL-AuNPs or OA-SL-AgNPs was diluted to 1 mL, thus giving a working nanoparticle suspension of 10^{-3} M. This solution was further diluted in a similar way. Thus, different OA-SL-AuNPs or OA-SL-AgNPs concentrations ranging from 10^{-4}, 10^{-5}, 10^{-6}, 10^{-7}, 10^{-8} and 10^{-9} M were made in Incomplete Modified Eagle's Medium (IMEM).

5.2.1.5 MTT assay

In brief, cells (10,000-15,000 cells/well in 100 µL of medium) were seeded in a 96 well plate and allowed to adhere for 24 h at 37 °C in 5 %-CO_2 95 % air atmosphere. Medium was replaced with serum free medium (IMEM) containing different concentrations of OA-SL-AuNPs or OA-SL-AgNPs ranging from 10^{-4} M to 10^{-9} M and incubated for 3 h at 37 °C. The treatments were discarded and 100 µL serum free medium and 10 µL MTT (5 mg/mL) in PBS were added to each well and re-incubated for another 1 h at 37 °C. The reaction mixture was carefully discarded and 200 µL of DMSO was added to each well and mixed thoroughly. After 10 min, the absorbance was read at 530 nm, using Multiwell Microplate Reader (Biotek,

USA). The untreated sets were also run parallel under the identical conditions and served as control. The relative cell viability in percentage was calculated as:

(*A*530 of treated samples/*A*530 of untreated samples) x **100**. …….(1)

The data presented are the mean ± SD from three independent experiments.

5.2.1.6 Morphological analysis

Morphology of cells before and after the OA-SL-AuNPs or OA-SL-AgNPs treatment was examined under the phase-contrast inverted microscope (Leica Germany). The changes in the cells were quantified using automatic image analysis software Leica Q Win 500, hooked up with the inverted phase-contrast microscope.

5.2.1.7 COMET assay

In a typical experiment, cells (70,000-80,000 cells/well in 1 mL of medium) were seeded into two separate 12 well plates and allowed to adhere for 24 h at 37 °C in the atmosphere of 5 %CO_2 95 % air. From both the plates medium was replaced with serum free medium (IMEM) containing OA-SL-AuNPs or OA-SL-AgNPs ranging from 10^{-4} M to 10^{-9} M concentrations and incubated for 3 h at 37 °C. After incubation, the medium was replaced with PBS and washed thoroughly. Now cells were gently harvested with 0.4 mL of 0.025 % trypsin (in PBS). The effect of trypsin was nullified by adding 0.3 mL of CMEM (supplemented with 10 % FBS) and collected in Eppendorf tubes. Additionally wells were rinsed with 0.3 mL of PBS and collected in to same Eppendorf tube. The COMET assay was performed according to the method described by Singh *et al.* with slight modification [28]. In brief, cell pellets were obtained by centrifugation (5000 rpm, 5 min), which were again resuspended in 100 µL of PBS. To this 100 µL of 1 % LMPA (low melting point agar) was added, mixed well at 37 ^{o}C and finally layered on top of the end-frosted slides that were precoated with 1 % normal melting point agarose. Now cover slips (24 mm x 60 mm) were placed on top of the slides and were kept at 4 °C. After 5 min the cover slips were removed and 100 µL of 0.5 % LMPA was again layered on top of the slides before placing the cover slips back and keeping the slides at 4 °C again. After overnight lysis at 4 °C in freshly prepared lysing solution (2.5 M of NaCl, 100 mM of EDTA, 10 mM of Tris, pH 10 and 1 % Triton X-100, pH 10), slides were kept

in an electrophoretic unit (Life Technologies, Gaithersburg, MD), filled with chilled and freshly prepared electrophoresis buffer (1 mM Na_2EDTA and 300 mM NaOH, pH ~13). The slides were left (in the electrophoresis solution) for 30 min to allow unwinding of DNA. Following the unwinding, electrophoresis was performed for 30 min at 0.7 V/cm using a power supply from Techno Source (Mumbai, INDIA). To prevent DNA damage from stray light, if any, all the steps starting from single cell preparation were performed under dimmed light. After electrophoresis, the slides were immediately neutralized with 0.4 M of Tris buffer (pH 7.5) for 5 min and the neutralizing process was repeated three times for 5 min each. The slides were then stained with ethidium bromide (20 mg/mL: 75 µL per slide) for 10 min in dark. After staining, the slides were dipped once in chilled distilled water to remove the excess stain and subsequently, fresh cover slips were kept over them.

The slides were examined within 3-4 h, using an image analysis system (Kinetic Imaging, Liverpool, UK) attached to a fluorescent microscope (Leica, Germany). The images were transferred to a computer through a charge coupled device camera and analyzed using Komet 5.0 software. All the experiments were conducted in triplicates and the slides were prepared in duplicates. Twenty-five cells per slide equaling 150 cells per group were randomly captured at a constant depth of the gel, avoiding the cells present at the edges and superimposed comets.

5.2.1.8 Statistical analysis

Data were analyzed using Analysis of Variance (ANOVA). The level of statistical significance was set at $P < 0.05$ and $P < 0.01$ wherever required.

5.2.2 *In vitro* toxicity of OA-SL reduced nanoparticles

OA-SL-AuNPs and OA-SL-AgNPs have mostly proposed to be used as drug delivery agents and for treatment of cancerous tissues. During this process, liver would be the most frequent organ to encounter these nanoparticles. These nanoparticles may accumulate within liver which being the major organ involved in metabolism, would be the most frequent to encounter these nanoparticles. These nanoparticles may accumulate within the liver and thus elicit a concentration dependent immune response. Therefore, looking at all the above-mentioned

possibilities, we have chosen HepG2 cells (equivalent to human liver cells) and observed the cytotoxic and genotoxic responses of nanoparticles on them.

5.2.3 MTT Assay of OA-SL-AuNPs

As it is very clear from Figure 5.3 that lower concentrations of OA-SL-AuNPs (10^{-5}, 10^{-6} and 10^{-9} M) show negligible toxicity to HepG2 cells as more than 75 % mitochondrial activity and hence cell survival was recorded. This finding could also be confirmed by the phase contrast microscope images of HepG2 cells taken after the incubation of OA-SL-AuNPs (Figure 5.4). Figure 5.4 D, E and F are HepG2 cell images taken after the treatment of 10^{-5}, 10^{-6} and 10^{-9} M concentrations of OA-SL-AuNPs respectively, which show cell morphology similar to untreated (Figure 5.4 A) HepG2 cells. HepG2 cells with elongated and well intact morphology adhered to the culture plate surface could be seen even after OA-SL-AuNPs treatment.

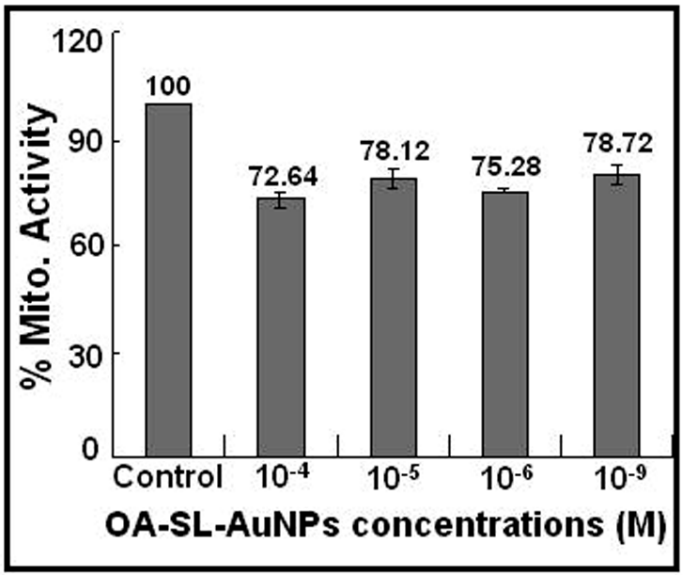

Figure 5.3: *Statistical data representing the % Mitochondrial Activity of human hepatic carcinoma (HepG2) cells after treatment with different concentrations of OA-SL-AuNPs for 3 h. Details are discussed in text.*

The phase contrast image taken from the HepG2 cells treated with 10^{-3} M of OA-SL-AuNPs showed no viable cells, as only black spots accompanied with cell debris could be seen and therefore concentration above 10^{-4} M was not taken for the experiments. These black spots could be attributed to the aggregates of OA-SL-AuNPs. The optical image of HepG2 cell treated with 10^{-4} M OA-SL-AuNPs (Figure

5.4 C) shows a little change in cell morphology, which could be attributed to cytotoxic effect of OA-SL-AuNPs as the corresponding MTT result shows ~ 72 % of cell survival. Therefore, it could be concluded here that OA-SL-AuNPs in concentrations below 10^{-4} M are not toxic. However, HepG2 cells treated with 10^{-4} M concentration of OA-SL-AuNPs showed little toxicity and 10^{-3} M resulted in complete disintegration of cells.

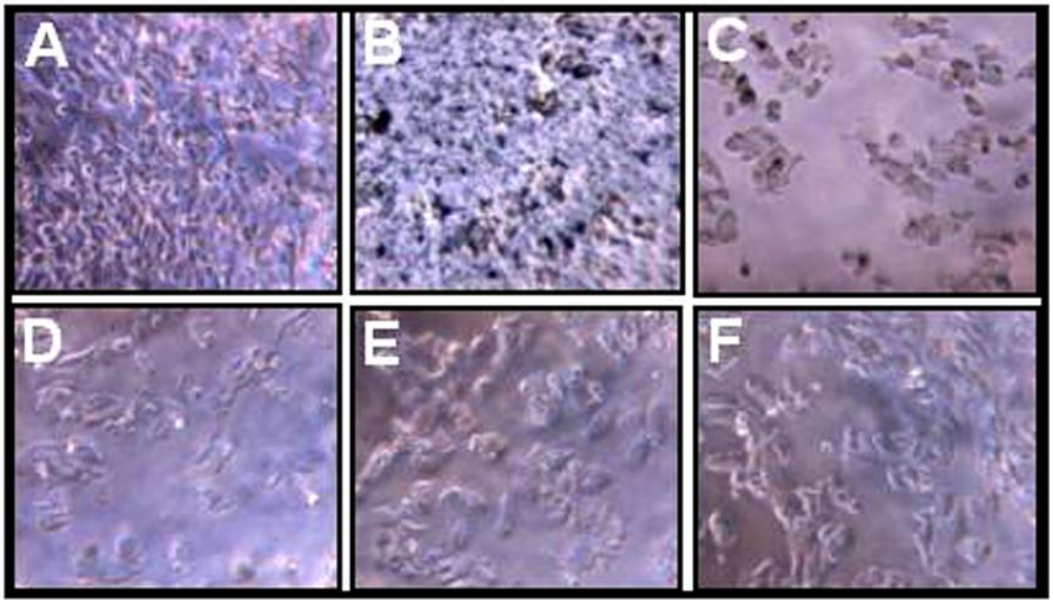

Figure 5.4: *Optical micrographs of HepG2 cells treated with different concentrations of OA-SL-AuNPs exposed for 3 h. Figure B, C, D, E and F are images of HepG2 cells after 3 h treatment with 10^{-3} M, 10^{-4} M, 10^{-5} M, 10^{-6} M and 10^{-9} M of OA-SL-AuNPs. Figure A shows the morphology of untreated (control) cells of HepG2 cells incubated for 3 h.*

5.2.4 COMET Assay of OA-SL-AuNPs

Further, the genotoxicity of OA-SL-AuNPs on HepG2 cells was also performed employing COMET assay. Though, MTT assay results show that nanoparticles below 10^{-4} M concentration do not show any significant toxicity, it becomes important that we study the genotoxic effects of the same concentration. The cytotoxicity is a way to record the immediate response of cells comes in contact with a foreign material whereas the genotoxicity reveals a long-term response. Thus, it is important that we investigate the genotoxicity of those concentrations that do not actually show any cytotoxicity. Figure 5.5 A shows the OTM pattern from the DNA of HepG2 cells after the treatment with different concentrations of OA-SL-AuNPs (0 M, 10^{-4} M, 10^{-5} M, 10^{-6} M and 10^{-9} M) for 3 h. All concentrations below 10^{-4} M (10^{-5}

M, 10^{-6} M and 10^{-9} M) do not show any significant increase in OTM (0.87 unit, 0.86 unit and 0.89 unit) when compared with control cell OTM (0.87 unit). However, OTM pattern of HepG2 cells treated with 10^{-4} M of OA-SL-AuNPs shows an increase in OTM (1.28 unit) as compared to control (0.87 unit). From the analysis by ANOVA, this dose was not found to be significantly toxic. This suggests that even though slight DNA damage occurs at this concentration, it is very minute and cannot be considered as toxic. This is again confirmed by the comet pattern of the cell DNA (Figure b) showing the entire cell DNA present in the head.

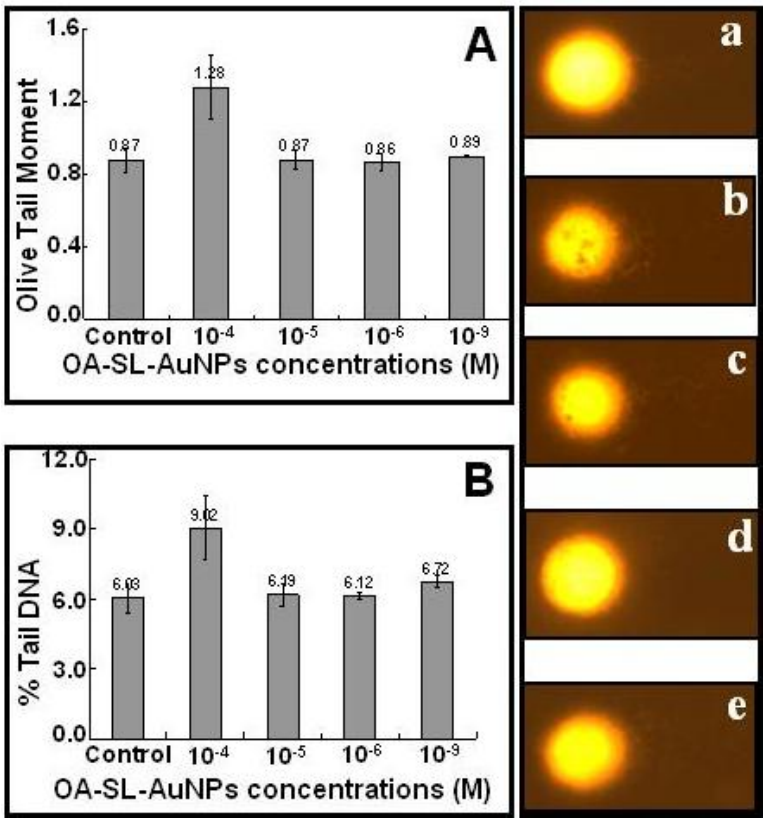

Figure 5.5: *COMET results obtained from 3 h exposure of HepG2 cells with different concentrations of OA-SL-AuNPs. Two comet parameters, % tail DNA (A) and olive tail moment (B) were considered as measure of DNA damage. Figure a, b, c, d and e are images of comet showing the pattern of DNA after the exposure of 0 M, 10^{-4} M, 10^{-5} M, 10^{-6} M and 10^{-9} M concentration of OA-SL-AuNPs to HepG2 cells respectively.*

Similarly, % tail DNA pattern of HepG2 cells treated with different concentrations (Figure 5.5 B) was also analyzed. The concentrations (10^{-5} M, 10^{-6} M and 10^{-9} M) showed almost similar % tail DNA pattern (6.29 unit, 6.12 unit and 6.72 unit) as compared to control (6.08 unit). Further, the so obtained comet pattern from the HepG2 cells treated with different concentration of OA-SL-AuNPs showing well

intact head and complete absence of DNA fragments in form of tail (Figure 5.5 b, c, d and e), suggesting that these doses are not genotoxic However, OA-SL-AuNPs at 10^{-4} M concentration show increase in % tail DNA (9.02 unit) when compared with control (6.08 unit). This increase in % tail DNA pattern was also found non-significant when analyzed with ANOVA. From comet pattern of cell DNA (Figure 5.5 b), it is clear that 10^{-4} M concentration of OA-SL-AuNPs show little DNA damage, as most of the DNA is intact in the form of comet head and looks similar to control COMET pattern (Figure a). This result again confirms our MTT observation.

As per COMET assay guidelines [30] and based on our MTT observations, concentrations of OA-SL-AuNPs above 10^{-4} M were not used. Also, the nanoparticle suspensions of 10^{-3} M or above were not stable rather it was forming the aggregates and settled on bottom of the vessel. Further, it may not be necessary to study the genotoxicity, if the cells are already dead due to cytotoxicity.

5.2.5 MTT Assay of OA-SL-AgNPs

Within similar experimental conditions, MTT assay of OA-SL-AgNPs was also performed on HepG2 cells. Figure 5.6 shows the cytotoxicity (MTT assay) response of HepG2 cells after 3 h treatment with different concentrations of OA-SL-AgNPs (10^{-4} M, 10^{-5} M, 10^{-6} M and 10^{-9} M). However, the lower OA-SL-AgNPs concentrations (10^{-5} M, 10^{-6} M and 10^{-9} M) showed ~ 90 % cell survival, which can again be correlated with the optical images showing cell morphology (Figure 5.7 D, E and F) with untreated (Figure 5.7 A) cells. HepG2 cells treated with these lower concentrations of OA-SL-AgNPs showed almost similar morphological characteristics to untreated cells.

HepG2 cells showed ~ 58 % cell survival when exposed to 10^{-4} M OA-SL-AgNPs concentration. This was further justified by the phase contrast micrograph of HepG2 cells treated 10^{-4} M OA-SL-AgNPs (Figure 5.7 C). Cells with regular morphology could not be seen; instead black aggregates (AgNPs) and damaged cell remains are quite visible. The concentration above 10^{-4} M was not taken because at these concentrations OA-SL-AgNPs showed formation of aggregates and settled over the cell surface and led to the cell death (Figure 5.7 B). The aggregates could also be

seen with the HepG2 cells treated with 10^{-4} M OA-SL-AgNPs (Figure 5.7 C). Here these aggregates are lesser in number, which could be clearly correlated with the lesser amount (10^{-4} M) of OA-SL-AgNPs added.

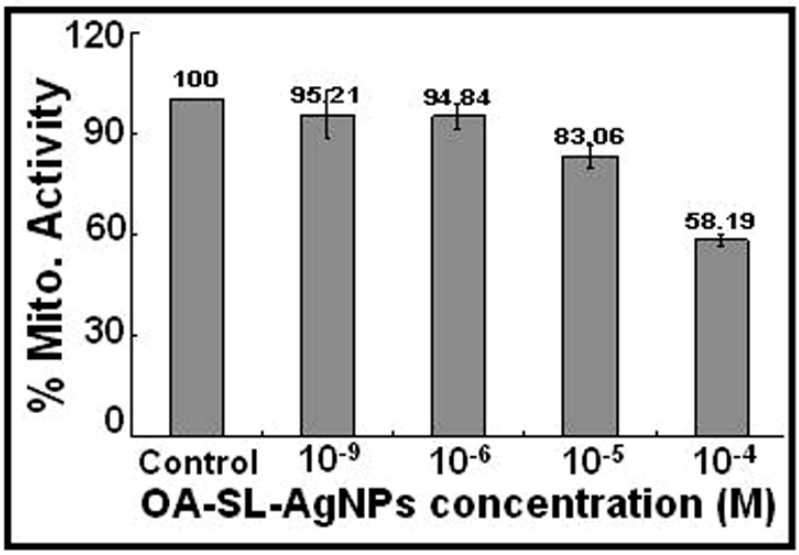

Figure 5.6: *Statistical data representing the % Mitochondrial activity of HepG2 cells after treatment with different concentrations of OA-SL-AgNPs for 3 h. Highest concentration (10^{-3} M) of OA-SL-AgNPs shows toxicity to the cells, while rest other concentrations do not show toxicity. Details are discussed in text.*

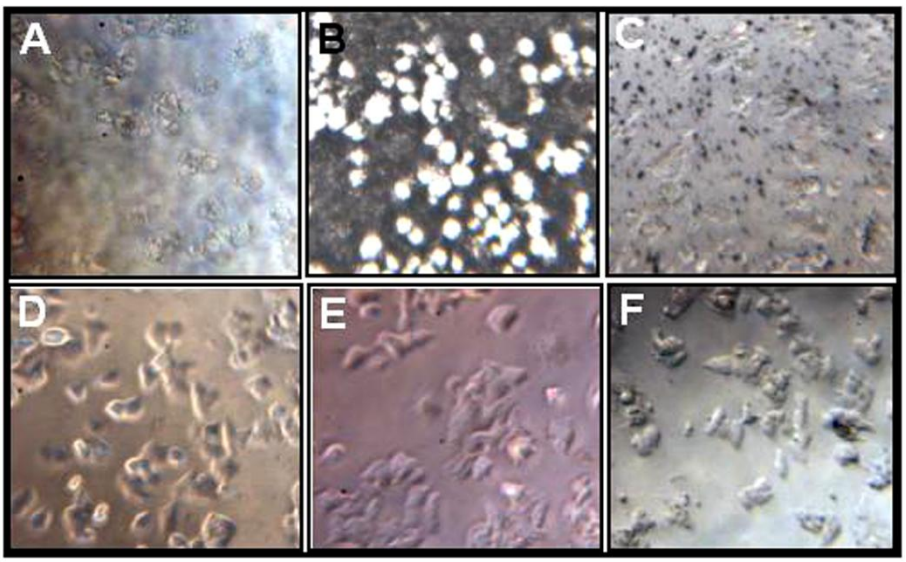

Figure 5.7: *Optical micrograph image of HepG2 cells treated with different concentrations of OA-SL-AgNPs exposed for 3 h. Figure B, C, D, E and F are images of HepG2 cells after 3 h treatment with 10^{-3} M, 10^{-4} M, 10^{-5} M, 10^{-6} M and 10^{-9} M of OA-SL-AgNPs. Figure A shows the morphology of untreated (control) cells of HepG2 cells incubated for 3 h.*

Therefore, it can be concluded that OA-SL-AgNPs below 10^{-4} M are fairly biocompatible to HepG2 cells. However, at 10^{-4} M and above concentrations they

show considerable cytotoxicity. Thus, OA-SL-AgNPs with the concentration below 10^{-4} M could be safely used for different bioapplications.

5.2.6 COMET Assay of OA-SL-AgNPs

In order to investigate the effect of OA-SL-AgNPs on DNA of HepG2 cells, COMET assay was performed in a similar way as was done with OA-SL-AuNPs. Here also two COMET parameters (olive tail moment and % tail DNA) were considered for genotoxicity evaluation.

Figure 5.8 A shows the percent tail DNA of HepG2 cells after 3 h of treatment with different concentrations of OA-SL-AgNPs (10^{-4} M, 10^{-5} M, 10^{-6} M and 10^{-9} M). The lower concentrations of OA-SL-AgNPs (10^{-5} M, 10^{-6} M and 10^{-9} M) showed almost similar % tail DNA (7.49 unit, 6.05 unit and 6.25 unit) and COMET pattern as untreated cells (6.26 unit). However, 10^{-4} M concentration of OA-SL-AgNPs caused an increase in % tail DNA (9.52 unit) as compared to untreated cells (6.26 unit). This increase in % tail DNA was found to be non-significant when analyzed with ANOVA. This suggests that 10^{-4} M concentration of OA-SL-AgNPs causes little DNA damage but this dose cannot be considered as genotoxic. These results could again be correlated with MTT assay results, obtained after 3 h incubation of HepG2 cells with OA-SL-AgNPs (10^{-4} M). The COMET pattern of HepG2 cells treated with 10^{-4} M concentration of OA-SL-AgNPs (Figure 5.8 b) also showed well intact DNA head with very little amount of DNA in the form of tail.

Further, OTM patterns were analyzed after 3 h incubation of HepG2 cells with OA-SL-AgNPs. Here also, lower concentrations (10^{-5} M, 10^{-6} M and 10^{-9} M) showed almost similar amount of OTM (1.01 unit, 0.86 unit and 0.89 unit) as was recorded for untreated cells (0.83 unit). Whereas HepG2 cells treated with 10^{-4} M of OA-SL-AgNPs showed increased amount of OTM (1.55 unit) as compared to untreated cells (0.83 unit), which is again non significant under ANOVA analysis. These results were further supported by COMET pattern obtained from respective OA-SL-AgNPs treated HepG2 cells (Figure 5.8 a, b, c, d and e). Therefore, it could be said that OA-SL-AgNPs are non-cytotoxic and non-genotoxic to HepG2 cells up to 10^{-4} M concentration and can be used safely for different applications.

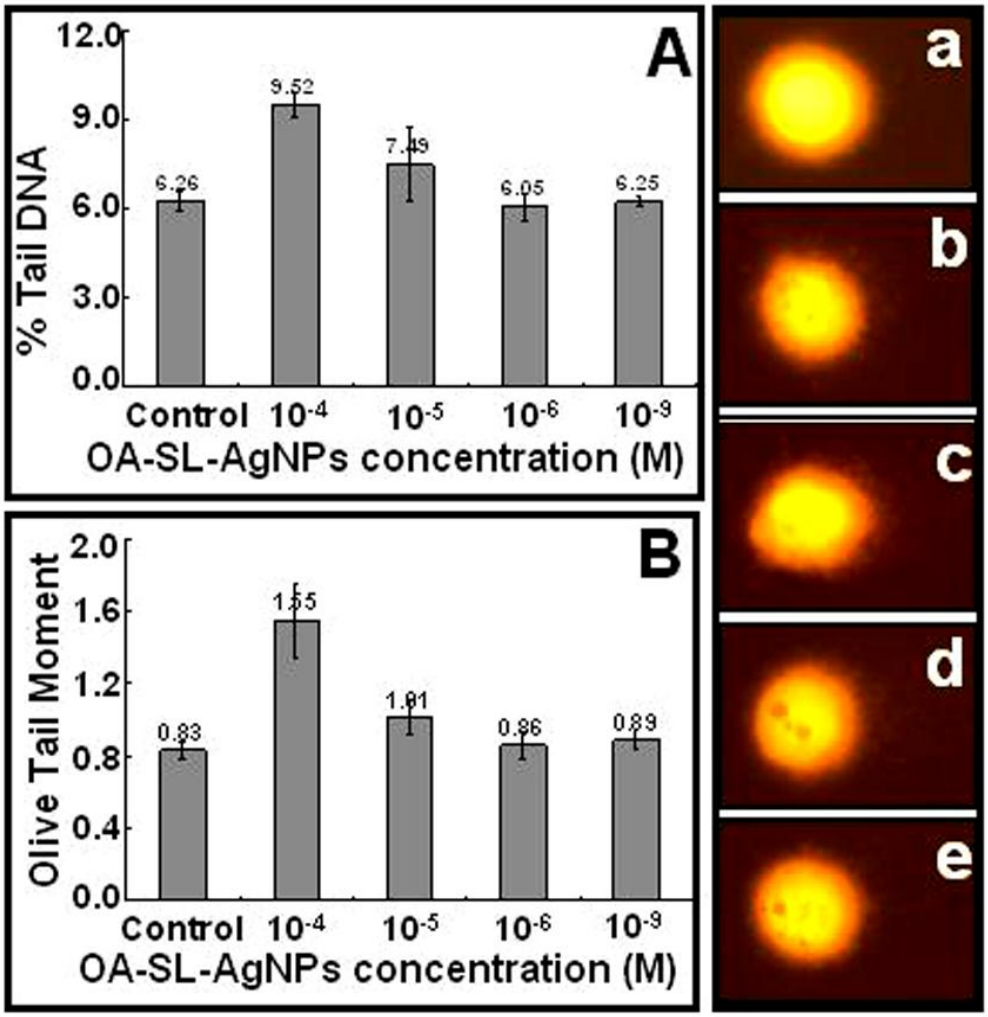

Figure 5.8: *COMET results obtained from 3 h exposure of HepG2 cells with different concentrations of OA-SL-AgNPs. Two comet parameters, % tail DNA (A) and olive tail moment (B) was considered as measure of DNA damage. Figure a, b, c, d and e are image of comet showing the pattern of DNA after the exposure of 0 M, 10^{-4} M, 10^{-5} M, 10^{-6} M and 10^{-9} M concentration of OA-SL-AgNPs to HepG2 cells respectively.*

On comparing MTT data of OA-SL-AuNPs and OA-SL-AgNPs, it was observed that 10^{-4} M concentration OA-SL-AgNPs showed only ~ 58 % cell viability while OA-SL-AuNPs showed ~ 72 %. Further, with 10^{-4} M of OA-SL-AgNPs showed more amount (3.26 unit) of % tail DNA (with comparison to control) than OA-SL-AuNPs (2.94 unit). Moreover, the same concentration (10^{-4} M) showed more difference in OTM (0.72 unit) with control than with OA-SL-AuNPs (0.41 unit). Even at lower concentration (10^{-5} M) of OA-SL-AgNPs showed increased % tail DNA (1.23 unit) and OTM (0.18 unit) than OA-SL-AuNPs which showed (0.21 unit) and (0.0 unit) respectively when compared with their respective controls. Thus, among

OA-SL-AgNPs and OA-SL-AuNPs, OA-SL-AuNPs could be considered as more biocompatible. As it well known that AgNPs undergo frequent oxidation than AuNPs (low reduction potential of Ag than Au) and thus leading to the formation of Ag^{+} ions, which thereby show the toxicity to the cells.

5.2.7 MTT Assay of OA-SL molecules

In order to completely understand the toxicity of OA-SL-AuNPs and OA-SL-AgNPs, toxicity study of OA-SL molecules becomes essential, as it is the only capping molecule present on nanoparticle surface. It is the capping molecule on nanoparticle surface, which first come in contact with cells. The details about the synthesis and characterization of these OA-SL molecules have provided in chapter IV.

Figure 5.9 shows the cytotoxicity response of HepG2 cells to different concentrations of OA-SL molecules exposed for 3 h. The lower concentrations (10^{-4} M, 10^{-5} M, 10^{-6} M, 10^{-7} M, 10^{-8} M, 10^{-9} M) show ~ 90 % of cell survival, which could again be confirmed by cell morphology images (Figure 5.10). Optical images of cells treated with these concentrations of OA-SL molecules show well-adhered and elongated cell morphology. Although, some cells of rounded morphology could also be seen, but their population is very less and this could be assigned to the normal cell death after completion of their cell cycle, which could be seen in untreated cell plate too. However, 10^{-3} M concentration of OA-SL molecules is cytotoxic as only ~ 18 % of cell survival is recorded. The corresponding cell morphology can be seen in Figure 5.10. It is very clear that cells have lost their normal elongated structure (as untreated cells exhibit these properties) and showing rounded morphology, indicating the dead cells. Also, cell number under a given area is reduced significantly, indicating the detachment of living cells from petriplate surface. Therefore it could be concluded that below 10^{-4} M concentrations of OA-SL molecules are quite biocompatible whereas above this concentration are highly cytotoxic.

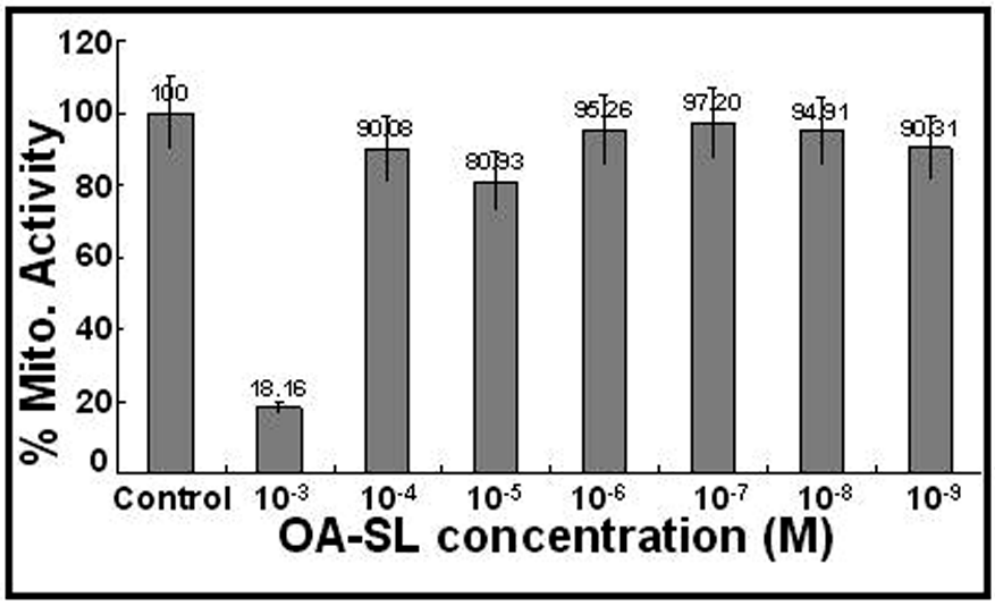

Figure 5.9: *Statistical data representing the % Mitochondrial activity of HepG2 cells after treatment with different concentrations of OA-SL molecules (10^{-4} M, 10^{-5} M, 10^{-6} M, 10^{-7} M, 10^{-8} M, 10^{-9} M) for 3 h.*

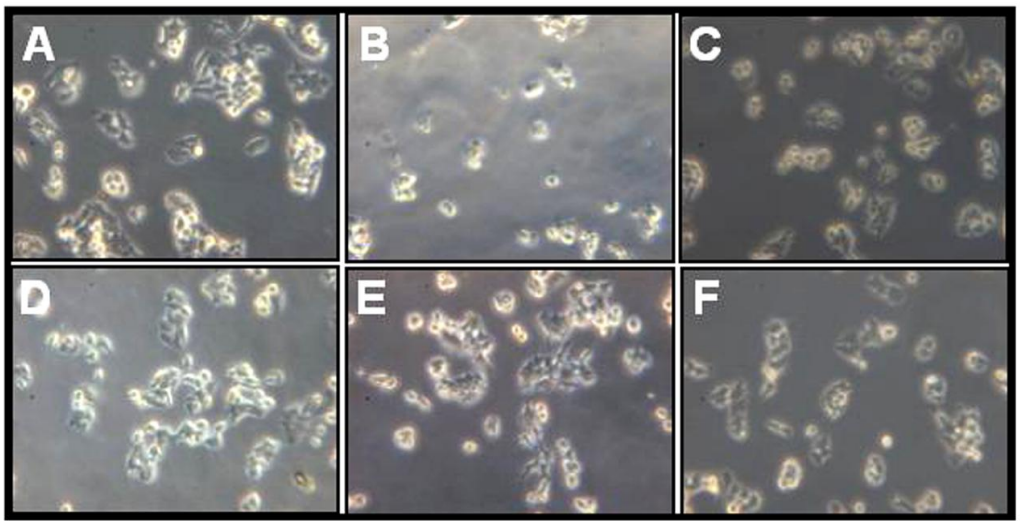

Figure 5.10: *Optical images of OA-SL treated HepG2 cells for 3 h. Untreated cells (A), cells treated with 10^{-3} M (B), 10^{-4} M (C), 10^{-5} M (D), 10^{-6} (E) and 10^{-9} M (F) concentration of OA-SL for 3 h.*

5.2.8 COMET Assay of OA-SL molecules

To further elucidate the effect of OA-SL molecules on the DNA of HepG2 cells, COMET assay was performed. Experimental setup was same as described earlier COMET experiments. Figure 5.11 show the extent of DNA damage in HepG2

cells by OA-SL molecules in terms of % tail DNA (Figure 5.11 A) and OTM (Figure 5.11 B).

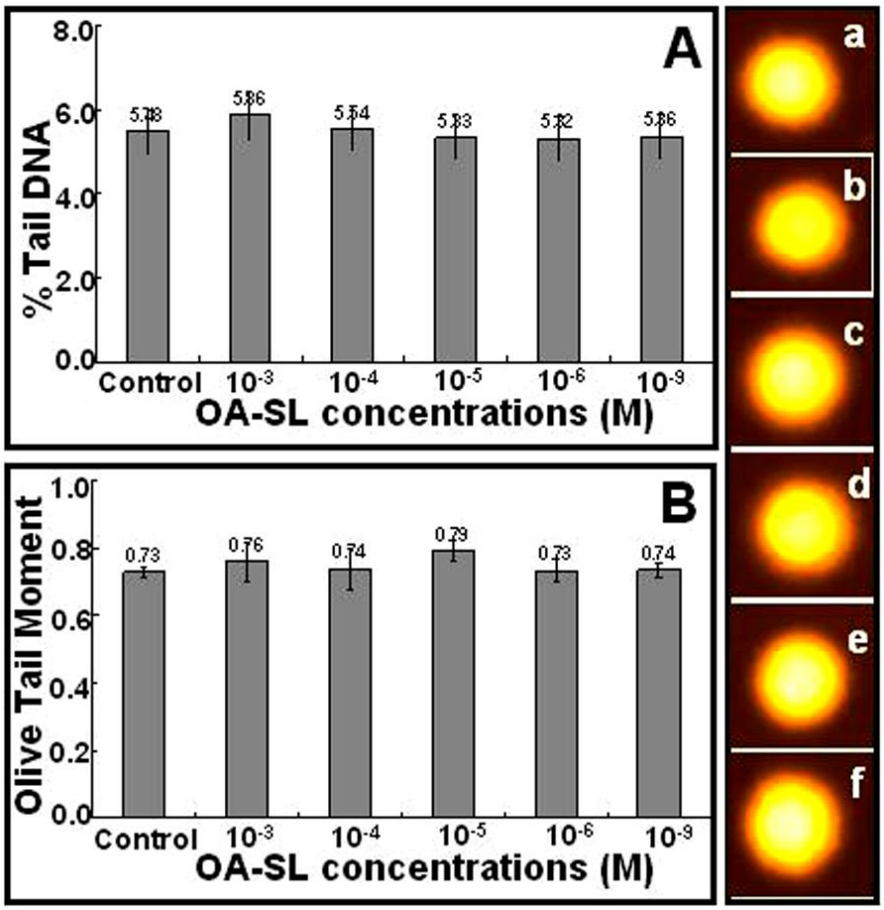

Figure 5.11: *Statistical representation of two COMET parameters, % tail DNA (A) and olive tail moment (B) obtained after 3 h exposure of HepG2 cells to different concentrations of OA-SL. Figure a, b, c, d, e and f are image of comet showing the pattern of DNA after the exposure of 0 M, 10^{-3} M, 10^{-4} M, 10^{-5} M, 10^{-6} M and 10^{-9} M concentration of OA-SL to HepG2 cells respectively.*

Almost no increase in % tail DNA (compared with control) was recorded when the cells were incubated with different concentrations of OA-SL molecules (10^{-3} M, 10^{-4} M, 10^{-5} M, 10^{-6} M and 10^{-9} M) for 3 h. Similarly, no increase in OTM was obtained when compared with control (untreated) HepG2 cells (Figure 5.11 B). These findings were again confirmed from COMET images (Figure 5.11 a, b, c, d, e and f) obtained from HepG2 cells treated with different concentrations (control, 10^{-3} M, 10^{-4} M, 10^{-5} M, 10^{-6} M and 10^{-9} M). Although, COMET assay result suggests that OA-SL molecules are non-genotoxic to HepG2 cells even at 10^{-3} M concentration, whereas MTT result showed cytotoxicity at this dose. The possible explanation to this

contradictory result could be considered as its activity at the cell membrane only. Sophorolipids are well known for membrane destabilization and thus causes increased permeabilization [32]. Therefore, it can be hypothesized that sophorolipids (10^{-3} M) are interacting with the cell membrane and thus causing damage to that, which thereby causes cell death due to the leakage of intracellular materials. However, the genetic materials (DNA etc.) remains unaffected from sophorolipid attack, as it is covered with nuclear membrane.

5.3 Toxicity responses of A431 cell towards biosynthesized TiO_2 and ZnO nanoparticles

This part of the chapter deals with the toxicity evaluation of biosynthesized TiO_2 and ZnO nanoparticles on A431 cells. Biosynthesized TiO_2 and ZnO nanoparticles were checked for their cytotoxicity (MTT assay) and genotoxicity (COMET assay). Since, these oxide nanoparticles are frequently being used as an active ingredient in modern day cosmetics, they may come in contact with skin cells and affect them. Therefore, we have chosen skin cell line (A431) to study the toxicity of biosynthesized TiO_2 (B-TiO_2) and biosynthesized ZnO (B-ZnO) nanoparticles. A comparative toxicity assessment is described herein.

5.3.1 Experimental Details

5.3.1.1 Materials

All the materials used were same as described earlier.

5.3.1.2 Synthesis of B-TiO_2 and B-ZnO nanoparticles

The synthesis and characterizations of these oxide nanoparticles have already been discussed in chapter III. Calcined sample was used for various toxicity experiments. A stock solution of 10^{-2} M was prepared in DMEM and further dilutions were made by serial dilutions as described earlier part of this chapter.

5.3.1.3 Cell lines

A431 cell line was used for the cytotoxicity study of B-TiO_2 and B-ZnO nanoparticles. The A431 cell line (ATCC No. CRL-1555) was initially procured from

National Centre for Cell Sciences, Pune, India and after then it has been maintained at Indian Institute of Toxicological Research, Lucknow, India. The cells were maintained in Dulbecco's Modified Eagle Medium (DMEM) supplemented with 10 % Fetal Bovine Serum (FBS), 1 mM sodium pyruvate, 2 mM glutamine, 50 U/mL penicillin, 50 mg/mL streptomycin and 100 mM non-essential amino acids. DMEM was purchased from GIBCO. Cells were cultured for 3-4 days (80 % confluency) before the assay. For MTT assay, the cells were seeded in 96 well plates at a density of 10,000-15,000 cells/well in 100 µL of complete medium. The cells were incubated for 24 h in a humidified incubator at 37 ^{o}C and in the atmosphere of 5 %-CO_2 95 % air. After incubation, the complete medium was discarded and 100 µL of freshly prepared B-TiO_2 and B-ZnO (different concentration) in DMEM were added to each well.

5.3.1.4 Sample Preparation for MTT and COMET assay

A stock solution of 10^{-2} M of B-TiO_2 was made by sonication of the 8.0 mg of B-TiO_2 in 10 mL of sterile millipore water. Sonication was performed with a pulse of 1 min, thrice and with a time interval of 30 sec at 15 Watt. This stock solution was further diluted to make other lower concentrations of B-TiO_2, described earlier. Similarly, 8.1 mg of B-ZnO nanoparticle in 10 mL of serum free DMEM was sonicated in a similar manner as for B-TiO_2 nanoparticle sample preparation.

5.3.1.5 MTT assay

In brief, cells (10,000-15,000 cells/well in 100 µL of medium) were seeded in a 96 well plate and allowed to adhere for 24 h at 37 °C in 5 %-CO_2 95 % air atmosphere. Medium was replaced with serum free medium (DMEM) containing different concentrations of B-TiO_2 and B-ZnO nanoparticles ranging from 10^{-2} M to 10^{-9} M and incubated for 3 h at 37 °C. The treatments were discarded and 100 µL serum free medium and 10 µL MTT (5 mg/mL) in PBS were added to each well and re-incubated for another 1 h at 37 °C. The reaction mixture was carefully discarded and 200 µL of DMSO was added to each well and mixed thoroughly. After 10 min, the absorbance was read at 530 nm, using Multiwell Microplate Reader (Biotek, USA). The untreated sets were also run parallel under the identical conditions and

served as control. The relative cell viability in percentage was calculated as described in equation (1). The data presented are the mean ± SD from three independent experiments.

5.3.1.6 COMET Assay

Comet assay was performed as described earlier, except the cell line used here was A431 and DMEM was used as the culture medium.

5.3.1.7 Statistical Analysis

Data were analyzed using Analysis of Variance (ANOVA). The level of statistical significance was set at $P < 0.05$ and $P < 0.01$ wherever required.

5.3.2 MTT Assay of B-TiO_2 and B-ZnO nanoparticles

Figure 5.12 represents the cytotoxicity (MTT assay) results of B-TiO_2 (Figure A) and B-ZnO (Figure B) nanoparticles on A431 cell lines after incubation for 3 h.

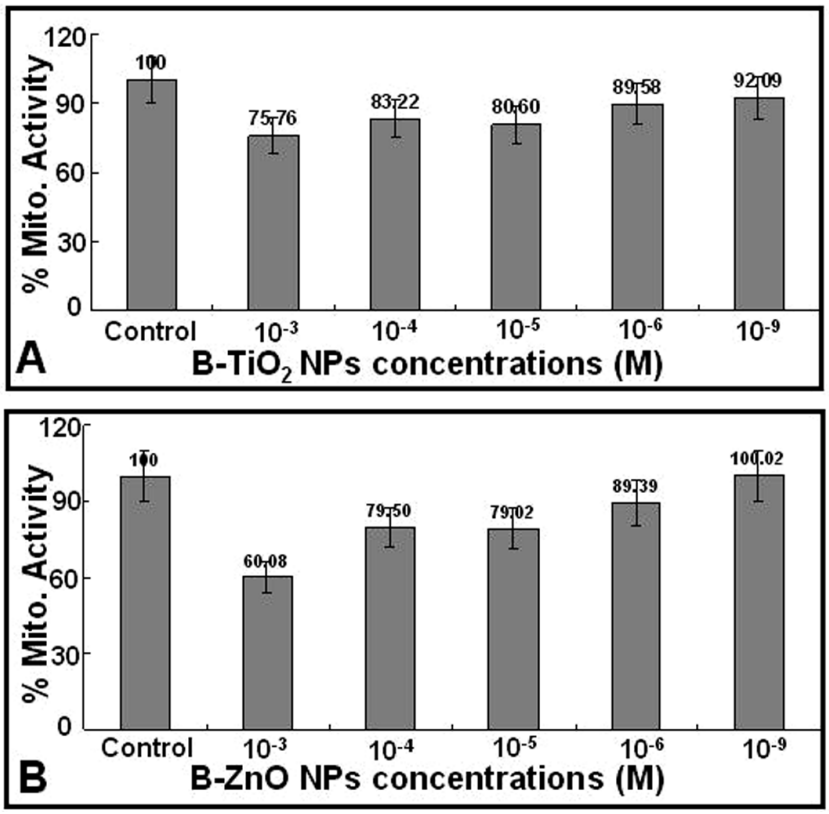

Figure 5.12: *Statistical data representing the % Mitochondrial activity of A431 cells after treatment with different concentrations of (10^{-3} M, 10^{-4} M, 10^{-5} M, 10^{-6} M, 10^{-7} M, 10^{-8} M, 10^{-9} M) B-TiO_2 and B-ZnO for 3 h.*

A slight fall in cell viability (25 %) was observed in the case of highest concentration (10^{-3} M) of B-TiO_2 nanoparticles after 3 h of incubation (Figure 5.12 A). When these results were compared with MTT results from B-ZnO nanoparticles (Figure 5.12 B), huge reduction in cell viability (40 %) was observed at the similar dose (10^{-3} M) of B-ZnO nanoparticles. Thus, at this point of time (from MTT results), it can be concluded that biosynthesized B-TiO_2 nanoparticles are more biocompatible than biosynthesized B-ZnO nanoparticles. However, other lower concentrations (10^{-4} M, 10^{-5} M, 10^{-6} M and 10^{-9} M) showed similar cell viability pattern. These findings were further confirmed by genotoxicity (COMET assay) results, described below.

5.3.3 COMET Assay of B-TiO_2 and B-ZnO nanoparticles

Interesting results were observed when COMET assay was performed in order to get information about the effect of these oxide nanoparticles on DNA of human skin cell lines. Although, slight increase in % tail DNA (Figure 5.13 A) was recorded (1.27 unit) in case of highest concentration (10^{-3} M) of B-TiO_2 nanoparticles (10^{-3} M) it did not show any significance when analyzed using ANOVA ($p < 0.05$). Therefore this dose cannot be considered as genotoxic. Other concentrations (10^{-4} M, 10^{-5} M, 10^{-6} M and 10^{-9} M) as expected gave almost negligible increase in % tail moment values (0.31, -0.12, -0.04 and -0.02 unit) when compared with control. This observation was again confirmed with the comet images taken from cells after exposure to various concentrations of B-TiO_2 nanoparticles (Figure 5.15 A-F), which showed a well intact comet head containing almost all the DNA and therefore absence of any DNA in tail. A few DNA fragments could be seen in COMET image (Figure 5.15 B) taken from A431 cells exposed to 10^{-3} M of B-TiO_2 nanoparticles, which could be easily correlated with the little increased % tail DNA and OTM values obtained at this dose.

Exposure of A431 cells to different concentrations (10^{-4} M, 10^{-5} M, 10^{-6} M, 10^{-9} M and 10^{-12} M) of B-ZnO nanoparticles (Figure 5.14 B) on the other hand show increase in % tail DNA (1.82, 1.13, 1.03, 0.72 and 0.25 unit) and two doses (10^{-4} M and 10^{-5} M) were found to be significantly genotoxic, when analyzed by ANOVA ($p < 0.05$). Respective comet images, taken from cells exposed to 10^{-4} M and 10^{-5} M of

B-ZnO nanoparticles (Figure 5.14 I and 5.14 J respectively); also confirm the significant DNA damage.

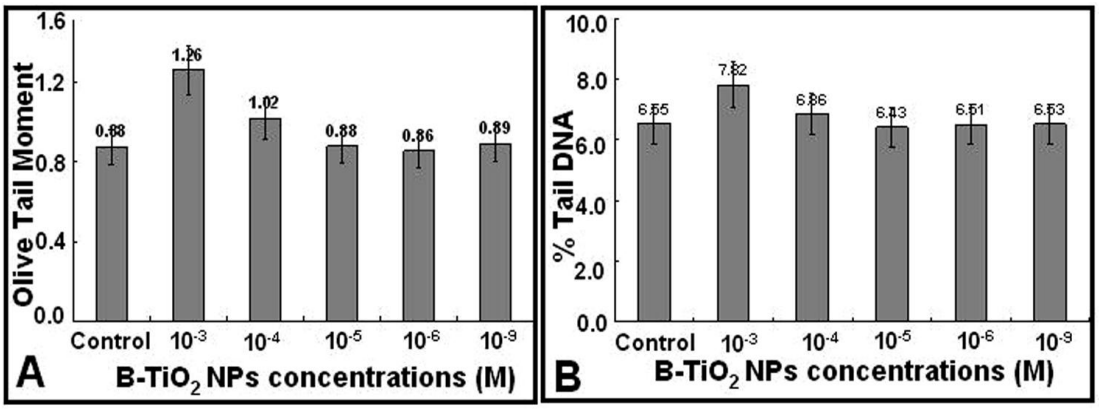

Figure 5.13: *Statistical data representing the two important COMET parameters: olive tail moment (A) and % tail DNA (B) obtained after 3 h exposure of A431 cells to different concentrations of B-TiO_2 nanoparticles.*

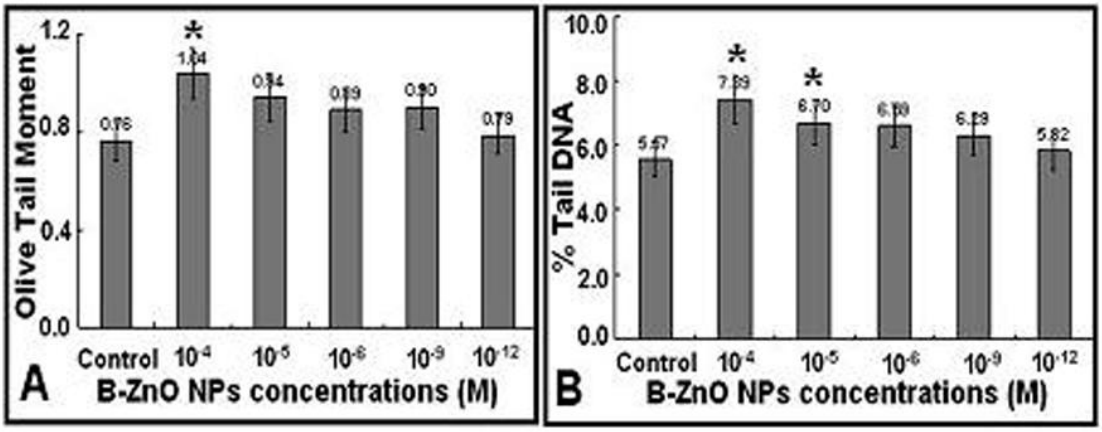

Figure 5.14: *Statistical data representing the two important COMET parameters: olive tail moment (A) and % tail DNA (B) obtained after 3 h exposure of A431 cells to different concentrations of B-ZnO nanoparticles.*

Although, very less fragments of DNA could be seen as tail (Figure 5.14 I and 5.14 J), a smaller DNA head seen suggest to loss of DNA. The concentration above 10^{-4} M was not taken for experiment as it resulted in apoptosis (Figure 5.14 H) and according to COMET assay guidelines this concentration should not be considered for the comet experiment. Again, slight increase in OTM values (0.38, 0.14, 0.0, 0.0, 0.0 unit) was obtained when A431 cells were exposed to different concentrations (10^{-3} M, 10^{-4} M, 10^{-5} M, 10^{-6} M and 10^{-9} M) of B-TiO_2 nanoparticles (Figure 5.13 A). But even the highest concentration (10^{-3} M) was not of any significance when analyzed using

ANOVA ($p < 0.05$). This result was further confirmed by respective COMET images (Figure 5.15 B to F). In contrast, B-ZnO nanoparticles show significant increase in OTM (0.28 unit) at the concentration (Figure 5.14 A) of 10^{-4} M when analyzed using ANOVA ($p < 0.05$). Other concentrations (10^{-5} M, 10^{-6} M, 10^{-9} M and 10^{-12} M) of B-ZnO also showed increase in OTM values (0.18, 0.13, 0.14 and 0.03 unit), which did not show any significance when analyzed using ANOVA ($p>0.05$). Corresponding COMET images shown in Figure 5.14 I to L further supported this result.

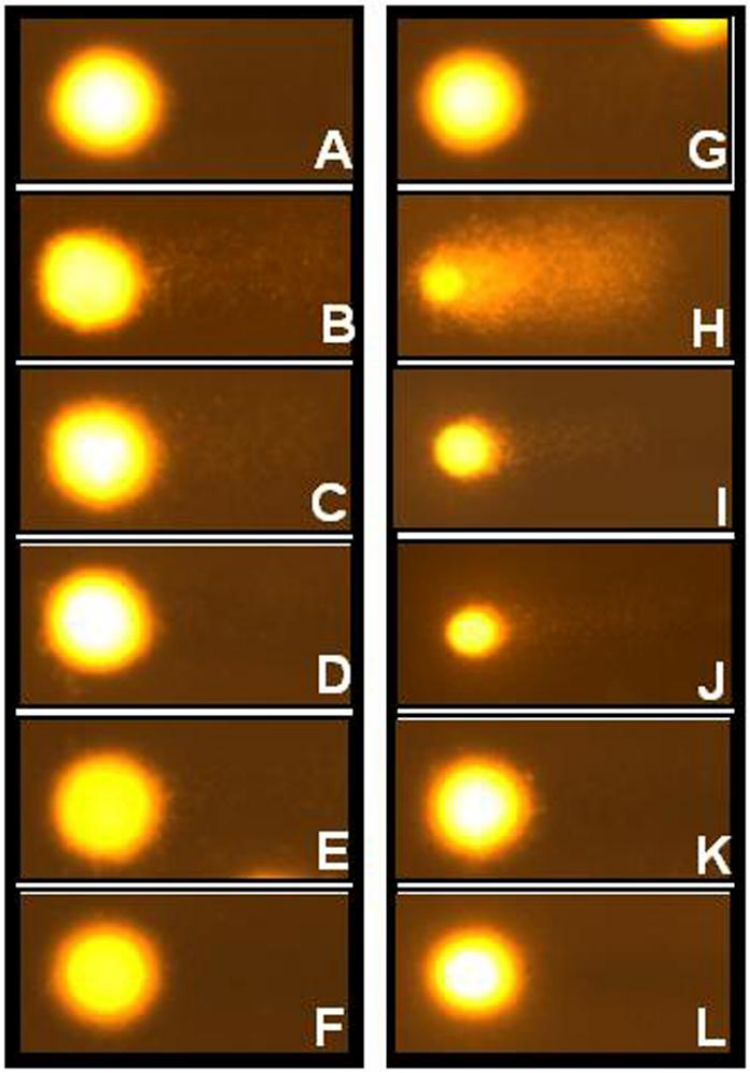

Figure 5.15: *COMET images showing DNA damage of A431 cells after exposure to different concentrations of B-TiO_2 (Control (A), 10^{-3} M (B), 10^{-4} M (C), 10^{-5} M (D), 10^{-9} M (E) and 10^{-12} M (F)) and B-ZnO (Control (G), 10^{-3} M (H), 10^{-4} M (I), 10^{-5} M (J), 10^{-9} M (K) and 10^{-12} M (L)).*

After the comparative analysis of cytotoxicity (MTT) and genotoxicity (COMET) data, it can be concluded that B-TiO_2 nanoparticles are more biocompatible

than B-ZnO nanoparticles as the former did not show any significant toxicity (cytotoxicity and genotoxicity) to human skin cell lines up to a concentration of 10^{-3} M. However, B-ZnO nanoparticles were found significantly genotoxic even at a concentration of 10^{-4} M. One important point could be noticed here, which would signify the importance as well as sensitivity of COMET assay over MTT assay. On the basis of MTT results, B-ZnO nanoparticles (10^{-4} M) could be considered as nontoxic, whereas COMET result revealed that this concentration is highly genotoxic. Thus, it could be hypothesized that smaller particles of B-ZnO could be internalized by cells through their pores of membrane and further could reach into the nucleus through nuclear pores. Further, these B-ZnO nanoparticles could lead to the generation of ROS within the nucleoplasm, leading to fragmentation of DNA.

5.4 Conclusions

This chapter describes the cytotoxicity and genotoxicity evaluation of sophorolipid reduced Au and Ag nanoparticles against human liver carcinoma cell lines (HepG2 cells). Also, toxicity study of biosynthesized TiO_2 and ZnO nanoparticles have been conducted on human skin cell lines (A431). Sophorolipid reduced Au and AgNPs showed biocompatability up to the concentration of 10^{-4} M, which is considerably higher than the reported values. Among OA-SL-AuNPs and OA-SL-AgNPs, the former showed better biocompatibility within the same concentration exposed to cells. Therefore, they can be safely used for different bioapplications. Further, B-TiO_2 showed better compatibility with skin cell line than B-ZnO up to a concentration of 10^{-3} M, thus suggesting the use of B-TiO_2 nanoparticles for various skin related applications, whereas B-ZnO could be recommended to be used below 10^{-5} M.

We would like to add a note with caution here that these were the general observation and conclusions on the basis of *in vitro* experiments, where “the body” is replaced by “a single mammalian cell” but the scenario could be different within *in vivo* experimental conditions. Moreover, the risk of any potentially toxic substance is not only a function of hazard but also chance of exposure. At the current scenario, it would be premature to conclude that nanoparticles are completely unsafe or

biocompatible, rather additional systematic studies are required before toxicity relationships can be understood in more complex human system at the molecular level. Also, future research should concentrate more to engineer relatively safer nanomaterials for clinical applications.

5.5 References

[1] (a) Schmid, G. *Nanoparticles from theory to Applications*, **2004**, Wiley-VCH, Weinheim (b) http://www.nano.gov.

[2] Erhardt, D. *Nat. Mater*. **2003**, *2*, 509.

[3] www.visionminerals.com.

[4] Dowling, A. *Nanotoday*. **2004**, 30.

[5] McIntosh, C. M.; Esposito, E. A.; Boal, A. K.; Simard, J. M.; Martin, C. T.; Rotello, V. R.; *J. Am. Chem. Soc.* **2001**, *123*, 7626.

[6] Zheng, M.; Davidson, F.; and Huang, X. Y. *J. Am. Chem. Soc.* **2003**, *125*, 7790.

[7] (a) Ogris, M.; Carlisle, R. C.; Bettinger, T.; Seymour, L.W. *J. Biol. Chem.* **2001**, *276*, 47550.(b) Kullberg, E. B.; Bergstrand, N.; Carlsson, J.; Edwards, K.; Johnsson, M.; Sjo¨berg, S.; Gedda, L. *Bioconjugate Chem.* **2002**, *13*, 737. (c) Leuschner, C.; Enright, F. M.; Melrose, P. A.; Hansel, W. *The Prostate* **2001**, *46*, 116.

[8] Connor, E. E.; Mwamuka, J.; Gole, A.; Murphy, C. J.; Wyatt, M. D. *Small* **2005**, *1*, 325.

[9] Pan, Y.; Neuss, S.; Leifert, A.; Fischler, M.; Wen, F.; Simon, U.; Schmid, G.; Brandau, W.; Jahnen-Dechent, W. *Small* **2007**, *3*, 1941.

[10] Shukla, R.; Bansal, V.; Chaudhary,M.; Basu, A.; Bhonde, R. R.; Sastry, M. *Langmuir* **2005,** *21*, 10644.

[11] Goodman, C. M.; McCusker, C. D.; Yilmaz, T.; Rotello, V. M *Bioconjugate Chem*. **2004**, *15*, 897.

[12] Chithrani, B. D.; Ghazani, A. A.; Chan, W. C. *Nano Lett*. **2006**, *6*, 662.

[13] Tsoli, M.; Kuhn, H.; Brandau, W.; Esche, H.; Schmid, G. *Small* 2005, *1*, 841.

[14] Yu, D.-G. *Colloids and Surfaces B: Biointerfaces* **2007**, *59*, 171.

[15] Hussain, S. M.; Hess, K. L.; Gearhart, J. M.; Geiss, K.T.; Schlager, J. J. *Toxicology in Vitro* **2005**, *19*, 975.

[16] Lee, K. J.; Nallathamby, P. D.; Browning, L. M.; Osgood, C. J.; Nancy Xu, X. -H. *ACSnano*, **2007**, *1*, 133.

[17] Sayes, C. M.; Wahi, R.; Kurian, P. A.; Liu, Y.; West, J. L.; Ausman, K. D.; Warheit, D. B.; Colvin, V. L. *Toxicological Sciences* **2006**, *92*, 174.

[18] Long, T. C.; Tajuba, J.; Sama, P.; Saleh, N.; Swartz, C.; Parker, J.; Hester, S.; Lowry, G. V.; Veronesi, B. *Environmental Health Perspectives* 2**007**, *115*, 1631.

[19] H. A. Jeng, J. Swanson, *Journal of Environmental Science and Health Part A*, **2006**, *41*, 2699

[20] (a) Smart, S. K.; Cassady, A. I.; Lu, G. Q.; Martin, D. J.; *Carbon* **2006**, *44*, 1034. (b) Rothen-Rutishauser, B. M.; Schu¨rch, S.; Haenni, B.; Kapp, N.; Gehr, P. *Environ. Sci. Technol.* **2006**, *40*, 4353. (c) Lynch, I.; Dawson, K.A.; Linse, S. Sci. STKE **2006,** *327*, pe 14.

[22] Nel, A.; Xia, T.; Madler, L.; Li, N. *Science* **2006**, *311*, 622.

[23] Oberdorster, G.; Oberdorster, E.; Oberdorster, J. *Environ. Health Perspect.* **2005**, *113*, 823.

[24] Dunford, R.; Salinaro, A.; Cai, L.; Serpone, N.; Horikoshi, S.; Hidaka, H.; Knowland, J. *FEBS Lett* **1997,** *418*, 87.

[26] Oberdorster E. *Environ. Health Perspect.* **2004,** *112*, 1058.

[27] T. Mosmann, *Journal of Immunological Methods*, 1983, **65**, 55.

[28] Singh, N. P.; McCoy, M. T.; Tice, R. R.; Schneider, E. L. *Exp. Cell Res.* **1988**, *175*, 184.

[29] (a) Olive, P. L., Banath, J. P. and Durand, R. E. *Radiat. Res*. **1990**, *122*, 86. (b). Olive, P. L. Wlodek, D., Durand, R. E. and Banath, J. P. *Exp. Cell Res*. **1992**, *195*, 259. (c) Bilbao, C.; Ferreiro, J. A.; Comendador, M. A.; Sierra, L. M. *Mutat. Res.* **2002**, *503*, 11.

[30] Hartmann *et al*. *Mutagenesis* **2003**, *18*, 45.

Chapter VI

Conclusions

This chapter contains conclusions of the salient features of the work described in this thesis and the scope for future potential developments in this field.

6.1 Summary of the work

The work presented in this thesis mainly focuses on biological methods for the synthesis of nanomaterials and their toxicity evaluation. All this has been described in different chapters and the summary for each chapter has been described here.

The bacterium *Actinobacter* spp. was isolated as a contaminant from a mixture of $K_4Fe(CN)_6$ and $K_3Fe(CN)_6$ left open for one week. It has been used for the synthesis of different technologically important nanomaterials such as Si/SiO_2 nanocomposites, TiO_2 and ZnO nanoparticles under environmentally benign conditions. The known chemical and physical methods for synthesis of these nanomaterials involve high temperature and pressure. In contrast to that the method we report is an attractive alternative to such methods. Elemental silicon embedded within SiO_2 matrix (Si/SiO_2 nanocomposites) has several applications in photonic devices. We have shown that two proteins reductases and hydrolases secreted by the bacteria probably lead to the reduction of Si^{4+} to Si^0 and subsequently to SiO_2. Other oxides (TiO_2 and ZnO) have also been extensively used for different applications and probably are the first ones to be used at market level as photocatalytic and UV-absorbent agents. Since visible light mediated photocatalytic technology has attracted much attention in the recent research trend, a successful attempt has been performed by simultaneous doping of C, N and F elements into the biosynthesized TiO_2 (B-TiO_2) lattice. Doping made this material a potential agent for photocatalytic degradation of methylene blue dye under sunlight illumination. A comparative study between doped B-TiO_2 and B-ZnO (biosynthesized ZnO) is also presented, which suggested B-ZnO, as better visible light phaotocatalyst than titania.

Glycolipid (sophorolipid) mediated synthesis of gold and silver nanoparticles have also been reported. Yeast (*Candida bombicola*) mediated synthesis/capping of this bio-surfactant, which has been employed successfully to obtain these nanoparticles in powder form, which could be completely redispersed in aqueous medium. The silver nanoparticles thus synthesized exhibited enhanced bactericidal activity against both Gram-positive and Gram-negative bacterial species. As most of the pathogenic microbes are gaining resistance to most of the available antibiotics,

silver nanoparticles have been used extensively especially as antimicrobial agent. The simple method for the synthesis of silver nanoparticles makes a cheap and best alternative to the antibiotics.

Toxicity studies of nanomaterials are very hot topics of research now days, as people are more concerned towards the possible short term and long term risk of nanoparticles. The fast developing field of nanoscience has also provoked researchers to look towards the potential environmental and biological effects of nanoparticles. We have also made an attempt to evaluate cytotoxicity as well as genotoxicity of the above-mentioned bio-mediated/biosynthesized metal and metal-oxide nanoparticles. These materials were found to be biocompatible up to the millimolar concentrations (except B-ZnO). B-ZnO nanoparticles showed DNA damage even at 10^{-5} M concentrations.

6.2 Scope for future work

One of the most challenging aspects of microbial synthesis of nanomaterials is to identify the proteins/enzymes and their subsequent DNA fragment, which actually governs the biochemical pathway. This would lead to synthesis of respective nanomaterials in bulk quantity and thus biotechnologists would be able to fulfil the industrial needs.

Sophorolipid molecules, by virtue of the presence of glucose moieties are expected to be able to cross the blood brain barrier. Therefore, quantum dots conjugated with these molecules could be used as potential agents for imaging as well as drug delivery in brain. Silver nanoparticles synthesized by biological means or conjugated with biomolecules can serve as good wound healing agents. To further improve on this idea, these nanoparticles could be incorporated into suitable matrices such as polymers to acts as wound dressing agents or can be formulated into creams for topical applications.

The toxicity evaluation of nanomaterials can be further studied in depth at the genetic level where the genes involved in the process can be identified in order to put forth well-accepted mechanism.

Appendix I

Microbiological Media

1) Luria Broth

Tryptone	1 %
Yeast Extract	0.5 %
NaCl	0.5 %
D/W	100 mL
pH	7.2

2) Luria Broth Agar

Tryptone	1 %
Yeast Extract	0.5 %
NaCl	0.5 %
Agar	2%
D/W	100 mL
pH	7.2

3) MGYP

Malt Extract	0.5 %
Glucose	1 %
Yeast Extract	0.3 %
Peptone	0.5 %
D/W	100 mL

Appendix II

List of Publications

[1] *Effect of halogen addition to monolayer protected gold nanoparticles*. **Sanjay Singh**, R. Pasricha, U. M. Bhatta, P. V. Satyam, M. Sastry**,** B. L. V. Prasad**.** *J. Mater. Chem.* **2007**, *16*, 1614-1619.

[2] *Nearly Complete Oxidation of Au^0 in Hydrophobized Nanoparticles to Au^{3+} ions by N-Bromosuccinimide.* **Sanjay Singh**, B. L. V. Prasad, *J. Phys. Chem. C* **2007**, *111*, 14348-14352.

[3] *Bacterial synthesis of Copper/Copper Oxide Nanoparticles*. S. S. Hasan, **Sanjay Singh**, R. Y. Parikh, M. S. Dharne, M. S. Patole, B. L. V. Prasad, Y. S. Shouche, *J. Nanosci. Nanotechnol.* **2007,** (ASAP).

[4] *Sophorolipid capped Co-nanoparticles: Synthesis of stable and water dispersible Co-nanoparticles.* M. Kasture, **Sanjay Singh**, P. Patel, P. A. Joy, A. A. Prabhune, C. V. Ramana, B. L. V. Prasad, *Langmuir* **2007**, *23*, 11409-11412.

[5] *Silicate nanoparticles by bioleaching of glass and modification of the glass surface.* S. Kulkarni, A. Sayed, **Sanjay Singh**, A. Gaikwad, K. Vijayamohanan, A. Ahmed, S. Ogale, *J. Non-crystalline Solids* **2008**, (ASAP).

[6] *Extracellular Synthesis of Crystalline Silver Nanoparticles and Molecular Evidence of Silver Resistance from Morganella sp.: Towards Understanding Biochemical Synthesis Mechanism.* R. Y. Parikh, **Sanjay Singh**, M. S. Patole, M. Sastry, B. L. V. Prasad, Y. S. Souche, *ChemBioChem* **2008** (ASAP).

[7] *Bacterial Synthesis of Si/SiO_2 nanocomposites and their Biocompatibility Studies.* **Sanjay Singh**, U. M. Bhatta, P. V. Satyam, A. Dhawan, M. Sastry, B. L. V. Prasad, *J. Mater. Chem.* **2008,** *18*, 2601-2606.

[8] *Enhancement of cell bound Penicillin V acylase activity through permeabilization of a newly identified source, Rhodotorula aurantiaca (NCIM 3425).* A. Kumar, **Sanjay Singh**, A. Prabhune, P. Poddar, A. Pundle, *Enzyme and Microbial Technology* **2007** (in press).

[9] *Bacterial Synthesis of Titania and Zinc Oxide nanoparticles and their Photocatalytic Activities.* **Sanjay Singh**, M. Sastry, B. L. V. Prasad (Manuscript under preparation).

[10] *Synthesis of Silver nanoparticles using Sophorolipids as capping and reducing agents and their antimicrobial activity.* **Sanjay Singh**, P. Patel, A. A. Prabhune, C. V. Ramana, B. L. V. Prasad **2008** (Communicated).

[11] *Genotoxicity and cyto-toxicity studies of biosynthesized metal oxide nanoparticles on human cell-lines.* **Sanjay Singh**, V. D' Britto, A. Dhawan, M. Sastry, B. L. V. Prasad, (Manuscript under preparation).

[12**]** *Glycolipid reduced metal nanoparticles and their cytotoxicity and genotoxicity studies* **Sanjay Singh**, V. D' Britto, A. Dhawan, M. Sastry, B. L. V. Prasad, (Manuscript under preparation).

[13] *Comparative toxicity assesment of chemically and biologically synthesized metal nanoparticles.* V. D' Britto, **Sanjay Singh**, A. Dhawan, B. L. V. Prasad (Manuscript under preparation).